Ultrafast Lasers in Additive Manufacturing

ULTRAFAST LASERS IN ADDITIVE MANUFACTURING

By

JACOB SAUNDERS, B.Sc.

A Thesis

Submitted to the School of Graduate Studies

In Partial Fulfilment of the Requirements for the Degree

Master of Applied Science

McMaster University

Master of Applied Science (2022) McMaster University
Department of Engineering Physics Hamilton, Ontario

TITLE: Ultrafast Lasers in Additive Manufacturing

AUTHOR: Jacob Saunders, B.Sc., McMaster University

SUPERVISOR: Professor Qiyin Fang

NUMBER OF PAGES: 145

Lay Abstract

Ultrafast pulsed lasers of <10 picoseconds pulse duration are commonly used to modify, melt, or ablate materials. As an important research and manufacturing tool, ultrafast lasers and techniques have seen great change in the past two decades. Additive manufacturing has emerged as an area in which ultrafast lasers are becoming increasingly prevalent. To make sense of this continuously evolving landscape, this thesis 1) reviews ultrafast laser additive manufacturing techniques, applications, and advances towards industrial use and commercialisation, 2) compares the setup, operability, and characteristics for two ultrafast laser designs, and 3) investigates the surfaces produced by ultrafast laser irradiation of an additively manufactured titanium alloy part. The surface morphologies that are produced are categorised into five main patterns: laser-induced periodic surface structures, undulating grooves, micro-ripples, grooves, and micro-cavities. Each is a distinct pattern that may allow for tuning of the surface properties with respect to the wettability and biocompatibility.

Abstract

Ultrafast lasers are valuable research and manufacturing tools. The ultrashort pulse duration is comparable to electron-lattice relaxation times, yielding unique interactions with matter, particularly nonlinear absorption, melting, and ablation. The field of ultrafast laser manufacturing is rapidly evolving with advances in related laser technologies. The applications of ultrashort pulse lasers in additive manufacturing aim to fill gaps left by conventional techniques especially on the nano- and micro-scale. Concurrently, uptake of ultrafast fiber lasers for micromachining has increased, and may replace the Ti:Sapphire laser as the ultrafast laser of choice. Both additive and subtractive manufacturing are accomplished with ultrafast lasers which presents the possibility of hybrid, all-in-one devices using a single laser source. As one such combination of laser techniques, ultrashort pulse surface modification of additively manufactured metals is an area of limited investigation.

This thesis aims to address the ever-changing landscape of ultrafast laser manufacturing by 1) reviewing ultrafast laser additive manufacturing techniques and recent advancements 2) comparing the design, operation, and micromachining potential of a commercial ultrafast Ti:Sapphire and ultrafast fiber laser, and 3) investigating femtosecond ablation of as-printed additively manufactured Ti-6Al-4V at a range of parameters to test the feasibility of surface feature control. Ultrafast laser additive manufacturing is still in its infancy with mostly niche applications. The ultrafast fiber laser architecture is found to deliver a platform that is easier to operate and maintain and has superior micromachining throughput relative to Ti:Sapphire lasers. In our experimental work, five main surface morphologies are obtained by femtosecond ablation of a rough Ti-6Al-4V surface: laser-induced periodic surface structures (LIPSS), undulating grooves, micro-ripples, grooves, and micro-cavities. Transitions between ablation regimes and evolutions of the surface under increasing pulse energy and number of pulses are observed. These patterns allow for control over the surface geometry without the need for post-printing polishing.

Acknowledgements

I would first like to thank my supervisor, Dr. Qiyin Fang for the opportunity to work in the McMaster Biophotonics research group. Thank you for the thoughtful advice you provided over the last few years, and the kind patience in all things. Thank you to Dr. Harold Haugen, for all of your help and guidance, in setting up and running the laser systems. Thank you both for the discussions we had about future careers, and the personal experiences that you have shared.

Thank you to everyone in the Biophotonics group, Ian Philips, Morgan Richards, Tianqi Hong, Michael Zon, Zach Minuk, Eric Mahoney, Guha Ganesh, for your companionship and for the many times that I asked for your help. I have great memories of my experience in this group, and I learned something from everyone. A special thanks to Dr. Mostafa Yakout for all of his help, from acquiring samples to answering my relentless questions.

Of course, thank you to my family, who have supported me in countless ways over the years, both in Undergrad and throughout Grad school. Thank you for everything.

Table of Contents

List of Figures

List of Tables

List of Abbreviations

1PP	One photon polymerisation
2PP	Two photon polymerisation
AM	Additive manufacturing
AOM	Acousto-optic modulator
CAD	Computer aided design
CARS	Coherent anti-Stokes Raman scattering
CCD	Charge-coupled devicer
CMOS	Complimentary metal-oxide semiconductor
CPA	Chirped pulse amplification
CW	Continuous wave
DLW	Direct laser writing
DMD	Digital micromirror device
DP	Double pulse
FLICE	Femtosecond laser induced chemical etching
FWHM	Full width half maximum
GVD	Group velocity dispersion
HAZ	Heat-affected zone
HSFL/LSFL	High/low spatial frequency LIPSS
KLM	Kerr-lens mode locking
LIBS	Laser-induced breakdown spectroscopy
LIFT	Laser-induced forward transfer
LIPSS	Laser-induced periodic surface structures
MEMS	Micro-electromechanical systems
MOPA	Master oscillator power amplifier
MPL	Multiphoton lithography
NA	Numerical aperture

PBF	Powder-bed fusion
PLD	Pulsed laser deposition
SAP	Surface as-printed
SEM	Scanning electron microscope
SESAM	Semiconductor saturable absorber mirror
SHG/THG	Second/Third harmonic generation
SLM	Selective laser melting
STED	Stimulated emission depletion
UHMWPE	Ultra-high molecular weight polyethylene
UTS	Ultimate tensile strength
UV	Ultra-violet
WDM	Wavelength division multiplexer

Chapter 1: Introduction

Ultrafast lasers, also referred to as ultrashort pulse lasers, are typically described as lasers with pulse duration shorter than 10 picoseconds and especially in the femtosecond regime. When a material is irradiated by an ultrashort pulse of sufficient intensity, it results in unique interactions when compared to longer pulses. This is because the pulse duration is on a timescale comparable to that of the electron-lattice processes of the irradiated matter [42]. The material modification that occurs as a result of these interactions enables a variety of novel, ground-breaking technologies and creates new processing windows and applications for existing technologies. All lasers allow for localized energy input that leads to heating, melting, ablation, and curing, but ultrafast lasers are capable of even greater localization of material modification and thus superior quality in manufacturing. Additionally, they can create extreme energy gradients that melt or ablate even the most problematic of materials [43]. Ultrafast lasers are well known for and excel in precise subtractive manufacturing: the removal of material to reveal the structure within. However, we have also seen rapid advancements in their use as additive manufacturing tools. Ultrafast laser additive manufacturing takes many forms and reviewing them and their advances towards industrial use is a contribution of this dissertation.

For decades Ti:Sapphire laser designs have been used for ultrashort pulse generation and research. Their broad gain bandwidth allows for the generation of femtosecond pulses, but their complicated architecture poses a challenge for operation. On the other hand, fiber lasers have become increasingly popular as ultrashort pulse sources. Commercial systems are compact and relatively cheap [44]. An experiential comparison of two such systems can provide insight as to the rapid adoption of fiber lasers.

Selective laser melting is an additive manufacturing (AM) method that can produce fully dense metallic parts from computer-aided design files. This is achieved by cyclically melting layers of loose powder with an intense beam. Although near-net-shaped parts can be manufactured, the surface finish is rough compared to that produced by conventional methods [45]. Powder at the edges of the part is partially sintered to the surface, increasing the roughness. Post-processing is often necessary, but the complex geometries of 3D-printed objects reduce the effectiveness of conventional surface processing techniques [46].

Ultrafast lasers can be used to modify surfaces by precise ablation. The intense pulses are focused at and repeatedly scanned over the sample surface. Depending on the laser parameters, a variety of patterns are obtained. Nano- and micro-scale features develop that alter surface properties such as the reflectivity, wettability, and biocompatibility [47]. Currently, only a few studies have investigated ultrafast laser surface modification of selectively laser melted parts [48], [49]. The surface morphologies that are obtained for a range of process parameters have not been expounded.

This dissertation presents an overview of ultrafast lasers from modern additive manufacturing techniques to a comparison of a Ti:Sapphire and fiber laser architectures to ultrashort pulse

surface modification of a selectively laser melted Ti-6Al-4V part. In this way, the future of ultrafast lasers is discussed from the perspectives of 1) additive manufacturing, 2) the laser system architectures that best support machining, and 3) subtractive (ablative) manufacturing.

Chapter 2 reviews the state of ultrafast laser additive manufacturing technologies and their advancements in process monitoring, throughput, and hybridisation, all of which contribute towards their adoption as a preferred manufacturing technique.

Chapter 3 compares the design, operation, and micromachining advantages/disadvantages for an ultrafast Ti:Sapphire system and an ultrafast fiber system.

Chapter 4 delivers an experimental investigation of femtosecond laser surface modification using the Ti:Sapphire system described in Chapter 3 of a selectively laser melted part. Laser parameters were varied in pulse energy, scanning speed, and number of passes, and the resultant surface was analysed by scanning electron microscope. Mechanisms for the formation of various patterns and engineering of the surface by variation of the parameters is discussed.

Chapter 5 summarizes each of the chapters and presents major connections and conclusions of the thesis.

This thesis contributes to future research and to our understanding of ultrafast laser manufacturing in several ways:

1) It identifies the key techniques in ultrafast laser additive manufacturing and curates their recent progress to provide a comprehensive overview in a single source. The limitations, gaps, and potential in additive manufacturing methods are outlined for readers to determine prospective research areas.
2) The critical comparison of fiber and Ti:Sapphire lasers confirms similar comparisons made in literature, and provides insight into how the commercial ultrafast laser space will evolve.
3) Development of a methodology and range of process parameters for ultrafast laser surface modification of selectively laser melted Ti-6Al-4V, the characterisation of surface morphologies obtained, and discussion of their applications and suitability for surface functionalisation. This is an initial step towards understanding the interaction between selective laser melting materials and ultrafast laser radiation and thus the hybridisation of two burgeoning laser technologies.

Chapter 2: Review of Ultrafast Lasers in Additive Manufacturing

This chapter contains material to be submitted to Frontiers in Physics: Sec. Optics and Photonics. Below is an accurate and detailed description of each author's contributions to the work included in this chapter. Jacob Saunders: literature research, conceptualisation, writing – original draft, visualisation; Dr. Qiyin Fang: conceptualisation, writing – review and editing.

2.1 Introduction

Additive manufacturing (AM) is an increasingly popular process by which a build or part is constructed in a layer-by-layer fashion. AM offers many benefits, such as the ability to produce true internal geometries, on-demand customized parts, freedom to design complex parts, and reduced environmental impact [50]–[52]. Lasers are an indispensable tool in AM because they are well controlled in space via focusing elements, interference patterns, etc., and well controlled in time by their pulse duration and repetition rate. Ultrashort pulse lasers have a niche in AM, and have potential in or are already used as tools for the powder bed fusion (PBF) of hard-to-process metals and ceramics, 3D multiphoton lithography (MPL), laser-induced forward transfer (LIFT), welding and joining, and pulsed laser deposition (PLD). It is the intention of this review to describe the development, past applications, and recent advancements of these techniques. As ultrafast laser AM technologies continue to mature, their adoption by industry and incorporation into commercial systems will be facilitated by key factors such as, but not limited to consistent build quality via process monitoring and control, high throughput, and ability to be integrated into hybrid manufacturing systems. These three named factors are considered here in the context of the aforementioned techniques.

2.2 Brief Description of Ultrafast Lasers

Since the first report of laser action in 1960, lasers have undergone significant advancement and played a crucial role in many seminal discoveries and publications [53]. Several Nobel Prizes have been awarded for work directly related to or involving lasers, such as the 1964 Nobel Prize in Physics to Townes, Basov and Prokhorov for work that "led to the construction of oscillators and amplifiers based on the maser-laser principle" [54]. Kastler received the 1966 Nobel Prize for optical pumping, Bloembergen and Shawlow in 1981 for contributions to laser spectroscopy, and most recently Mourou and Strickland in 2018 for their chirped-pulse amplification (CPA) technique. Lasers can be operated in a continuous wave (CW) mode, in which their output intensity is constant over time, or they can be pulsed. Two essential ways for pulsing a laser are Q-switching and mode locking.

2.2.1 Ultrashort Pulse Generation

Q-switching was first demonstrated with a ruby maser and Kerr cell shutters in 1961 [55]. The technique involves periodically reducing the "Q factor", or "quality factor", of the resonant cavity of a laser or maser, such that the population inversion in the gain material builds while round-trip lasing action cannot occur. When the Q factor is restored, the stored energy in the gain medium results in a swift buildup of resonating light in the cavity that depletes the population inversion and prevents further lasing [56]. Ultimately, a short pulse of high intensity is produced. Although conventional Q-switching produces nanosecond pulses, they have difficulties producing pulses of picosecond duration due to large cavity lengths [57][58][59]. To generate the ultrashort pulses of interest, down to single-digit femtosecond durations, mode locking is the universal technique [60]. It was first observed in a HeNe laser in 1964 [61], but ultimately the narrow gain linewidth of HeNe limited pulse durations to the nanosecond regime. Self mode locking was soon demonstrated in an Nd:glass laser in 1966 [62]. For many years the field of ultrashort optics was dominated by dye and rare-earth doped solid-state lasers, which contributed greatly to our understanding of mode locking and the methods of achieving this operational mode [63]–[65]. Rare-earth doped solid-state lasers (e.g., Nd^{3+}, Er^{3+}, Yb^{3+}) readily provide picosecond pulses at fixed wavelengths and have a high energy storage capacity that make them proficient amplifiers but are limited in the mode locking techniques that apply to them and can easily Q-switch when saturable absorbers are present in the cavity [63], [66]. Organic dye media constituted a wide range of tunable wavelength lasers, whose high gain cross sections and broad gain linewidths allowed for the generation of femtosecond pulses [67]. Dye lasers formed a significant part of the basis upon which our understanding of ultrashort laser physics stands, but came with their own challenges, most notably that they were inefficient, impractical, and primarily found in high-end research labs [64]. In 1986, a new high-gain cross section, broad absorption and emission linewidths, solid-state lasing medium came onto the scene: titanium-doped sapphire ($Ti:Al_2O_3$) [68]. Ti:Sapphire lasers combine advantages from both dye and rare-earth doped lasers and were a promising candidate for a more practical femtosecond laser. Indeed, Spence et al. [69] discovered self-mode-locking in a Ti:Sapphire laser due to the Kerr-lens mode locking (KLM) effect. The optical Kerr effect results from the intensity-dependent index of refraction in the Ti:Sapphire gain medium, resulting in a "lensing" pulse effect that will see less loss than the CW spatial mode if the cavity is effectively aligned [70]–[72]. This effect, in addition to other improvements such as dispersion compensation methods and the introduction of semiconductor saturable absorber mirrors (SESAMs), allows for the reliable generation of pulses as short as 6.5 fs [73]. As a practical and tunable femtosecond source, Ti:Sapphire lasers are responsible for significant advancement of scientific understanding in the behaviour of physical systems at these timescales, spectroscopy, nonlinear optics, and with increased amplification, material processing and manufacturing [65].

2.2.2 Amplification

Amplification of ultrashort pulses is a challenge due to the high peak power and the nonlinear optical effects it can produce in air and gain media, leading to plasma formation and damage [74]. Strickland et al. [75] introduced a method of amplification, referred to as chirped pulse amplification, in which the pulses are stretched to reduce the peak intensity, amplified in a gain medium while remaining below the damage threshold, and then compressed in the opposite manner of the stretching so that the ultrashort pulse is recovered with peak intensities in the TW regime. The typical configuration utilises diffraction gratings for stretching and compression of the beam, and a regenerative amplifier cavity for amplification.

The resultant setup for most high-power, ultrashort laser systems, is that of the master oscillator power amplifier (MOPA) design. The master oscillator is a mode locked laser that is optimised for pulse duration, centre wavelength, and spatial beam qualities. The (comparatively) low-energy pulses are passed into a power amplifier consisting of stretching, regenerative amplification, and compression. Regenerative and multipass amplifiers are typical schemes for accomplishing high power pulses. Commercial ultrafast systems commonly provide > 1 W average power and mJ pulse energies. Such pulses are sufficiently powerful to initiate unique interactions with many materials that lead to manufacturing techniques such as nanoscale and micron scale ablation, multiphoton polymerisation, additive manufacturing, pulsed laser deposition, and others. Ultrashort laser matter interaction is discussed in Section 3.

2.2.3 Fiber Lasers

Parallel to the emergence of KLM Ti:Sapphire lasers, mode locked Nd-doped fiber lasers generating ultrashort pulses were developed [76], [77]. While the interest originally came from communications and data transmission applications, integration of fiber lasers into MOPA designs allowed for pulse energies that enable micromachining and other manufacturing procedures that will be discussed later. Commercial ultrashort Er-fiber (1.55 μm) and Yb-fiber (1.03 μm) lasers are now prevalent, and are more adaptable, compact, and require less alignment than their rod-shaped counterparts [44]. For industrial applications, their high average power and repetition rate (tens of MHz) are also attractive for efficient material processing. There are many recent reviews on ultrafast fiber lasers, such as [44], [78], [79].

2.3 Ultrashort Pulse Laser-Matter Interaction

Ultrashort laser pulses and their interactions with matter are explained by the pulse duration and intensity. For material modification purposes, focused beams deliver high peak intensities (~10^{15} W/cm^2) over a period that is shorter or comparable to the subatomic processes that are responsible for heat and energy transfer within a bulk material [80], [81]. Highly localised nonlinear absorption occurs, causing extreme energy gradients and rapid heating (10^{14} K/s) and

cooling rates that result in melting, ablation, and/or complex structural and phase changes (Figure 2.1) [82]–[86].

2.3.1 Metals and the Two-Temperature Model

In strongly absorbing materials such as metals, ultrashort pulse radiation is absorbed by conduction-band electrons via inverse Bremsstrahlung. Electron subsystem thermalization is on the order of femtoseconds, and the electrons transfer their energy to atomic lattice vibrations (electron-phonon coupling) picoseconds after irradiation [84]. Since the pulse duration is shorter than the electron-lattice equilibration time, the nonequilibrium situation is described by a two-temperature model wherein the time evolution of electron and ion temperatures are treated separately and connected by an electron-lattice coupling constant [87]–[89]. The two-temperature model fundamental equations:

$$C_e \frac{\partial T_e}{\partial t} = \nabla(\kappa_e \nabla T_e) - \Gamma_{e-l}(T_e - T_l) + Q(x_a, t) \quad (1)$$

$$C_l \frac{\partial T_l}{\partial t} = \nabla(\kappa_l \nabla T_l) - \Gamma_{e-l}(T_e - T_l) \quad (2)$$

Where *e* and *l* refer to electron and lattice parameters, *C* the heat capacity, *k* the thermal diffusivity, Γ the electron-lattice coupling constant, and *Q* the irradiating laser.

If the intensity is high enough, the transfer of energy from the superheated electrons into the lattice subsystem results in a violent phase change and material ejection with micron- and even nano-scale resolution [90] [91], [92]. Since thermal diffusion into the bulk material occurs on a longer timescale, the surrounding material heats less appreciably. Thus, the heat-affected zone of ultrafast laser modification is significantly smaller than that of ns or continuous wave lasers, producing minimal collateral damage and making it desirable for micro- and nano-machining applications. If the fluence is below the ablation threshold, there are melting regimes in which the nonequilibrium situation rapidly heats the lattice to the melting point. For sufficiently high intensities, superheating of the lattice gives way to homogeneous nucleation and melting mere picoseconds after the pulse [93]–[95].

2.3.2 Bandgap Materials

In bandgap materials such as semiconductors and dielectrics, electrons are first excited into the conduction band and then continue to absorb photons and increase in energy. For longer pulses,

these electrons transfer energy to the lattice and cause subsequent heating and damage [96]. The electronic excitation by high intensity ultrashort pulses that promotes a significant portion of electrons from the valence band (about 10%) may affect the interatomic bonding such that melting or other phase transformations occur [97][98]. Such transformations are considered athermal, as they are not a result of lattice equilibration and heating. From the conduction band, free electrons gain kinetic energy by absorbing additional photons, leading to a plasma state or, in the case of extreme ionisation, Coulombic explosion [1], [99], [100].

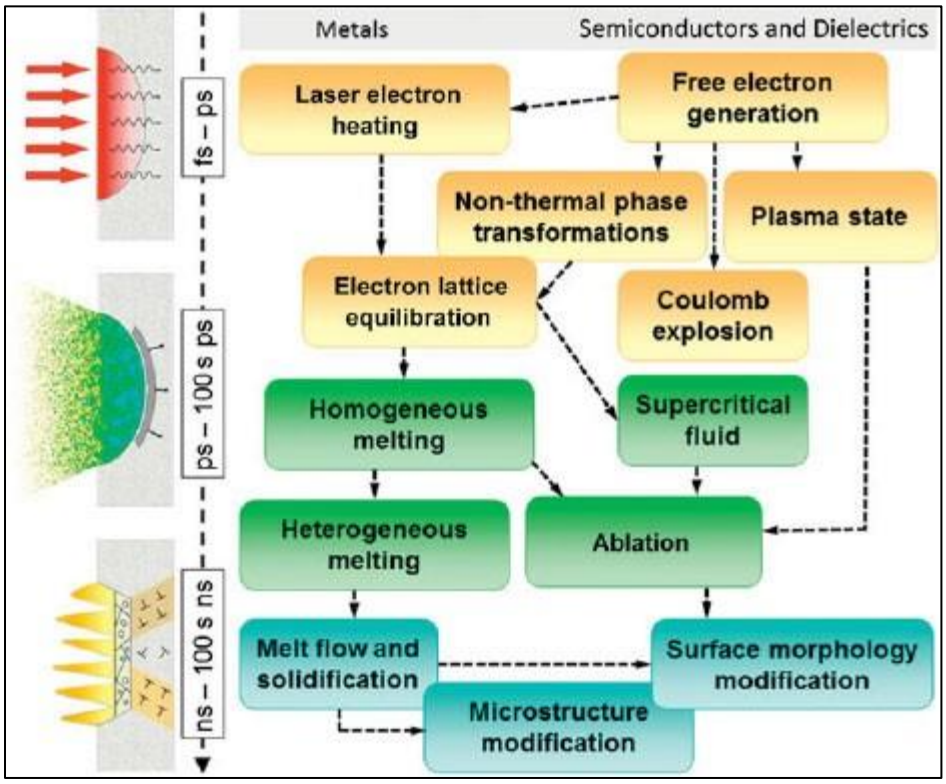

Figure 2.1: Ultrafast laser-matter interaction pathways for different materials [1]. – Permission requested from the publisher.

In the case of wide band gap materials in which the photon energy is less than the energy needed for excitation into the conduction band, the main processes for ionisation are multiphoton, tunneling, and avalanche ionisation [101]. A nonlinear optical process, multiphoton absorption is the simultaneous absorption of two or more photons by an electron. This strongly intensity-dependent phenomenon allows ionisation if the combined energy is greater than the bandgap. Since the probability of multiphoton events is small, ultrafast pule lasers are in the unique position of producing this phenomenon due to their immense peak energies. Electrons can also be promoted by tunneling ionisation, a phenomenon initially described by Keldysh [102] for dielectrics in strong electromagnetic fields. For high intensity fields, a qualification often met by ultrashort laser pulses, the Coulomb potential barrier is distorted, making tunnel ionisation

easier. Under varying laser parameters and material properties, tunneling ionisation transitions to multiphoton ionisation, and thus both are part of the theoretical treatment in [102]. Conduction band electrons undergo free carrier absorption, attaining higher energy states. If the electrons are further excited by the equivalent of an additional bandgap energy, they can knock other electrons from the valence band to the conduction band, generating additional free carriers [42]. In the presence of sufficient and sustained electromagnetic field strength, newly promoted free carriers undergo the same impact ionisation process, giving rise to an ionisation "avalanche" [103]. Multiphoton and tunneling ionisation produce the seed electrons for the avalanche process [96]. These phenomena facilitate micromachining inside of transparent materials since the light intensity is only sufficient for multiphoton ionisation at the laser focal spot [104]. In fact, the pulse energy can be controlled such that only a small portion of the focal spot surpasses the transformation threshold, for creating features shorter than the laser wavelength [105].

2.3.3 Ultrashort Pulse Ablation

Ultrafast lasers are well known for their use in precision ablation and micromachining. Virtually any material can be ablated by ultrafast lasers, with applications in, but not limited to, metal [106], semiconductor [107], dielectric [108], and bone [109] micromachining, thin film machining [110], microfluidic structure fabrication [111], microelectromechanical systems (MEMS) device manufacturing [112], laser induced breakdown spectroscopy (LIBS) [113], and implant modification [114]. There are many ablation mechanisms that have been proposed, and they occur under different irradiation parameters and in different materials, as often modelled by hydrodynamic and molecular dynamics simulations [115], [116]. Generally, ablation mechanisms include photomechanical spallation, phase explosion, and Coulomb explosion [116], [117]. In photomechanical spallation, also referred to as inertial stress confinement, the pulse duration is shorter than the mechanical relaxation time and intense compressive stresses are imparted on the irradiated surface area. These stresses relax to generate tensile waves that lead to the formation of subsurface voids and a separation of the surface layer [1]. The ejected layer carries away some of the residual heat, which contributes to the reduced heat-affected zone (HAZ). As the fluence is increased, a threshold is reached where the target is superheated beyond thermodynamic stability of the liquid phase, and a mixture of vapour and liquid droplets are ejected [118], [119]. This is referred to as phase explosion. Coulomb explosion is a phenomena whereby sufficient numbers of electrons are ionised from the surface such that the now positively charged irradiated volume decomposes due to overwhelming Coulombic repulsion. The occurrence of Coulomb explosion in bulk materials by ultrafast ablation is debated [120], and there is simulation and observational evidence for it [100] [99].

2.4 Ultrafast Laser Techniques in Additive Manufacturing

A common application of ultrafast lasers is for the surface modification and post-processing of metals and dielectrics via ablation. As a well-established technique with high precision and control, ultrafast ablation can be combined with other burgeoning manufacturing methods such as additive manufacturing by powder-bed fusion to provide further control over build morphology [48]. The utility of these lasers is not just limited to post-processing, however, as they offer great potential as additive manufacturing tools. Over the past few decades, several techniques capitalising on the unique abilities of ultrafast lasers have been developed. These are described below.

2.4.1 Selective Laser Melting/Selective Laser Sintering

Additive manufacturing offers the ability to produce complex internal geometries and low-volume customised parts, enables low-cost rapid prototyping, and may have sustainability advantages over conventional manufacturing [121], [122]. Continuous mode or nanosecond pulse laser-based AM enables direct transfer of energy to a material in a small focal region and leads to curing, sintering, or melting with a better resolution compared to extrusion-based methods [123]. Prominent examples of these methods are selective laser melting (SLM) and selective laser sintering (SLS). Metals that are commonly used are stainless and tool steels, aluminum alloys, titanium and its alloys, nickel alloys, and some cobalt alloys [124]. Optimal part orientation, laser parameter optimisation and consistency, high residual stresses, and surface quality are just some of the challenges within AM, particularly powder-bed fusion processes [125], [126]. Managing these challenges for a wide variety of metals with different melting points, laser absorption spectra, and heat conductivity behaviours further complicates the technology. Ultrafast lasers offer possible solutions to hard-to-process metals, and may be used in microfabrication, nanoparticle processing, and glass and ceramic AM.

2.4.1.1 Copper

Pure copper is a relatively stable and ductile material with excellent thermal and electrical conductivity [127]. Additive manufacturing of copper is especially attractive because it enables the production of complex geometries that may improve heat transfer devices and does not require additional manufacturing steps like welding [128], [129]. The laser processability of copper is limited primarily by its most useful property: high thermal conductivity. Copper absorbs laser energy and dissipates it via significant local thermal gradients, which increases the energy needed to achieve melting and the risk of defects such as porosity, delamination, and layer curling [130]–[132]. Additionally, high reflectivity (low absorbance) results in a compounded need for greater laser power and risks damage to optical components [131] [133]. An initial attempt at selective laser melting of copper via ultrafast lasers was demonstrated in Figure 2.4, yielding cuboids and thin-wall microstructures (<100 µm) with a high porosity [3]. A 1030 nm laser parameter process window was determined at a repetition rate of 20 MHz and

pulse energy from 0.75-1.50 µJ, below which superficial sintering occurs and above which ablation occurs. The authors suggested that fully dense structures may require an increased focal spot size or reduced grain sizes. Following up with additional experiments at 515 nm, Kaden et al. [3] found enhanced density in the first several layers by using a steel building platform with a significantly lower thermal conductivity. After approximately 10 layers, the benefits of the steel platform were reduced and the porous structure emerged. Further increases in laser power could improve heat accumulation and result in more dense structures. In these experiments, however, with a filling factor of 64% and specific heat and electrical conductivity 10% that found in literature, much more progress needs to be made [2].

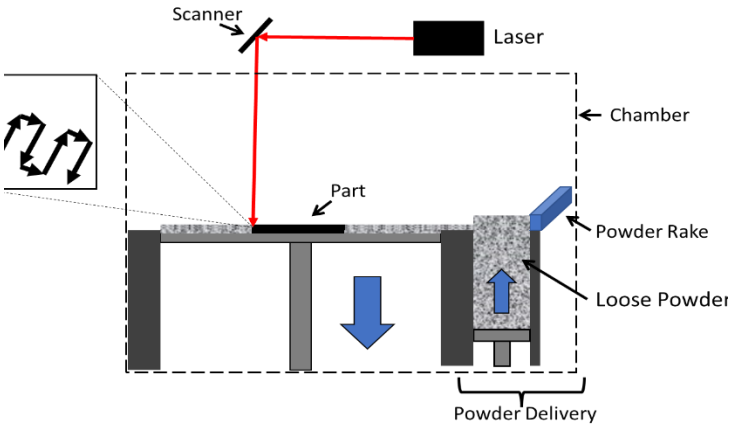

Figure 2.2: Example of SLM setup. A uniform layer of powder is deposited on the building platform, selectively melted by laser scanning, and then the subsequent powder layer is deposited by the rake.

For 2D printable and flexible electronic devices, Cu patterning via the laser sintering of nanoparticles has been investigated [134]. Femtosecond lasers may be able to confound challenges posed by copper's material properties, and Cheng et al. [135] demonstrated femtosecond sintering of Cu nanoparticle ink on a glass substrate. They also constructed a one-dimensional two-temperature model for this process. A similar process that instead reduces CuO by laser irradiation can also produce microstructures on glass and flexible polydimethylsiloxane (PDMS) [136], [137]. This was achieved with a lower average power compared to CW and nanosecond lasers, but is hampered by higher oxide concentrations in the patterns [138]. In the same instance, purity was improved by performing the experiments in argon or nitrogen atmospheres. Although the Cu nanoparticle sintering average power requirements for femtosecond lasers are lower than CW, evidence shows it results in a smaller processing window that makes consistent quality difficult to achieve [139], [140].

Figure 2.3: Sample objects produced by ultrashort pulse SLM of 10 µm copper powder. a) Mirror mount with mechanically optimized inner structure, b) turbine wheel, c) thin-wall sample with >100 µm wall thickness [2]. – Permission requested from the publisher.

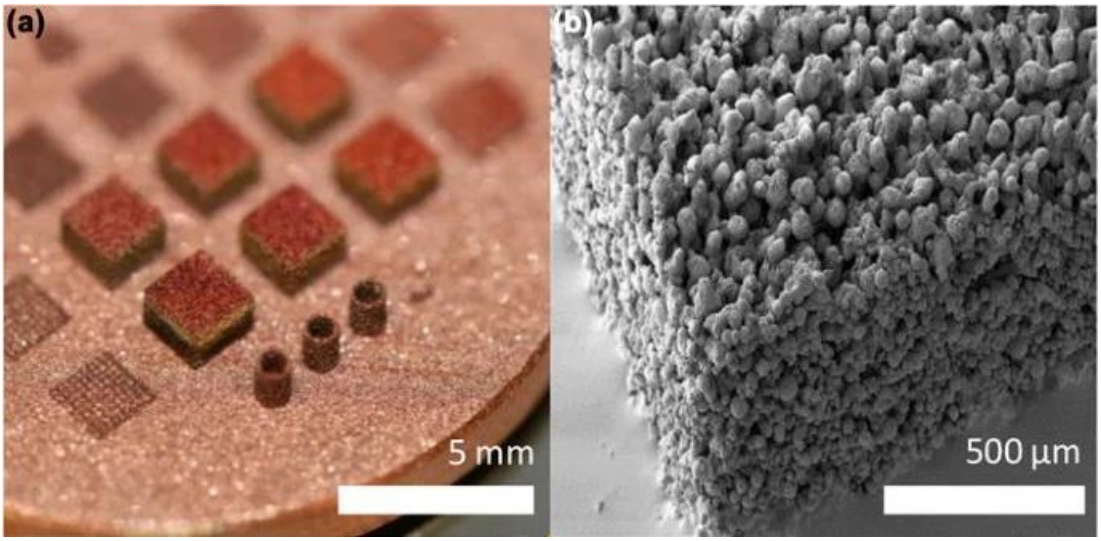

Figure 2.4: a) Cuboid samples produced by ultrashort pulse SLM, b) SEM of cuboid that shows porosity [3]. – Permission requested from the publisher.

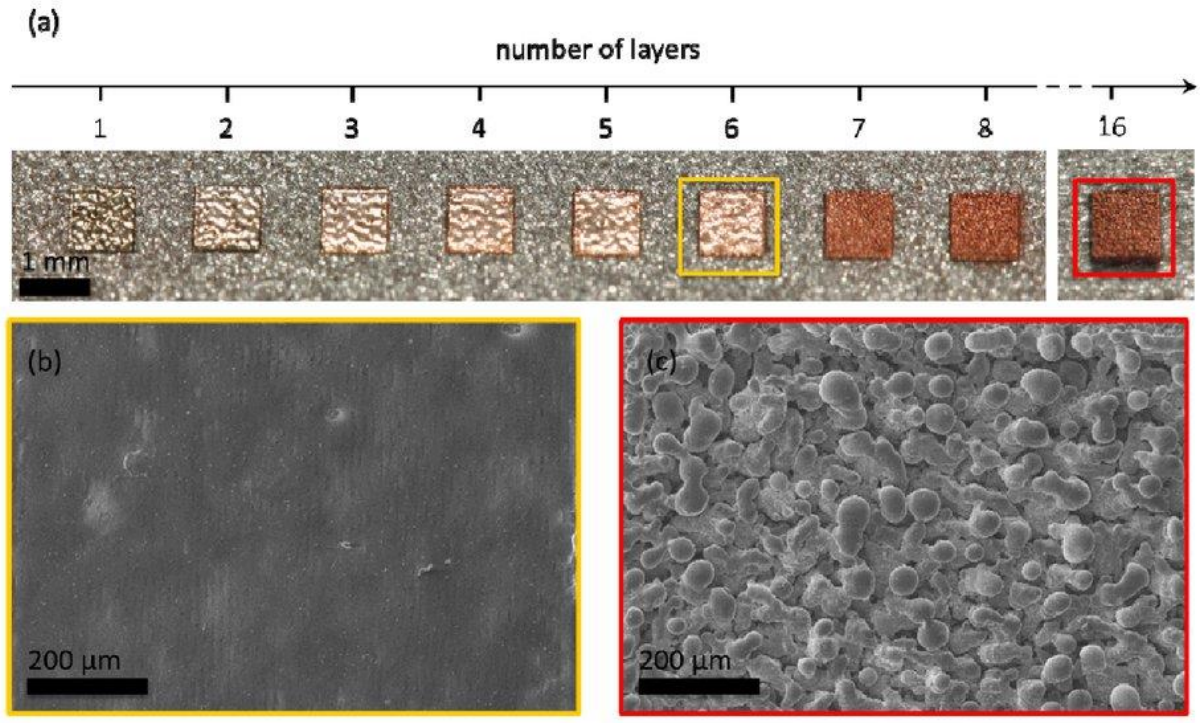

Figure 2.5: a) Demonstration of structures produced by increasing number of layers. b) and c) are SEM images of 6-layer and 16-layer structures, respectively. Shows the change in porosity as additional layers are added, thought to be due to the high thermal conductivity of copper which results in incomplete melting [3] – Permission requested from the publisher.

2.4.1.2 Tungsten

Tungsten, also known as wolfram, is a rare metal with a high melting point of 3,695 K (for comparison, aluminum melts at about 933 K), good thermal conductivity (174 W/m K), and has potential for use in extreme environments such as nuclear fusion reactors [141].Consequently, its processability is challenging. In an effort to reduce manufacturing cost and waste, Xie et al. [142] manufactured Tungsten tiles by directed energy deposition with a non-ultrashort pulse, >3000 W source. The layers deposited were relatively thick (about 1 mm) and suffered from cracks and pores. Conventional SLM has been accomplished with lower laser powers (around 400 W) and with possibly reduced microcrack formation by substrate preheating up to 1000 C [143]. It is thought that the ductile to brittle transformation and large thermal gradients imposed by laser beam melting are responsible for crack formations [144]. Ultrafast lasers may be a more practical and effective source for additively manufacturing Tungsten, as the intense peak power is simulated to produce localised temperatures exceeding 4000 K [87]. Femtosecond selective laser melting is feasible, as shown in [4]. A 0.5 mJ (45 W average power) Yb-fiber laser, with 400 fs pulse width operating at 1 MHz, was used to successively melt more than 100 layers of 1-5 micron powder. Ultimate tensile strength (UTS) and microhardness were measured, UTS was

found to be 388.4 MPa compared to the conventional UTS > 580 MPA, and the microhardness corresponded to a Vickers hardness of 395 compared to that of the conventional 450. Bai et al. [5] compared pulse durations between 750 fs and CW mode. They found that the fs-based process produced parts with up to 99% density, and fewer defects and greater hardness compared to the ps and CW modes. Micron-scale structures were also shown, featuring walls of 100 µm thickness, and a finer microstructure was detected (Figure 2.7). However, defects are still clearly visible with the ultrafast process. Further testing of material properties (e.g., ductility, dimensional accuracy) will be important to distinguish the ultrafast laser method as an improvement relative to conventional SLM, as well as its capability in demanding applications. As a relatively unexplored technique for SLM, layer-wise ultrashort pulse fabrication is a potential avenue for 3D manufacturing of Tungsten.

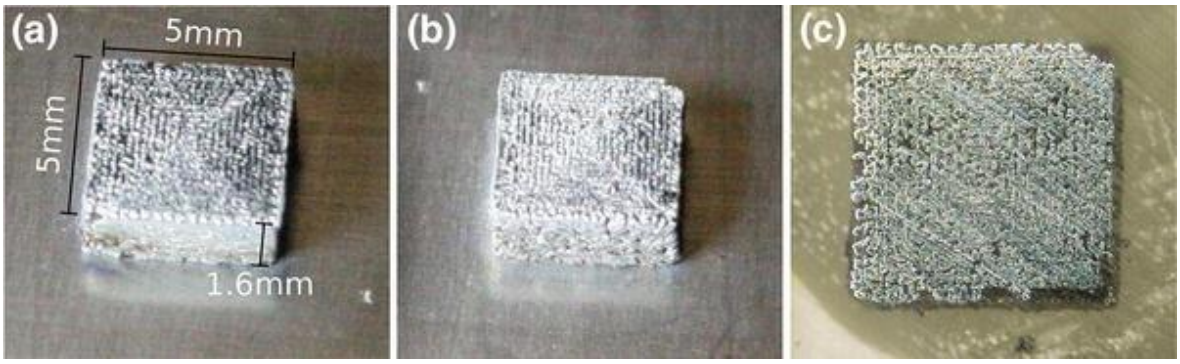

Figure 2.6: Tungsten cube at different angles [4] – Permission requested from the publisher.

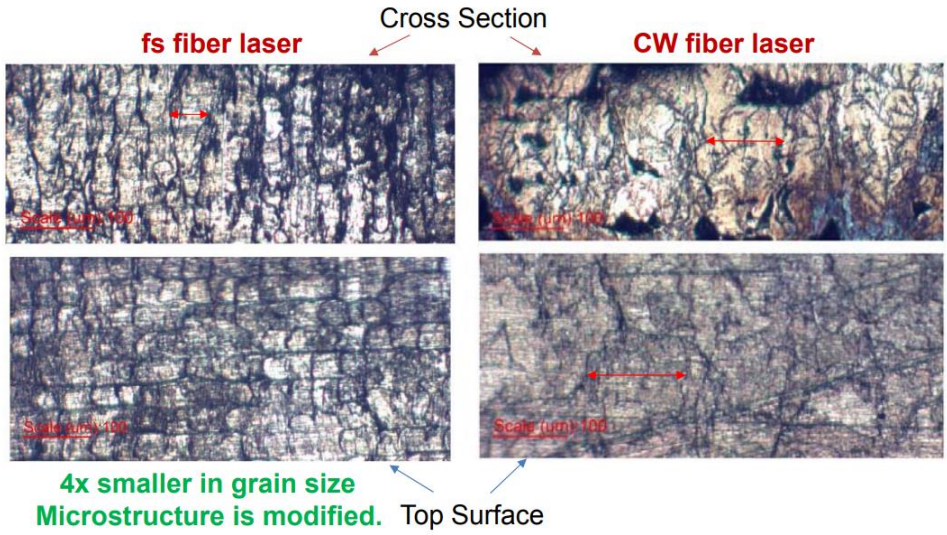

Figure 2.7: Comparison of microstructure between fs-SLM and CW-SLM of tungsten. Fs-SLM resulted in smaller grains, which is correlated to superior strength [5]. – Permission requested from the publisher.

2.4.1.3 Other Materials

Attempts at additively manufacturing a variety of other materials by ultrashort pulses have been made. Ultrafast lasers provide the potential to both heat target materials to extreme temperatures and greatly limit the heat-affected region. Therefore, it is interesting to study how they perform when faced with the challenges of high melting point or low absorption materials as well as the differences in material properties such as thermal conductivity, melting point, thermal expansion coefficient, etc., at play when dissimilar materials are irradiated simultaneously. Ultrashort pulse laser powder-bed fusion of borosilicate glass [6], aluminum alloys [7], [145], ultra-high molecular weight polyethylene (UHMWPE) [146], bimetallics [147], rhenium, and diboride ceramics [43] has been demonstrated. Depending on the investigated material, laser parameters are varied such that as close to complete melting as possible is achieved (Table 1). Thus, in these preliminary studies on the very feasibility of melting and additive construction, viable laser parameters are at the core of the investigation.

Table 1: Summary of recent work in laser melting of powder by ultrafast laser.

Material	Justification for Ultrashort Pulse	Wavelength	Average Power	Pulse Duration	Repetition Rate	Pulse Energy	Scanning Velocity
Borosilicate glass [6]	Controlled thermal diffusion in bulk, short resolidification times	1030 nm, frequency doubled to 515 nm	11 W	Femtoseconds, unspecified	20 MHz	0.55 mJ	20 mm/s
Al-Li, Al-Si [7], [8], [145]	Stronger refinement of microstructure, smaller melt pool and higher shape accuracy, reduced evaporation of Li in-process	1030 nm	25-30 W	500 fs – 800 ps	6-20 MHz	1.5 µJ	700 mm/s
UHMWPE [146]	Multi-photon absorption for more localised energy deposition, improved ultimate tensile strength	1030 nm	30 W	500 fs	10 MHz	3 µJ	100 to 500 mm/s
Bimetallic (12Cr2Si/9Cr1Mo, SS316L/SA508) [147]	Conventional L-PBF is challenged by dissimilar materials	unspecified	200 W	Femtosecond, unspecified	unspecified	unspecified	unspecified
Rhenium, Hafnium diboride, Zirconium diboride [43]	High melting temperatures (5596 C, 3250 C, 3246 C, respectively)	1030 nm	Up to 35 W	400 fs	1 MHz	Up to 35 µJ	mm/s

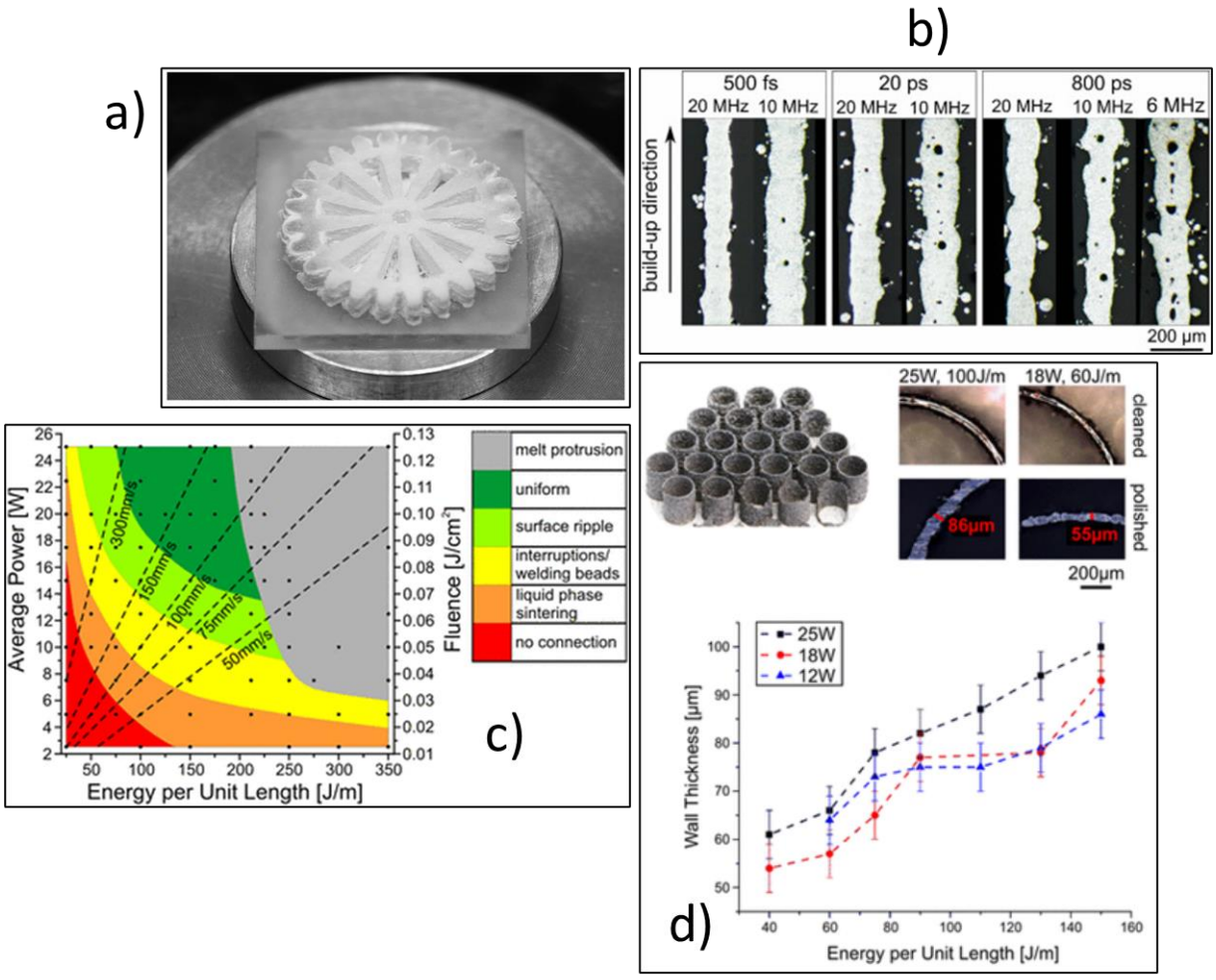

Figure 2.8: a) gear wheel, 10.5 mm diameter, 1.5 mm height [6] – Permission requested from the publisher. b) cross section optical microscopy of Al-Si walls by SLM at different laser parameters – Reproduced from [7] (CC BY 4.0). c) Melting morphologies/regimes for Al-Si40 SLM and d) Top left: Al-Si40 cylinders by SLM, Top right: wall thickness measurements, Bottom: wall thickness vs. energy per unit length (average power divided by scanning velocity) - Reproduced from [8] (CC BY 4.0).

2.4.2 Multiphoton Lithography

Stereolithography, a manufacturing process by which light induces a photochemical structural change to print patterns and objects, allows for layer wise production of arbitrary 3D objects from computer drawn designs. Conventionally, a photopolymer is transformed from the liquid state to a solid polymeric state by UV laser curing [148]. The excitation of a photoinitiator to a state that produces ionic or radical species initiates cross-linking chain reactions in photoresist materials like epoxies and acrylates. Excitation, and thus photopolymerization, can be achieved

by multiphoton absorption of lesser energy photons that equates to the energy that would normally be absorbed by singular UV photons. Due to the nonlinear dependence on laser intensity and the transparency of the material to single photon absorption, multiphoton absorption occurs in a tight focal region for ultrafast lasers, meaning that higher resolution and internal modification is accomplished (Figure 2.9) [149]. Direct laser writing by multi-photon absorption has been discussed in several reviews [9], [149]–[151].

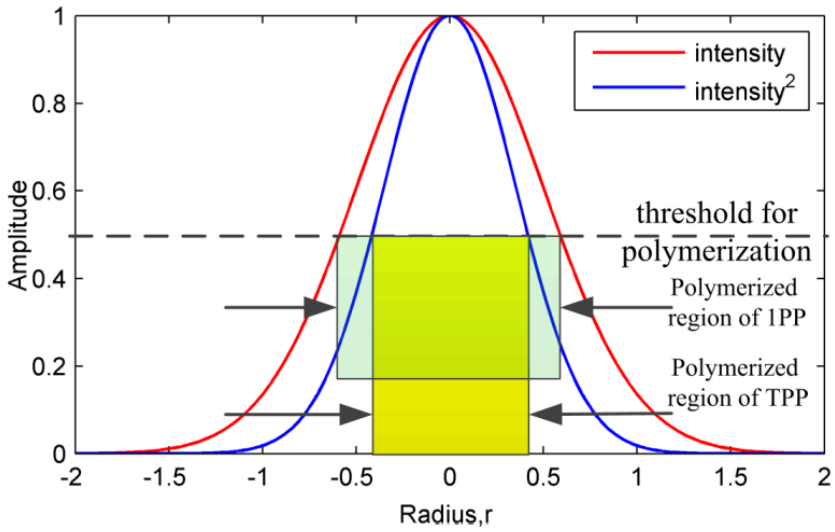

Figure 2.9: Intensity distribution of Gaussian beam $I(r) = I_0 e^{-2r^2/\omega_0{}^2}$. I (red) and I^2 (blue) correspond to 1PP and 2PP, respectively. At polymerization threshold, the region for 2PP will be smaller (higher resolution) than for 1PP – Figure reproduced from [9] (CC BY 3.0).

The multiphoton lithography technique (also referred to as 3D laser lithography (3DLL), multiphoton direct laser writing (MP-DLW)) typically utilised Ti:Sapphire femtosecond lasers, since the doubled wavelength is in the UV range, but as second harmonic fibre lasers have become more viable, they are increasingly common [152].

2.4.2.1 High Resolution and STED-MPL

Many examples of nanoscale structures have been published, possibly none more iconic than the "microbull" with 120 nm spatial resolution, fabricated via two-photon polymerisation (2PP) of SCR500 resin (Figure 2.10) [9], [10]. The deterministic threshold and nonlinearity of ultrafast laser 2PP enables manipulation of the laser intensity profile so that only an area smaller than the diffraction-limited spot leads to polymerisation [9], [149]. Interestingly, this allows lateral and axial fabrication resolutions smaller than the Abbe diffraction limits and structures that are sub-100 nm [11], [153], [154].

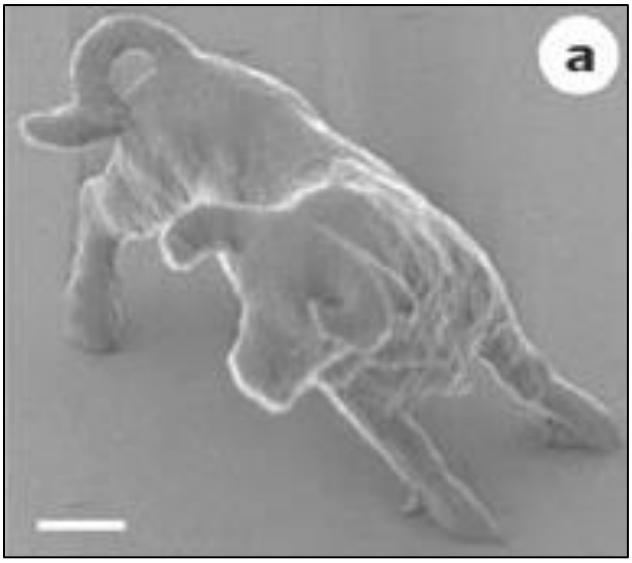

Figure 2.10: The iconic micro bull, 2 µm scale bar [10]. – Permission requested from the publisher.

A key technique for facilitating this is known as STED-lithography. Stimulated emission depletion (STED) is a technique first implemented for super resolution microscopy in which fluorophores around the focal point are deactivated, minimizing the illumination area [155]. In general, photo initiators are excited by the usual ultrashort pulse to a state S1, which normally relaxes to a radical-producing state (and thus polymerising state) by intersystem crossing. If a limited surrounding region is irradiated immediately after by a second pulse that initiates de-excitation by stimulated emission from the S1 state to a state that does not produce radicals (e.g., the ground state), then the extent of polymerisation will be confined, improving resolution (Figure 2.11) [11]. STED-lithography techniques differ according to the depletion mechanism, giving rise to methods such as two-color photoinitiation/inhibition (2PII) [156] and resolution augmentation by photo-induced deactivation (RAPID) lithography [157].

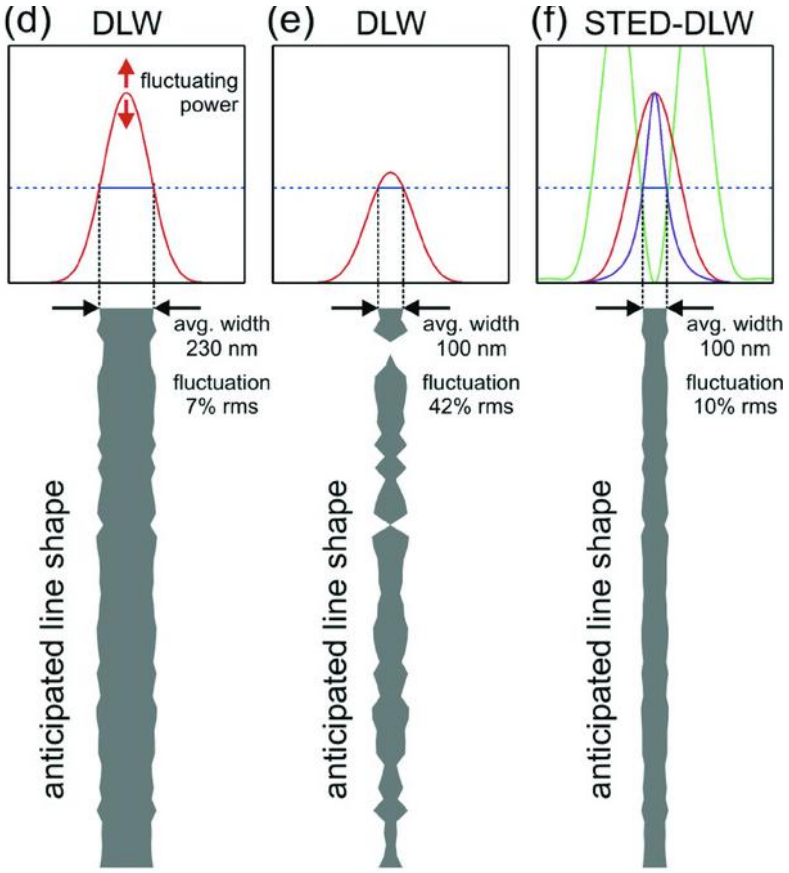

Figure 2.11: d) intensity profile (red) of standard MPL and corresponding line writing shape. Power fluctuations result in line width fluctuations. E) thresholded MPL, results in smaller line width, but fluctuations are below polymerisation threshold (blue line), lack of polymerisation can occur. F) STED-MPL, depletion intensity distribution (green) reduces the effective exposure profile (purple) and results in a consistent, smaller line width. – Adapted from [11] (CC BY 3.0).

2.4.2.3 Materials and Applications

A variety of materials are available for two-photon polymerisation, such as organically modified ceramics (Ormocers) [158], [159], the epoxy-based SU-8 negative photoresist [160], metal-containing sol-gel composites [153] [161], and various acrylates [162], [163]. There are applications in chemical sensing [164], microfluidic devices [165]–[167], and microneedles [168], [169], but recently micro/nano optics and biological and tissue engineering have received significant attention [170], [171].

2.4.2.4 Tissue Engineering

Regenerative medicine is a field that can greatly benefit from bespoke, biocompatible 3D microstructures, since it relies upon cell proliferation on cell matrices and scaffolds [172]. Biological tissues are complex composite materials with the extracellular matrix (ECM) providing the supporting structure for cells. For this purpose, 2PP of bovine serum albumin (BSA), modified gelatin, collagen, fibrinogen, fibronectin, concanavalin A, and others has been achieved [173]. Scaffolds of varying geometries and biomaterials fabricated by femtosecond direct laser lithography are being investigated for the best compatibility and *in vivo* results [174], [175].

It was demonstrated by Flamourakis [12] that a bowtie auxetic structure composed of the organic-inorganic hybrid material SZ2080 allows directional fibroblast proliferation (Figure 2.12). The fabrication of such structures is recently unfettered by MPL. The XYZ piezoelectric stage setup incorporated a Ti:Sapphire (800 nm) laser operating at 20 fs, fluence of 106 Mj/cm^2, and 80 µm/s scanning speed, focused with a 100x NA=1.4 objective lens. The biocompatible SZ2080 photoresist was written into a bowtie geometry with 8.6 µm and 40 µm unit cell size, mechanically tested, and seeded with fibroblasts from the NIH-3T3 cell line.

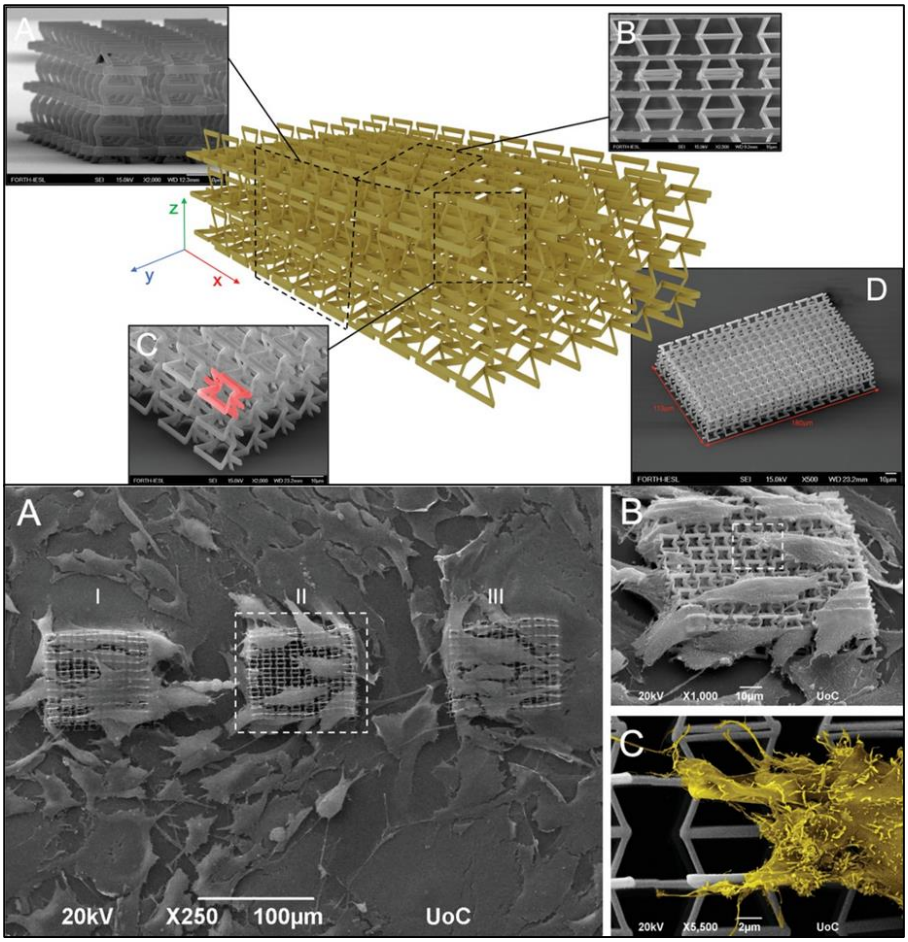

Figure 2.12: Top: CAD design (center) of bowtie auxetic scaffold and surrounding SEM images of MPL-fabricated SZ2080 scaffold. Bottom: SEM images of auxetic scaffold after seeding with fibroblasts. B) magnified image of dotted square in A). C) magnified image of dotted square in B) with yellow pseudocolor to visualize filopodia. Directional growth because of scaffold structure can be observed [12]. – Permission requested from the publisher.

Further complexity to designer scaffolds has been introduced by inclusion of a second photoresist for improved spatial control over cell binding domains and thus cell distribution [176]. Polyethylene glycol diacrylate (PEG-DA) formed a protein-repelling framework upon which the protein-binding ormocer photoresist was built, both were deposited by DLW. The crosslinking agent pentaerythritol tetra-acrylate (PETA) was added for additional stability, which at high enough concentrations moderated the cell repellency of PEG-DA. Therefore, by using multiple photoresists, not only can one control the geometry and mechanical properties of a primary scaffold, but they can also create site-specific functionality and potentially a tailored distribution of differing degrees of cell compatibility. A more recent work utilised three different photoresists to selectively functionalise the freestanding scaffold with two different ECM proteins, finding that they could alter cell adhesion behaviour by choosing proteins for which A549 cells have different affinities [177].

2.4.2.5 Micro- and Nano-Optics

Multiphoton lithography is an effective tool for the realisation of micro- and nano-metre sized optical systems. Photoresists with good optical properties, the geometric freedom of this additive manufacturing process, and the high resolution enable the fabrication of refractive and diffractive elements on an extremely small scale [178], [179]. Microlenses with 15 micron diameter and focal lengths of tens of microns have been produced with the Zr-based hybrid photopolymer SZ2080 [180]. Significant work has been done fabricating microlenses, photonic crystals, and other elements on the tips of optical fibers [14], [179], [181], with He et al. [13] having designed and produced swappable fiber sockets and holders for improved alignment and to eliminate the need for printing directly on the fibre head (Figure 2.13). These devices have exciting implications for integrated optics, photonic circuits, and fiber-based endoscopy and tomography [181], [182].

Gissibl et al. [183] use a commercially available lithography system to construct a compact triplet lens objective with a diameter of about 120 µm and superior resolving powers and higher fields of view compared to alternative printing methods. Free-form multi-lens objectives were also demonstrated [184]. While nanoscale control over the device dimensions has been achieved, control over the refractive index would lend even greater versatility to multiphoton direct laser writing. To this end, [185] developed a method dubbed subsurface controllable refractive index via beam exposure (SCRIBE) which can produce graded index (GRIN) micro-optics. By using a

porous silicon (PSi) host, the degree of polymer infilling, and thus the effective refractive index, is varied with the laser power.

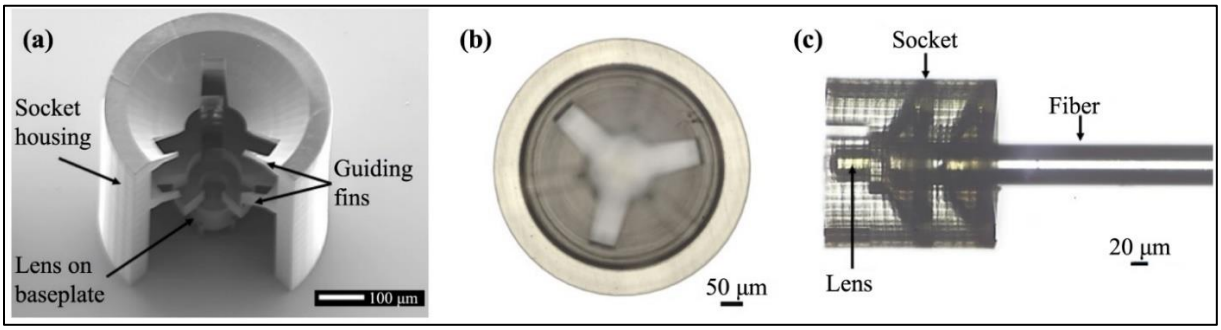

Figure 2.13: a) SEM image of fiber socket with micro lens, b) optical micrograph of top view, c) optical micrograph of fiber inserted. – Adapted from [13] (CC BY 3.0).

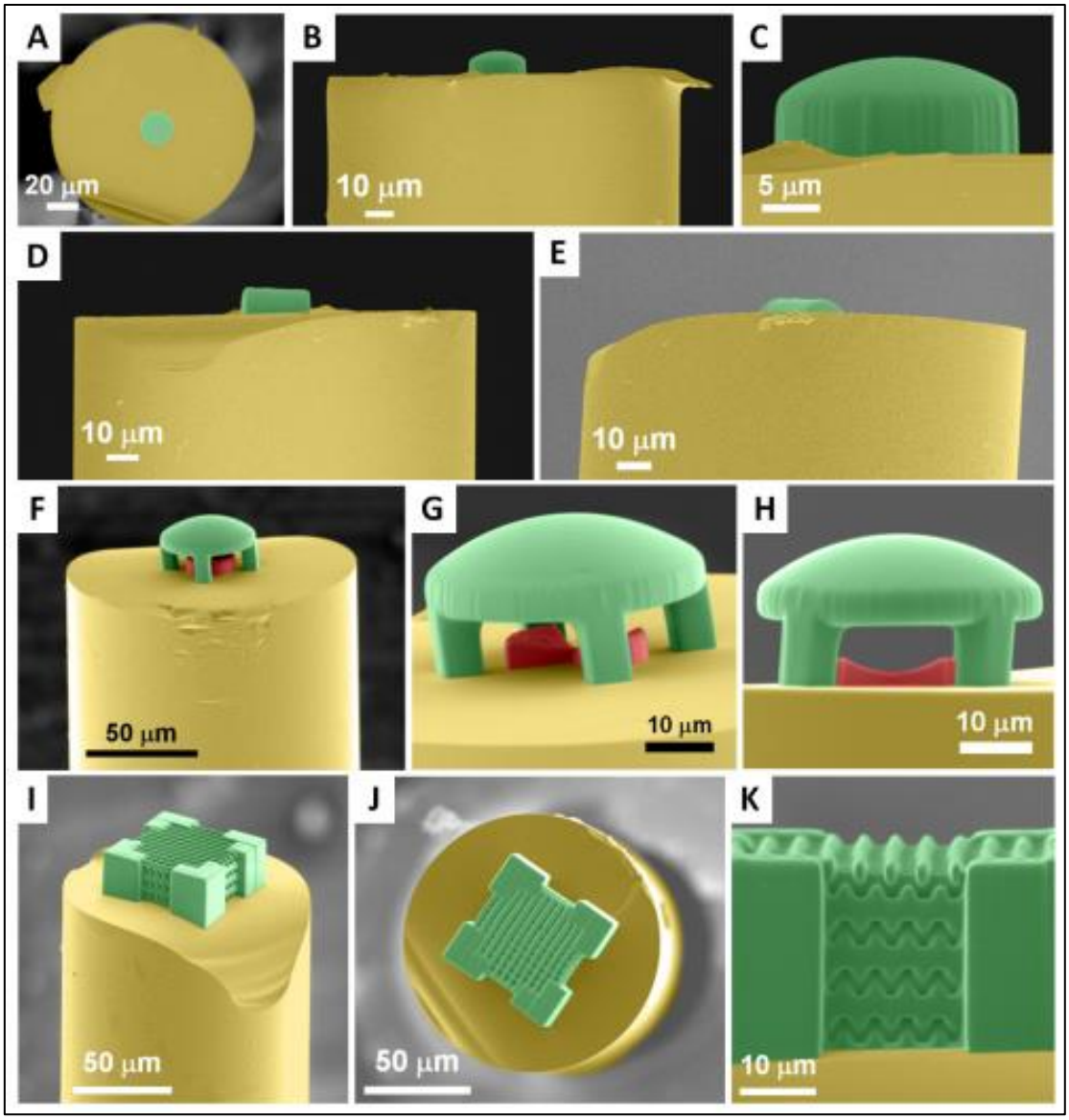

Figure 2.14: SEM pseudocolor images of microstructures on end of optical fiber. A)-c) plano-convex lens, d)-e) cylindrical lens, f)-h) suspended plano-convex lens (green) and plano-concave lens (red), i)-k) woodpile photonic crystal [14]. – Permission requested from the publisher.

2.4.2.6 Metallic Deposition

With the past and growing interest in microelectronic devices, MEMS, metamaterials, and plasmonic devices, the desire for a method of metallic fabrication on the microscale with unfettered control over the geometry is inescapable. Limitations on the resolution of existing AM leave a gap that is currently filled by metal particle ink extrusion, electrohydrodynamic printing or droplet ejection, laser-assisted electrophoretic deposition, LIFT, and other techniques [186], [187]. Alternative techniques based on or involving the use of multiphoton direct laser writing

are being researched, since it offers the tantalising benefits seen in the polymerization domain. Metallic deposition has also been reviewed in several recent articles [187]–[189]. One way metallic structures are produced is by first utilising MPP to create a polymer template upon which metal is layered by electroless deposition or plating [190]–[193] or by electrochemical deposition [194], [195].

Alternatively, direct deposition of metals can be accomplished by multi-photon laser photoreduction of dissolved metals for the nucleation and growth of 3D-printed structures [187]. For example, the femtosecond pulse photoreduction of silver nitrate or tetra chloroauric acid (gold) to produce conductive microstructures or diffraction gratings [196], [197]. This solution-phase deposition suffers from roughness and granularity of the structures, impurities, and poor mechanical strength [149], [189]. Metallic ions can also be fused into the polymer matrix, creating a hybrid material, but has limited conductivity and its properties are highly dependent on the photoresist [198]–[200]. Blasco et al. [201] developed a gold-containing photoresist and employed this simultaneous photopolymerization and photoreduction method to create conductive micro-arches 20 μm in length and 3 μm in height. A novel method capable of complex 3D geometries utilises two-photon lithography to produce 91.8 wt% Ni structures [15]. Following the trend of integration of metal-containing compounds into a photoresist, they combined nickel acrylate with pentaerythritol triacrylate and the photoinitiator 7-diethylamino-3-thenoylcoumarin (Figure 2.15a, b). Nanolattices were polymerized and then underwent pyrolysis at 1000 C in argon followed by 600 C in forming gas. The resulting unit cells were 4 μm in size with 0.4 μm beam diameter. The feature resolution is significantly better than contemporary metal AM methods and compression experiments suggests without compromising mechanical strength.

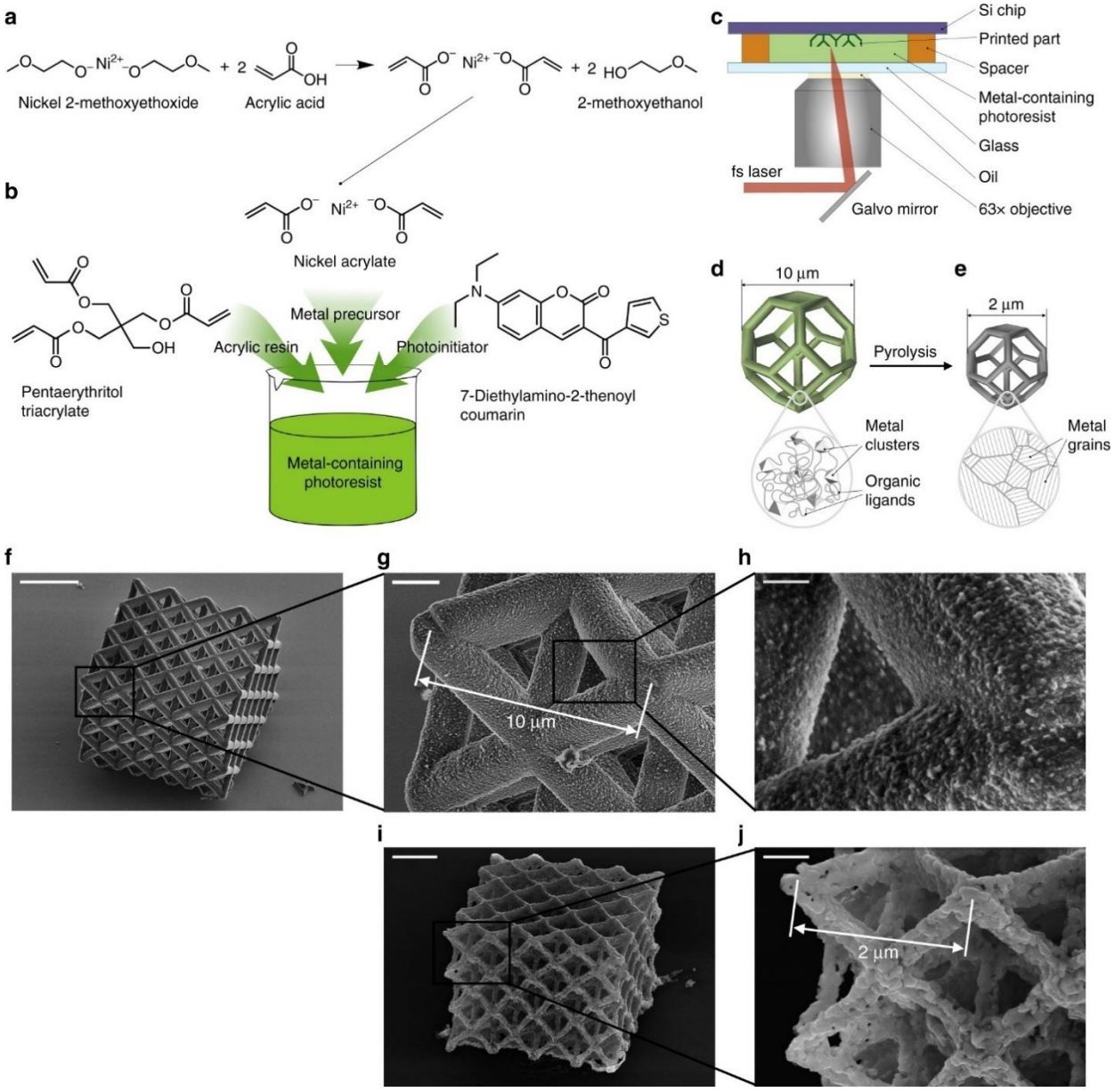

Figure 2.15: a-b synthesis of Nickel containing photoresist, c) MPL process, d) diagram of metal-containing polymer structure that is pyrolyzed to metal structure. F-h lattice of nickel-containing polymer, i-j lattice after pyrolysis. G and I scale bars are 2 µm, h and j scale bars are 500 nm. F scale bar is 15 µm. – Reproduced from [15] (CC BY 4.0).

2.4.3 Laser-Induced Forward Transfer

Laser-induced forward transfer (LIFT) is a method for depositing discrete portions of a donor material onto a receiving substrate [202]. The LIFT process is depicted in Figure 2.16. By

mounting a target or donor film onto a transparent substrate, a pulsed laser operating above an intensity threshold for material ejection can eject discrete voxels onto a receiving substrate. The laser is focused on the donor substrate-donor interface, and the ejection mechanism is similar to that of ablation, where the material is vaporised and expands to force a localised detachment of the substrate. LIFT is a type of additive laser direct writing, and as such can be used to build layer-wise structures of nearly any class of material. Its advantages lie in its simplicity of implementation, operation in ambient conditions, preservation of electrical, chemical, and biological properties of the donor, high resolution micro-structuring, and that the same laser setup can be used for subsequent processing or modification [203]. LIFT is similar to an ink-jet process, but is not restricted by the viscosity or degree of solid loading of the material [16].

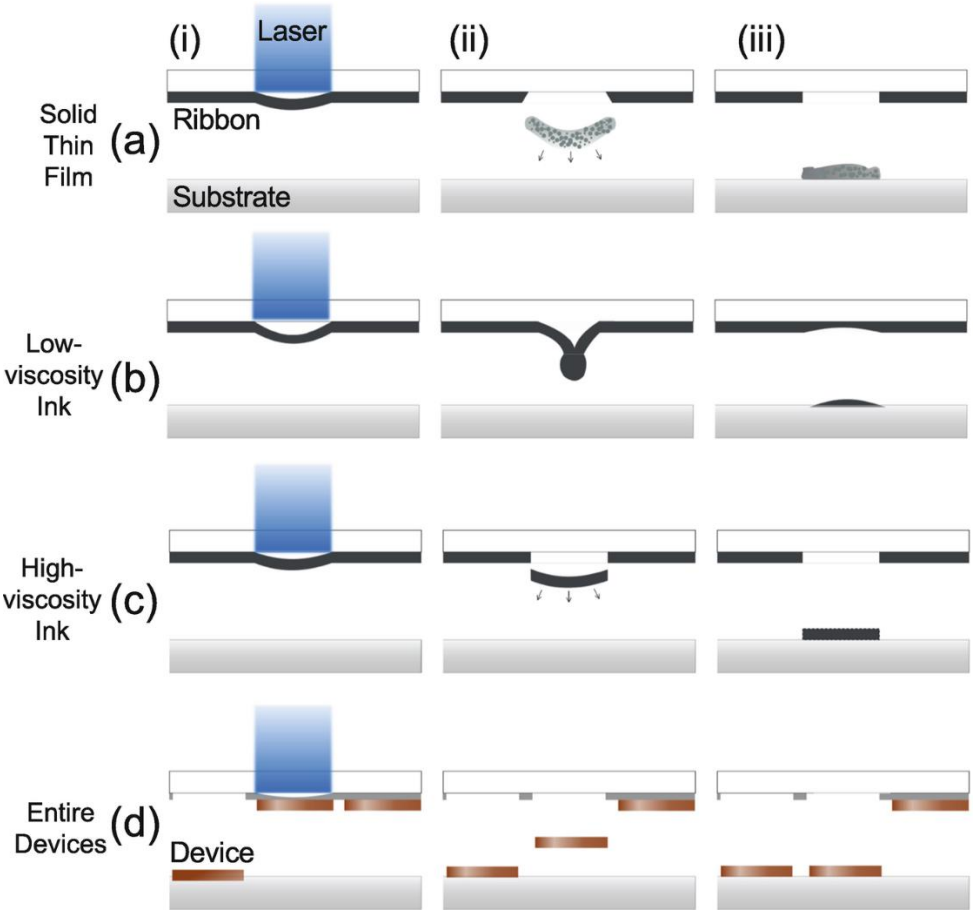

Figure 2.16: LIFT process for various donor material phases. Steps from i to iii are i) absorption of laser pulse, ii) vaporisation of donor material at substrate interface results in localized ejection, iii) material is deposited on receiving substrate [16]. – Permission requested from the publisher.

Nanosecond pulse lasers are well established for this technique, but experiments with picosecond and femtosecond lasers have yielded metal film material transfer at lower fluence thresholds and with greater precision [204], [205]. This is expected due to our understanding of the differences between nanosecond and femtosecond ablation. However, a comparison of nanosecond and picosecond LIFT of silver nanoparticle inks indicates that at higher fluences the differences in jet dynamics and surface area evolution narrow [206]. Much of the research into ps- and fs-LIFT involves metal film donor layers such as Cu, Au, Zn, Cr, Ti, and thus applications in printed electronic microdevices and components [207]–[209]. It was found that the ejected material in fs-LIFT had a narrower angular divergence, and the highly localised heat-affected zone limits damage to sensitive donor materials [210]–[213]. A two-temperature thermomechanical model can be applied, revealing how gold, chromium, and zinc are deposited in different phase states despite the same irradiation conditions [214]. Micron-sized droplets of metals can be deposited by picosecond LIFT, rivalling the resolution that may be obtained by ultrashort pulse selective laser melting or sintering [215]. By stacking multiple droplets in the same location, the 3D-printing of freestanding metal microstructures is achieved (Figure 2.17) [17]. These micro-pillars exhibit extremely high aspect ratios and maintain conductivity. Feinaeugle et al. [18] have developed a sacrificial support structure technique whereby Cu supports are chemically etched to reveal a gold helix (Figure 2.18).

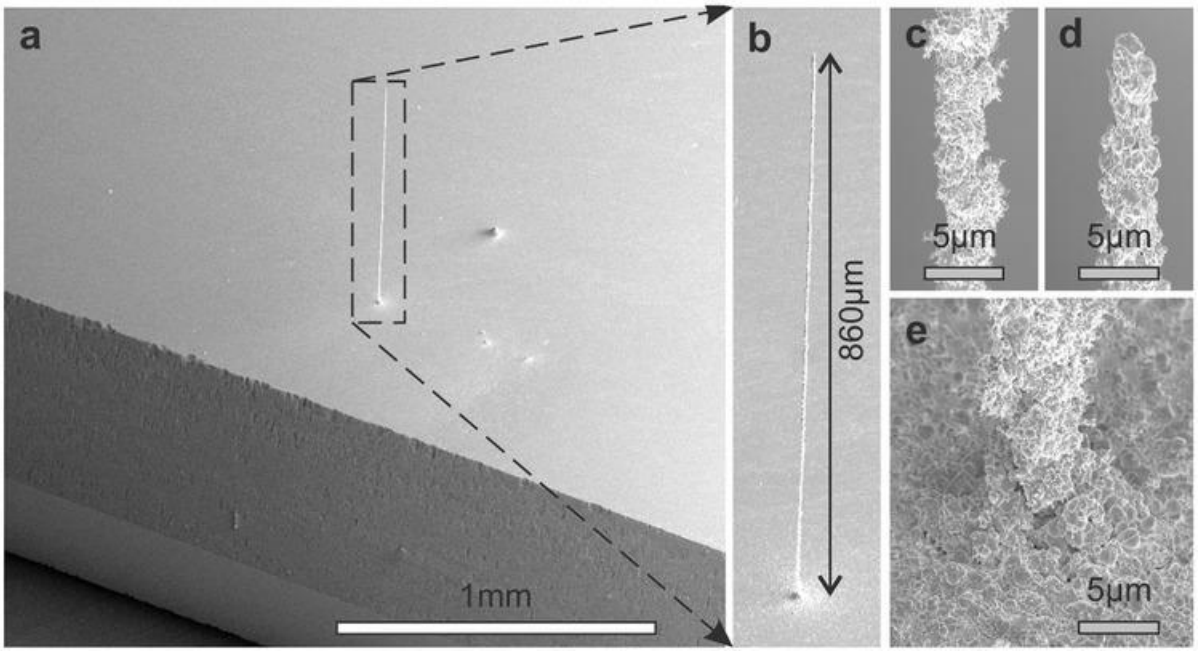

Figure 2.17: Copper micropillar fabricated by ultrafast-LIFT [17]. – Permission requested from the publisher.

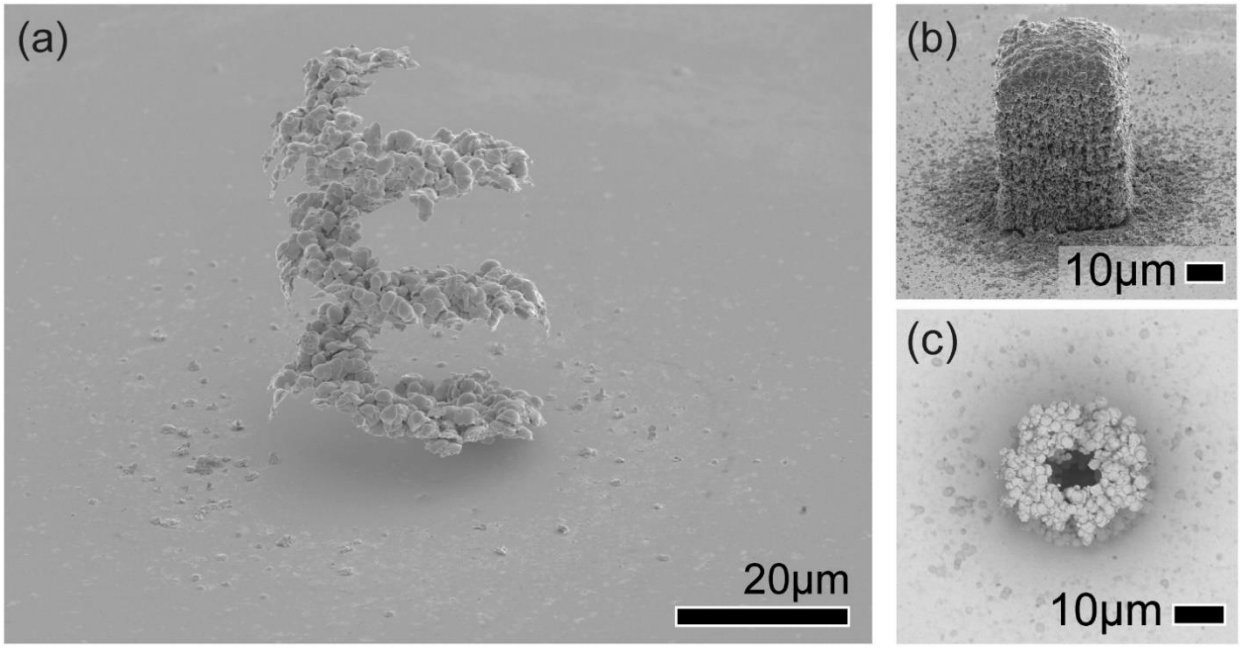

Figure 2.18: a) gold helix deposited by LIFT after etching to remove copper support structure, b) structure before etching, c) top view of gold helix after etching. – Reproduced from [18] (CC BY 4.0).

The use of multiple pulses can affect copper voxel morphology, as shown in Figure 2.19 [19]. They utilised an initial microsecond laser pulse to melt the donor film, followed by a 500 fs pulse to induce material ejection (time between pulses varied from 195 us to 375 us). Thus, providing the ability to tune the droplet geometry. Improved control over the size and shape of depositions will be essential for broadening the application space of ultrashort pulse LIFT techniques. Double femtosecond pulses temporally separated by up to 10 ps were used to study the nature of the material ejection mechanism and how it relates to ultrafast dynamics [209].

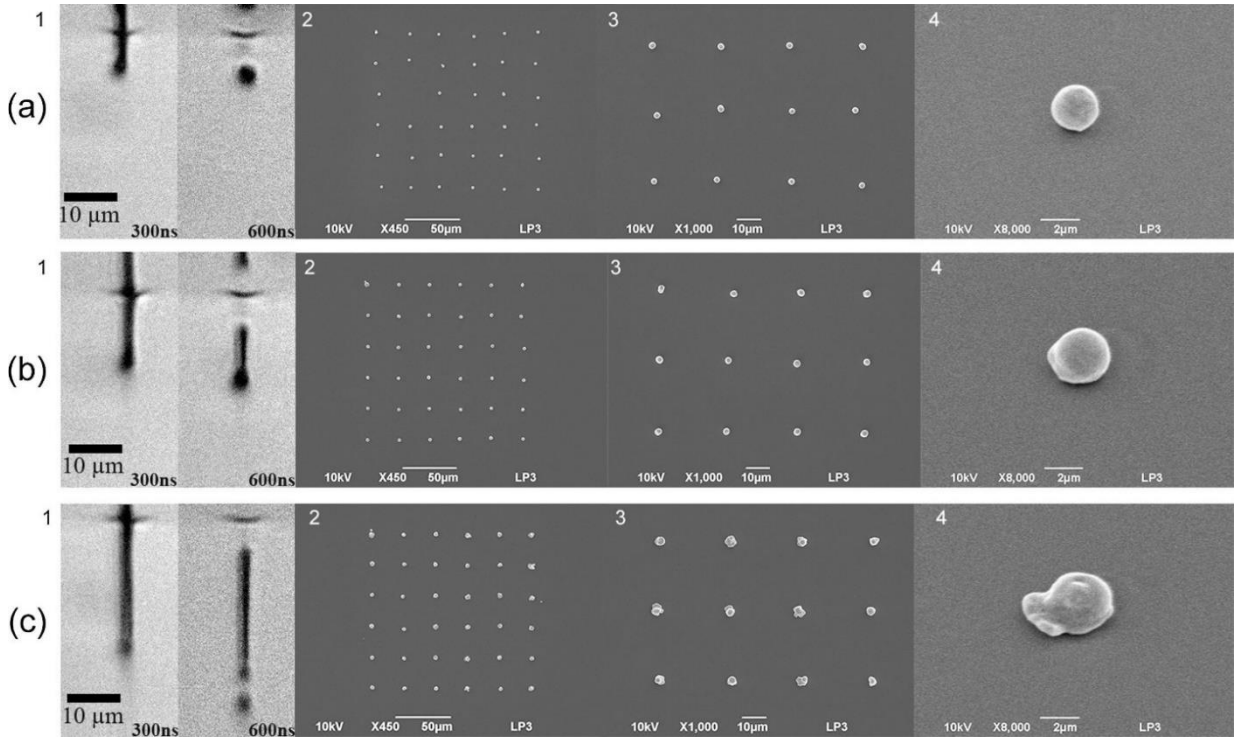

Figure 2.19: Double-pulse LIFT depositions at different time delays between the double pulses. Coloumn 1 is ejection from donor, coloumns 2 to 4 are depositions at increasing magnification. A) 195 us delay, b) 275 us delay, c) 375 us delay [19]. – Permission requested from the publisher.

The characterisation of LIFT of varying viscosity fluids is important for understanding the advantages that ultrashort pulses may have as this technique continues to develop. High viscosity metallic pastes can also be printed via LIFT, with recent work attempting to characterise the effect of process parameters on the fabrication of silver lines from a commercial paste containing 1-4 µm particles (250 Pa·s) [216]. When consecutive pulses are not separated by a sufficient distance on the donor material, deformations of the paste from the previous pulse can impair material ejection of the following pulse. Munoz-martin et al. [216] outlined the need for a threshold pitch distance between pulses, short enough such that deposited voxels are adequately overlapped, but long enough to avoid previous pulse deformations. Medium viscosity liquid films (0.3 Pa·s) deposited by fs-LIFT were recently observed by time-resolved shadowgraphy [217]. Three laser fluence regimes were noted for producing jet transfer states that, as fluence is increased, transition from a stable state with <100 µm depositions to an unstable splash state with messy material transfer, and then to larger <100 µm depositions.

If material transfer can be reliably tuned by controlling and changing laser fluence, consecutive pulse pitch, number of pulses, and other parameters, it not only increases the versatility and number of applications of ultrashort pulse LIFT, but could also open up a niche in which the parameters are changed mid-process to produce increasingly complex devices.

2.4.4 Pulsed Laser Deposition

Pulsed laser deposition (PLD) has been used as a method of film deposition for many years [218]. The procedure is relatively simple: a laser pulse is incident on a material to be deposited, and the pulse wavelength, energy density, and duration are chosen such that the target undergoes ablation, resulting in an ejection plume and film growth on a nearby substrate. PLD is able to transfer the composition of the target to the substrate, maintaining stoichiometry even for complex multicomponent oxide materials [218]. This is facilitated by performing the technique in a vacuum chamber filled with reactive gas species (oxygen for oxides) and by heating the substrate. Stoichiometric transfer can be achieved due to the ablative nature of this process and plasma formation, since for lower laser energy densities the material flux would be due to evaporative processes which are dependent on the vapour pressures of the constituents. PLD is a versatile technology as the transfer of virtually any class of material is possible, such as metals, semiconductors, polymers and biomaterials [219]–[221].

Nanosecond pulse lasers with high pulse energies and low repetition rates are used often, but because material is transferred by ablation, ultrafast lasers are inevitably considered. As discussed, ultrashort pulse ablation is noted for having a lower threshold, smaller heat affected zone, and clean and high-resolution material removal. These features correlate to advantages in PLD, as the pulse energy can be reduced by multiple orders of magnitude compared to nanosecond pulse energies and produce smoother films [222]. Improved quality is due to reduced particulates formed by greater thermal loading of the target for nanosecond pulses, and by operating at higher repetition rates [223], [224]. Higher repetition rates (MHz range) match nanosecond pulse growth rates, result in a more continuous flux of atoms, and may also reduce the ablation threshold via an incubation effect. The obvious disadvantage to ultrafast lasers is the relative cost and maintenance and operation complexity [218]. Deposition of epitaxial and nanoparticle films has been demonstrated for amorphous carbon (60 ps Nd:YAG, 1064 nm), atomically-smooth chalcogenides (60 ps Nd:YAG, 532 nm), diamond-like carbon (DLC) (120 fs Ti:Sapphire), and zinc oxide (ZnO) (130 fs Ti:Sapphire, 790 nm) with thicknesses as low as 25 nm, 2.5 µm, 20 nm, and 15 nm respectively [222], [225]–[227].

In the case of ZnO, initial efforts to improve film quality using femtosecond lasers found that the crystalline quality was poorer compared to those grown with nanosecond lasers [228], [229]. By controlling the laser fluence, it was possible to grow ZnO nanorods on a sapphire substrate [20]. A fluence below 1 J/cm2 was used to seed the subtrate with nanoparticles, followed by a high fluence above 3 J/cm2 to produce a plasma plume and grow directional rods (Figure 2.20), thanks in part due to the nitrogen background.

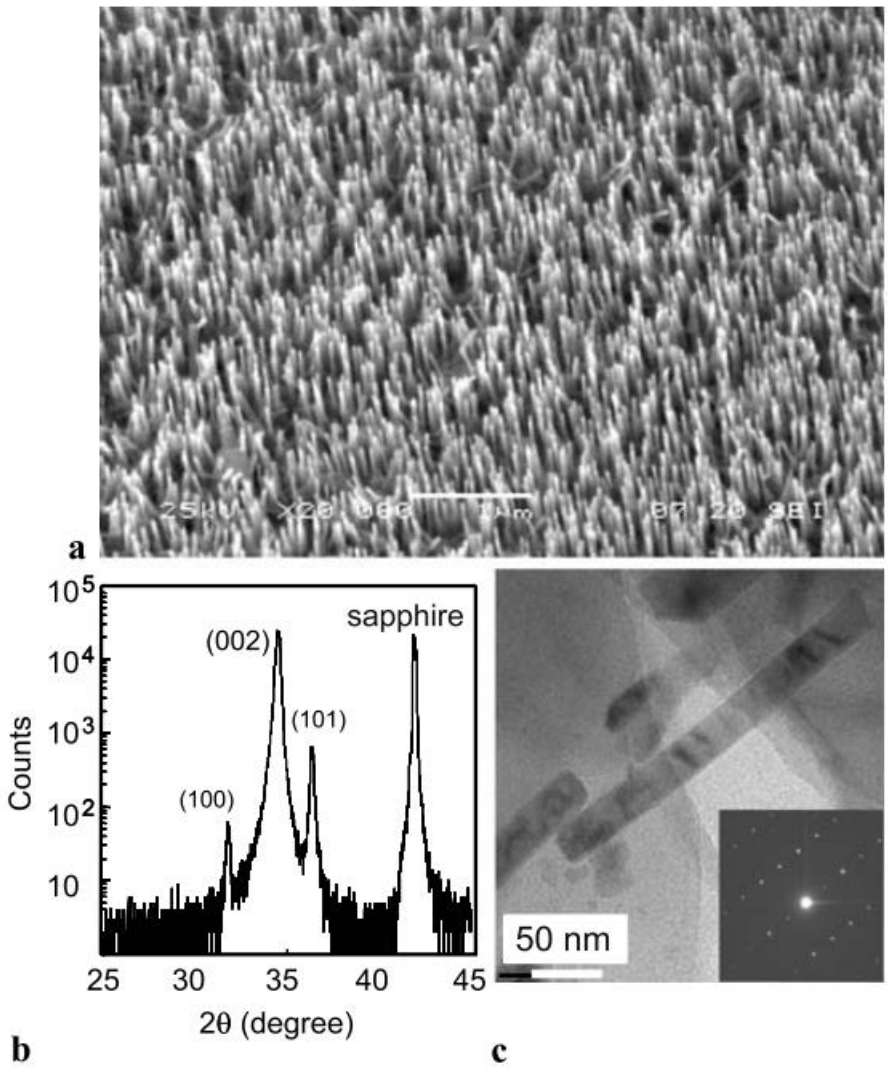

Figure 2.20: a) ZnO nanorods grown by fs-PLD, b) XRD pattern, c) TEM image of single nanorods, inset is SAED pattern which indicates good crystal qualities [20]. – Permission requested from the publisher.

Interactions with the background gas can enable unique micromanufacturing techniques, as has also been demonstrated for TiO2 nanoparticles [30] and carbon nanostructures [230]. As a wide bandgap semiconductor (3.0 to 3.2 eV), Ti02 is of significant interest to the scientific community [231]. Nanoparticle-assembled films (spherical diameter around 25 nm) have been deposited on Si in vacuum by a frequency-doubled Nd:glass laser with 300 fs pulse duration [29]. Amoruso et al. [30] tuned the film morphology from glue-like nanoparticle agglomerates to a porous collection of individual nanoparticles by changing the background oxygen pressure between high vacuum and 10 mbar. Deposition morphology can also be altered by delivering varying pulse trains to the TiO2 target [232].

So-called burst-mode fs-PLD, utilising multiple 700 fs pulses temporally spaced down to 20 nanoseconds, enabled nanoparticle size control and, with the right parameters, atomically smooth epitaxial thin film growth. More recently, fs-PLD has been investigated for the production of

nanometer sized Eu:LiCAF particles as a fast-decay scintillator to replace 3He in thermal neutron detectors [233]. Ultrashort pulse ablation was chosen to prevent the formation of large droplets by the aforementioned process. The authors were able to create 280 nm mean-sized particles and reduce the decay time of the bulk crystal by at least an order of magnitude (approx. 1700 ns to 40 ns). Fs-PLD has been used for depositing atomically thin rare-earth (Yb^{3+}) doped MoS_2, since the high melting and boiling points of rare-earth doped sulfides makes chemical vapor deposition challenging, and the ultrafast-produced ablation plasma ensures mixing of the target species [234].

2.4.5 Welding

Welding and joining is an essential process in modern manufacturing. Any device that cannot be created in a single step, due to geometric or functional complexity, or because it involves a multiplicity of different materials, requires reliable, strong joining that does not impede necessary material properties such as electrical or thermal conductivity. Since welding is the addition of one material to another, it can be considered under the umbrella of additive manufacturing. Despite being an age-old manufacturing method, ultrafast lasers have widened frontiers in the bonding of similar and dissimilar glasses and ceramics, particularly on the microscale, as well as on the nanoscale for the joining of nanowires and nanorods.

2.4.5.1 Glass Welding

A challenge in the optical welding of glass is that good interfacial melting inside the transparent material is difficult to achieve when single photon absorption of the wavelength is either strong at the surface or extremely low. This is the case for CO2 lasers and other common laser wavelengths in the visible and near-infrared [235]. Ultrafast lasers can induce multiphoton absorption in solid, transparent media. Some of the excited electrons ultimately relax to create intrinsic defects, and some relax by transferring energy to lattice vibrations and heating within tens of picoseconds [101], [236]. Lattice heating leads to melting at the interface and solidification that bonds the initially separate components (Figure 2.21). By utilising repetition rates such that the time between subsequent pulses is shorter than the time for out-of-focal-volume heat dispersion, the temperature (and thus melting) can be precisely controlled [22]. As previously established, the nonlinear absorption that is essential for this process is highly dependent on peak intensity which is readily provided by ultrashort pulses. Predominantly, the joining or microwelding of fused silica [237]–[239], borosilicate glass [21], [240], [241], and photostructurable Foturan glass [242], [243] has been developed. Dissimilar glass welding has also been demonstrated, for example in borosilicate and fused silica [244], [245] and in optical fiber and glass slides [246]. For a review of glass bonding the reader is directed to [236]. The

effect of process parameters like pulse energy, pulse duration, repetition rate, Keldysh parameter, and nonlinear absorptivity were recently reviewed in [247].

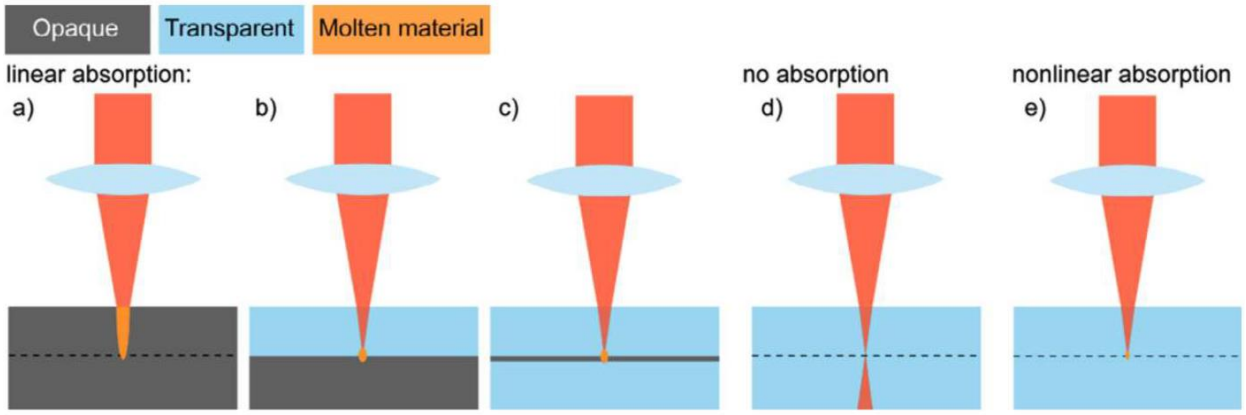

Figure 2.21: Comparison of laser-material interaction for different material properties. Linear absorption occurs at any point where light reaches for opaque materials (a to c) and nonlinear absorption occurs only at the focus position for transparent materials (e). – Reproduced from [21] (CC-BY-NC-ND).

Effective and high quality bonding in laser welding requires extremely close contact between the two surfaces, such that the melted volume – which may not be much larger than the focal volume - bridges the gaps [247]. Optical contact meets this need and occurs when sufficient surface area is close enough for intermolecular forces to hold them together. This requires high smoothness (e.g. 2 nm roughness [239]) which may necessitate additional processing and is difficult to achieve for large area samples or samples with irregular surface geometries [248]. Efforts to increase the bridgeable gap include increased laser power [22], [248]. Higher repetition rates [249] and alternative beam profiles [250] have been attempted to remedy this limitation. Recently, an Nd:YVO4 ps laser at 1064 nm and MHz-repetition rate was rapidly scanned in concentric circles over the welding gap [251]. The method generates a larger horizontal melt pool in soda-lime glass to provide the necessary material to bridge a “natural” stacking gap of approximately 10 µm. The weld appears to be free of defects and exhibits shear strength up to 64 MPa. Soda-lime samples welded under optical contact have previously been reported to have shear strength well over 200 MPa [252].

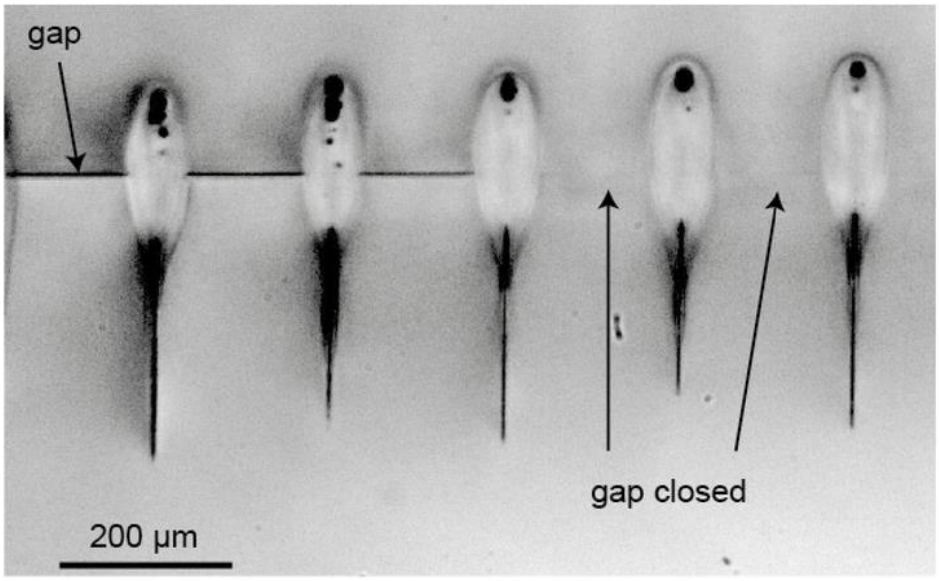

Figure 2.22: Ultrafast laser weld seams in fused silica without optical contact. Laser propagation direction is from top to bottom, and from left to right laser focus position is shifted up from interface. At a particular focus position the gap is closed [22]. – Permission requested from the publisher.

2.4.5.2 Ceramic Welding

Ceramic materials are notorious for their thermal resistance, high melting points, and strength. This is their greatest engineering advantage but also their greatest manufacturing disadvantage. Ceramic joining techniques are numerous and technically challenging, and often subject the entire sample to extreme conditions such as high temperatures and/or vacuums [253]. Thus, welding devices with sensitive components or materials by techniques such as diffusion bonding is not possible [254]. Ultrafast lasers, with their affinity to induce non-linear absorption and potential to induce melting in thermally resistant materials, may provide solutions. Penilla et al. [254] investigated this potential and found that they could weld polycrystalline alumina and yttria-stabilized zirconia via two different approaches. One approach was to tune the single-photon and two-photon transparency of YSZ using thermal treatments so that the ultrafast laser could be focused inside of the material and induce localised melting to form a weld. Welded components were able to hold a high vacuum up to 3.2x10^7 mbar. Alternatively, if the transparency is not favorable, the parts to be welded can be separated by a 12.5 µm gap and the laser is focused into the gap. The authors argued that the ultrashort picosecond regime (~2 ps) of pulse duration is more favorable for welding since it generates a larger melt pool without ablation when compared to the femtosecond regime.

2.4.5.3 Dissimilar Material Welding

While most research has focused on the welding of similar, transparent materials, the feasibility of welding of dissimilar materials such as glass and metals has been investigated. Since one of the materials is transparent to linear absorption, the laser can still be focused at the interface and directly generate a melt region for bonding. While other methods exist for dissimilar material bonding, the space-selectivity provided by an ultrafast laser gives rise to facile, precise joining with reduced collateral change. In the case of femtosecond laser bonding, thermal stresses due to differences in the coefficients of thermal expansion are limited by the smaller heat-affected zone [245], [255]. Ozeki et al. [256] demonstrated direct welding of copper and glass with a femtosecond Ti:Sapphire laser and found greater precision in welded regions compared to a nanosecond source. Copper, aluminum, and steel were each bonded with glass via a similar laser system, and the shear strength was tested as a function of pulse energy [257]. As the pulse energy increased, the shear joining strength also increased but plateaued after 15 µJ. The welding mechanism is that of ultrafast ablation in which ejected plasma and molten particles are confined between the substrates and resolidify as a bonded material. Use of a femtosecond fiber laser capable of repetition rates up to 400 kHz in the welding of 304 stainless steel and soda-lime glass revealed the strong dependence of joint strength on repetition rate [258]. Shear strength of the 400 kHz weld (8.79 MPa) was an order of magnitude greater than that of the 100 kHz weld (0.82 MPa). Aluminum-glass welding via picosecond fiber laser also with repetition rate of 400 kHz has been reported [23], [255]. In such cases, thermal accumulation by shorter pulse to pulse times generates a melt pool in the glass that contributes to superior bonding. The higher melting points of the metal constituents produces high density plasma that penetrates the glass melt (Figure 2.23c). While there is evidence for improved welding with picosecond pulses for ceramics, to our knowledge a direct comparison between picosecond and femtosecond pulses has not been made for dissimilar materials.

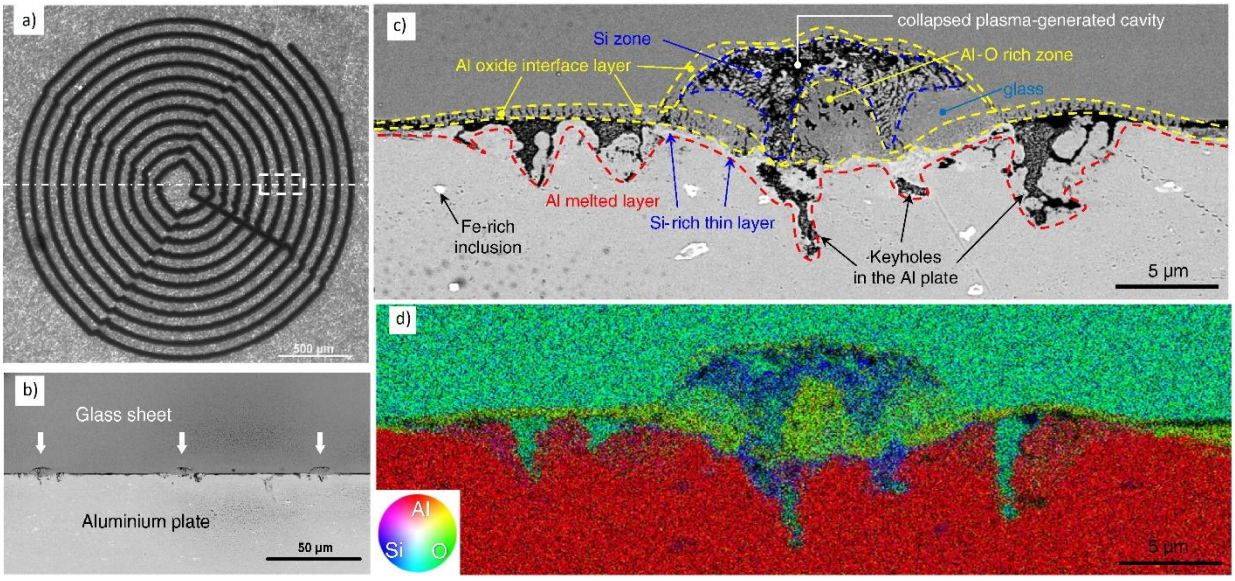

Figure 2.23: Ultrafast laser welding of fused silica and commercially pure aluminum. a) Top-view of spiral weld pattern, b) cross section of white rectangle in a), c) cross section of single weld bead, d) EDS map of region in c) [23] – Permission requested from the publisher.

2.5 Advances in Process Techniques

2.5.1 Process Monitoring

For any manufacturing process, structural quality, surface quality, and minimal variation between parts is highly desired. In a commercial industrial setting, these things are essential for reducing costs and meeting safety expectations and quality standards. In an academic setting, experimental repeatability and costs are also important. To this end, process monitoring, via sensors that measure temperature, acoustics, light, etc., is a critical tool. Additionally, it can be leveraged to further our understanding of the physical processes that occur during manufacturing. Process monitoring in additive manufacturing is an active area of interest. Widespread adoption of AM is hindered by ever-present issues of quality and repeatability [259], [260]. One of the greatest advantages of AM – the ability to produce complex 3D structures and internal morphologies – presents inherent challenges for non-destructive testing and quality control. Furthermore, complexity of the underlying physical phenomena of AM methods presents an overwhelming number of variables, which limits the efficacy of predictive modelling to ensure part quality. For example, laser powder bed fusion techniques such as selective laser melting rely on a consistent and stable melt pool, determined by laser parameters like laser power, scanning speed, hatch spacing, and powder layer thickness [261]. Builds can suffer from inconsistent microstructure (and therefore yield and ultimate tensile strength anisotropy), porosity, and lack of fusion [262]. Studies have used CCD and CMOS cameras, pyrometers, photodiodes, to better understand the effects that process parameters have on the microstructure and build quality [263]–[265]. This allows the correlation of types of defects to a particular origin, and Clijsters et al. [264] linked the melt pool variations during the process to pores that can be found post-process. By knowing which process errors or parameter instabilities cause which defects, effort can be concentrated towards solving those issues. There is interest to identify symptoms of defects or potential defects so that real-time process monitoring can be used to control and affect the process, ensuring build quality throughout [266]. Thus, the layer-wise manufacturing approach of AM offers an additional advantage over specific conventional techniques because it allows online monitoring that reduces dependencies on post-production inspection [267].

Cameras are the essential tool for monitoring ultrashort pulse manufacturing. Ultrafast ablation setups are often accompanied by a coaxial CCD or CMOS sensor by which the machining process can be tracked. One can refer to [268] for a recent review of observation techniques of ultrashort pulse laser-material interactions for investigating the fundamental physics of ablation. Of the applications discussed in Section 2.4, except for MPL and possibly fs-PLD, they cannot

be considered as fully matured manufacturing processes with widespread use in industrial settings or sold as commercial systems [269]. As such, monitoring and observation techniques are primarily demonstrated in literature for the investigation of fundamental phenomena. As these techniques mature and enter development for industrial use, an increased consideration of these factors is predicted. Below is a discussion of monitoring of ultrashort pulse additive manufacturing in literature with a focus on those methods that are utilised for, or have potential to be used for, *in situ*, online monitoring and process control.

2.5.1.1 Monitoring of Multiphoton Lithography

Multiphoton lithography can be monitored by similar techniques as ablation, but the illumination contrast between polymerised regions and air or between polymerized regions and unpolymerized regions is inherently low. Imaging of the submicron features sizes, of which multiphoton direct laser writing is capable, *in situ* is also nontrivial. The mechanical properties of MPP produced microstructures can vary significantly from larger bulk materials [270], which means that direct control over the degree of polymerisation is necessary for improvement of the fabrication technique. The change in refractive index of the polymerized region permits interferometric monitoring [271] and quantification of the polymerization rate [272], but lacks the spatial resolution for identifying fine features.

Baldacchini et al. [24] developed a coherent anti-Stokes Raman scattering (CARS) microscopy setup for real-time monitoring (Figure 2.24). A Ti:Sapphire laser (800 nm, 100 fs pulse, 80 MHz repetition rate) was separated into two beams, one for 2PP and the other was further separated into the 800 nm pump beam and a Stokes beam composed of a broad supercontinuum from 800 nm to >1100 nm generated by a photonic crystal fiber. The pump and Stokes beam were raster scanned over the sample by galvanometric mirrors. Authors also fabricated a closed box containing thin walls of 2 μm thickness and demonstrated the ability of this setup to discover internal warping. The dense cross-linking of polymerized regions exhibits stronger signals due to a larger concentration in vibrational modes, enabling real-time imaging at 2 frames per second. Thus, *in situ*, online defect detection may be feasible with this method, reducing the need for post-production quality assurance as well as saving costs on unnecessary development steps for failed builds.

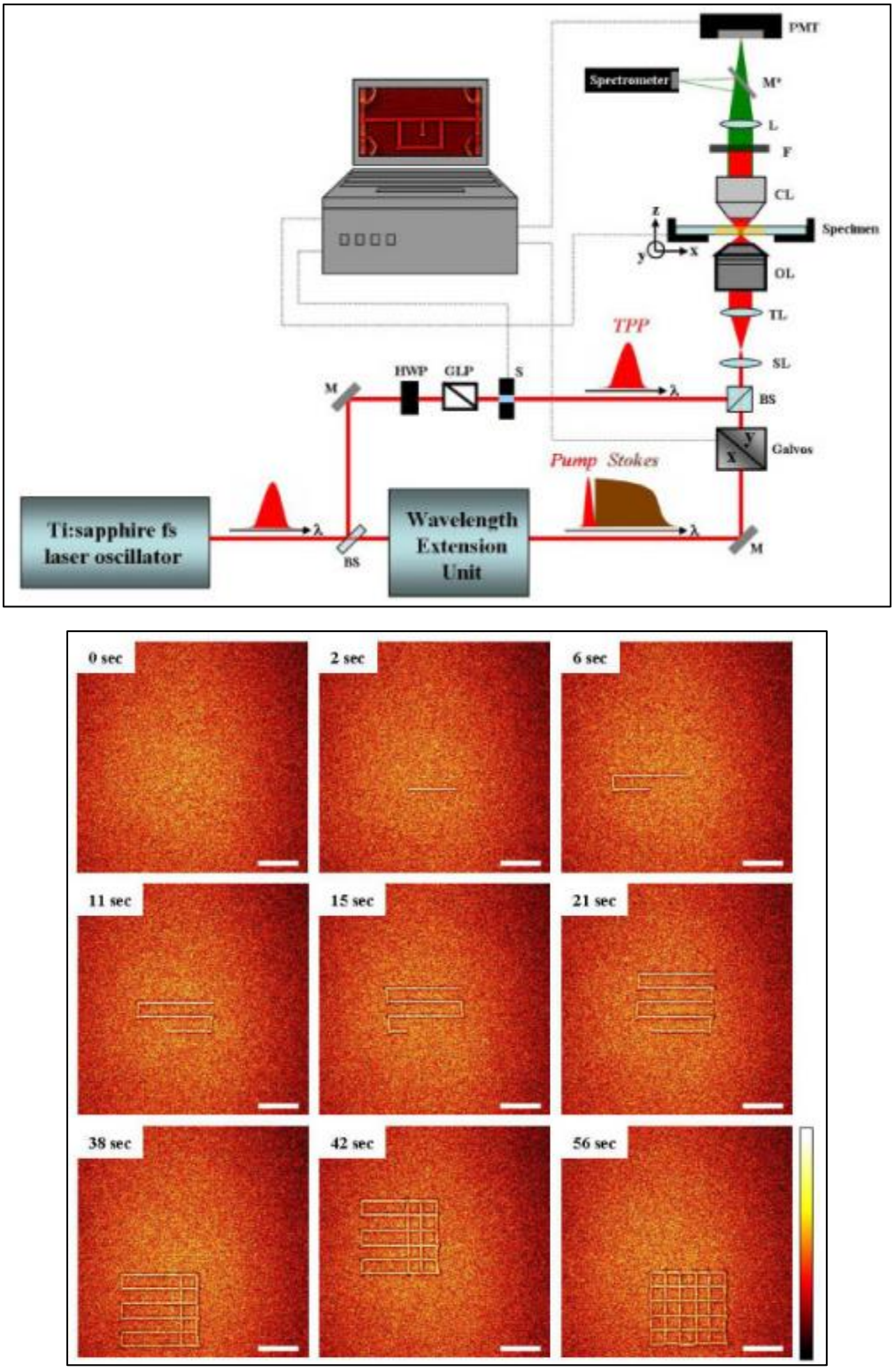

Figure 2.24: Top: Setup for MPL and online CARS microscopy using single laser source. Beamsplitter (BS) diverts beam for 2PP and to wavelength extension unit (WEU) to deliver pump and Stokes beam with set delay. Bottom: Real-time, *in situ* broadband CARS microscopy of MPL. Scale bar is 25 µm [24]. – Permission requested from the publisher.

An alternative technique for imaging polymerized structures that does not require additional, pricey equipment is to utilise photoinitiators that exhibit photoluminescence quenching [25]. After multiphoton lithography, the same laser is used at a lower intensity to generate photoluminescence, resulting in a spatially varying intensity pattern from which the previously exposed structure is recorded with high resolution (~0.5 µm laterally, ~1.4 µm axially). This technique is only applicable where photoinitiator photoluminescence quenching occurs, and the authors report successful imaging for SZ2080 and Irgacure 369. Since the laser power must be switched between a lithographic mode and photoluminescence imaging mode, it cannot operate as a true online monitoring technique, nor can it enable real-time process control. A potential solution is to siphon a second, low power, laser line off the primary lithographic beam and scan it independently over the sample.

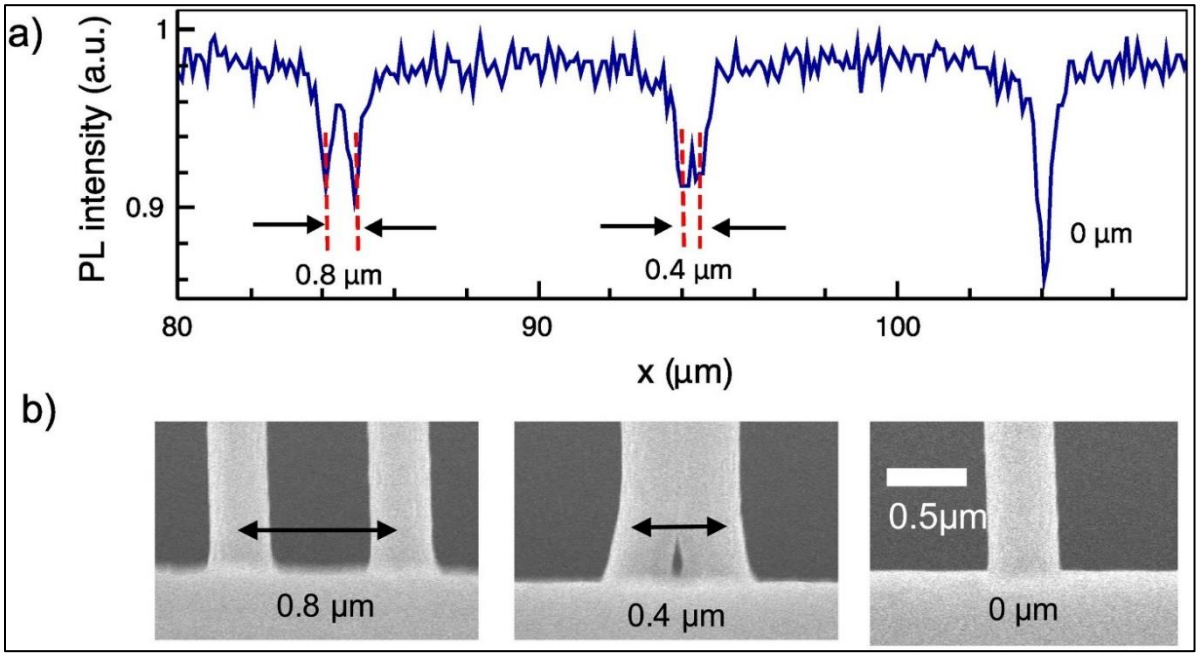

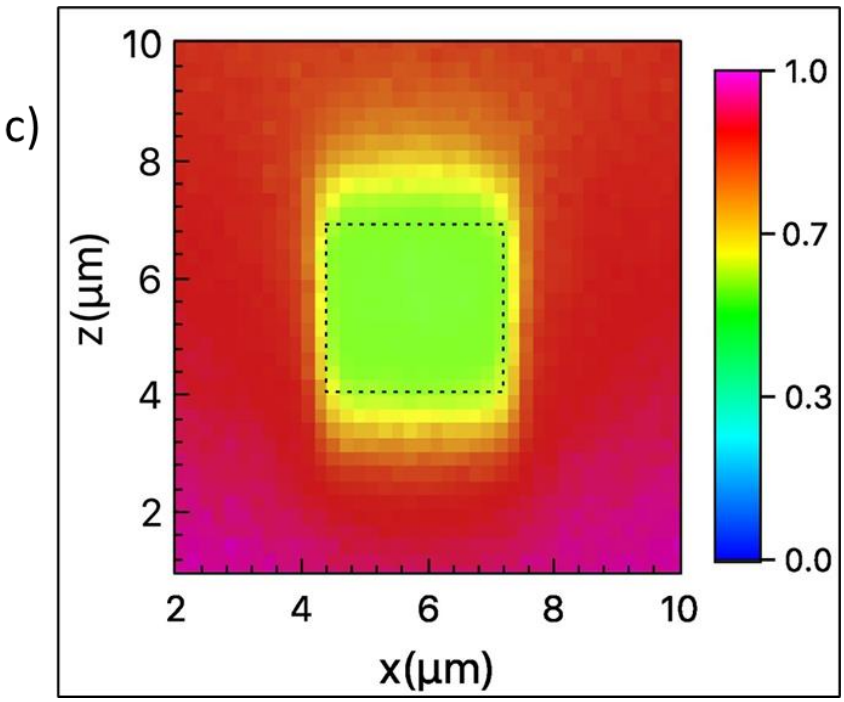

Figure 2.25: a) Photoluminescence intensity scan with minima that correlate to the MPL features in b). Scans can be taken *in situ*. c) 2D Photoluminescence scan of a square rod with dimensions of 3 µm (dotted lines) [25] – Permission requested from the publisher.

Triple harmonic generation (THG) microscopy has been applied to visualise photopolymerized structures, which offers a similar advantage of using the same laser source at a lower average power [26]. However, the *in situ* results appear to have comparatively low contrast (Figure 2.26d)).

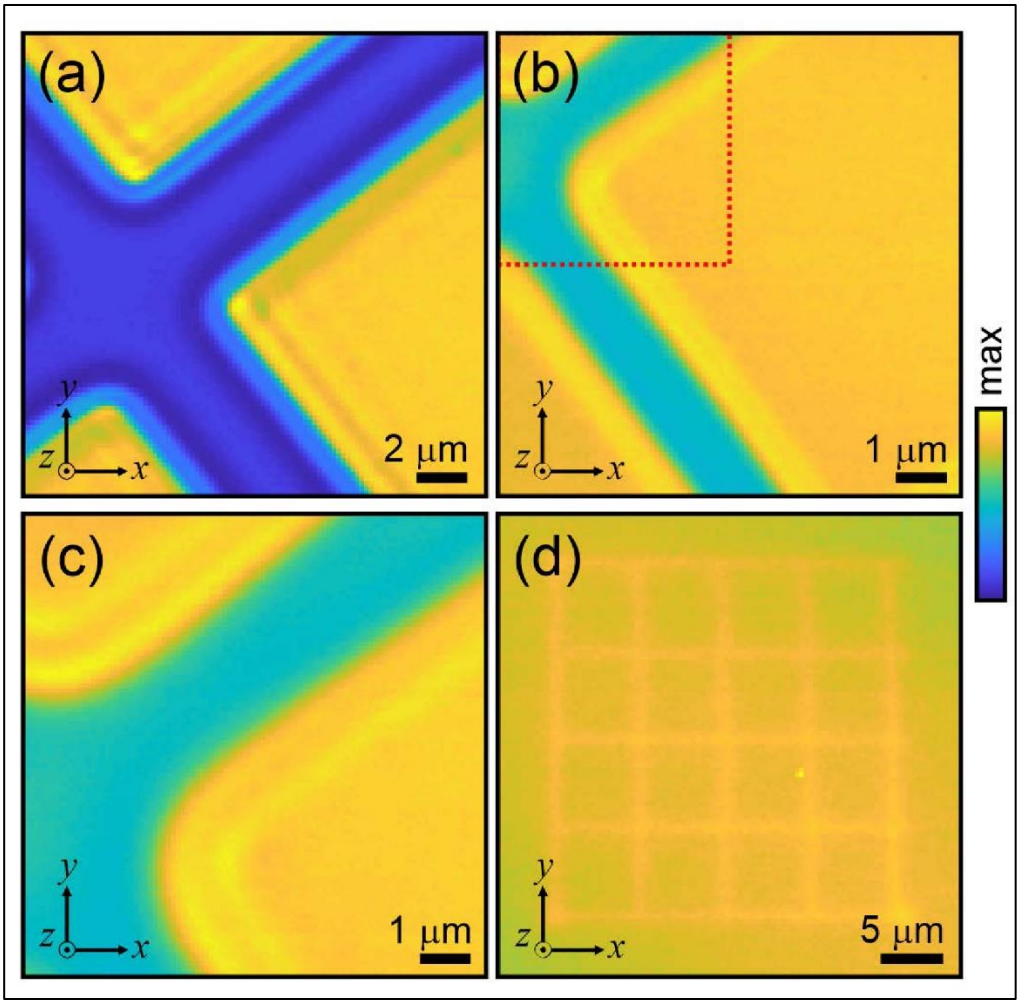

Figure 2.26: THG microscopy images of SU-8 wafers. A) developed structures, b) and c) undeveloped, c) is magnified area demarcated in b). d) *in situ* THG microscopy, features are visible but the contrast is considerably lower [26]. – Permission requested from the publisher.

2.5.1.2 Monitoring of LIFT

For observing and understanding the behaviour of material transfer in laser-induced forward transfer, time-resolved imaging of the ejected material is performed. The inherent challenge of this approach is that when material is ejected by LIFT, small particles (often micron sized) present a high spatial resolution requirement and the high speeds they are accelerated to (up to 2 km/s [273]) presents a high temporal resolution requirement. Time-resolved shadowgraphy reveals important information regarding ejection dynamics, mechanisms, and transfer states in ultrashort pulse LIFT [27], [274], [275]. In general, the light source and sensor are electronically coupled, with camera gating and exposure triggered by a photodiode collecting a sample of the forward transfer-inducing laser pulse. Spatial resolution of the setup is determined by the

diffraction limit, optical quality, and/or motion blur. The temporal resolution is determined by the illumination pulse duration, sensor integration time, and gating/shuttering speeds. A review of LIFT monitoring by material types can be found [276].

Much is still to be understood regarding fundamental principles of LIFT, and the laser-material interaction for many materials is yet to be fully characterised. Recently, Pohl et al. [27] utilised flash illumination from a nanosecond Nd:YAG laser and diffuser combination, coupled into a dual-shot CCD by a 50x objective (Figure 2.27). They typified ejection regimes of copper and gold films according to increasing laser fluences, and described threshold ejection fluences, and cap, jet, and spray ejection phenomena. Precisely controlling transitions between ejection regimes through understanding of the fluence thresholds between them gives the ability to switch deposition types for the fabrication of more complex structures.

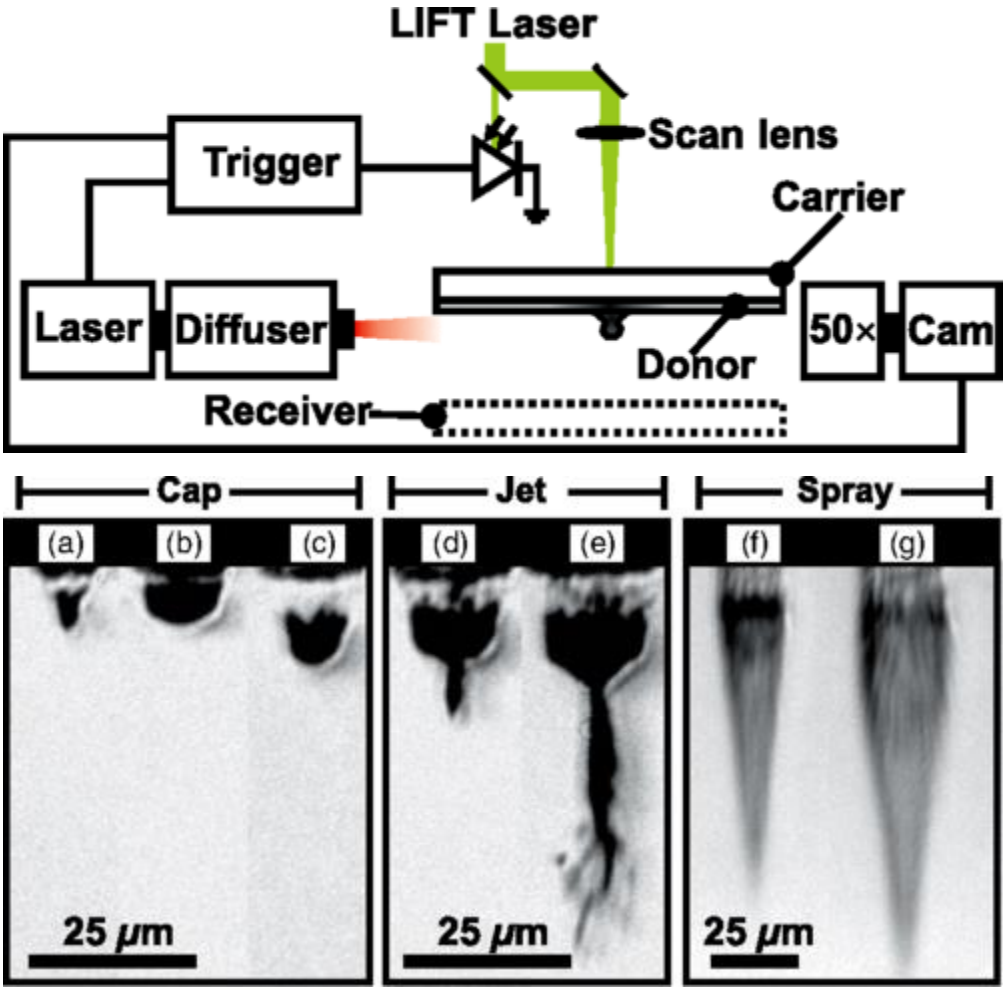

Figure 2.27: LIFT monitoring setup used by Pohl et al. [27] and ejections of 200 nm copper film. All images taken 125 ns after LIFT laser pulse, a) to g) are increasing laser fluence. Droplets in g) seen as lines are travelling about 700 m/s. – Permission requested from the publisher.

In a similar approach, a nanosecond flash lamp and CCD elucidated jetting regimes for double-pulse LIFT of copper film (Figure 2.28) [28]. In the double-pulse method, a longer laser pulse (quasi-continuous wave) locally melts the target so that a subsequent pulse initiates ejection in the liquid phase. Because there are differences in the underlying process between conventional LIFT and double-pulse LIFT, shadowgraphic characterisation is necessary. This monitoring technique will remain important for other materials and any novel, alternative LIFT methods that are developed in the future. Process control of LIFT is enabled by such research. Although it has not been demonstrated to the author's knowledge, it may be possible to perform online analysis of the ejection material imagery and corresponding process control to ensure a high degree of consistency between depositions occurring in the same ejection regime. While high resolution substrate observation could also indicate deposition quality consistency, the ejecta may provide additional information for diagnosis of the cause of defects.

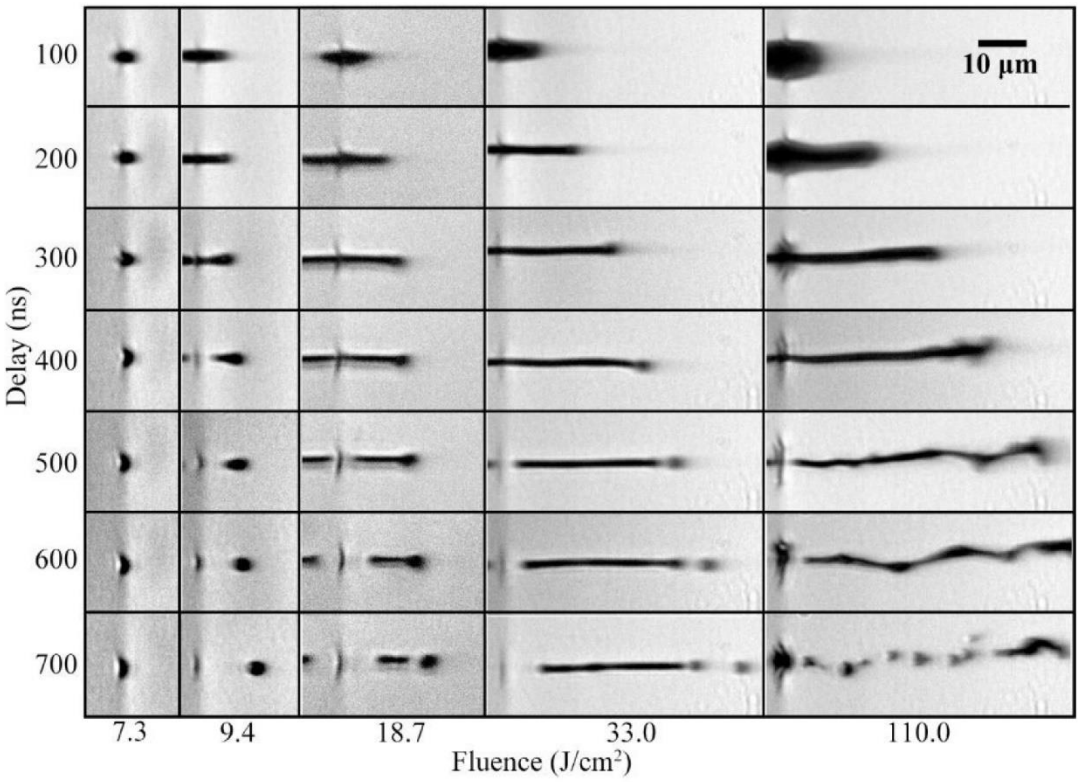

Figure 2.28: Time-resolved shadowgraphy of DP-LIFT of 1000 nm copper film. Delay between the QCW pulse and fs pulse is varied as well as the fluence [28]. – Permission requested from the publisher.

2.5.1.3 Monitoring of PLD

Pulsed laser deposition monitoring is separated into two general categories: plume analysis and deposition rate monitoring. Techniques do not seem to differ from those used for nanosecond pulse PLD and ultrashort pulse PLD. Plume spectral analysis is performed by focusing emitted light onto grating spectrometers, the light detected by charge-coupled device (CCD) or intensified CCD (ICCD) (Figure 2.29) [29], [222].

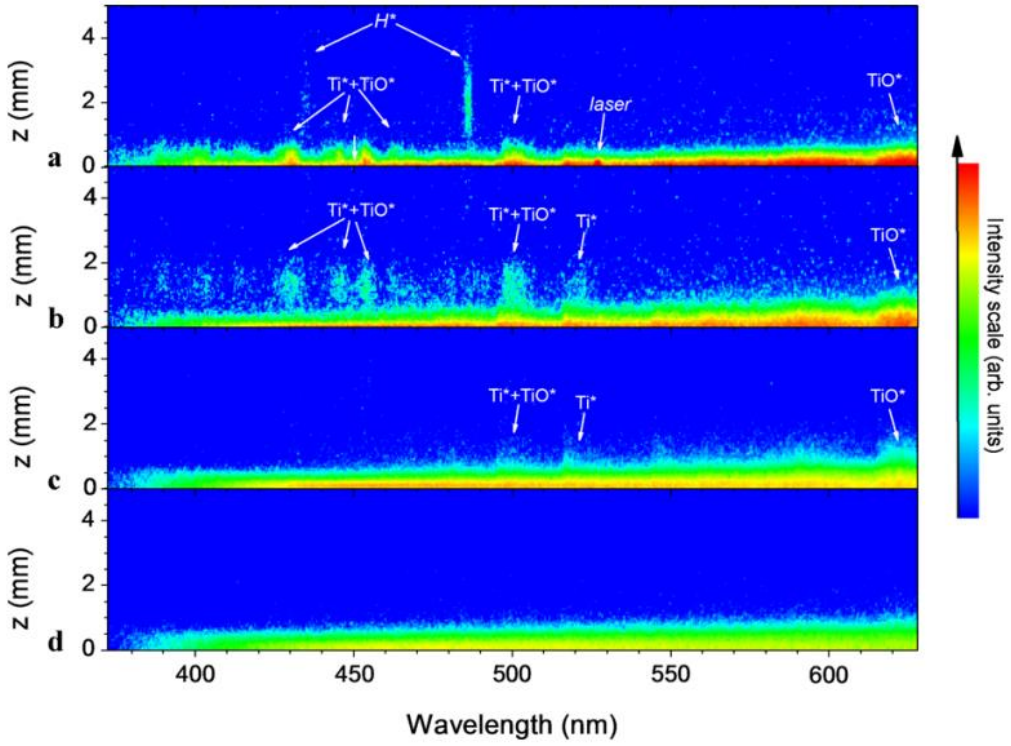

Figure 2.29: 1D, temporal sequence of plume spectral results and height from target surface. A) to d) are 20, 70, 150, 350 ns after incident pulse [29]. – Permission requested from the publisher.

Plume temperature can be inferred by applying Planck's radiation fit and pyrometers provide target surface temperature. A CCA can provide plume images and spatially resolved temperature readings [222]. Plasma within the plume may be characterized via Langmuir probe to determine electron temperature and ion density (and thus ion flux) [20]. Plume analysis aids in characterising the ultrafast laser-material interaction and comparing it to, for example, nanosecond laser modes, but does not provide much towards online process control that may improve the manufacturing method. The deposition rate is the most important metric to measure and monitor, and this is done using a quartz crystal microbalance (QCM) [30]. Film growth rates can be controlled by increasing or decreasing the pulse repetition rate or the laser fluence.

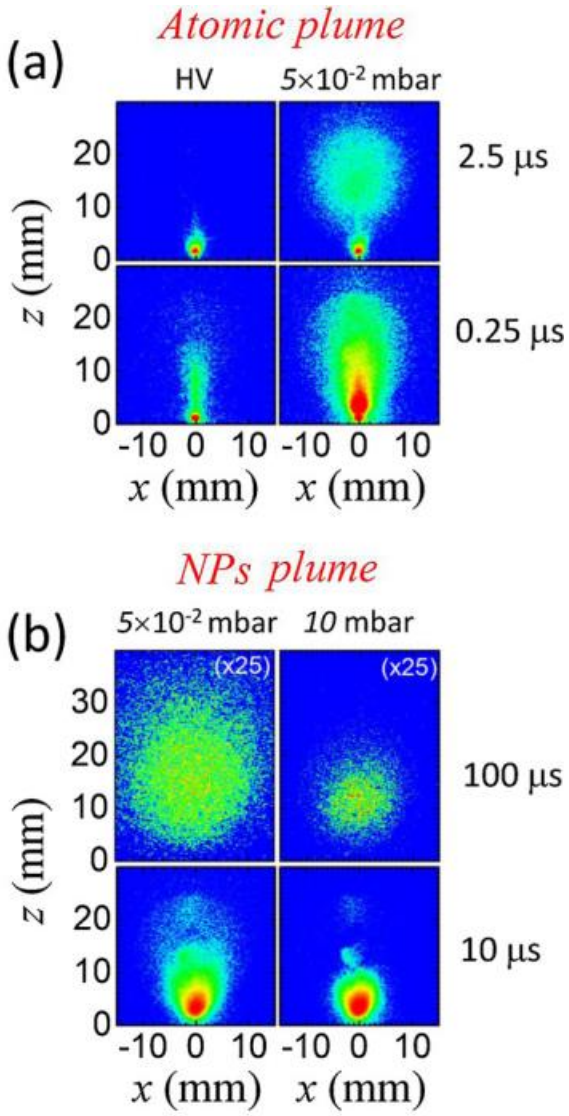

Figure 2.30: TiO2 plume emission after different time delays (0.25, 2.5, 10, 100 us). Atomic plume precedes the nanoparticles (NPs) plume and the extent of material ejection (deposition rate) is dependent on background gas pressure [30]. – Permission requested from the publisher.

2.5.1.4 Monitoring of SLM/SLS

The studies discussed in section 4.1 are recent and are focused on the feasibility of manufacturing. In the case of femtosecond PBF of UHMWPE, in-situ video monitoring was used for process observation [146]. The plasma emitted by laser irradiation was treated as a proxy for process stability, and the monitoring was used for estimation of the cooling time. In-depth analysis of the detectable signals and their relation to the process quality is required for further understanding.

If powder-bed fabrication by ultrafast laser proves to be an effective micro-additive manufacturing method, it is expected that process monitoring and control will become a priority. Detailed models of ultrashort pulse powder sintering and melting would be needed to take advantage of in-situ monitoring. The unique laser-material interactions compared to nanosecond or CW modes means that the connections between process parameters such as laser power and repetition rate and the thermal and mechanical properties of the builds would be different from conventional PBF. Fortunately, conventional PBF research such as the creation of process maps [277] can act as a template for the work that needs to be done to make ultrashort pulse PBF a reliable process with consistent quality.

2.5.2 Increased Throughput

Ultrafast lasers were historically not easily accessible due to the significant capital investment and difficulty of operation and maintenance. As these barriers are overcome, and ultrafast lasers become more prevalent and ever more integrated into manufacturing procedures, industrial applications will accelerate. Widespread industry and private sector adoption of new manufacturing technologies is driven by the throughput capabilities, quality consistency, initial capital investment, and hardware reliability of the technology. Ultrashort pulse lasers offer the distinct advantage of precise, single-point feature processing down to the nanoscale, which inherently opposes high-throughput fabrication. This phenomenon is described by Tennant's law (adapted by [278] for 3D laser writing) for the throughput of a micro- or nano-fabrication process as a function of resolution [279]:

$$T_{2D} = (R/2.3)^5$$

Where T_{2D} is the two-dimensional throughput and R is the feature resolution. Techniques for enhancing laser throughput typically fall into two categories: 1) faster scanning, and/or 2) parallelisation. Some of these techniques as applied to additive manufacturing are discussed below.

2.5.2.1 Multiphoton Lithography

While academic, research, and rapid prototyping purposes may be content with lower throughput, there is significant interest in greater volumetric fabrication speeds. An intuitive way to improve throughput capabilities of any laser writing system is to increase the speed of the beam scanning. Commercial MPL systems typically utilise two galvanometric scanners for X-Y plane raster scanning and a precision XYZ stage for axial scanning. As the scanning speed increases, the total optical dose decreases, and so lasers with greater intensities are required. The working area of the objective limits the structure size, and so synchronization between the galvanometric and linear scanners is needed to maintain high translation velocities (cm/s)

without introducing stitching [280]. However, laser writing is limited by the speed that the beam can be deflected and the speed the target can be moved.

An alternative approach to increasing throughput is parallelisation, which uses multiple focal spots to simultaneously fabricate identical structures in multiplicities. This can be done with a microlens array, diffractive beam splitter, [281], [282] or by sending holographic data to a spatial light modulator that modulates the laser beam phase [31]. Yang et al. [283] demonstrated the flexibility of SLM by implementing different computer-generated holograms to construct a variety of foci patterns. These enable parallel fabrication of microlens arrays and photonic structures with different spatial distributions. Advances and research in hologram generation algorithms for SLMs is ongoing, as the quality and versatility of the parallel processing depends upon it [284], [285]. While these methods dramatically increase throughput and excel at producing periodic structures, producing truly arbitrary structures is challenging.

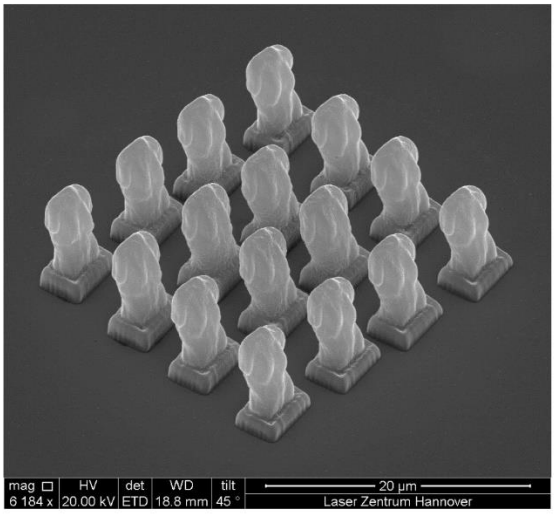

Figure 2.31: SEM image of Venus statues parallelised by multi-beam MPL [31]. – Permission requested from the publisher.

Laser beam spatial modulation can be performed by digital micromirror devices (DMDs) which are arrays of microscopic mirrors that may be individually tilted. Hundreds of thousands of reflecting elements can compose a single device, and they allow spatial shaping of the laser intensity profile at an improved cost and switching speed [286], [287].

Saha et al. [32] utilised a DMD to project femtosecond laser light sheets of arbitrary 2D patterns and demonstrated significant versatility in polymerised structures that maintained submicron resolution (Figures 2.32 and 2.33). This areal method permits a projection area of up to 165 µm x 165 µm with approximately 1 million pixels per exposure. Layers can be fabricated at thicknesses between 1 and 4 µm, which corresponds to volumetric 3D printing rates between 5 and 20 mm^3/hour. An important aspect of their technique was the temporal focusing of the beam. The broad wavelength spectrum of ultrashort pulses combined with the dispersive effects of the periodic DMD array results in pulse stretching and suboptimal intensity gradients at the focal

plane. To compensate, the optical system was arranged so that the objective lens image plane is the conjugate plane of the DMD mask and therefore the path lengths for each wavelength are the same at the focal plane. In this way, the axial resolution could be controlled to submicron widths.

Geng et al.[33] combined a DMD setup and binary holographic methods to generate laser foci for parallel nanofabrication but demonstrate an ability to develop arbitrary structures at a writing speed of up to 5 mm/s and axial resolution of 1.6 µm. In a method similar to Saha et al. [32], Hahn et al. [288] devised a DMD projection method with continuous stage translation and the changing 2D patterns, resulting in a ~5x faster volumetric printing rate, and has a voxel printing rate comparable to other modern systems. They also demonstrated arbitrary 3D structure printing capabilities.

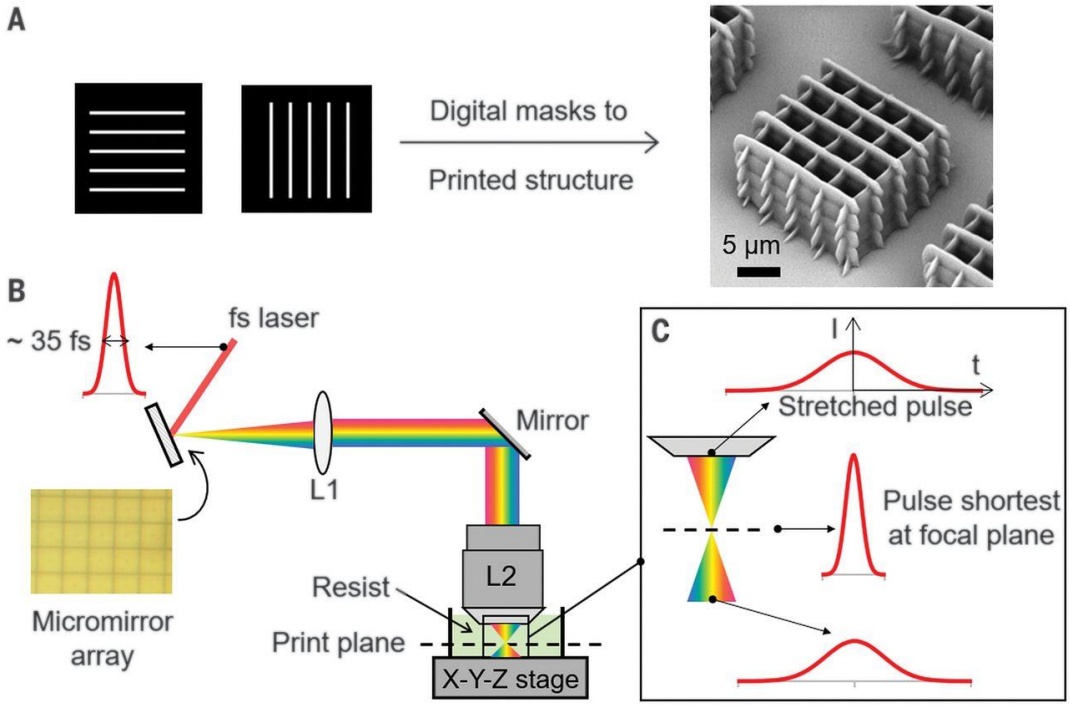

Figure 2.32: A) Digital masks generated by DMD and the lattice structure produced with them. B) MPL setup with DMD array, showing beam dispersion. C) Temporal focusing diagram, greatest intensity localisation is achieved at the objective focal plane [32]. – Permission requested from the publisher.

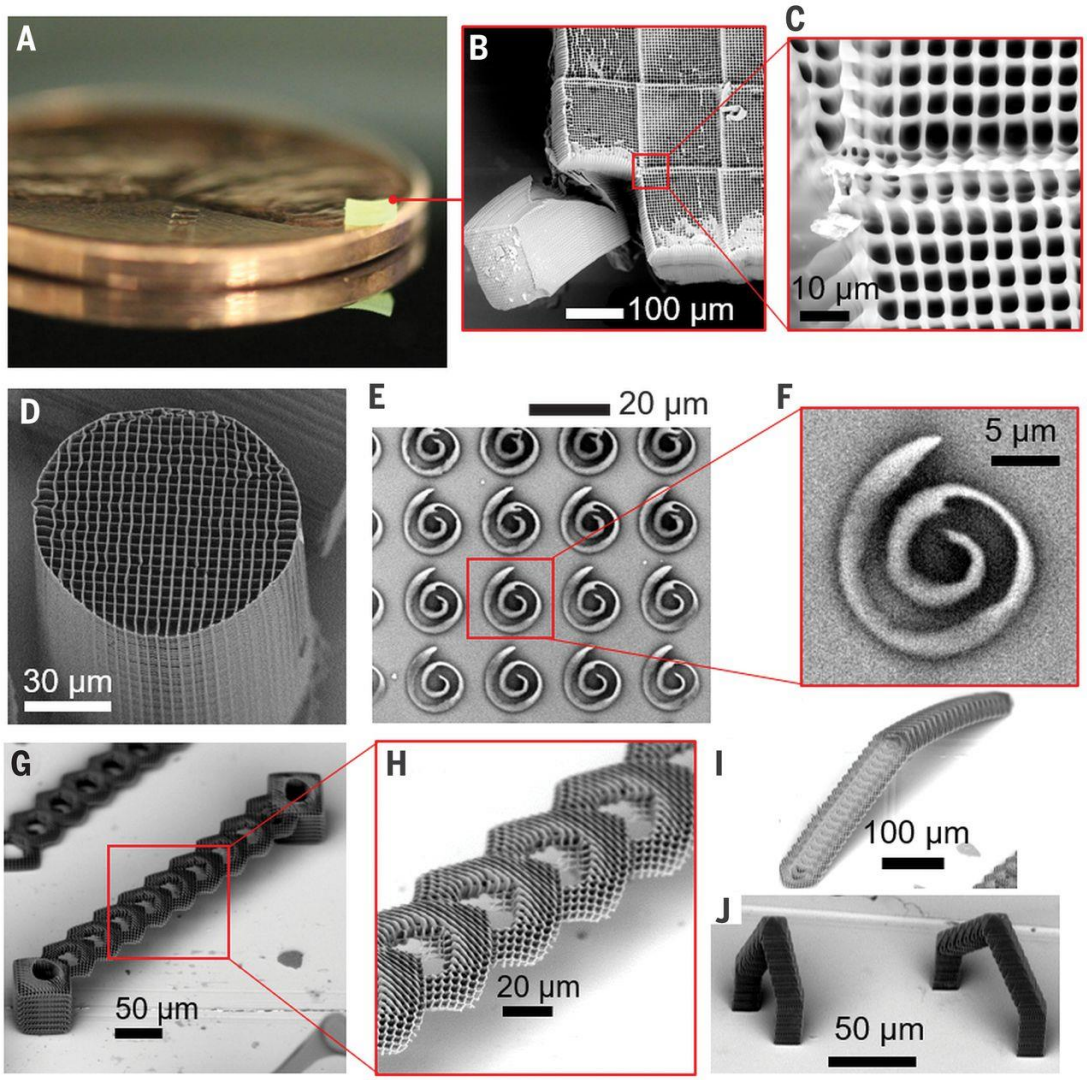

Figure 2.33: Various structures produced by the high throughput method by Saha et al. [32], demonstrating the geometric freedom obtained by DMD spatiotemporal focusing. Patterns still have a degree of repetition. – Permission requested from the publisher.

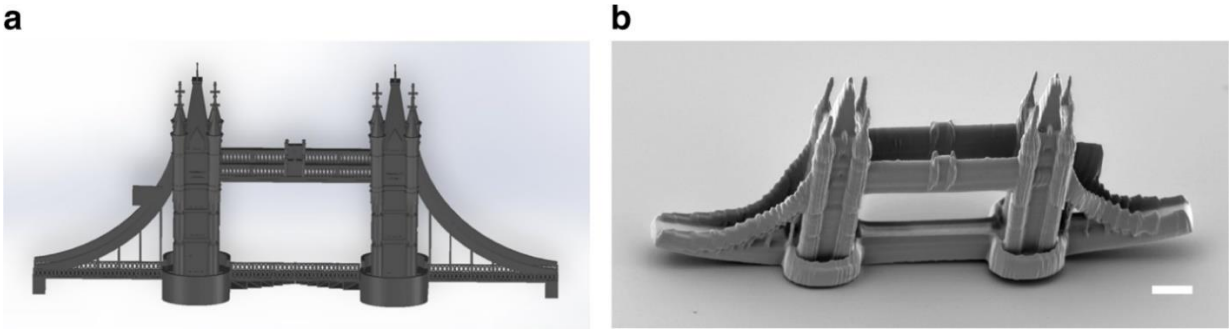

Figure 2.34: Incorporation of binary holography generation into a DMD permitted MPL of this arbitrary structure, the London Bridge at high speed. Scale bar is 10 µm. – Reproduced from [33] (CC BY 4.0).

2.5.2.2 LIFT

Efforts for improving laser direct writing throughput are not just limited to MPL. In the typical implementation of LIFT, the laser beam is serially scanned across the donor substrate. Galvanometric scanners are used for faster scanning which, combined with an increased laser repetition rate, results in higher throughput [289], [290]. As with MPL, this limits the speed of pattern generation to the speed that the beam can be scanned over the surface or to the speed the substrate can be moved relative to the beam. There is an additional challenge in LIFT, caused by the temporal and spatial proximity of consecutive ejections [290]. Instability of the donor substrate after a pulse therefore may impose a limitation on throughput. When maximising throughput, a balance must be found between the scanning speed and the laser repetition rate to prevent jet-jet interactions [291].

Spatial light modulation has been applied to LIFT, providing the advantage of both arbitrary pattern deposition (parallelization) and increased throughput [34]. DMDs have again been used, but for profile modulation of nanosecond laser pulses resulting in single-shot ejection of silver nanoparticle paste patterns [34], [292], [293]. The single-shot pattern transfer of a solid phase polymer material, poly(methyl methacrylate), via DMD modulation of ultrafast-LIFT (Ti:Sapphire, 150 fs, 1 kHz, up to 1 mJ) was demonstrated by [294]. 2D deposits up to 100 µm x 100 µm with minimum feature size of 10 µm could be made with a single pulse. Further research is necessary to optimise fabrication speeds by increasing pulse repetition rates, laser power, DMD size and switching rates. A direct comparison of volumetric 3D printing rates to alternative fabrication methods should also be made.

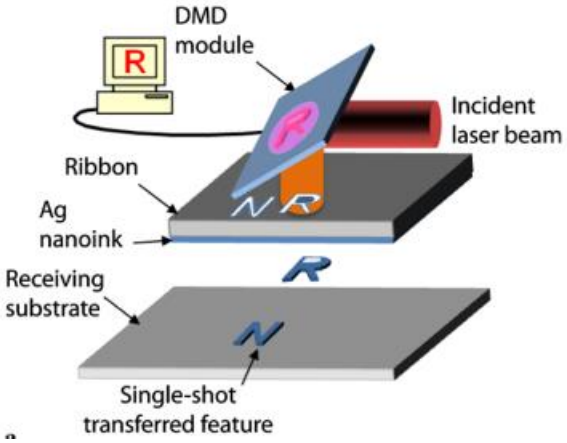

Figure 2.35: Top: Single-shot pattern deposition in LIFT. Bottom: SEM image of deposited pattern [34]. – Permission requested from the publisher.

A derivative technique of LIFT, called laser-induced dot transfer (LIDT), can deposit an array of submicron particles in a single shot [210]. A top-hat beam that passes through a photo-mask will result in a grid-like projection onto the donor substrate, and cause a corresponding grid-like ejection [295]. This greatly increases throughput compared to single-shot single-deposition techniques. Recently, a femtosecond laser source was passed through a diffractive optical element to separate it into 4 beams which were recombined to produce an interference pattern at the donor substrate, composing the grid-like projection (Figure 2.36) [35]. The diameter of the deposited dots is in the hundreds of nanometres, the number of which depends on the laser parameters.

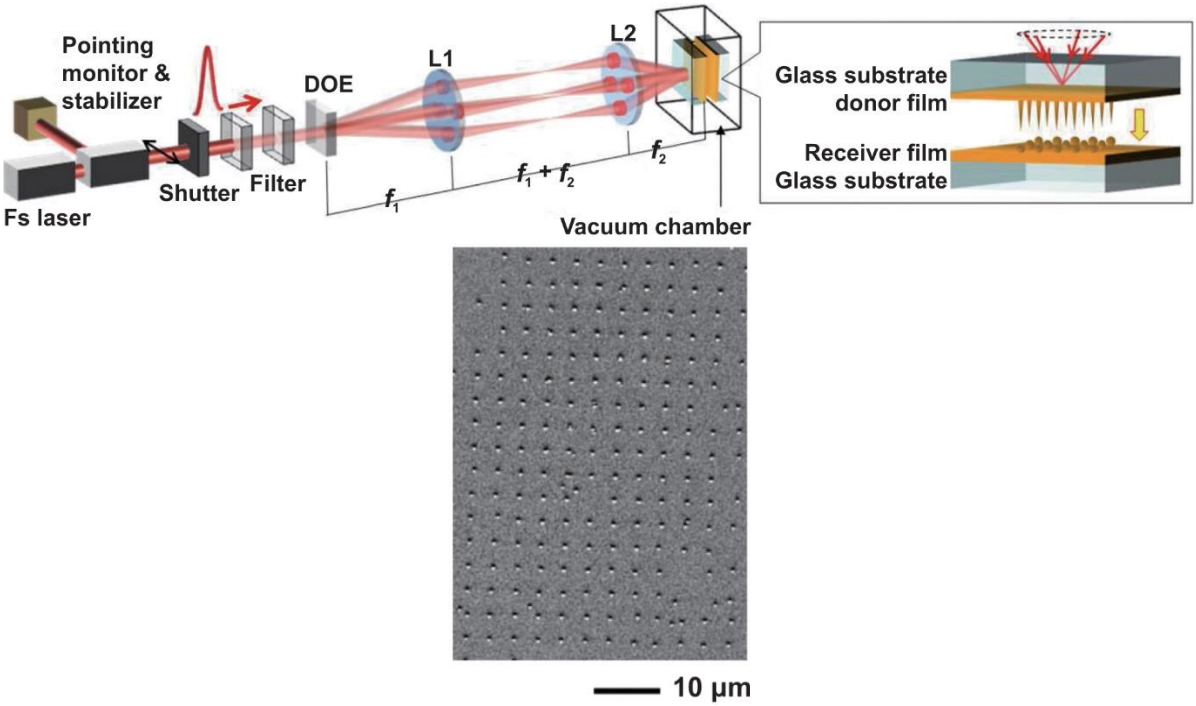

Figure 2.36: Top: LIDT technique whereby a DOE separates the fs laser source into 4 beams, which are recombined to produce an interference pattern at the donor film. Bottom: Resultant drop array. – Adapted from [35] (CC BY 3.0).

2.5.3 Hybrid Manufacturing

Lasers are unique manufacturing tools. As long as one is using a wavelength that is readily absorbed, they allow a directed, highly localized input of energy into virtually any target. The amount of energy that is put into the target is simply controlled by the laser power. As power is increased, the target temperature increases and the material enters a melting regime followed by an evaporation and ablation regime. Melting and resolidification enable additive manufacturing, and evaporation and ablation enables subtractive manufacturing. Thus, using the same experimental setup and laser, it is possible for modern ultrafast lasers with broad tunability (wavelength, pulse duration, repetition rate) to switch between additive and subtractive manufacturing modes. The prospect of hybrid, all-in-one manufacturing devices with a lower capital cost is attractive, and the use of multiple laser techniques has been demonstrated.

Microfluidic device fabrication can benefit from such hybridization. Ultrafast subtractive manufacturing of microfluidics can be done via femtosecond laser induced chemical etching (FLICE) [296], [297]. This is also known as femtosecond laser induced selective etching (FLISE) and femtosecond laser assisted etching (FLAE). Non-linear photon absorption is induced by focused ultrashort pulse laser radiation inside of a transparent medium such as fused silica. The material undergoes a highly localised irreversible transition that causes it to be preferentially removed in a subsequent exposure to an etching compound such as hydrofluoric acid (HF) or potassium hydroxide (KOH). In this way, microchannels with diameters less than 60 µm and 1 cm size can be created inside of the bulk material [298]. Wu et al. [36] combined this subtractive ultrashort pulse laser micro-processing method with multiphoton polymerization to create customisable glass microfluidic devices with integrated polymeric microstructures (Figure 2.37). An Er-fiber laser operating with 360 fs pulse duration and 200 kHz repetition rate was used for both FLICE (5 mW, NA=0.46) and MPP (0.1 mW, NA=1.4). Microchannels with rectangle, round, elliptical, pentagram, triangle, and hexagon cross sections were produced by FLICE, and nanowires, microfilters, and woodpile photonic crystals were integrated into the channels by multiphoton DLW. FLICE resolution is limited to ~10 µm by the chemical wet etching process, which is far surpassed by multiphoton DLW. The hybrid devices benefit from FLICE due to the favorable mechanical and chemical properties of glass as well as the quicker process times for mesoscale structures, and they benefit from multiphoton DLW by the superior resolution and wide array of possible functionalities of the photoresist.

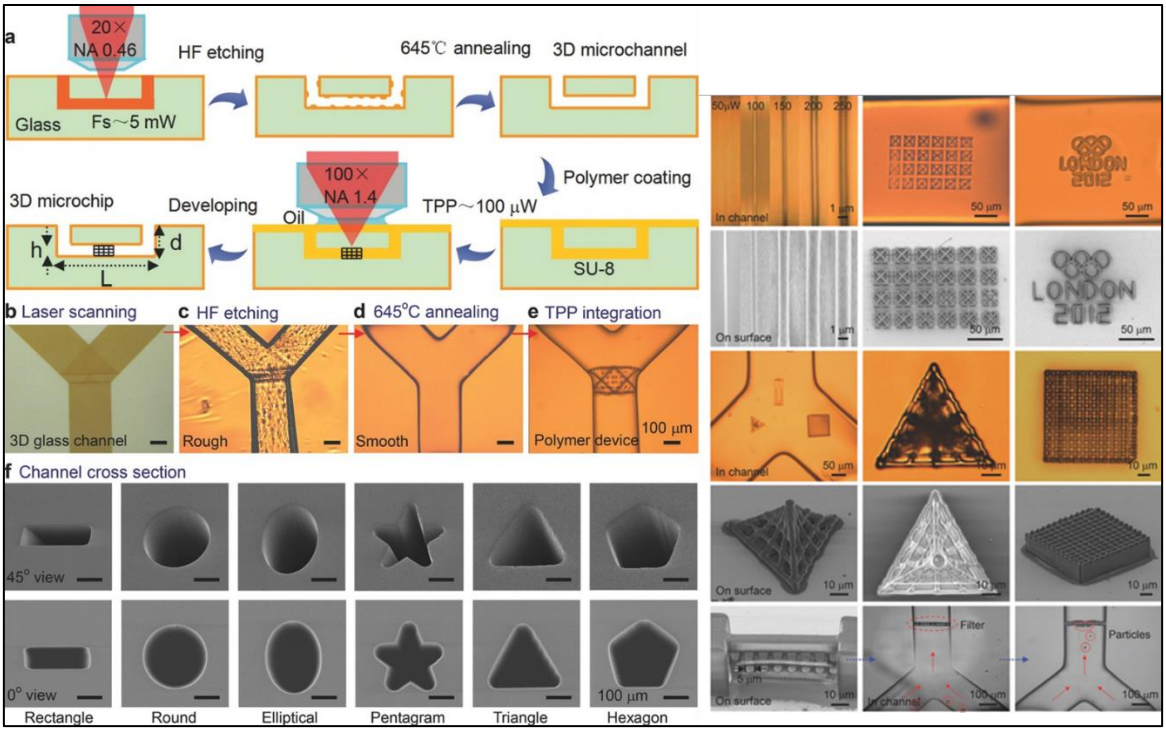

Figure 2.37: a) Schematic of hybrid FLICE-MPL process. B) to e) Y-channel after scanning, etching, annealing, and MPL steps. F) Controllable cross-section of microfluidic channels Right: Array of images displaying complex morphologies and lattice structures. – Adapted from [36] (CC-BY-NC).

Hybrid subtractive-additive fabrication of microfluidic devices can also be achieved without the implementation of FLICE, but instead with femtosecond laser ablation [37]. In this case, ablated microchannels on the surface of a borosilicate glass microscope slide remove the need for a chemical etching setup and process. Microfilters (~6 μm pore size) of various geometries were integrated directly into the microchannels by multiphoton DLW of the SZ2080 photoresist doped with 1 wt. % Irgacure 369 photoinitiator (Figure 2.38). A cover glass side was placed on top of the carved channels and they were joined to form a seal by a third femtosecond laser process: direct laser welding. All three manufacturing processes were performed by an Yb:KGW femtosecond laser. Ablation and welding are done at the fundamental 1030 nm wavelength (25 KHz and 196 TW/cm^2 for ablation, 12.5 TW/cm^2 and 200 kHz for welding), and polymerization at the 515 nm second harmonic (200 kHz, 0.525 TW/cm^2). As discussed, welding of similar or even dissimilar materials by femtosecond laser melting is possible and applied here. Sealing can also be achieved by use of a special polymer binder and additional MPP and development stages [299].

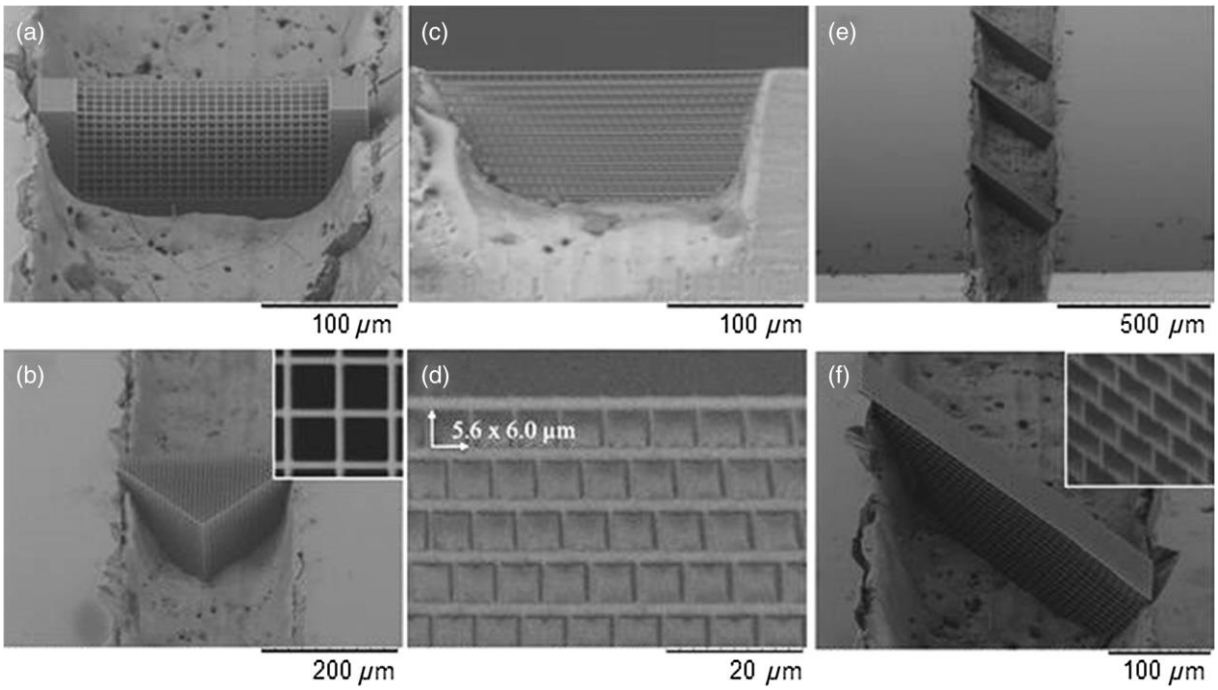

Figure 2.38: SEM images of integrated filters. A) perpendicular channel, b) chevron geometry, c) filter side view, d) magnification demonstrating pore size, e) multiple filters in single channel, f) magnification of filter in e) [37]. – Permission requested from the publisher.

Many combinations of laser manufacturing techniques are possible. Two-photon polymerization (Ti:Sapphire, 120 fs, 80 MHz, 780 nm) of PEG was used to fabricate a hexagonal cell scaffold (Figure 2.39, top) with cylindrical pores for growing ovine vascular smooth muscle-like cells (vSMC) and endothelial cells (EC) on the same structure but localized to the outer and inner area of the scaffold, respectively [38]. Laser-induced forward transfer is then used to selectively seed the scaffold with the two cell types (Figure 2.39, bottom). The cells are initially dispersed onto a 55 to 60 nm thick gold-coated glass slide, and a nanosecond pulse laser is focused at the interface of the glass and gold layer. The gold layer absorbs the pulse and locally expands to eject the cell compound onto the hexagonal scaffold without significantly damaging the organic material. Although a separate nanosecond laser was used for LIFT in this application, an ultrashort pulse laser may be able to perform the same core function, with smaller droplet sizes and in the same setup.

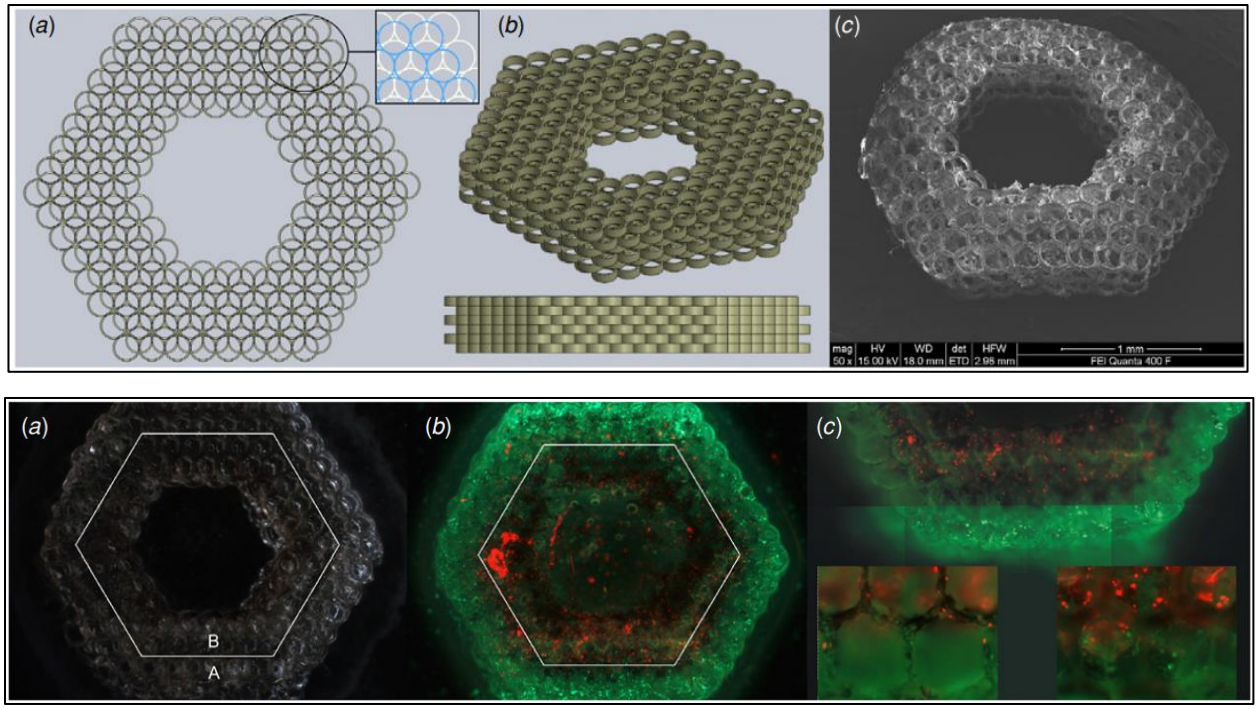

Figure 2.39: Top: Scaffold design in CAD (a and b) and SEM image of MPL-fabricated structure (c). Bottom: a) dark-field image, white border demarcates the two regions that were seeded with vSMCs (A) and ECs (B). b) fluorescence imaging. c) magnified images [38]. – Permission requested from the publisher.

Wang et al. [39] used a single ultrafast laser micromachining setup to perform three processes: LIFT of Ag paste, laser sintering of the LIFT-deposited Ag paste, and LIFT of graphene oxide suspension (Figure 2.40). The interdigital electrode device acts as a humidity microsensor fabricated in an all-in-one setup. The sintering step improves the electrical conductivity, which demonstrates the feasibility of laser sintering as another process for combinational ultrashort pulse laser manufacturing methods.

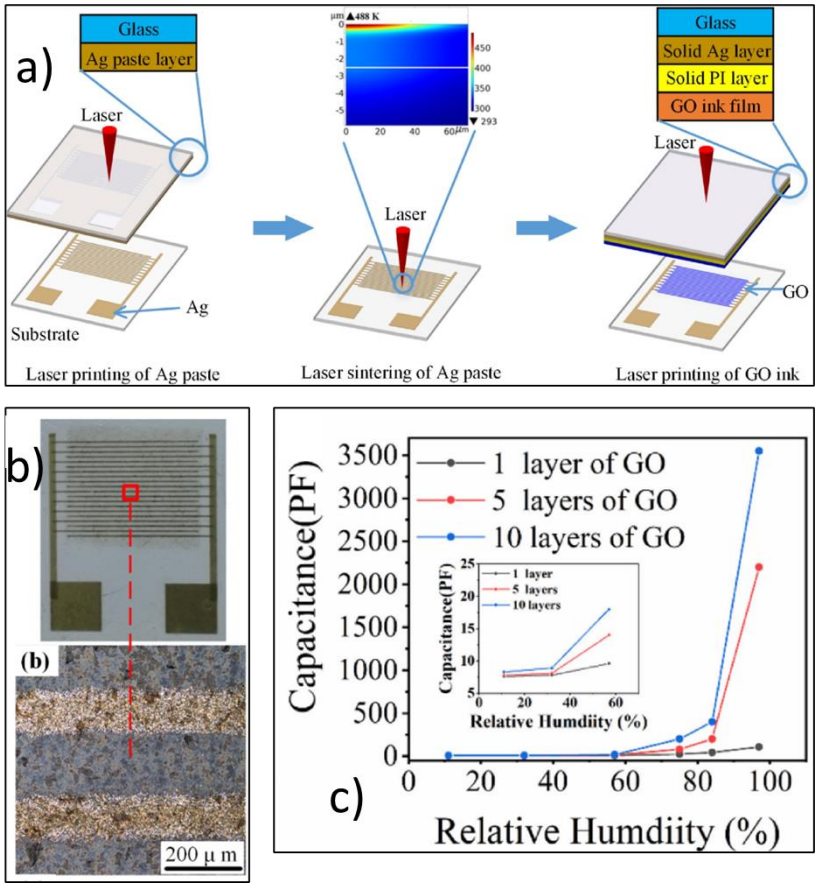

Figure 2.40: a) Microsensor fabrication schematic. LIFT of Ag paste to sintering of Ag paste to LIFT of GO. b) Fabricated IDE structure. c) Testing the sensitivity of the humidity microsensor [39]. – Permission requested from the publisher.

Ultrafast laser ablation should also be possible for devices that utilise LIFT. In particular, nanoscale or microscale patterning of LIFT-deposited metals with laser-induced periodic surface structures (LIPSS) may provide additional functionality in terms of wettability, antibacterial properties, and tribological performance [300]–[302]. Along the same vein, post-processing of conventional metallic AM by ultrafast micromachining can reduce surface roughness, produce nanogratings, alter wettability, and improve biomedical implants [48], [49], [303]. Structures fabricated by ultrashort pulse SLM/SLS could be immediately post-processed with the same laser simply by changing the operating parameters and have their surface qualities enhanced or new functions imparted. This development would provide greater control over the surface structure and ultimate functionality and performance of the device.

2.6 Summary and Outlook

Many manufacturing techniques and applications were discussed in which ultrafast lasers provide or have future potential to provide a distinct advantage over alternative tools and methods. The processability of high melting point, low optical absorption materials in a selective laser melting/sintering process by ultrafast laser has been confirmed.

In most other cases, ultrafast lasers possess a significant share of the micro- and nano-fabrication domain. The precision afforded by non-linear absorption phenomena and massive instantaneous power underpin the future utility of ultrafast lasers from nanoscale to mesoscale. Sub-micron resolution in MPL delivers the freedom to fabricate complex 3D nanostructures on-demand, but is limited to materials that can be integrated into photoresist solutions. In particular, metals and ceramics are difficult to fabricate, though progress is ongoing. On the other hand, LIFT presents little material constraint, but further efforts are needed to provide the same degree of resolution and geometric freedom as MPL. The diversity in not just the material, but the material phase (solid, liquid, high or low viscosity paste) presents an enormous challenge in understanding the underlying LIFT processes as well as their optimisation. PLD, while it can see improvements by incorporating ultrafast lasers, is restricted mostly to uniform film growth.

The success of a manufacturing technology can be measured by its utilisation in industry. Commercial MPL systems are already available by companies such as microlight 3D and Multiphoton Optics GmbH, and Femtika offers a hybrid MPL, selective laser etching, and ablation “nanofactory”. Greater adoption of ultrashort pulse systems by industry will be accelerated, if not wholly enabled by, consistent build quality (by *in-situ* process monitoring and control), increased throughput, and greater return on investment by greater versatility in product features. While current monitoring efforts are focused primarily on furthering our understanding of the techniques discussed herein, deep learning may be a key tool in the future [304]. Due to the diversity in complexity of femtosecond laser-matter interactions, deep learning may be an ideal solution for simply improving quality, as it bypasses the need to truly understand the underlying physics [305].

The leveraging of a single ultrafast laser source for 1) precise subtractive manufacturing of virtually any material, 2) bespoke high resolution 3D printing, and 3) precise welding of dissimilar materials is an exciting prospect. In addition, ultrafast lasers could be integrated into current AM systems to impart additional functionality and complexity to builds. We foresee such integration within traditional L-PBF machines to achieve precise manufacturing at the nano and micro scale while maintaining efficiency through the use of CW or short pulse lasers for the bulk structure.

Chapter 3: Description and Comparison of Ultrafast Ti:Sapphire and Fiber Laser Systems

3.1 Description of the Systems

Bulk Ti:Sapphire lasers and fiber lasers are perhaps the two most common architectures for femtosecond micromachining. The bulk system is representative of the laser types that were prevalent from the late 90's to the late 2000's, while the fiber laser is representative of the systems that became increasingly common after 2010. Extensive work in the setup and utilisation of two ultrafast laser systems was performed. The commercial systems are an amplified femtosecond Ti:Sapphire system (Spectra-Physics) and an Ytterbium-doped fiber laser (PolarOnyx) with a picosecond pulse duration. Their design, ease of operation, setup process, and respective advantages and disadvantages are considered in this chapter.

3.1.1 Ti:Sapphire System

The commercial (Spectra-Physics) Ti:Sapphire architecture consists of four main components: a diode-pumped solid state laser (Millennia Vs), a mode locked Ti:Sapphire oscillator (Tsunami), a Q-switched Nd:YLF laser (Empower), and a regenerative Ti:Sapphire amplifier (Spitfire). A simplified diagram of this can be seen in Figure 3.2.

The Millennia Vs is a CW laser operating at 532 nm with output up to 5 W. Neodymium (Nd^{3+}) doped yttrium orthovanadate ($Nd:YVO_4$) crystal is the gain medium, and thus must be optically pumped. This is accomplished with fiber-coupled diode bars that longitudinally pump the lasing medium with an optimal coupling between the fiber output mode and the laser mode. This mode matching is the efficient overlapping of the region of the lasing medium that is energised by the pump source and the region that will be occupied by the laser mode action – often corresponding to the TEM_{00} spatial mode. The primary lasing transition of Nd^{3+} following the diode pumping results in emission of 1064 nm light. This light undergoes intracavity frequency doubling (second harmonic generation) by a lithium triborate (LBO) crystal. The resultant output is a stable CW 532 nm beam.

The output from the Millennia Vs pumps the Tsunami, a Ti:Sapphire solid-state laser system capable of producing ultrashort pulses in the range of tens of femtoseconds. Ti^{3+} ions in the Al_2O_3 crystal absorb and emit light according to Figure 3.1. Thus, the 532 nm output from the Millennia is readily absorbed and the Tsunami is configured for output in the 720 to 850 nm range. Longitudinal pumping again optimises mode overlap and round-trip gain. Ultrashort pulses are achieved via mode locking, whereby a fixed phase relationship between permitted resonant cavity modes results in a train of narrow pulses. While various schemes can induce a fixed phase relationship, an acousto-optic modulator (AOM) is used here. The AOM is driven by

a piezoelectric transducer to generate a standing sound wave in the optical material at a particular frequency. This modulates the index of refraction such that the interaction of laser light with the AOM sinusoidally diffracts and frequency shifts some of the incident light. If the acoustic frequency is matched to the cavity round-trip time $\tau = \frac{2L}{c}$, then longitudinal modes oscillating out of time will repeatedly see higher loss. In the frequency domain, the amplitude modulation of light because of the diffraction of the beam results in sidebands at $f_{optical} + f_{modulator}$ and at $f_{optical} - f_{modulator}$. These sidebands correspond to adjacent longitudinal modes and will be driven in phase. Repeated passes generate additional sidebands at the other mode frequencies. The greater the gain bandwidth, the shorter the pulse that can be achieved. Hundreds of thousands of modes are typically supported in Ti:Sapphire systems allowing for femtosecond pulse durations. Due to the large bandwidth required for such short pulses, the wavelength dependence of refractive index for many optical elements affects the ultrashort pulse shape. Often, red light will see a lower refractive index than blue light, causing the pulse to become positively chirped as it travels in a medium. High peak intensities of femtosecond pulses also induce non-linear effects such as self-phase modulation that further shifts the front of the pulse to lower frequencies and the trailing edge of the pulse to higher frequencies. Positive group velocity dispersion (GVD) of materials leads to pulse width broadening which must be countered to maintain minimum pulse duration. Intracavity pulse compression in the Tsunami is controlled by a four-prism sequence such that blue light travels through less optical material and experiences less delay than red light. Degree of insertion of the middle pair of prisms corresponds to the amount of intracavity GVD. A slit in between the middle pair allows wavelength selection. The Tsunami used in Chapter 4 is capable of producing pulses with FWHM durations below 35 fs, with nJ pulse energy and a repetition rate of 80 MHz.

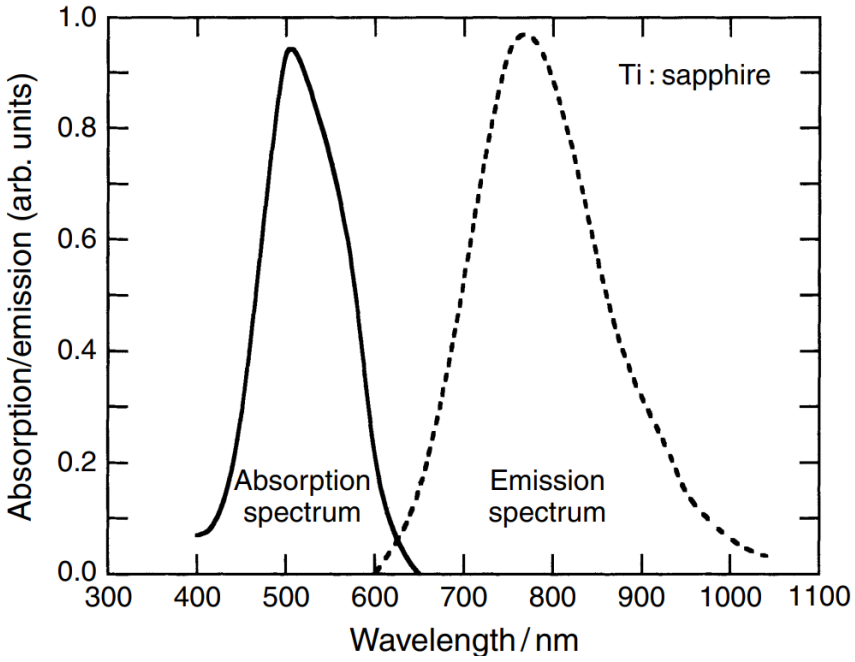

Figure 3.1: Absorption and emission spectra of Ti:Sapphire crystal [40]. – Permission requested from the publisher.

The Spitfire system is a chirped pulse amplification (CPA) scheme utilising a regenerative amplifier pumped by the 527 nm Q-switched Empower laser. Ultrashort pulses from the Tsunami first enter the stretcher where a diffraction grating introduces negative GVD to spread the pulse and reduce the peak intensity. The pulse enters the regenerative amplifier, consisting of a Ti:Sapphire rod that is pumped by the Empower with nanosecond pulses at 1 kHz. High saturation threshold of Ti:Sapphire makes it possible for a seed pulse to extract the energy and be amplified over multiple cavity round-trips. Pockels cells act as shutters for accepting, retaining, and releasing a single seed pulse from the cavity. Their timing is determined by trigger signals from the Tsunami and Empower for maximum amplification. Following amplification, a pulse enters the compressor where it undergoes a reversal of the process seen for stretching. Here, the compressor grating has a different groove density to compensate for higher order dispersion that occurs for even shorter pulses (<100 fs). The nJ pulse energy from the Tsunami can be amplified 1,000,000-fold to the mJ level in this way, maintaining femtosecond pulse durations, 800 nm wavelength, and 1 kHz repetition rate.

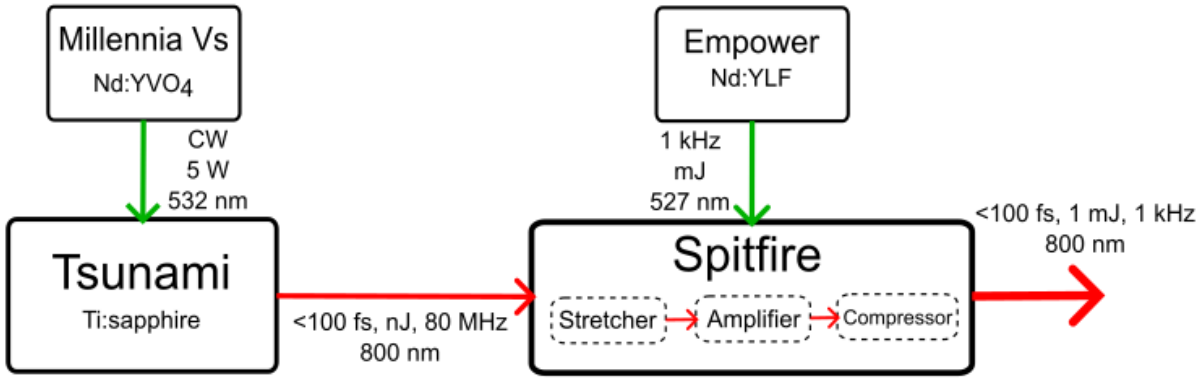

Figure 3.2: Schematic of Ti:Sapphire laser system, composed of four main components: Millennia, Empower, Tsunami, and Spitfire.

3.1.2 Fiber System

The fiber laser is a PolarOnyx Uranus ytterbium laser operating at 1035 nm, a 1 picosecond pulse duration, pulse energy up to 40 µJ and repetition rate variable between 100 kHz and 1 MHz. The laser architecture can be broken down into three main sections: the mode locked seed laser, the pre-amplifier, and the power amplifier. It is depicted in Figure 3.3. A chirped-pulse amplification scheme is also used, with stretching taking place between the seed and pre-amplifier, amplification being done in two stages with the pre-amplifier and the power amplifier, and compression as the final stage between power amplifier and output.

The rare-earth ion Yb^{3+} is a suitable dopant for mode lockable fiber gain media due to its wide emission bandwidth from about 1000 to 1100 nm. High absorption around 900 nm enables

pumping of the seed laser by 980 nm laser diodes. Wavelength division multiplexing elements (WDM) couple the pump light into an active Yb fiber loop. The system is passively mode locked, taking advantage of non-linear polarization rotation to do so. Fiber birefringence and self-phase modulation of a high intensity pulse alters its polarization state as it propagates in a fiber. Waveplates or polarisation controllers can be used to make it so maximum transmission occurs for the most intense pulse i.e. it functions as an intensity dependent loss. The operating principle is similar to a saturable absorber, except it is primarily a consequence of the Kerr effect and thus has the "fast" recovery time needed for ultrashort pulses. The PolarOnyx utilises two polarisation controllers that squeeze the fiber at a point in its length via adjustable screws that apply or relieve pressure by manual rotation. This alters the polarisation state of the light passing through it and combined with a polarising beamsplitter, can be optimised to induce mode locking. Mode locked pulses from the seed laser have a 10 ps pulse duration and a 38 MHz repetition rate.

Seed pulses must first be stretched prior to amplification to prevent strong nonlinear effects associated with the typically long path lengths in active fibers. Pulses are siphoned from the seed laser ring cavity by the beamsplitter and stretched to 100 ps pulses by a fiber stretcher. This optical fiber is polarization maintaining and stretches the pulse due to its negative group delay dispersion, becoming negatively chirped. A WDM couples the stretched pulses and pump light from 980 nm diodes into another Yb-doped fiber for pre-amplification. Separation of amplification into stages allows for the use of smaller mode area fibers in the pre-amplifier for better gain efficiency and reduced non-linear effects. Additionally, the inclusion of an AOM between the amplification stages is used to select pulses and change the repetition rate of the laser prior to high power amplification. During pre-amplification, the power is increased from single mW to ~10 mW.

Pulses enter the high-power amplification portion of the laser system via a WDM that, again, also couples 980 nm diode laser light into an Yb-doped fiber. A larger mode area fiber means a greater active area and greater energy storage for an energy saturated pulse, but a lower gain efficiency also prevents gain saturation. Amplification up to 4W of average power is possible. Coupling into a photonic band gap fiber prevents emission of the pump wavelength, and the pulses are emitted into the compressor. An open (free space) 2x dispersion grating compressor design is used which allows the user to adjust the dispersion by changing the grating distance. Compression results in pulses with 1 ps duration, 40 μJ pulse energy (at 100 kHz) and 1035 nm central wavelength.

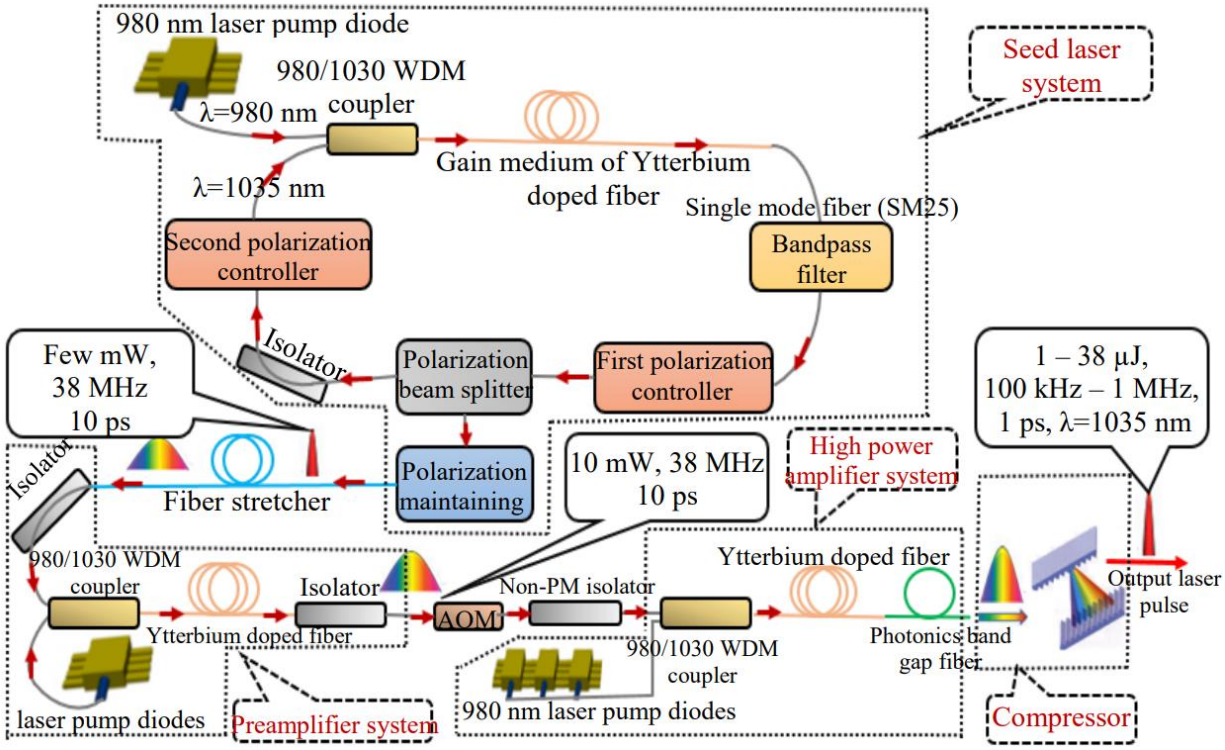

Figure 3.3: Fiber laser system schematic.

3.2 Setup and Operation of Ti:Sapphire and Fiber Laser Systems

3.2.1 Ti:Sapphire System

Installation and complete setup of the Ti:Sapphire system and all of its components requires the assistance of a field service engineer or technician over the course of several days. Consequently, it is an expensive undertaking. Regular (every 1 to 2 years) maintenance via service calls are important for continued optimal operation, to diagnose existing or future issues with the system, and to limit downtime in the event of a preventable issue.

3.2.1.1 Operation and Maintenance

Various maintenance and alignment was performed to keep the Ti:Sapphire system performance at the desired level. Water chillers are used to pump cool water over each of the laser crystals. These chillers require infrequent maintenance in the form of topping up with distilled water, flushing out with cleaning solution, and filter replacements. Adjustment to the Tsunami input coupling mirror was done every few days to maximise the output power. On occasion, the end

mirror would be adjusted if a large drop in power ~10% could not be compensated for with the input mirror alone. Increasing in the pulse duration out of the Spitfire would have to be compensated by small adjustments in either the prism dispersion compensation in the Tsunami or by translating a compressor retroreflector. In the event of a more major issue, such as an inability to mode lock the Tsunami, more significant re-alignment procedures had to be taken. Careful and precise adjustment to laser rod orientation or focusing mirrors solved these issues, but overall sensitivity to alignment meant that alignment into the Spitfire stretcher was no longer ideal.

3.2.1.2 Diagnosing and Fixing Problems

As can be seen in the previous description of the Millennia Vs, Tsunami, and Spitfire, the entire system is complex to own and operate. In the event of a malfunction or any other issue in which the laser output is not as expected, diagnosis can be difficult. Since each component forms a link in a chain (Millennia pumps Tsunami, Tsunami seeds Spitfire, Empower pumps Spitfire), issues encountered further down the chain may have a multitude of possible causes. Only by understanding the preceding components can a problem (e.g. low power at Spitfire output, or failure for seed laser to mode lock) be addressed. One needs to carefully diagnose the issue so as to determine the correct action to be taken, as undertaking an alignment procedure that does not address the root cause of an issue costs time and/or money and may cause issues further down the chain. Proper diagnosis requires an understanding of both the individual components (Millennia, Tsunami, Empower, Spitfire) and how they interact. For example, appropriate pulse selection in the regenerative amplifier occurs on the basis of normal operation of each of the other laser devices. A small issue in seed laser alignment may affect Pockels cell timing but otherwise the seed laser gives no indication of a problem. Isolating the problem to the Tsunami can be done by understanding that pulse selection relies on a stable 80 MHz RF signal from the seed laser, which may not be present despite indications the laser is mode locked. The knowledge and experience needed for adequately dealing with the problems that arise is a major drawback to such free-space configurations. Even with an experienced operator, servicing of the system is inevitable and a significant capital expense.

3.2.2 Fiber System

Fiber system setup is simpler than the Ti:Sapphire system. Initial installation may require a service technician but is less labour intensive in comparison. Regular service calls are not necessary; however, the system design poses other challenges in the form of mode locking difficulties and a closed configuration.

3.2.2.1 Operation and Maintenance

In general, ultrafast fiber lasers such as the PolarOnyx have a significant advantage over Ti:Sapphire and other similar bulk free-space lasers when it comes to maintenance and alignment stability. Due to total internal reflection, light is well-confined to the fiber and optical elements such as reflectors, waveplates, polarization controllers, are integrated in-line with the fiber. In addition to the WDM couplers between pumps and active fibers and the efficient fiber coupling between the laser stages, beam steering and alignment is mostly eliminated. Beam walk-off is not a concern and does not require adjustment in the same way that it is required for a Ti:Sapphire system. Consequently, it was found that fiber laser architectures are easier to operate and maintain as a black box system. Furthermore, the gain medium is sufficiently cooled by air circulation driven by fans, eliminating water chiller maintenance.

The greatest challenge in operation of this fiber system is achieving mode locking. At start-up, the system did not always mode lock despite a warm-up period of 1 to 2 hours. Increasing and decreasing of pump diode currents by 10 to 20 mA between a range of 100 and 350 mA as a method of perturbing the light in the laser cavity would sometimes result in the spontaneous mode locking. If that should fail, iterative adjustment of the polarization controllers while changing pump diode currents would likely lead to mode locking. This procedure can extend start-up time by 2 to 3 hours. Once mode locking was achieved, it was stable over multiple days.

3.2.2.2 Diagnosing and Fixing Problems

When a problem beyond day to day alignment arises in the Ti:Sapphire system, it is possible to find the problem and address it. The challenge is that the complexity of the beam path can make for a time-consuming procedure and creates more opportunity for the system to be moved further from the ideal. In contrast, finding and fixing a problem in a commercial fiber laser such as the PolarOnyx is more difficult. The means for testing and diagnosis are limited to the monitor signals provided by the manufacturer and the laser output after the high-power amplifier. Problems are constrained to electrical issues and hardware failure, meaning that a malfunction almost certainly means a service visit or repair shipment. Such failures are few and far in between, and significant misalignment drift which presented issues in the Ti:Sapphire is nonexistent.

3.2.2.3 Temperature and Humidity Instability

It is recommended by the PolarOnyx manual to keep relative humidity below 40% for optimum operation. Indeed, it was observed that for humidity levels above 60%, mode locking was unachievable or relatively unstable. This made operation during summer months challenging, in which the relative humidity of the laboratory could reach 80%. Use of a dehumidifier alleviated these challenges. Mode locking was also unstable at temperatures above 24°C, though laboratory temperatures were more stable, between 21°C and 23°C. Therefore, to take full advantage of the

benefits of fiber systems, it is necessary to operate in a laboratory with good environmental control.

3.3 Comparison of Ti:Sapphire and Fiber Laser Systems for Use in Machining

3.3.1 Pulse Energy

The Ti:Sapphire system is capable of significantly higher pulse energy, up to 1 mJ at 1 kHz. In contrast, the fiber system can at most emit 40 µJ at its lowest repetition rate of 100 kHz. A wide variety of materials are effectively ablated by ultrashort pulses at pulse energies below 50 µJ, such as glass [306], metal [307], and acrylic [308]. However, some ablation experiments are carried out with pulse energies in the hundreds of µJ [309]. Pulse energy requirements in additive manufacturing applications vary. Multiphoton lithography is accomplished with pulse energy in the pJ to nJ range, such that Ti:Sapphire oscillators can be themselves used for the process without amplification [10], [12]. Pulse energies used in laser-induced forward transfer vary depending on pulse duration, material, film thickness, and whether it is solid or low/high viscosity fluid, but lie between nJ and tens of µJ [209], [215], [216]. [216] experimented with pulse energies > 50 µJ in silver paste LIFT. Furthermore, arrays of microspheres were deposited via LIFT using pulse energies from 0.6 to 1 mJ spread over a 5 mm beam spot [208]. Selective laser melting of copper was achieved with pulse energies of 1 µJ, lower than that used for ablation in order to cause melting and avoid ablation effects [310]. Evidently, the PolarOnyx fiber laser offers enough pulse energy to cover a wide range of ultrafast manufacturing applications but may reach its limit in some cases. Therefore, the Ti:Sapphire system provides greater versatility for experiments that explore the effects of the most intense ultrashort pulses.

Higher pulse energy also provides the opportunity to use a focusing lens with a longer focal length, resulting in a wider beam spot and area of effect with an equivalent energy density compared to a lower pulse energy, smaller beam spot. While this might present an advantage in higher throughput, the 100 kHz to 1 MHz repetition rate of the fiber system is considered a superior tool for manufacturing where the lower pulse energies are sufficient, as discussed in the next section.

3.3.2 Repetition Rate

A notable difference between the Ti:Sapphire laser output and fiber laser output is the difference in the repetition rate. For Ti:Sapphire amplifiers, a limiting factor in the repetition rate is thermal accumulation in the laser rod [311]. Maintaining large pulse energies for a greater number of pulses necessarily means an increase in the pumping average power. Since refractive index is

dependent on temperature, laser heating of the crystal produces a refractive index gradient and a focusing effect [312]. For fiber gain media, thermal loading is spread over a greater area. Consequently, higher average powers for higher repetition rates are obtained. The fiber laser can deliver the same number of pulses and the same energy dose in a shorter period of time compared to the amplified Ti:Sapphire laser. For the purposes of micromachining, this means that the laser beam can be scanned over a sample at a faster rate, enabling the use of piezoelectric scanners for higher throughput.

Although throughput can be increased for Ti:Sapphire systems by using a larger beam spot while maintaining the fluence due to greater pulse energy, a beam spot large enough to compensate for the difference in repetition rates (100 to 1000 times) sacrifices modification resolution. For applications where the beam spot size is constrained e.g. ablating 20 μm wide grooves, the Ti:Sapphire system is confounded in throughput. Thus, a higher repetition rate – as provided by the fiber system - delivers greater versatility in increased throughput.

3.3.2.1 Heat Accumulation and Shielding

As the repetition rate increases, the time between consecutive pulses decreases. Some thermal energy deposited in a target does not contribute to ablation but remains as excess [313]. If the time between pulses is shorter than the time it takes for the excess energy to be diffused into the bulk, thermal accumulation in the target is no longer negligible. The effect that this has on ablation is strongly dependent on the material properties and laser parameters, but has been observed in metals and glass for repetition rates in the hundreds of kHz [314]–[316]. Due to heating of the target, the ablation threshold is reduced and/or the melting point is exceeded, and the removal rate increases [317]. Additionally, the surface morphology and drilling quality deteriorates with an increase in heat-affected zone and associated melting [318]. However, for waveguide writing the thermal accumulation associated with increased repetition rate results in lower losses [316], [319]. The effect can also be utilised for localised melting of glass for welding [22].

Another consideration when the time between pulses becomes increasingly short is that of ejecta/plasma shielding. Ejection of ablated material, primarily plasma, occurring hundreds of nanoseconds after irradiation suggests that pulses with similar delays will be absorbed, reflected, or scattered by suspended particles [320]. Transmission of ablation plumes as a function of time for aluminum and steel were studied by [321], who found that the transmission fully recovers after several microseconds, corresponding to repetition rates of hundreds of kHz. These shielding effects appear to reduce the effectiveness in material removal of additional pulses [315].

Control over the repetition rate, as provided by the fiber system, makes it a more diverse tool for machining applications. Not only are much faster scanning speeds possible in the 1 to 100 kHz range, but thermal accumulation effects can also be leveraged for greater removal rates and faster processing where less clean ablation is tolerated. If necessary, repetition rates can be kept below certain limits at which shielding is significant. Except for specific effects provided by the pulse

to pulse interactions (e.g. in the case of waveguide writing), the Ti:Sapphire system can achieve the same machining features but with more processing time, so it remains a valuable tool in a research environment.

3.3.3 Pulse Duration

Pulses of <100 femtosecond duration are readily emitted from the Ti:Sapphire system, whereas the fiber laser emits 1 picosecond pulses. Both are considered to be ultrafast systems, a definition that relates the time between the start and end of the pulse to the coupling time between the electronic subsystem and the material lattice [117]. Although the coupling depends on the specific material, with respect to machining, for sufficient peak intensity the same ablation mechanisms are generally present for pulses in the 1 picosecond regime as in the 100 femtosecond regime. This is supported by observations in literature for ultrashort pulses that are within the "ultrafast" regime [91], [322], [323]. Minor differences in ablation characteristics are observed, with the longer pulses producing more hydrodynamic features and slightly larger ejected nanoparticles. Thresholding of the peak laser intensity is used in nanomachining and multiphoton lithography [9], [324]. In which case, a shorter pulse duration may produce smaller features. However, the lower peak intensity of picosecond systems may be advantageous when melting is desired, as in SLM/SLS. Further, thermal accumulation effects should be more easily obtained for a temporally broader pulse. In the course of experimentation of Ti:Sapphire ablation of Ti-6Al-4V (Chapter 4), a longer pulse duration of ~5 picoseconds did not result in different surface morphologies, but at the lowest pulse energies they were shifted such that the morphology obtained at t = 100 fs, 5 µJ was instead obtained at 10 µJ for t = 5 ps. This is believed to be due to the differences in peak intensity, which can be increased with pulse energy for the longer pulse mode in order to obtain the very same structures. Thus, the shorter Ti:Sapphire pulse duration does not provide a significant advantage in micromachining and the pulse durations provided by many commercial fiber systems, although longer on the scale of hundreds of femtoseconds, is not expected to inhibit adoption.

3.3.4 Wavelength

Between the systems in question, there is a ~200 nm wavelength difference. Because of the broad gain bandwidth, ultrafast Ti:Sapphire lasers are tunable over a 300 nm range that makes them a versatile tool for spectroscopy and microscopy [79]. However, for ultrafast machining, the wavelength does not seem to impact the ablation in the relevant range between the fundamental fiber and Ti:Sapphire wavelengths [325]. The absorbance of a material depends on the wavelength, and so the ablation threshold will vary [326]. For industrial applications where throughput is paramount, the choice of wavelength for the lowest threshold is important [327]. In the context of surface modification, laser-induced periodic structures can feature a periodicity that is dependent on the wavelength [92]. If a specific application requires higher frequency

structures, the Ti:Sapphire system would have an advantage. Concerted efforts to improve the wavelength tunability of fiber lasers are ongoing [79]. For higher pulse energy modification, as long as a material is sufficiently absorbent (single or multi-photon) at the laser wavelength, neither system can be said to have an advantage.

3.4 Conclusion

Femtosecond laser design, operation, and maintenance for a bulk Ti:Sapphire and Yb-doped fiber laser were discussed. The Ti:Sapphire architecture consists of several components that can be individually considered as lasers. Each must be optically pumped and the alignment optimised resulting in a complex overall beam path and alignment procedure. Occasional small adjustments to alignment is sufficient to ensure good performance from day to day. On the other hand, the fiber laser consists of stages of active fiber loops that are coupled together and do not require precise optical alignment nor the same kind of alignment maintenance as experienced with the bulk laser. Due to the active AOM mode locking, the Ti:Sapphire laser is more reliably mode locked at start-up, while the fiber laser's dependence on passive mode locking can contribute to longer start-up times. The systems were also compared in their advantages and disadvantages in micromachining, which are most affected by the achievable pulse energies and repetition rates. A much greater pulse energy can be obtained with the bulk laser than the fiber laser (~50x) whereas a much greater repetition rate can be obtained with the fiber laser than the bulk laser (~1000x). In many micromachining applications the peak pulse energy for the fiber laser is sufficient but is also limiting. Shorter pulse to pulse times are becoming more important for increasing throughput as ultrafast laser machining becomes more accessible for commercial purposes (aided by the lower capital cost of fiber lasers), and have benefits in specific applications.

Overall, the fiber laser is cheaper, easier to operate and maintain, and has clear processing benefits. For these reasons, the ultrafast fiber laser industry has seen rapid growth in the past decade. High-power Ti:Sapphire lasers have been the ultrafast workhorse in machining research for many years, but based on the observations made here - which reflect those made at large - it is possible they will be supplanted in this capacity. However, they will remain an essential tool for their ability to generate the most intense pulses.

Chapter 4: Ultrafast Laser Surface Modification of 3D-Printed Ti6Al4V

4.1 Introduction

Laser-based additive manufacturing has received significant attention for its ability to rapidly manufacture 3-dimensional, fully dense, metal parts from CAD models [125], [328]. Specifically, selective laser melting (SLM) has emerged as one such manufacturing technique capable of building complex parts with internal morphologies for a variety of metals. As a powder-bed fusion process, SLM manufactures parts in a layer-wise fashion by locally melting loose powder with an intense laser source. Process parameters such as laser power, scanning speed, hatch spacing, and layer thickness are optimised to produce parts with mechanical properties comparable to those made by conventional manufacturing techniques [329]–[331]. Of the many materials that can be processed via SLM, Ti-6Al-4V has received much attention [332], [333]. Ti-6Al-4V is an $\alpha+\beta$ alloy of titanium where the alpha phase is stabilised by aluminum and the beta phase is stabilised by vanadium [334]. As a high strength, low density, corrosion resistant, biocompatible alloy, Ti-6Al-4V has applications in various fields and industries such as medicine [335], aerospace [336], [337], automotive, and marine [45], [338].

Despite being able to accurately produce near-net-shaped components, the surface finishing of selective laser melting processes is sub-optimal for many applications [339]. As a violent and chaotic process, rapid laser melting of metals generates spatters, debris, bulging and concave areas, and partially sintered powder close to the melt pool adheres to the finished surface [45], [340]. Consequently, a surface roughness comparable to the average powder size - typically tens of microns - can be expected. Techniques to modify the surface include milling, polishing (mechanical and electrochemical), chemical etching, and laser polishing/re-melting [46], [339], [341], [342]. However, these techniques either damage delicate components or do not provide precise tailoring of surface properties and features. There is an interest in modifying the surface of Ti-6Al-4V beyond merely a reduced roughness, particularly in the case of biomedical implants in which periodic structures may improve integration with native bone [303], [343].

Ultrafast lasers are a well-known tool for surface modification. They are uniquely suited for micromachining purposes due to ultrashort pulse ablation mechanisms that produce only a small heat-affected zone, limiting damage to the focused beam spot. Ultrafast lasers have recently been explored as a method of SLM post-processing [48], [49]. There is evidence that they can reduce the surface roughness as well as generate periodic surface structures, but the extent to which different morphologies are obtained for a range of process parameters is still unclear.

To further investigate the feasibility of engineering the as-printed surface morphology, selectively laser melted Ti-6Al-4V is ablated via the amplified femtosecond Ti:Sapphire laser described in Chapter 3. The pulse energy, laser scanning speed, and number of layers was varied, and the resultant effects observed under scanning electron microscope (SEM).

4.2 Methods

4.2.1 L-PBF

A 10x10x16 mm block was manufactured via selective laser melting using Ti-6Al-4V Grade 23 powder (Renishaw Canada) feedstock with size range 15 to 45 µm. The tested part was produced with average laser power of 200 W, average scanning speed of 1000 mm/s, hatch spacing of 0.1 mm, and layer thickness of 0.04 mm. It was removed from the build plate by wire EDM. Samples were cleaned with 70% ethanol prior to laser ablation.

4.2.2 Ultrafast Laser Micromachining Setup

Ablation of the sample was performed using the Ti:Sapphire system described in Chapter 2. The micromachining setup is depicted in Figure 4.1. Laser output from the Spitfire is horizontally polarised and is approximately 10 mm in diameter which is reduced to 4 mm by an f = 50 cm achromatic doublet (focusing) lens and an f = -20 cm plano-concave singlet lens to prevent clipping on subsequent components. The beam passes through a manual rotary half-wave plate (0RP44-3, Newport) which shifts the linear beam polarisation from horizontal to vertical depending on the angle of the birefringent crystal relative to the beam. A thin film polariser (11B00UP.26, Newport) acts as an analyser and permits transmission of horizontally polarised light. Adjustment of the half-wave plate angle allows continuous adjustment of the laser intensity. A flip-up mirror is used to direct the beam to an autocorrelator for pulse duration measurement (Section 4.2.2.6) and a fused silica window is used for power sampling of the beam (Section 4.2.2.4). A mechanical shutter (VS25 with VMM-D1 controller, Uniblitz). allows beam propagation to the machining stage where the beam is directed to the sample from above. The beam was focused into the stage chamber by a 5x Mitutoyo M Plan NIR objective (f = 40 mm, NA = 0.14, working distance = 37.5 mm), resulting in a diffraction-limited ~10.2 µm $1/e^2$ beam diameter at the focal plane and a 204 µm depth of field. The ablation chamber is driven in the X and Y directions by motorised translation stages (UTM150PE.1 Newport) and covered with a steel lid with embedded 2” window to prevent debris from reaching the objective.

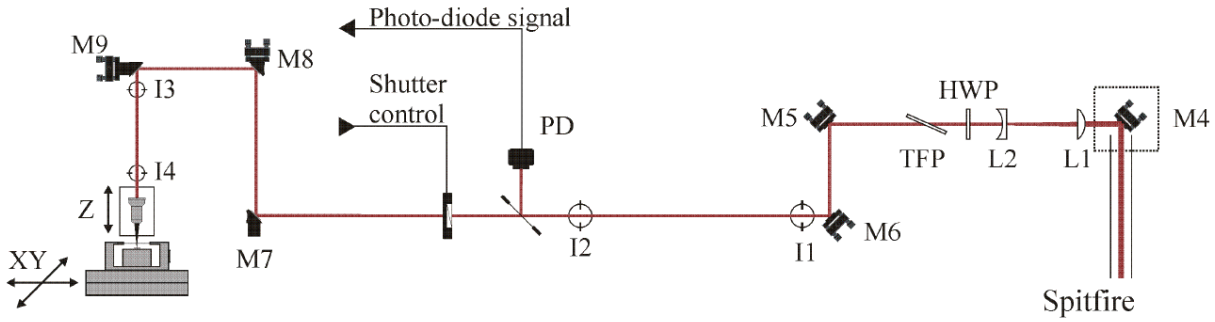

Figure 4.1: Depiction of the machining setup. A fused silica window is used to sample the beam for continuous power monitoring (see Section 4.2.2.4).

4.2.2.1 Ultrafast Laser Characterisation

Several devices and methods were used to characterise the ultrafast laser beam. To ensure normal operation, the wavelength spectrum, average power, beam profile (spatial intensity), pulse duration were measured.

4.2.2.2 Wavelength Spectrum

The wavelength spectrum of the Tsunami and Spitfire were both monitored using an Ocean Optics fiber-coupled spectrometer (PC2000 PC). Central wavelength was measured at 800 nm and spectrum width at 22 nm FWHM. Laser light is diffusely reflected off of a business card and coupled into the fiber for detection.

4.2.2.3 Average Power

Average laser power was primarily measured with a silicon photodiode detector (PD300-3W, Ophir Optronics). This was used to confirm the laser power for the Tsunami, Spitfire, and after the wave plate intensity reducer. An Ophir NOVA 1Z01500 power meter and sensor was used to measure the average power at the stage.

4.2.2.4 Continuous Power Monitoring

It is important to monitor the laser power immediately before an ablation experiment to know that it has not changed from previous experiments at the same intensity, and during an ablation experiment to ensure the output was stable over the experiment duration. To this end, a fused silica window is placed in the beam path for photodiode beam sampling via Fresnel reflection. The photodiode signal is processed by a boxcar integrator which in turn outputs a voltage reading corresponding to the strength of the photodiode signal. The voltage signal is calibrated to the laser power by placing a power meter at the machining stage after the chamber window and focusing objective to account for all optical losses. Both the photodiode signal and power meter signal are averaged over 1000 readouts to generate a statistical value for the stability. The power meter is removed for experiments and the photodiode provides a constant readout for power monitoring.

4.2.2.5 Beam Profile

Spatial intensity distribution was measured with a silicon CCD profiler (Ophir Optronics, BeamStar). An approximately Gaussian profile was confirmed. The profiler was also used to optimise alignment in the machining setup, ensuring beam propagation parallel to the objective's optical axis.

4.2.2.6 Pulse Duration

Measurement of an ultrashort pulse duration is non-trivial. Response times of electronic detectors are generally too slow to provide femtosecond resolution. A common method for estimating the temporal pulse shape is autocorrelation and this method was adopted here (Figure 4.2). After the thin film polariser, a flip-up mirror directs the beam into the autocorrelator setup. In a Michelson interferometer-type setup, the beam is split into two arms by a broadband beam splitter. Each arm travels some path length and is reflected back to the beam splitter by roof mirrors but are horizontally offset by a few millimetres. The two beams are focused into a thin 0.5 mm nonlinear crystal (potassium dihydrogen phosphate). This crystal exhibits second harmonic generation (400 nm) for both beams. If the beams are spatially overlapped in the crystal and the pulses from both beams are temporally overlapped because they travelled the same arm path length, a third beam is generated in between them whose intensity is measured by a photodiode. One of the interferometric arms is scanned with a translation stage (Newport) parallel to its beam to vary the path length while the photodiode signal is recorded. In this way, an autocorrelation trace is produced which is related to the pulse width by a deconvolution factor. Background intensity is eliminated due to the non-collinear configuration. The pulse duration of the Ti:Sapphire system was measured to be <100 fs.

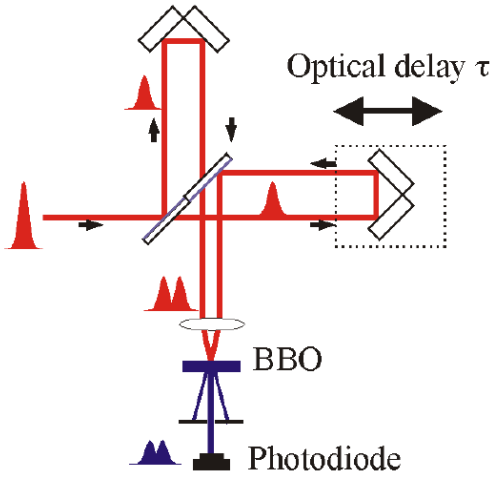

Figure 4.2: Intensity autocorrelator schematic with a BBO nonlinear crystal.

4.2.3 Ultrafast Laser Ablation Parameters

The Ti-6Al-4V sample was ablated at five pulse energies: 1, 5, 10, 25, 50 µJ at two different scanning speeds: ν = 500 µm/s and ν = 2000 µm/s. The effect of additional laser passes was also investigated, at 1, 3 and 6 passes. In addition, a third scanning speed of 250 µm/s was performed for each pulse energy but only for a single pass. Scanning occurred in a bi-directional pattern, with Δy = 5 µm between adjacent lines. The laser polarisation vector is roughly parallel to the scanning direction, which was from top to bottom for all SEM images. The side wall of the SLM part was ablated, because the partially sintered powder simulates the roughness found on inclined surfaces [344]. Furthermore, if the objective is to assess the feasibility of surface patterning of the SAP, it provides a middle ground between the smooth top surface and the roughest possible surfaces (down-skin). A 1 kHz repetition rate was used.

Laser fluence F is defined as the optical energy per unit area, and thus can be calculated using the equation:

$$F = \frac{E_p}{\pi w_0^2} \quad (3)$$

Where E_p is the pulse energy in µJ and w_0 is the radius at the Gaussian beam waist. The beam waist corresponds to the smallest size spot that is achieved when focusing a laser beam. The spot size is limited by the diffraction of light. The beam waist radius for a perfectly Gaussian beam is given by the equation:

$$\omega_0 = \frac{2\lambda f}{\pi D} \quad (4)$$

Where λ is the laser wavelength, *f* is the lens focal length, and D is the beam diameter at the lens. As previously stated, the diffraction limited beam spot diameter for the Mitutoyo 5x objective is 10.2 µm. As the beam is scanned, consecutive pulses overlap and ablate some of the same area. Since the line separation is less than the beam spot diameter, overlapping between scan lines will also occur. The number of effective pulses characterises the dosage and in 2D is given by the equation [302]:

$$N_{eff\_2D} = \frac{\pi \omega_0^2 f}{v \cdot \Delta y} \quad (5)$$

Equations (1), (2), and (3) are used to calculate the laser parameters displayed in Table 2 and 3.

Table 2: Summary of the effective number of pulses for the 3 scanning speeds used, Δy = 5 µm, $2w_0$ = 10.2 µm.

Scanning Speed (µm/s)	N_{eff_2D}
2000	326
500	1304
250	2608

Table 3: Summary of fluence values for each pulse energy, $2w_0$ = 10.2 µm.

Pulse Energy (µJ)	Fluence (J/cm^2)
1	1.23
5	6.14

10	12.27
25	30.68
50	61.36

4.2.4 Surface Analysis

Analysis of surface morphology was performed by SEM (JEOL6610), with feature measurement done using ImageJ tools.

Surface profile and roughness measurements were taken with an Alicona Infinite Focus G5. S_a is defined as the arithmetical mean height (average areal surface roughness) for a surface, generally given by the equation [345]:

$$S_a = \frac{1}{MN}\sum_{i=1}^{i=N}\sum_{j=1}^{j=M}\left|Z(x_i y_j)\right| \quad (6)$$

Where *M* and *N* are the number of x and y points and *Z(x,y)* is the height.

4.3 Results

Surface modification results are included here. It should be noted that for ablation experiments, the laser scanning direction was from top to bottom in all SEM images included here, while the AM build direction is from right to left. Thus, the ablation scanning vector is parallel to the AM layers and perpendicular to the build direction.

4.3.1 Surface As-Printed

Scanning electron microscopy of the as-printed surface shows large quantities of partially sintered powder (Figure 4.2). Swathes of fully solidified material are observed to extend out of

the surface to form peaks and valleys, and appear to flow opposite to the build direction. The regions that are devoid of adhered powder are smooth and continuous with some ripples. At higher magnification, powder size can be more easily distinguished (Figure 4.3). The elevation differences between some of these points are many tens of microns.

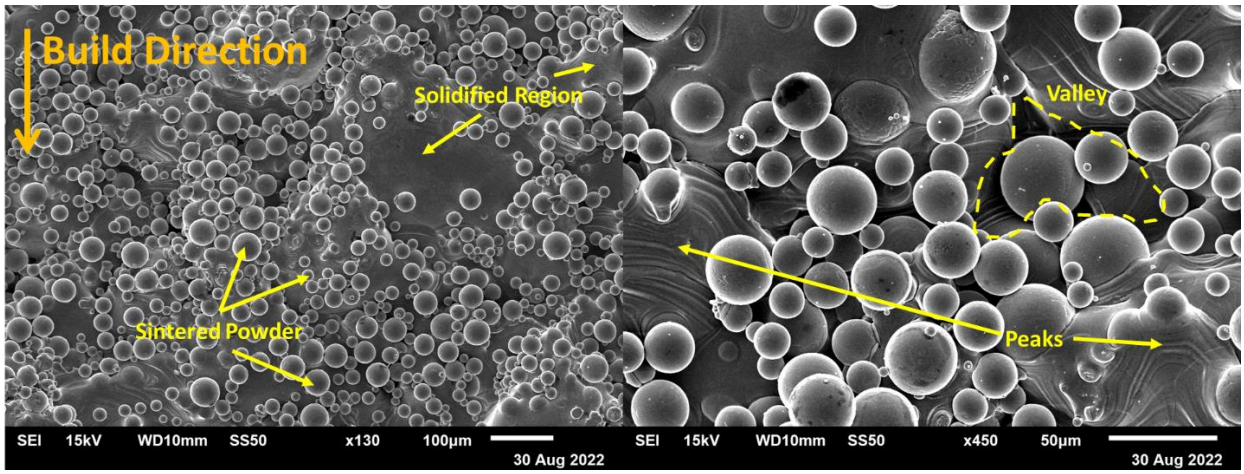

Figure 4.3: SEM of surface as-printed. Left: 130x magnification. Right: 450x magnification, the larger particle in the valley region is approximately 30 µm in diameter.

From an area of approximately 600x600 µm, the average surface roughness for the SAP was measured to be S_a = 26.2 µm. From the selected area, the distance between the lowest point and the highest point (S_z) was 181.5 µm.

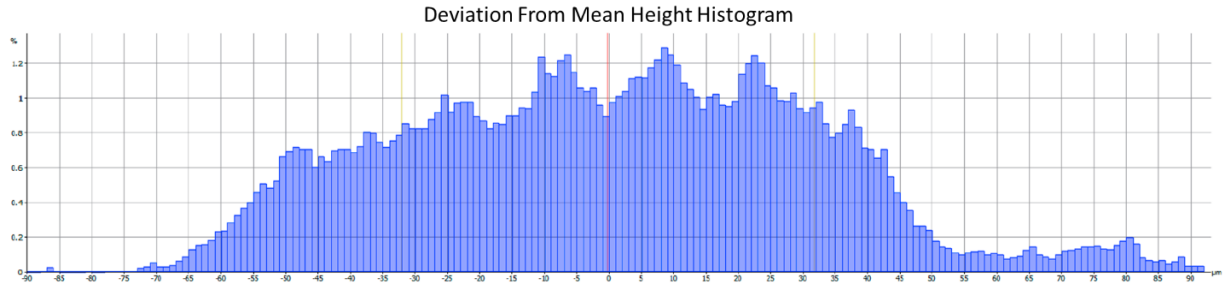

Figure 4.4: Histogram for the deviation in µm of each measured point from the mean height of the sample. σ = 31.9 µm.

4.3.2 2000 µm/s Scanning Speed

Figure 4.4 shows surface morphology at 1 µJ pulse energy for 1, 3, and 6 passes. After 1 laser pass, wave-like surface structures form across the modification area, perpendicular to the laser scanning direction. Periodicity of these ripples vary from 0.6 µm to 1.1 µm. Nano-sized holes can also be observed along the periodic structures and in distinct lines. The average diameter of

the holes is 0.49 ± 0.17 µm. These features are less well-formed and consistent on the powder particles. Additional waves radiate out from the surface underneath the powder, in some cases the nano-holes here are larger. The morphology after 3 passes is similar, but the nano-holes appear to be forming into distinct, meandering lines. At 6 passes, the nano-hole-lines are clearer, rings have formed around the powder particles, and the periodic structures are well-formed on the edges of the powder.

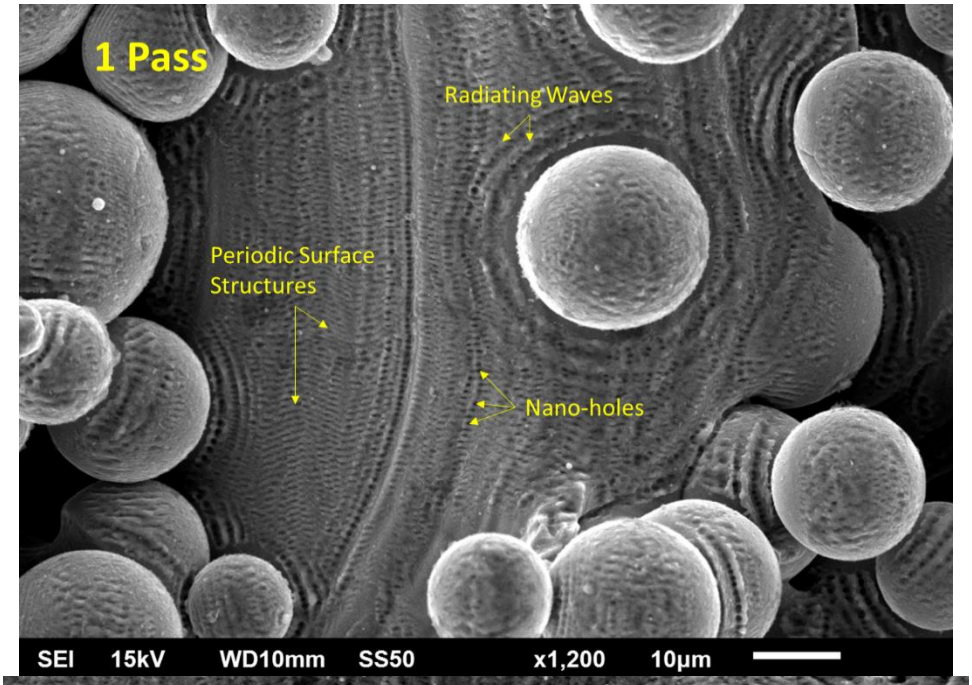

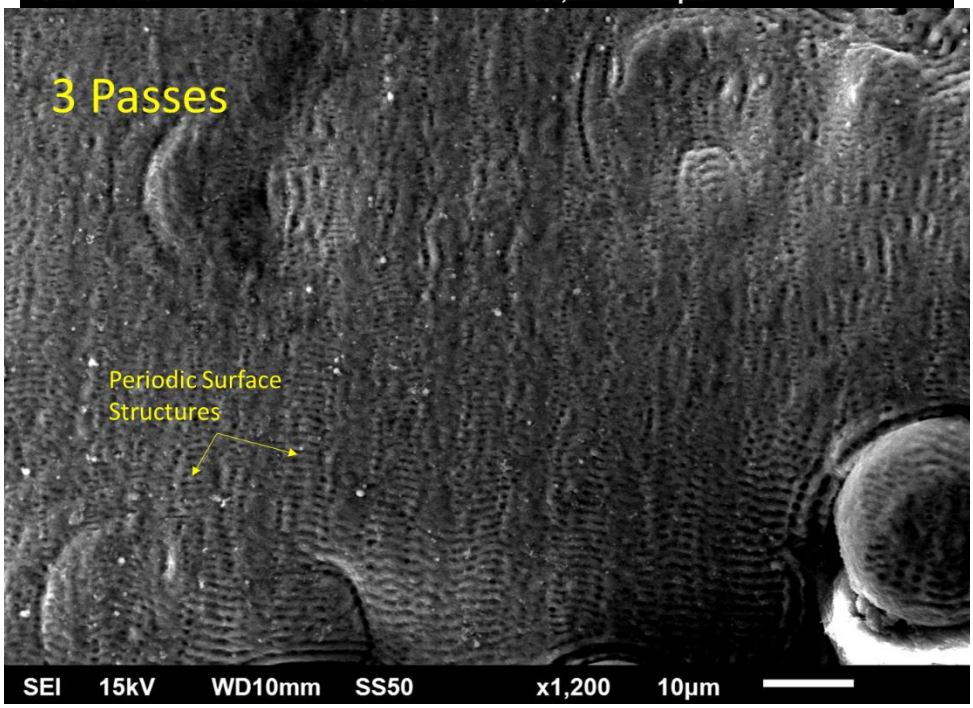

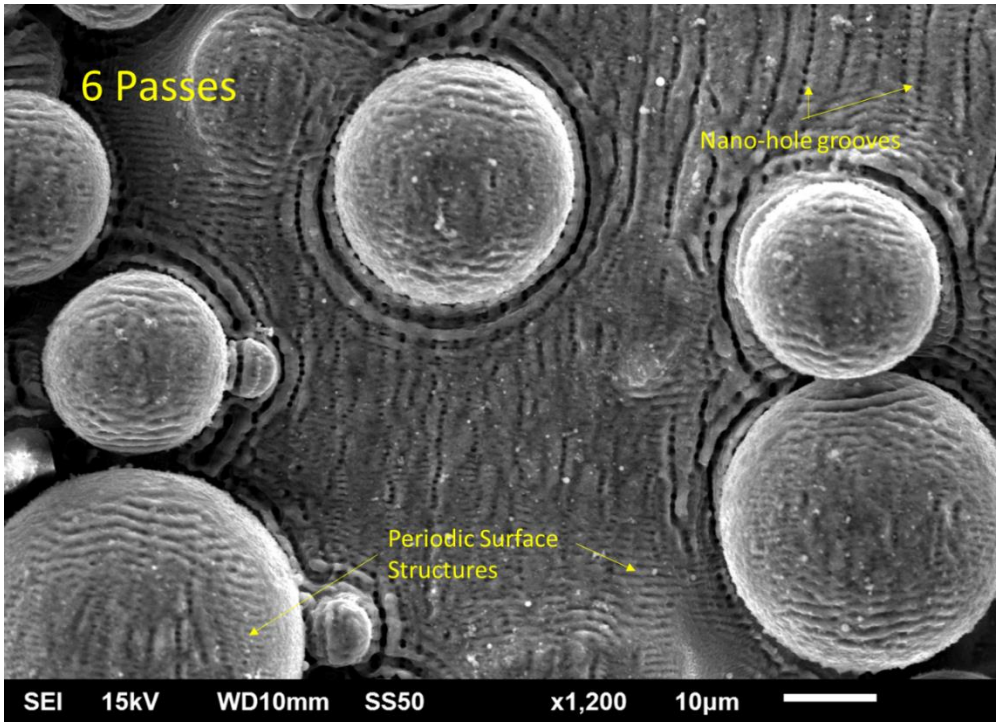

Figure 4.5: Surface morphology at 1 µJ pulse energy, 2000 µm/s scan speed. Top to bottom: 1, 3, and 6 passes.

At 5 µJ pulse energy (Figure 4.5), a corduroy-like pattern is observed, covering the powder particles and (previously) smooth solidified regions. The distinct lines are angled with respect to the laser scanning direction and appear to arc. The average distance between angled lines was measured to be 1.82 ± 0.17 µm, and the average distance between the vertical tracks was measured to be 5.25 ± 0.17 µm. There were no observable differences for additional laser passes.

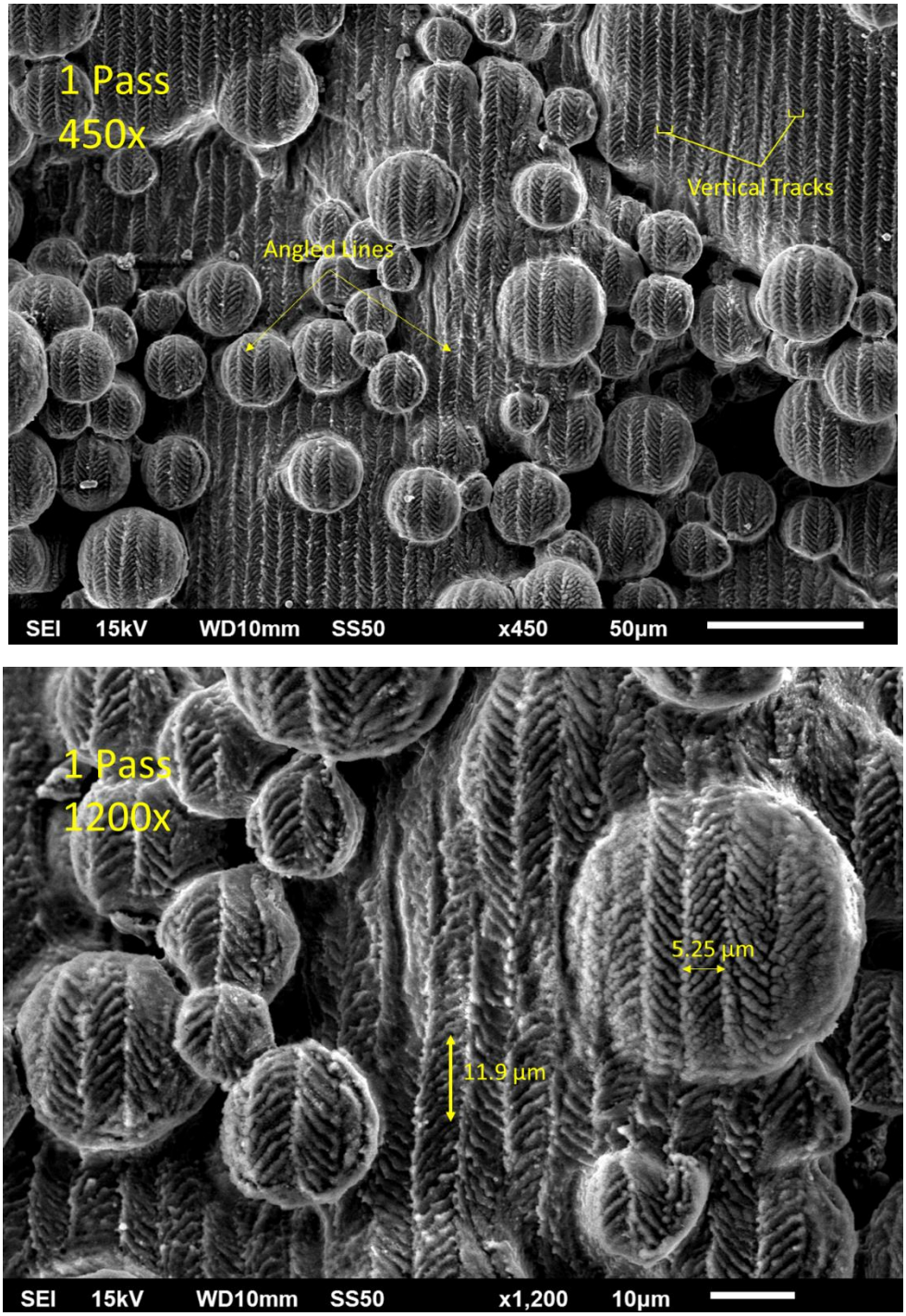

Figure 4.6: Surface morphology at 5 µJ, 2000 µm/s, single pass. Top: 450x magnification. Bottom: 1200x magnification, example measurements taken in ImageJ. 7 angled lines are spanned by the 11.9 µm distance, giving an average distance between lines of 1.7 µm.

When the pulse energy is increased to 10 µJ, the surface morphology is largely similar to 5 µJ but the angled lines are less structured, more chaotic, and globular features are visible at their

edges as if they were frozen mid-spatter (Figure 4.6). The average distance between angled lines was larger, measured to be 2.16 ± 0.17 µm, and the average distance between vertical tracks was measured to be 5.22 ± 0.17 µm. At a large, flat region of the surface, the ordered pattern disappears and is replaced by a cracked and random surface.

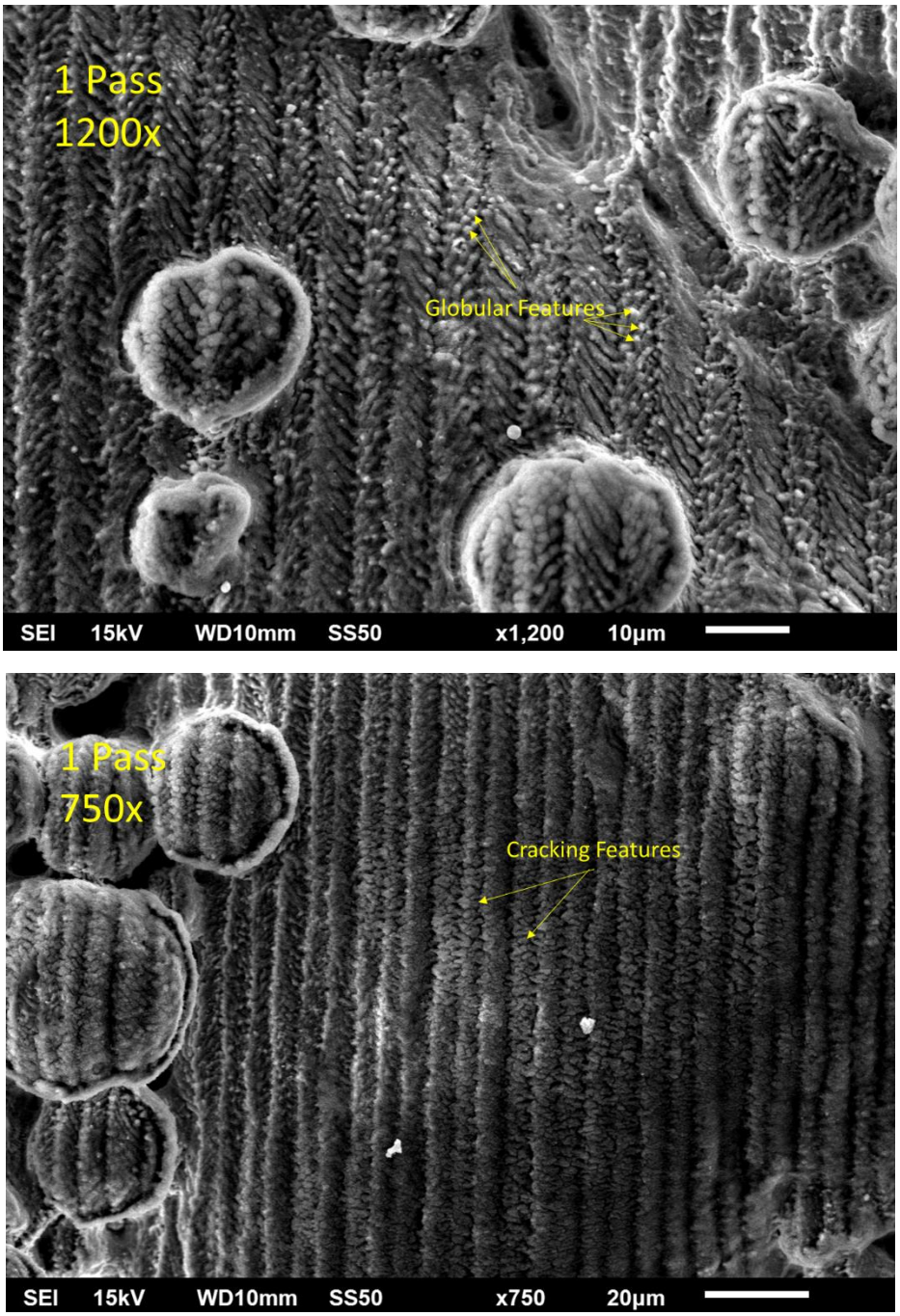

Figure 4.7: Surface morphology at 10 µJ, 2000 µm/s, single pass. Top: Typical surface. Bottom: Flat surface with cracking morphology.

At 25 µJ, some periodicity can be observed as vertical grooves (Figure 4.7). In some locations the tracks are higher frequency i.e. shorter distance between them, and in others they are low frequency i.e. longer distance. Deep cavities have formed along valleys and next to powder particles. With additional passes, the number of cavities appears to increase, and in some places the surface appears to be smoother and more covered with the ripple-like periodic structures seen at 1 µJ. Powder particles are still recognizable.

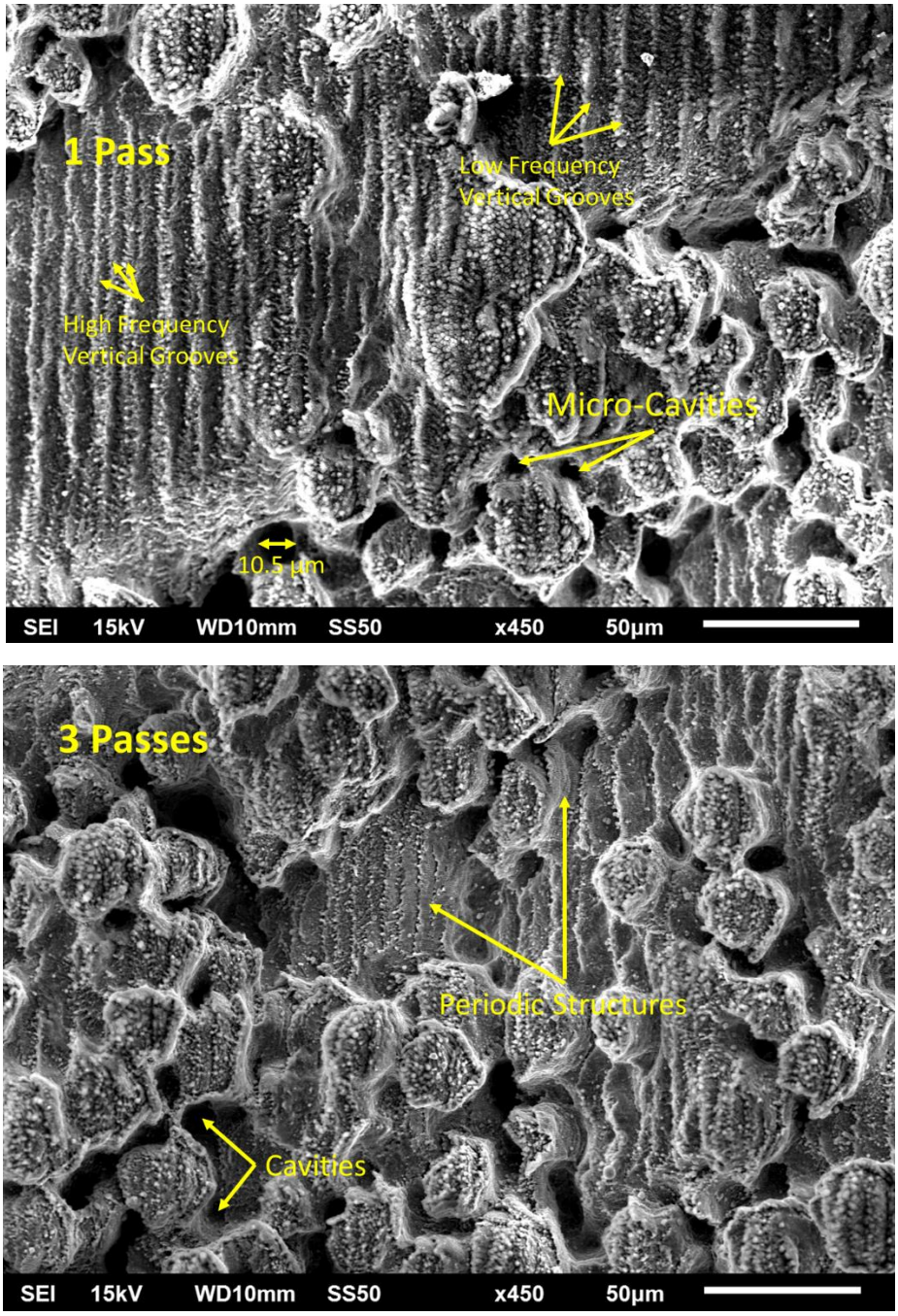

Figure 4.8: Surface morphology at 25 µJ, 2000 µm/s. Top: 1 pass, separation distance between high frequency vertical tracks is 4.68 ± 0.44 µm, average separation between low frequency vertical tracks is 10.3 µm ± 0.44. Bottom: 3 passes.

With a single pass at 50 µJ, there is an increased prevalence of cavities which primarily form along the valleys and around powder particles (Figure 4.8). A transition between high and low frequency vertical grooves can be seen at 1 pass. At 3 passes, cavities dominate and their preference for low-lying regions has dissipated. The diameter of circular and well-formed cavities were measured, and have an average diameter of 13.1 ± 0.8 µm. After 6 passes, there is little observable difference except for a slight increase in the number of cavities.

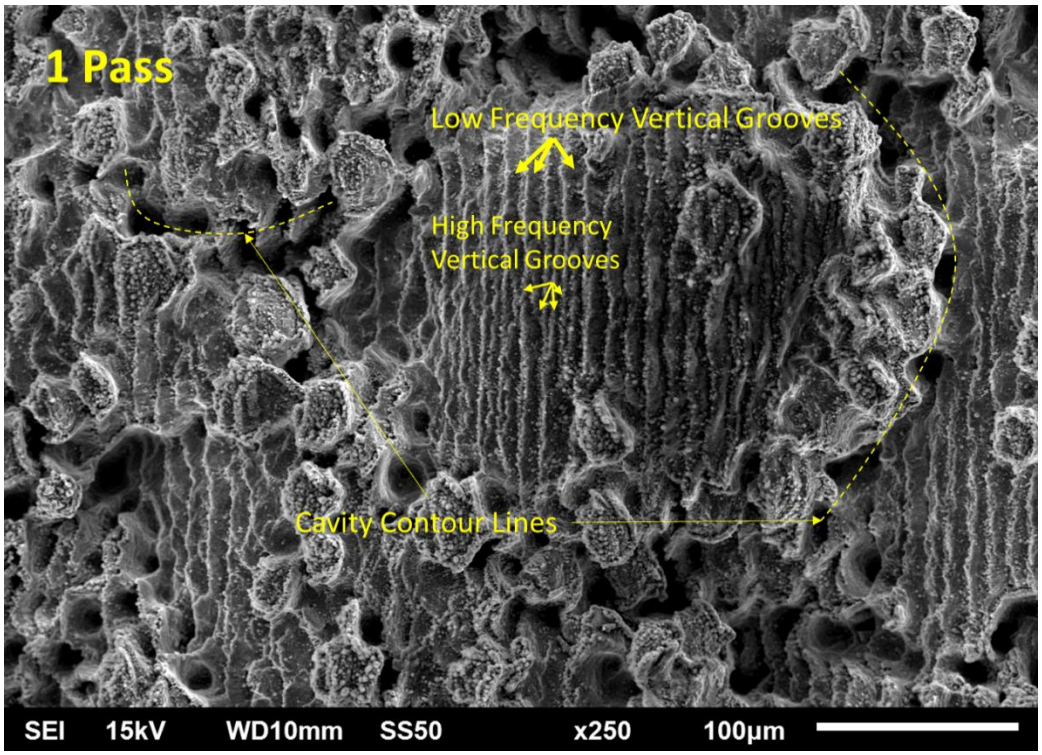

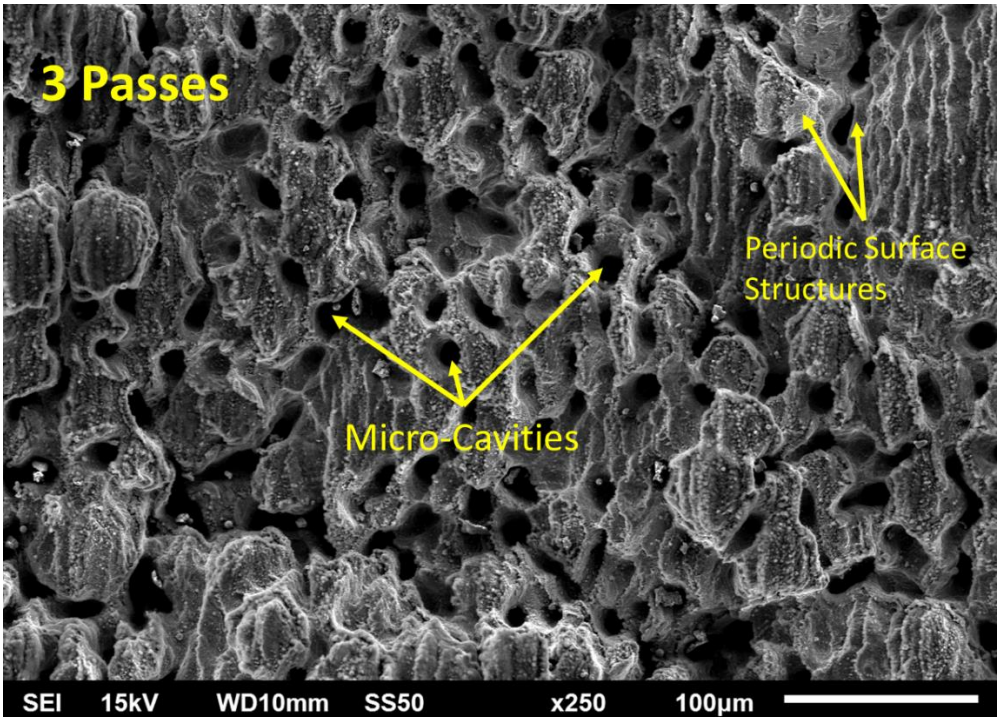

Figure 4.9: Surface morphology for 50 µJ pulse energy. Top: 1 pass, high frequency vertical grooves have separation distance (periodicity) of about 5 µm, low frequency are 10 µm. Bottom: 3 passes.

4.3.3 500 µm/s Scanning Speed

With a 500 µm/s scanning speed, consecutive laser pulses are closer together. For a 1 kHz repetition rate, there is an approximate distance between pulses of 0.5 µm. Thus, the pulse overlap and total energy dose is increased and more material removal is expected.

For 1 µJ of pulse energy and a single pass, periodic surface structures are again observed (Figure 4.9). Nano-holes are prevalent, and they mostly form grooves. Elevated ridges appear next to the grooves, possibly as a result of material re-deposition. With increasing number of passes, the nano-holes become less distinct as continuous, undulating grooves form. Periodic surface structures are superimposed on the resultant ridges.

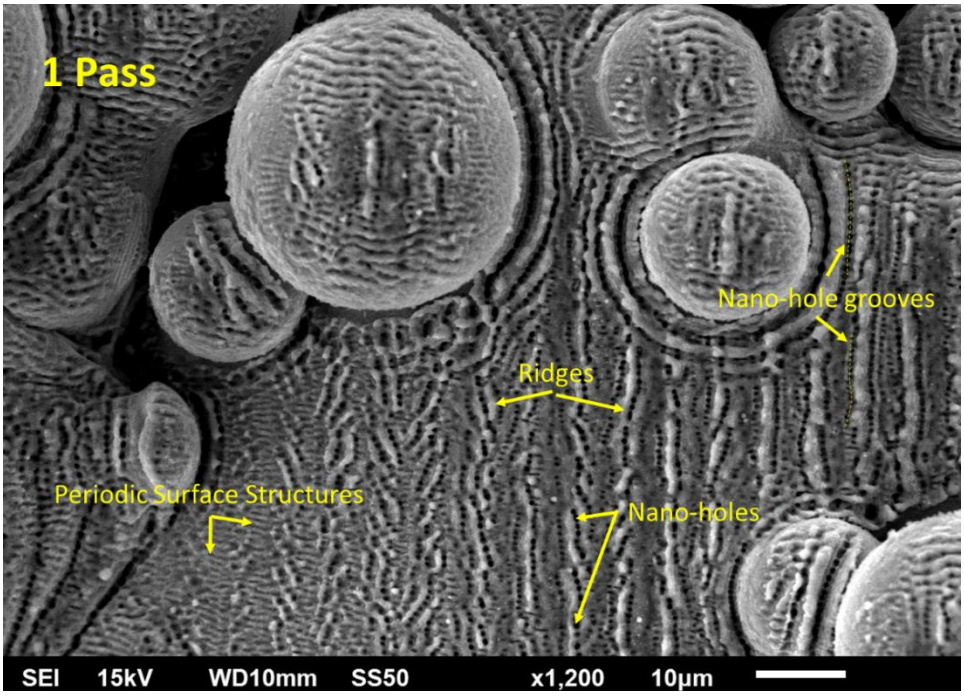
1 Pass
Nano-hole grooves
Ridges
Periodic Surface Structures
Nano-holes
SEI 15kV WD10mm SS50 x1,200 10µm

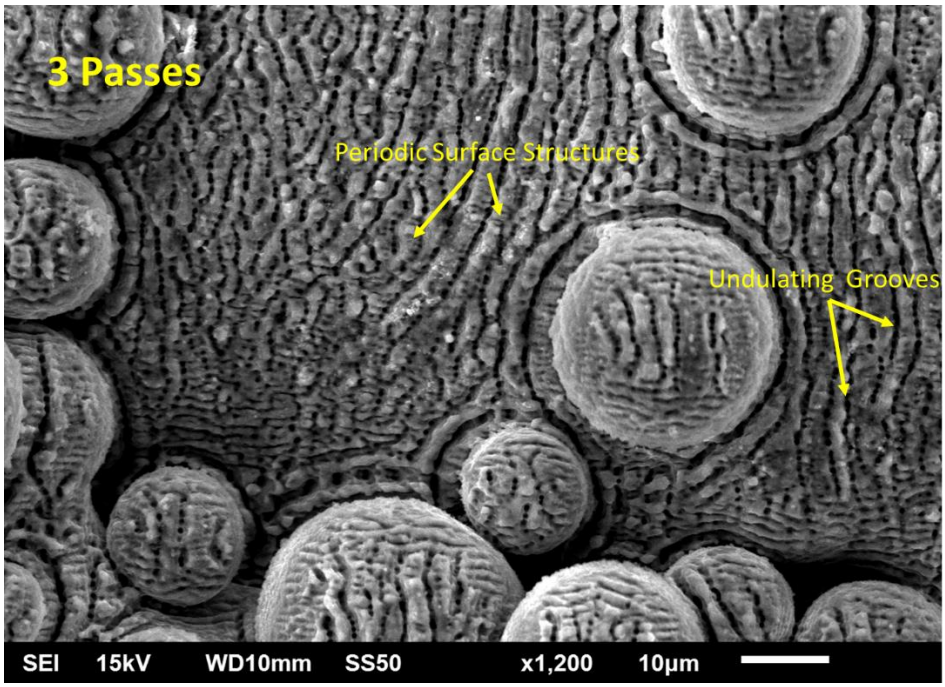
3 Passes
Periodic Surface Structures
Undulating Grooves
SEI 15kV WD10mm SS50 x1,200 10µm

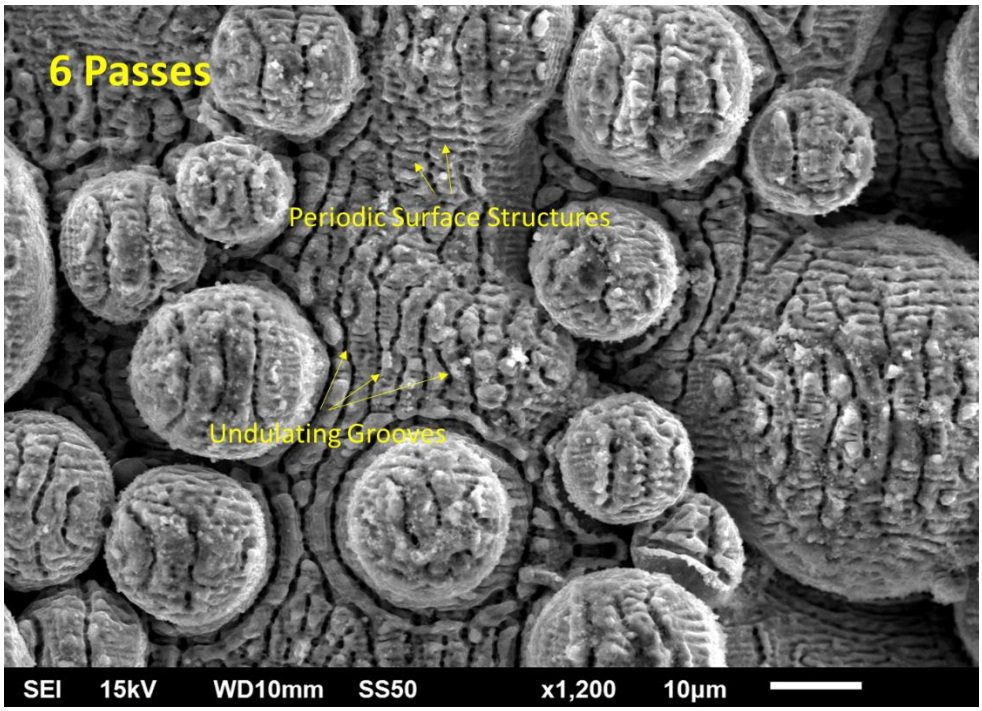

Figure 4.10: Surface morphology at 1 µJ, 500 µm/s. Top to bottom: 1, 3, 6 laser passes.

For 5 µJ, the surface is covered in grooves with an approximate spacing of 5 µm (Figure 4.10). In the single pass experiment, an area of cracking morphology is again found on top of a large, flat surface. After 3 passes, the grooves improve in definition, and at 6 passes they are well-defined and consistent, even on top of the powder particles.

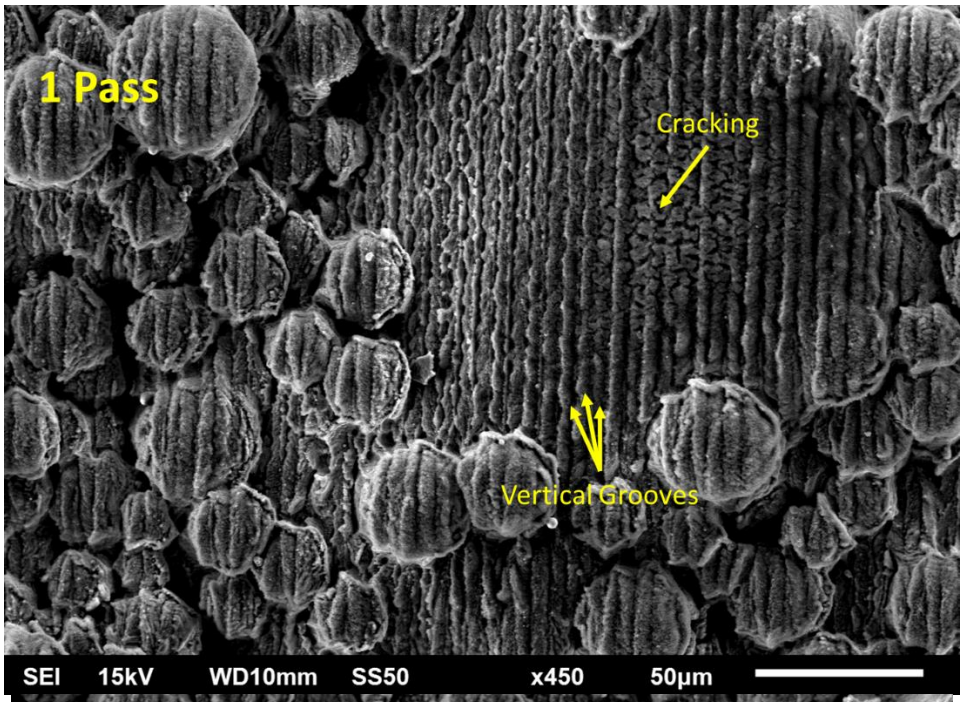
1 Pass
Cracking
Vertical Grooves
SEI 15kV WD10mm SS50 x450 50µm

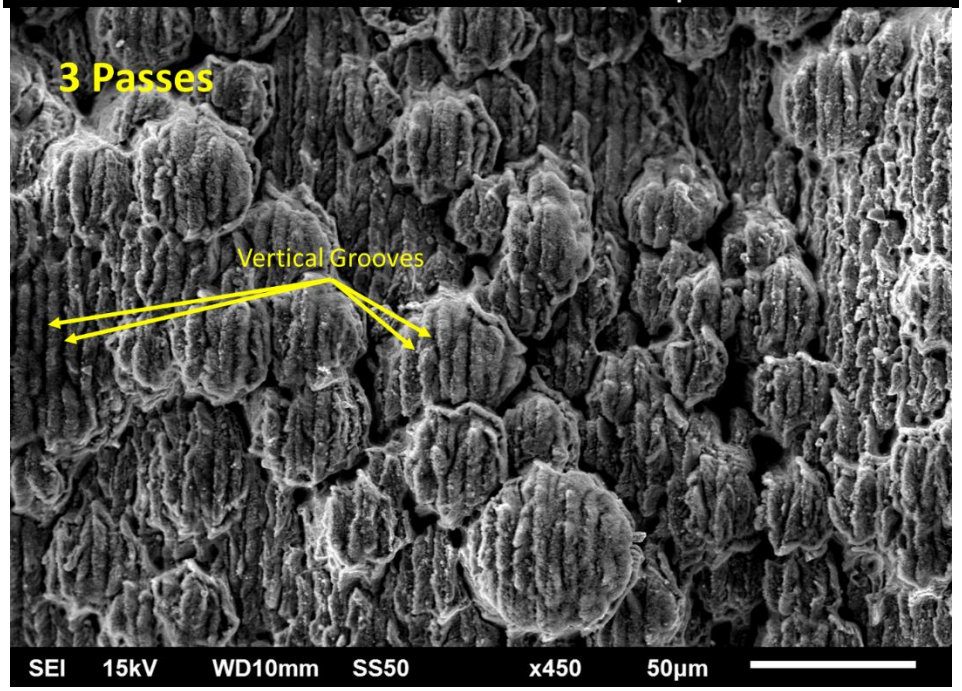
3 Passes
Vertical Grooves
SEI 15kV WD10mm SS50 x450 50µm

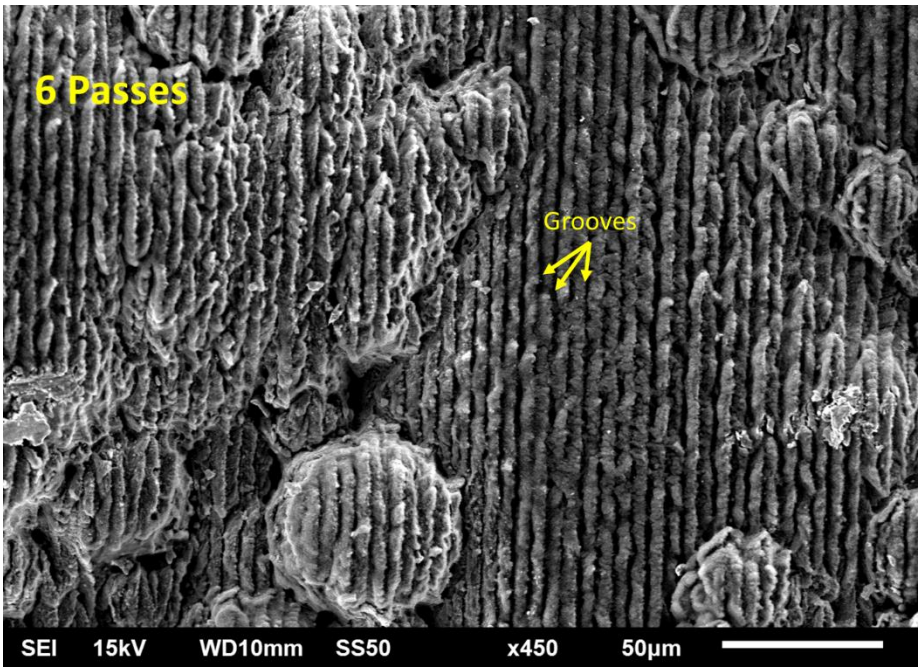

Figure 4.11: Surface morphology at 5 µJ, 500 µm/s. Top to bottom: 1, 3, and 6 passes.

When the surface is scanned with 10 µJ of pulse energy the surface develops scan line grooves and additional features such as angled ridges and shallow cavities (Figure 4.11). This is most evident in flatter areas of the surface with a lack of adhered powder. With additional laser passes, these features give way to flared micro-cavity structures. Powder particles progressively become less recognisable as the number of passes increases and more material is removed.

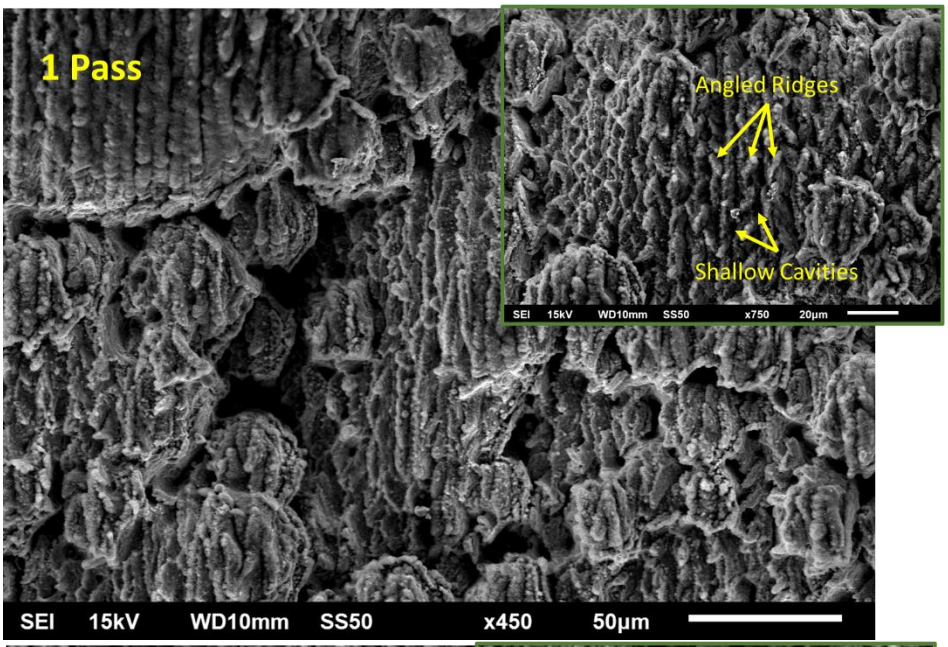
1 Pass
Angled Ridges
Shallow Cavities
SEI 15kV WD10mm SS50 x750 20µm
SEI 15kV WD10mm SS50 x450 50µm

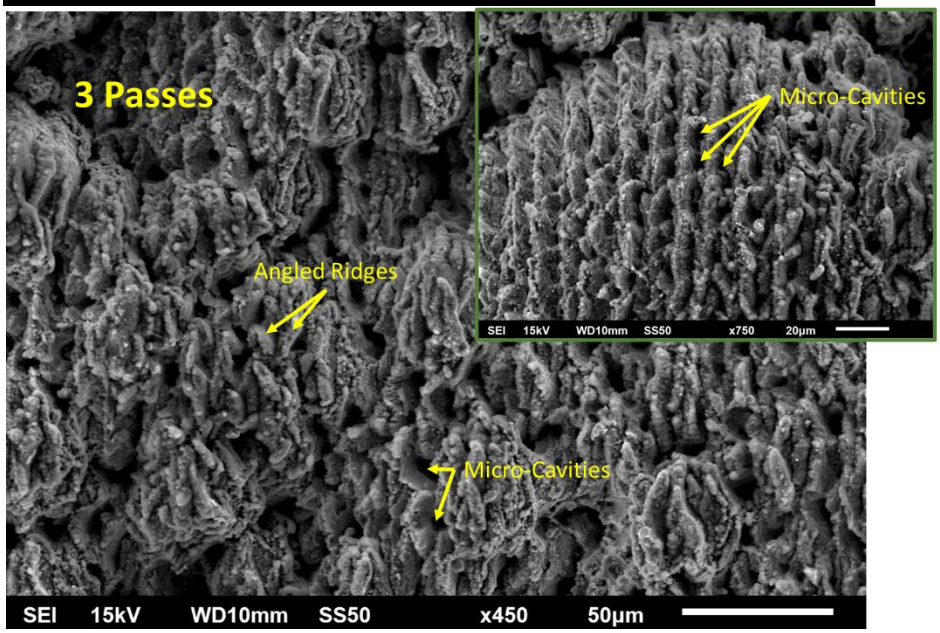
3 Passes
Micro-Cavities
Angled Ridges
Micro-Cavities
SEI 15kV WD10mm SS50 x750 20µm
SEI 15kV WD10mm SS50 x450 50µm

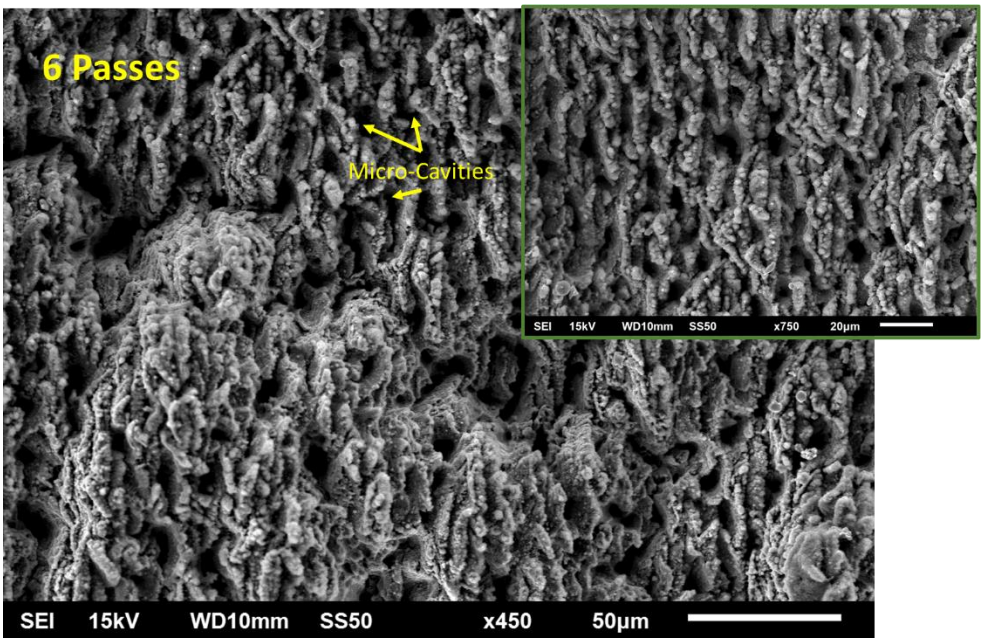

Figure 4.12: Surface morphology at 10 µJ, 500 µm/s. Top to bottom: 1, 3, and 6 passes. Insets (green border) show regions with flatter area.

At 25 µJ pulse energy and a single pass, micro-cavities are immediately apparent and dominate the surface (Figure 4.12). They are loosely arranged in lines parallel to the scanning direction and are irregularly shaped. With more laser passes they grow in size and become more circular. At this intensity and scanning speed, the adhered powder is mostly ablated, and the only remnants of the as-printed surface are the low frequency bulges.

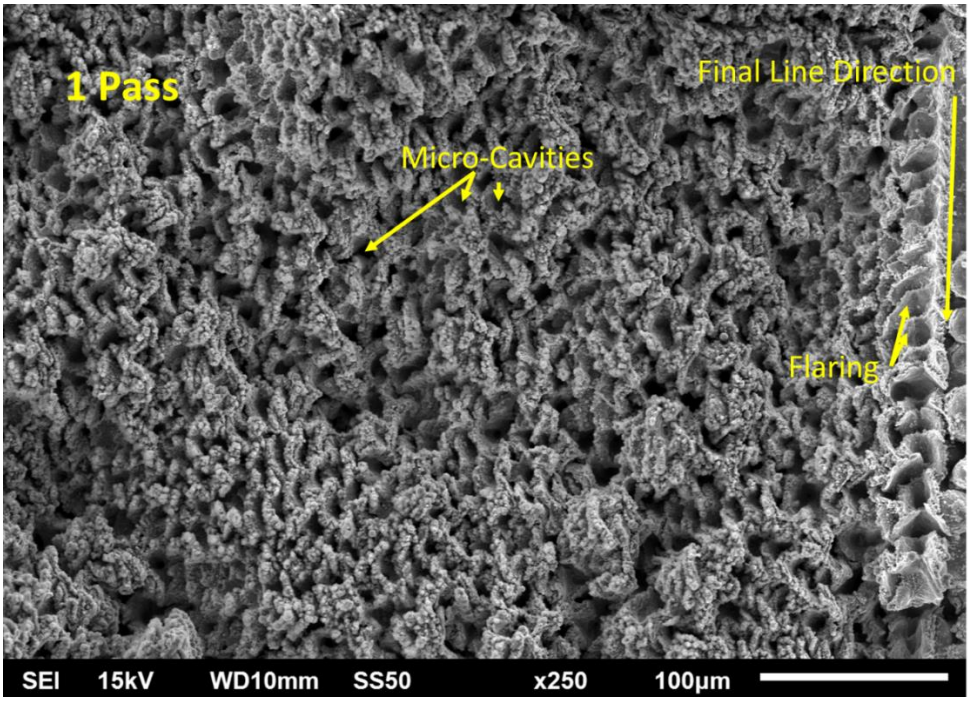

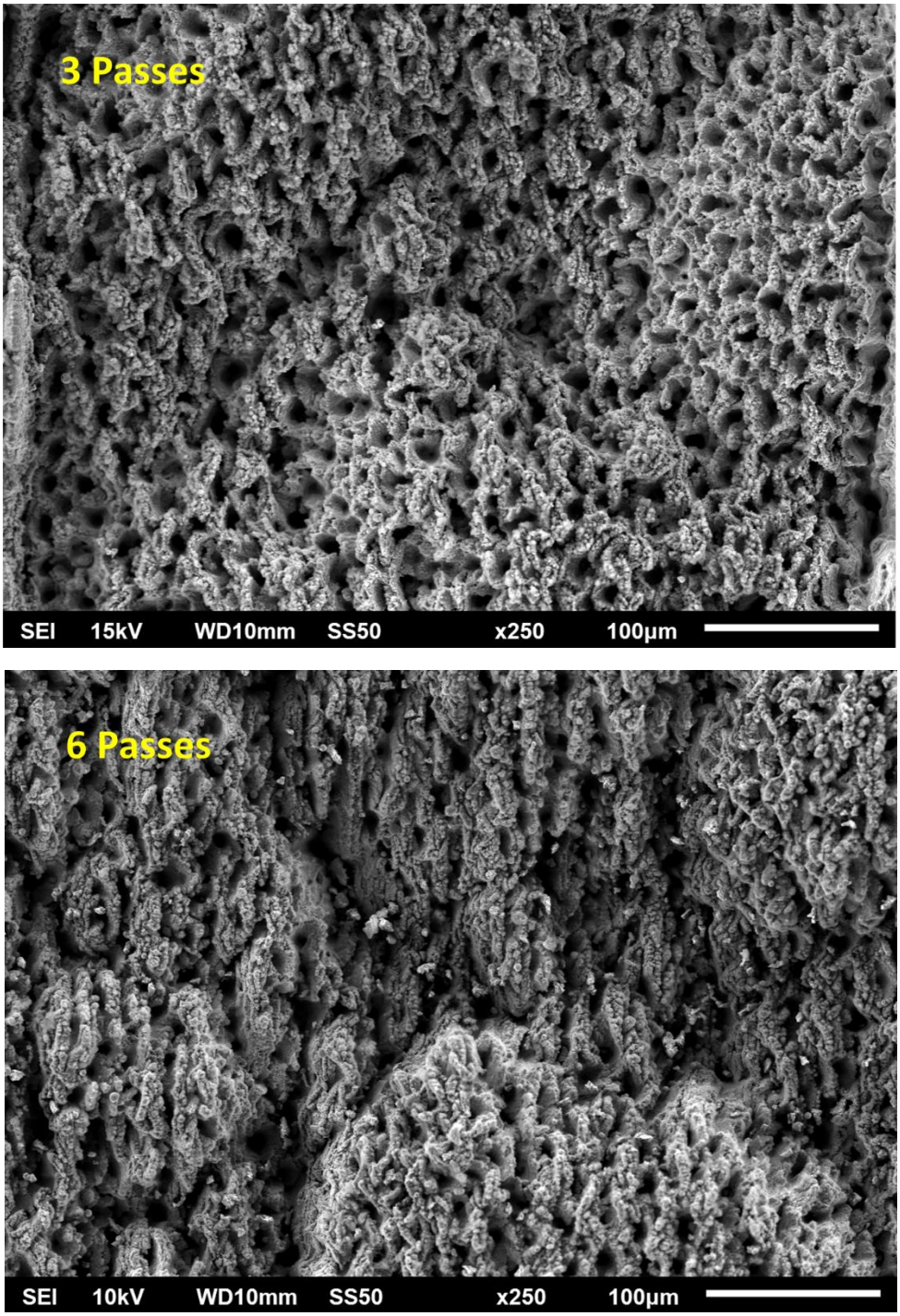

Figure 4.13: Surface morphology at 25 µJ, 500 µm/s. Top to bottom: 1, 3, and 6 passes.

At the highest tested pulse energy of 50 µJ, the surface resembles that at 25 µJ (Figure 4.13). Much of the as-printed surface has been ablated and micro-cavities are the pre-eminent structure. Additionally, there are peaks with a high degree of nano-roughness caused by crystal-like formations. The micro-cavities for 1 laser pass are relatively shallow and in some cases small or

covered by the peaks. With increasing laser passes, the surface at large is brought to a more consistent elevation and the micro-cavities become deeper and more rounded. The average cavity diameter is 16.4 ± 0.8 µm. There is a slight dependence of the cavity position on the laser scanning direction.

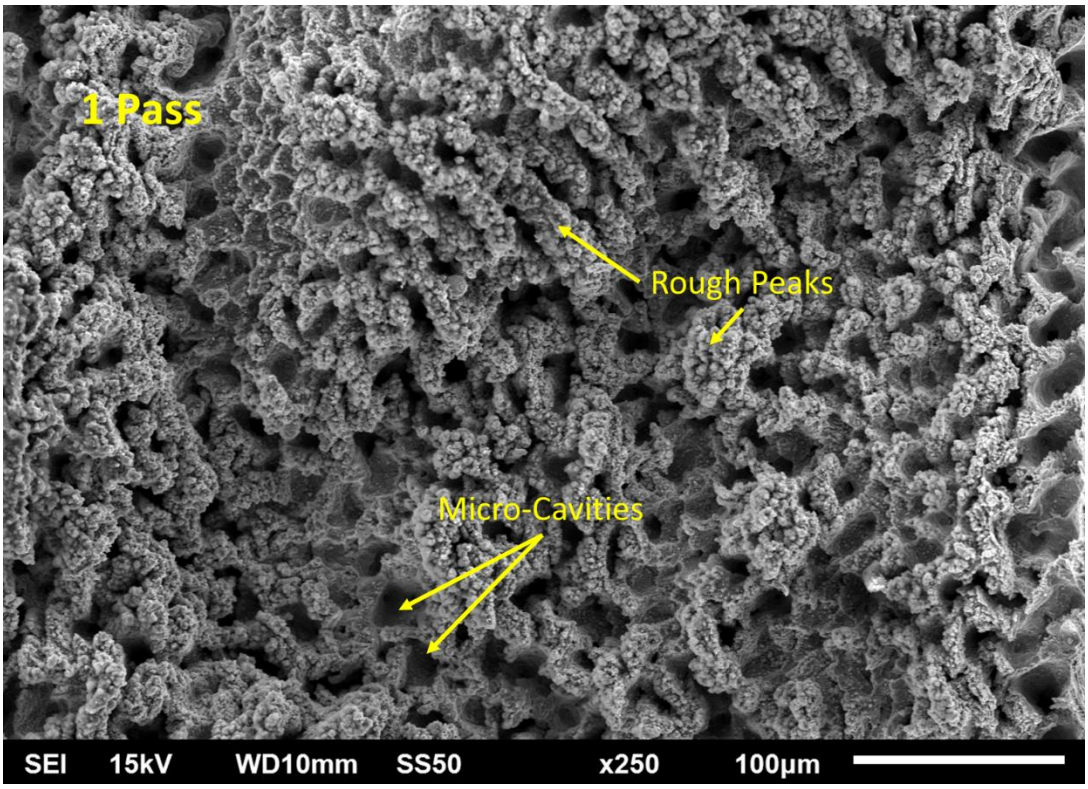

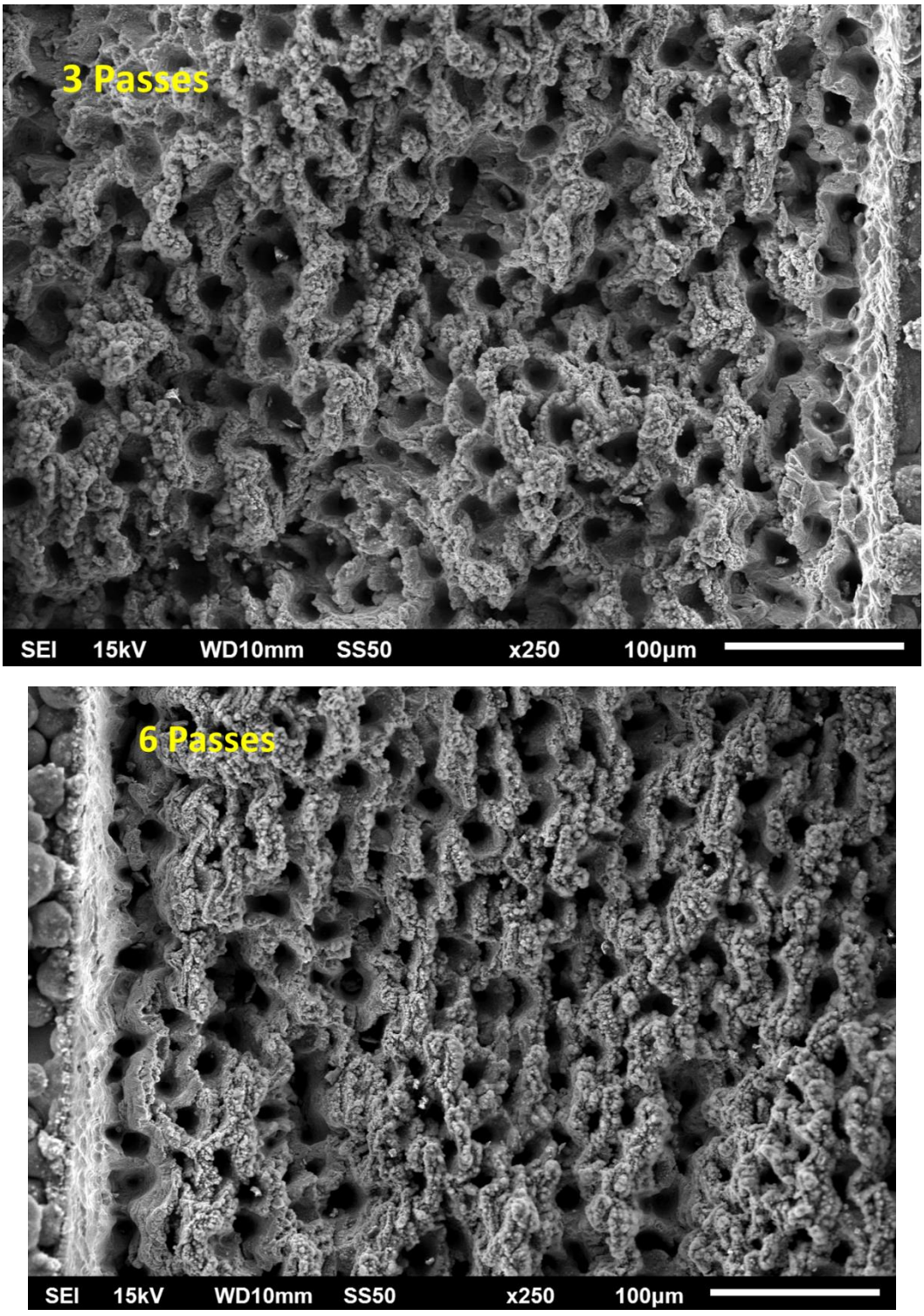

Figure 4.14: Surface morphology at 50 µJ, 500 µm/s. Top to bottom: 1, 3, and 6 passes.

4.3.4 250 µm/s Scanning Speed

The Ti-6Al-4V surface was ablated at a slower scanning speed of 250 µm/s for the five pulse energies with a single pass (Figure 4.14). For the 1 µJ pulse energy, the periodic surface structure and ridges morphology was produced. At 5 µJ, ridges form a chevron-like pattern with a vertical track periodicity of 5.3 µm ± 0.44 µm, and an average distance between angled lines of 6.76 ± 0.44 µm. corresponding to the line spacing. At 10 µJ, the micro-cavity morphology is obtained. With an increase to 25 µJ, some micro-cavities are still visible, but the surface is primarily composed of random, chaotic structures with high roughness. A doubling of the pulse energy to 50 µJ results in a more open surface, with regions that have a blasted-like appearance but still with the chaotic structures seen at 25 µJ.

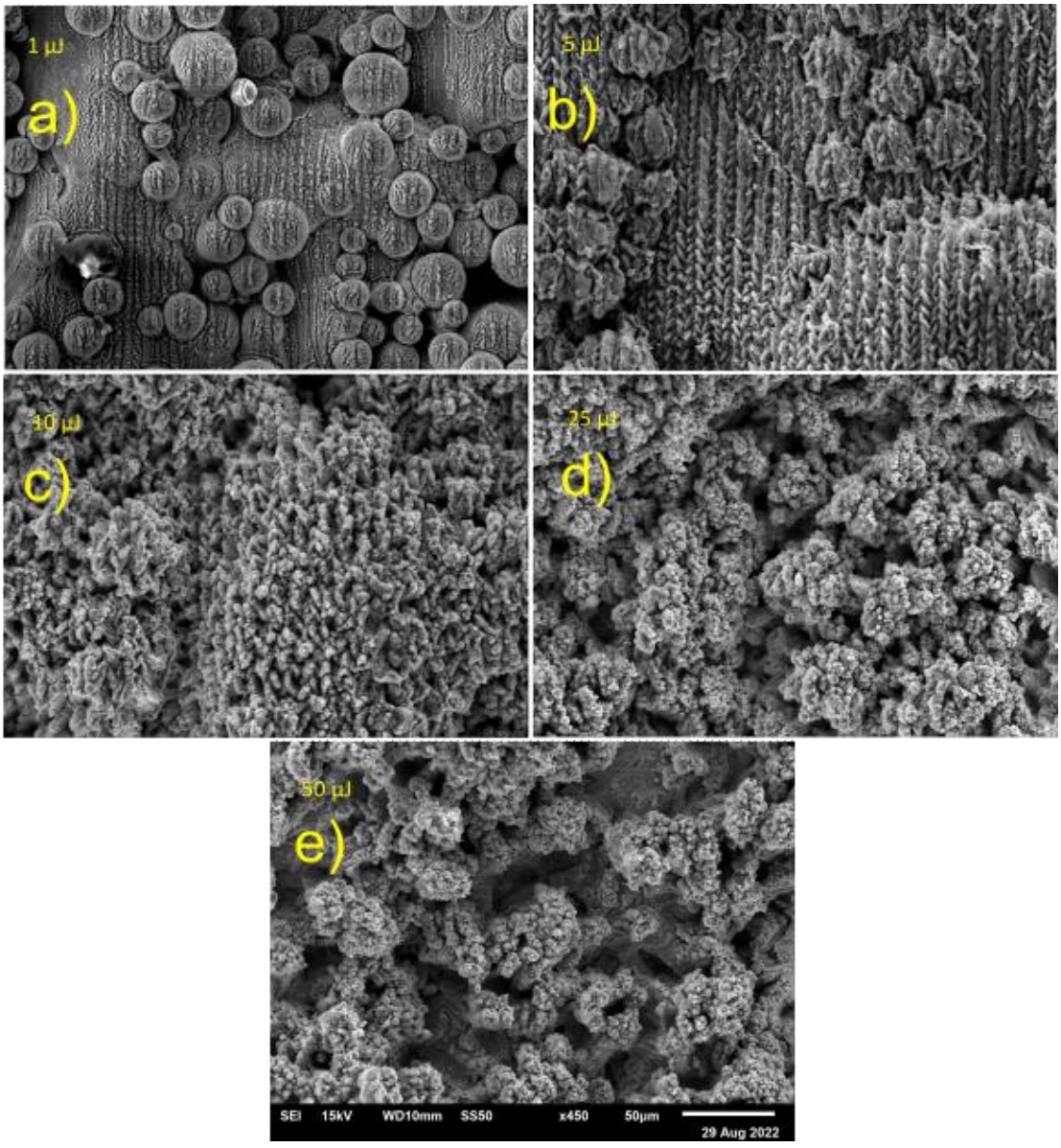

Figure 4.15: Surface morphologies at 250 µm/s scanning speed. The scale bar in the 50 µJ image indicates the scale for all.

4.4 Discussion

A significant amount of partially sintered powder is observed on the surface as-printed. The surface depicted in Figure 4.2 is the side wall of the Ti-6Al-4V part and during printing is perpendicular to the build plate. As an inclined surface (90°), its roughness is greatly affected by adhered powder [344]. The physical features of a SLM-produced part are determined by the melt pool characteristics, which are in turn determined by the laser parameters as well as the local heat conduction properties. During melting, most of the heat is conducted away from the surface towards the build plate through solid material, but at the edges of the part the effective thermal conductivity to the build plate is reduced and both the melt pool temperature and size increase [346]. While contour scanning can be done with alternative laser parameters to alleviate this effect, in this work the parameters were the same as the hatching parameters [342]. Many complex forces act upon the melt pool, and surface tension of the melt pool is counteracted by gravitational and capillary forces, causing it to extend into the powder bed and increase surface roughness [342]. This effect is observed in Figure 4.2, where molten pools have flowed opposite to the build direction, creating asymmetric structures with a gently sloping side and a sheer side. Combined with adhered powder, the average surface roughness of the powder (S_a = 26.2 µm) is comparable to the middle of the powder size range. Both the S_a and the S_z for this sample are greater than the R_a (17.9 µm) and R_z (121.9) found in [339].

The sample has a complicated surface. Ultrafast laser surface modification is often performed on comparatively smooth surfaces (S_a or R_a < 1 µm) which are obtained by mechanical and chemical polishing [302], [347], [348]. Then the distance from the sample to the focusing lens remains relatively constant, and so does the beam spot size and fluence. Homogenous surface patterning is readily achieved in this way, but at the cost of polishing processes. A Gaussian beam radius evolves along its propagation axis (z) according to [349]:

$$\omega(z) = \omega_0 \sqrt{1 + \left(\frac{\lambda z}{\pi \omega_0^2}\right)^2} \quad (7)$$

Figure 4.3 shows that most points on the SAP lie within the -50 to 50 µm range. Assuming best-case focusing where the focal plane is at 0, the beam spot size will be largest at z = ±50 µm, corresponding to a beam spot diameter w_0 = 11.36 um. The fluence for this diameter is reduced by 24%. This is a significant deviation in the fluence. Despite this, many of the surface patterns show good homogeneity e.g., Figure 4.5 (5 µJ, 2000 µm/s). According to the results here, surface geometry like the sphericity of the powder particles and steep elevation changes has a greater impact on the ablation pattern. This is most evident at lower pulse energies, for which periodic surface structures do not form at the center of the powder particles, and for which wave-like structures surrounding the powder particles form (Figure 4.4). Since the laser wavelength is of a comparable magnitude to the smaller powder particles, the wave-like structures may be caused by diffraction. Furthermore, at higher pulse energies (> 5 µJ) in which more material is being

removed, patterns are partly formed as a result of the local redeposition of material. On a flat surface, the local geometry is the same at each point and the ablation morphology for each pulse will be the same. The local geometry of the Ti-6Al-4V sample changes drastically, from the curved surfaces of powder particles to wide, flat regions. Despite the irregularities, five main surface morphologies were identified: laser-induced periodic surface structures (LIPSS), undulating grooves, micro-ripples, grooves, and micro-cavities.

4.4.1 LIPSS and Undulating Grooves

At the lowest tested pulse energy (1 µJ), periodic surface structures, so-called LIPSS, are generated. LIPSS are a common phenomenon in ultrafast laser ablation and are induced to make surfaces icephobic [350], antifouling and antibacterial [351], to reduce friction [352], to modify wettability [353], as molds for micro-injection molding [354], and more [92]. LIPSS vary widely in periodicity and formation mechanism, depending on material properties and the wavelength of light [92]. They are broadly categorised into high spatial frequency LIPSS (HSFL) and low spatial frequency LIPSS (LSFL). Of particular interest are Type I LSFL, which are characterised by a periodicity close to the laser wavelength [47]. Most of the LIPSS produced at 1 µJ have a periodicity between 0.7 and 0.9 µm, so are of LSFL-I classification (Figures 4.4 and 4.9). Further evidence for this is that their formation is largely perpendicular to the laser polarisation vector, a characteristic of LSFL-I. The generally accepted explanation for the formation of these structures is the interference of the incoming radiation with a surface electromagnetic wave at the rough surface and involving the excitation of surface plasmon polaritons [92]. Typically, LIPSS formation is reinforced by multiple laser exposures, and as the number of pulses or the pulse energy increases, columnar structures also referred to as undulating grooves are formed [355], [356]. The results here demonstrate the process of this transition (Figure 4.4). LIPSS and nano-holes form after 1 pass at 2000 µm/s, and after 6 passes the nano-holes begin to form distinct grooves. When the scanning speed is reduced to 500 µm/s and the effective number of pulses increases, the undulating groove morphology becomes apparent and increasingly so for additional laser passes. Superimposition of LIPSS on the groove morphology presents an ordered, hierarchical structuring of the surface. Such surface roughness organisations are desired for their hydrophobic tendencies [357].

4.4.2 Micro-ripples

The herringbone pattern observed at 5 and 10 µJ for the 2000 µm/s scanning speed is quite interesting (Figures 4.5 and 4.6). With a periodicity twice that of the wavelength, they do not fall into LIPSS classifications. Additionally, they are unchanged with an increase in laser passes. The vertical track separation corresponds to the 5 µm line spacing process parameter. At 1.82 µm, the average distance between the angled lines is much closer to the distance between individual laser pulses. The angled line direction changes between scan lines, which would correspond to the

bidirectional scanning. To investigate, the Ti-6Al-4V surface was irradiated by individual laser scans (Figure 4.15). The "angled lines" are revealed to be caused by the rims of craters produced by individual laser pulses. As the beam is scanned, the rims from subsequent pulses overlap the previous feature. This also explains why the line angle flips depending on the scanning direction. To the author's knowledge, these features have not been expounded for ultrashort pulse ablation of Ti-6Al-4V.

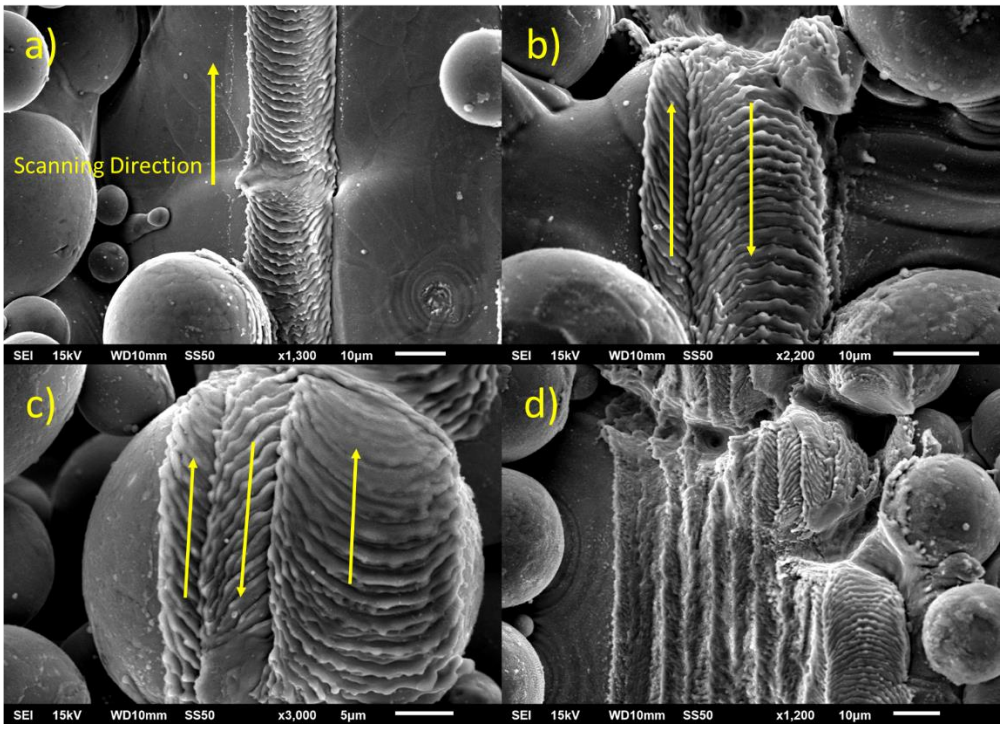

Figure 4.16: Individual scan lines at 10 µJ, 2000 µm/s. a) Single scan line, b) two bidirectional scan lines, c) three scan lines, d) 10 scan lines.

At 10 µJ in particular, the pulse craters appear to have hydrodynamic features in the form of droplets on the rims. Contrary to popular belief, this demonstrates that thermal effects are present under femtosecond laser ablation. Under both photomechanical spallation and phase explosion ablation regimes, material is transformed into transient liquid structures that, under rapid cooling, freeze to produce splatter-like features [1], [358]. Based on the initial investigation, it may be possible to alter the micro-scale surface roughness of micro-rippled surfaces by changing the scan line space and the scanning speed. Figure 4.16 demonstrates subtle engineering of the surface by performing unidirectional scanning. It is uncertain if this will have an effect on the wettability or directionality of fluid transport.

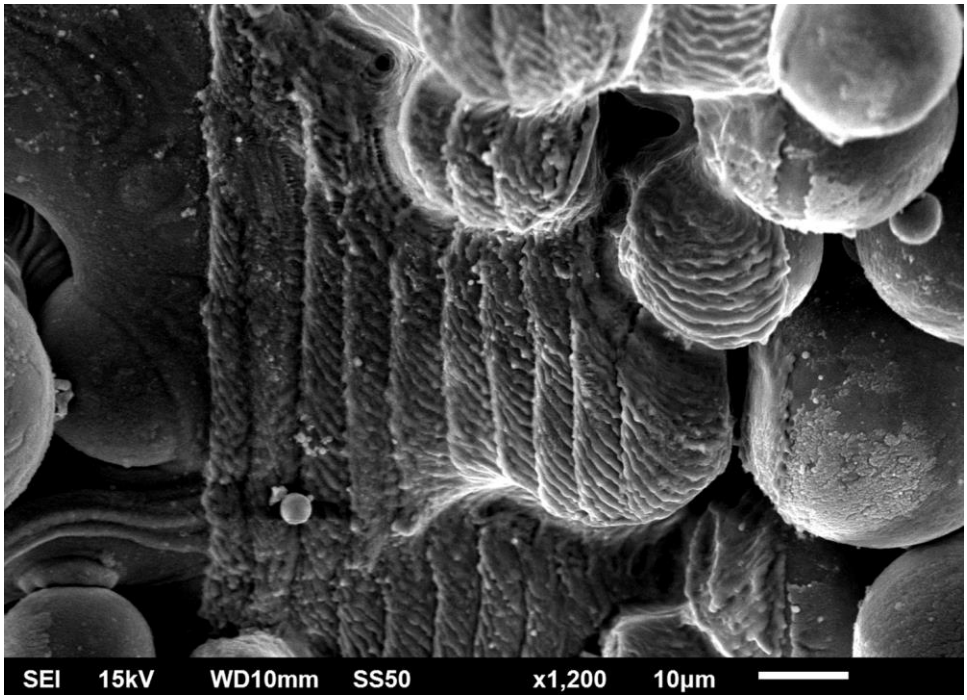

Figure 4.17: 10 scan lines at 10 µJ and 2000 µm/s. Scanning direction is from bottom to top for all tracks.

4.4.3 Grooves

Regular grooves formed at a range of parameters and with slightly different appearances. Under 25 and 50 µJ ablation at 2000 µm/s scanning speed vertical grooves are formed by the laser scan lines (Figures 4.7 and 4.8)). The groove surface itself is random, with nano-scale roughness. At these pulse energies, the dominant ablation mechanism may have transitioned to phase explosion in which material is directly transformed into a mixture of liquid droplets and vapor [1]. This transition is said to occur as the pulse energy increases [118]. The increase in pulse energy will also increase the affected area, and this is reflected in the joining of adjacent laser scan lines to form wider vertical grooves. With additional laser passes, the density of micro-cavities increases, particularly at 50 µJ.

Decreasing scanning speed to 500 µm/s results in better defined grooves at 5 µJ (Figure 4.10). While at 2000 µm/s this pulse energy produced micro-ripples, here the pulse-to-pulse distance is much shorter, and the crater rims are lost. At 10 µJ and 500 µm/s (Figure 4.11), a transition from 1 pass to 6 passes can be seen in which the groove ridges are increasingly angled and crescent-shaped micro-cavities replace the grooves. Thus, these grooves appear to be precursors to the micro-cavity morphology.

4.4.4 Micro-cavities

Micro-cavities are first produced at 25 µJ and 2000 µm/s (Figure 4.7). With an increase in pulse energy their distribution increases but it implies a correlation to the initial surface morphology. Since they are first noticed at valleys and next to powder particles, micro-cavity formation seems to depend on features that further couple incident radiation. If this is the case, slight depressions in the initial surface will grow after multiple laser passes to form a cavity. Results displayed in Figure 4.7 demonstrate this, and is consistent with previous findings [359], [360]. At slower scan speeds (500 µm/s), cavities are again observed but are present even on initially flat surfaces despite the pulse energy being unchanged (Figure 4.12). The number of pulses incident per unit area has increased to a point where micro-cavity formation nucleates regardless of the local geometry. Many of these cavities are crescent shaped due to the interaction between adjacent scan lines. Due to the high pulse energy, the ablated area is larger and adjacent scan lines are competing for dominance. It is hypothesized that an increase in line spacing will produce more circular cavities at the 25 µJ pulse energy. At 50 µJ and 500 µm/s, it is clear that increasing laser passes results in a refinement of the micro-cavity structure (Figure 4.13). Initially competing micro-cavities have resolved. Chichkov et al. [359] showed that for steel, micro-cavity formation occurs when thermal energy transport plays a more dominant role. It was posited that dense plasma is formed from the intense irradiation energy that expands to etch the surrounding surface. The supporting evidence for this is that at higher atmospheric pressures the plasma is contained at the irradiation site resulting in deeper, larger holes with more flaring. Observation of micro-cavities in this context indicates the “strong” ablation regime where plasma ablation becomes more prevalent [361].

4.4.5 250 µm/s Scanning Speed

Ablation at 250 µm/s resulted in three surface morphologies not seen in other experiments (Figure 4.14). Despite the lower pulse energy, the chevron-like surface at 5 µJ is similar to the flat region at 10 µJ and 500 µm/s. This is largely attributed to the energy dose being equivalent. That is, the amount of laser energy irradiating the surface per pass is equivalent for 5 µJ at 250 µm/s and 10 µJ at 500 µm/s. Due to the lower peak fluence, the micro-cavities are smaller and their flares more regular. At 25 and 50 µJ, the 250 µm/s scan speed produces irregular surfaces with a high degree of nano-roughness. Similar structures are observed in [359] for high fluences.

4.4.6 Towards Engineered Surfaces

Across the five morphologies identified, the surface can be processed to significantly alter its geometry. Although it is outside the scope of this work to assess which properties can be modified and to what extent, the open literature holds clues as to the potential.

LIPSS have been used in many innovative ways. Ti-6Al-4V is a common medical implant material and it has been found that the topography of implants affects cellular response [343]. Sub-micron surface structures, as produced by ultrafast lasers, have the potential to improve implant osseointegration [348]. Alternatively, they can provide antibacterial properties [351]. The combination of selective laser melting technology with the production of LSFL LIPSS, as demonstrated here, may be able to provide a combined benefit for implant performance and procedure recovery rate. The transition between LIPSS and undulating grooves offers some control over the surface at this scale but it remains to be seen whether the difference in cellular proliferation – bacteria or osteoblasts – will be significant.

Ultrafast laser-induced patterns have been widely investigated for their effects on wettability [362]. Kirner et al. [302] produced regions on 42CrMo4 with different surface morphologies that, when combined, resulted in directional fluid transport. This demonstrates a micron-scale dependence for wettability but did not include a micro-cavity surface. Moradi et al. [347] found that micro-cavity regions were superhydrophobic, with water contact angles of 147° to 164° for 316 stainless steel. The five morphologies identified here will likely have similar differences in hydrophobicity/hydrophilicity, since the ordered features upon them range from sub-micron (LIPSS) to tens of microns (micro-cavities). Additional tunability within the morphologies may be possible. In particular, the micro-ripples and the micro-cavities display a strong dependence on the process parameters. Micro-ripple directionality is confirmed to be controlled by the laser scanning direction. Unidirectional scanning would produce a rippled structure without the herringbone pattern. Based on the formation mechanism, the horizontal periodicity can be altered by the line spacing, and the vertical periodicity can be altered by the scanning speed. Micro-cavity density and uniformity can be controlled by the number of laser passes. In these ways the wettability and surface roughness have the potential to be tuned.

4.5 Conclusion

Several distinct surface morphologies were obtained on the 3D-printed Ti-6Al-4V surface via femtosecond laser ablation and elucidated. Type 1 LSFL, undulating grooves, micro-ripples, grooves, and micro-cavities were produced. Despite a roughness that can cause fluence variations up to 24%, homogeneity of the surface patterns generated on this ultra-rough as-printed surface indicates that the morphologies can be formed on conventionally hard-to-process 3D-printed structures. Ultrafast laser surface micro- and nano- patterning of SLM surfaces with a high sintered powder density and without additionally surface treatment has been demonstrated. Overall, the range of process parameters in this initial study was quite limited. To fully understand the transitions between ablation mechanisms and thus between morphologies, additional experimentation on the SAP is required. Mechanisms behind pattern formation could be further investigated or otherwise confirmed by ablation of reference samples such as conventionally manufactured Ti-6Al-4V or polished SLM Ti-6Al-4V. Testing of the wettability of the morphologies via water contact angle measurements will provide more insight into the potential applications of these methods.

Chapter 5: Summary and Conclusions

5.1 Summary

In this work, many aspects of ultrafast laser manufacturing were discussed. Additive manufacturing, surface modification, and ultrafast laser architectures were addressed in the context of rapidly evolving technologies in an effort to shed light on the future of ultrafast lasers.

First, the contribution of ultrafast lasers to the field of additive manufacturing was reviewed. Ultrafast lasers, also referred to as ultrashort pulse lasers, generate pulses of <10 picoseconds duration. At these short timescales, light interacts with matter in unique ways. Initially utilised for probing matter on subatomic timescales to explore underlying physical phenomena and, when amplified, for ablation of materials with minimal collateral damage, ultrafast lasers have grown to inhabit a niche in additive manufacturing. By delivering intense energy gradients to electronic subsystems, hard-to-process metals and ceramics are superheated past their melting point at comparatively low average energies and in a confined volume. Bandgap materials undergo multiphoton absorption and avalanche ionisation. These phenomena are leveraged for powder-bed fusion, multiphoton lithography, laser-induced forward transfer, pulsed laser deposition, and welding technologies. Powder-bed fusion of copper, tungsten, glass, aluminum alloys, polyethylene, bimetallics, rhenium, and hafnium diboride has been achieved via ultrafast laser. These processes require less average power than conventional powder-bed fusion, but so far research is limited to feasibility and proof-of-concept studies. Multiphoton lithography, a method by which photoinitiators begin a polymerisation reaction under nonlinear absorption of an ultrafast laser source, enables true geometric freedom in the additive manufacturing of materials such as resins, organically modified ceramics, and even metal. Sub-diffraction limited structures are manufactured for a variety of purposes from tissue scaffolding to nano-optics. Laser-induced forward transfer is a simple method for deposition of micro- and nano-scale droplets. Virtually any material can be ejected via focused ultrafast pulses from a thin layer attached to a donor substrate to be deposited on a receiving substrate below, and with greater precision that for longer pulsed lasers. High aspect ratio micropillars, nano-droplets, and other 3D structures can be produced. Thin films of metals, semiconductors, polymers, and biomaterials may be stoichiometrically deposited with smoother features compared to nanosecond lasers. Glass-glass, glass-metal, and ceramic-ceramic welding is enabled by ultrashort pulse lasers. Nonlinear absorption allows weld beads to be formed inside of materials with limited heat-affected zones. These additive manufacturing techniques are exciting for industrial applications, but they face many challenges when it comes to their adoption. While process errors and failures may be acceptable – even expected – in academia, the associated costs in industry are not. Ensuring build quality of an additive manufacturing process is nontrivial since internal features are not normally visible. In-process monitoring can provide quality control, and experimental monitoring provides information regarding the physics of the manufacturing processes. Methods for multiphoton *in-situ* monitoring have been demonstrated but each have respective limitations. As a commercial technology, MPL will face increasing pressure to develop these methods. LIFT

ejection dynamics are examined via time-resolved shadowgraphy. Increased throughput will greatly improve the attractiveness of these technologies. To this end, galvanometric scanners, microlens arrays, and digital micromirror devices all increase the rate of laser processing. As the individual technologies continue to develop, their hybridisation is an exciting prospect. Since ultrafast lasers can additionally be used for subtractive manufacturing, and each of the AM technologies rely on ultrafast laser sources, it is possible for a single laser source or beam delivery setup to be used for multiple manufacturing methods in the same device. For example, microfluidic devices can be femtosecond laser etched, microscopic structures can be constructed inside via MPL, and they can be welded together all with a single laser source. A versatile, all-in-one laser fabrication device would be of great benefit to many industries, and ultrafast lasers present many of these features.

In Chapter 3, the architecture and setup of an ultrafast Ti:Sapphire laser system and an Yb-doped fiber laser system were discussed. Their ease of use and maintenance considerations were compared. It was found that the Ti:Sapphire system is more complex in its setup, operation, and troubleshooting. While the fiber system had difficulties in start-up due to a poorly controlled laboratory environment, it functions more effectively as a "black box" system. For the purposes of micromachining, Ti:Sapphire systems provide a wider range of possible pulse energies, while the fiber laser offers a wider range of possible repetition rates, both of which can be exploited for unique laser-material interactions. In the case of the experiments performed in Chapter 4, the higher possible pulse energy of the Ti:Sapphire system was exploited.

Finally, Chapter 4 presented femtosecond ablation of SLM Ti-6Al-4V using the Ti:Sapphire system discussed in Chapter 3. The surface as-printed was analysed and the surface area modified for 1, 5, 10, 25, and 50 µJ pulse energies, 2000 µm/s, 500 µm/s, and 250 µm/s, with 3 laser passes and 6 laser passes also performed at 2000 and 500 µm/s. The average areal surface roughness of the SAP was measured to be 26.2 µm, with many points deviating from the mean up to 50 µm. Consequently, the fluence across the surface varies significantly. Five main surface morphologies were identified and discussed in the context of their feasibility to provide surface pattern tuning: LIPSS, undulating grooves, micro-ripples, grooves, and micro-cavities. LIPSS were categorised as LSFL Type 1 according to their periodicity ~λ. Undulating grooves formed from LIPSS with an increase in the effective number of pulses. Micro-ripples, composed of crater rims from individual pulses were observed and their directionality controlled. Micro-cavities form readily at pulse energies above 10 µJ at slow (~500 µm/s) scanning speeds. Their shape and distribution vary slight with the process parameters, which may offer additional potential for surface control. Areas for future work were outlined in the conclusion.

5.2 Conclusions

Many conclusions have been drawn in this work, since many technologies, processes, devices, and applications were discussed. Development of ultrafast laser additive manufacturing techniques is ongoing. While there are many exciting applications, it is a common pitfall to

believe that some new manufacturing process will supplant or otherwise revolutionise a field. Ultrafast laser powder-bed fusion, laser-induced forward transfer, and welding are poised to fill specific manufacturing niches in which conventional methods may fall short. This may be in the form of processing the most stubborn of materials or the manufacturing of fragile micro-interconnects between microdevices. On the other hand, multiphoton lithography is a burgeoning commercial industry. Studies on process monitoring and increased throughput have increased steadily, but our understanding of the fundamental processes needs to be improved. With better understanding of the individual methods, hybridisation such as that for ultrashort pulse ablation, welding, and multiphoton lithography has appeared. Commercial laser systems will need to support this growth. Based on the conclusions from Chapter 3, it is predicted that fiber lasers will become the ultrashort pulse machining workhorses that drive this progress. Ti:Sapphire systems will remain relevant in the realm of micromachining. Indeed, their utility was demonstrated in this work. With the elucidation of ultrafast laser patterning of an as-printed SLM surface, this dissertation contributes to the wider body of knowledge of SLM post-processing. This surface structuring may provide functionalization of 3D-printed parts by altering the wettability, adhesivity, and biocompatibility. The micrometre and nanometre level of control over the surface geometry further suggests advantages in micro and nanofabrication. More research is required to determine the exact benefits these methods bring to additive manufacturing. At the very least, it is another tool in the toolbox.

References

[1] M. v. Shugaev *et al.*, "Fundamentals of ultrafast laser–material interaction," *MRS Bull*, vol. 41, no. 12, pp. 960–968, Dec. 2016, doi: 10.1557/MRS.2016.274.

[2] L. Kaden, G. Matthäus, R. Ramm, T. Ullsperger, B. Seyfarth, and S. Nolte, "Additive manufacturing of pure copper using ultrashort laser pulses," *https://doi.org/10.1117/12.2507401*, vol. 10909, pp. 49–55, Mar. 2019, doi: 10.1117/12.2507401.

[3] L. Kaden, B. Seyfarth, T. Ullsperger, G. Matthäus, and S. Nolte, "Selective laser melting of copper using ultrashort laser pulses at different wavelengths," in *Laser 3D Manufacturing V*, Feb. 2018, p. 41. doi: 10.1117/12.2289959.

[4] B. Nie, L. Yang, H. Huang, S. Bai, P. Wan, and J. Liu, "Femtosecond laser additive manufacturing of iron and tungsten parts," *Appl Phys A Mater Sci Process*, vol. 119, no. 3, pp. 1075–1080, Jun. 2015, doi: 10.1007/S00339-015-9070-Y/FIGURES/8.

[5] S. Bai *et al.*, "Femtosecond fiber laser additive manufacturing of tungsten," *https://doi.org/10.1117/12.2217551*, vol. 9738, pp. 96–105, Apr. 2016, doi: 10.1117/12.2217551.

[6] B. Seyfarth, G. Matthäus, T. Ullsperger, S. Nolte, L. Schade, and A. Tunnermann, "Selective laser melting of borosilicate glass using ultrashort laser pulses," *https://doi.org/10.1117/12.2289614*, vol. 10523, pp. 52–57, Feb. 2018, doi: 10.1117/12.2289614.

[7] T. Ullsperger *et al.*, "Ultra-short pulsed laser powder bed fusion of Al-Si alloys: Impact of pulse duration and energy in comparison to continuous wave excitation," *Addit Manuf*, vol. 46, p. 102085, Oct. 2021, doi: 10.1016/j.addma.2021.102085.

[8] T. Ullsperger *et al.*, "Selective laser melting of hypereutectic Al-Si40-powder using ultra-short laser pulses," *Appl Phys A Mater Sci Process*, vol. 123, no. 12, pp. 1–6, Dec. 2017, doi: 10.1007/S00339-017-1337-Z/FIGURES/8.

[9] X. Zhou, Y. Hou, and J. Lin, "A review on the processing accuracy of two-photon polymerization," *AIP Adv*, vol. 5, no. 3, p. 030701, Mar. 2015, doi: 10.1063/1.4916886.

[10] S. Kawata, H. B. Sun, T. Tanaka, and K. Takada, "Finer features for functional microdevices," *Nature 2001 412:6848*, vol. 412, no. 6848, pp. 697–698, Aug. 2001, doi: 10.1038/35089130.

[11] J. Fischer and M. Wegener, "Three-dimensional optical laser lithography beyond the diffraction limit," *Laser Photon Rev*, vol. 7, no. 1, pp. 22–44, Jan. 2013, doi: 10.1002/LPOR.201100046.

[12] G. Flamourakis *et al.*, "Laser-made 3D Auxetic Metamaterial Scaffolds for Tissue Engineering Applications," *Macromol Mater Eng*, vol. 305, no. 7, p. 2000238, Jul. 2020, doi: 10.1002/MAME.202000238.

[13] Z. He *et al.*, "3D printed fiber sockets for plug and play micro-optics," *International Journal of Extreme Manufacturing*, vol. 3, no. 1, p. 015301, Nov. 2020, doi: 10.1088/2631-7990/ABC674.

[14] D. J. Freppon, H. E. Williams, M. A. Melino, R. C. Rumpf, and S. M. Kuebler, "Fabrication of three-dimensional micro-photonic structures on the tip of optical fibers using SU-8," *Optics*

Express, Vol. 19, Issue 23, pp. 22910-22922, vol. 19, no. 23, pp. 22910–22922, Nov. 2011, doi: 10.1364/OE.19.022910.

[15] A. Vyatskikh, S. Delalande, A. Kudo, X. Zhang, C. M. Portela, and J. R. Greer, "Additive manufacturing of 3D nano-architected metals," *Nature Communications 2018 9:1*, vol. 9, no. 1, pp. 1–8, Feb. 2018, doi: 10.1038/s41467-018-03071-9.

[16] A. Piqué and K. M. Charipar, "Laser-Induced Forward Transfer Applications in Micro-engineering," *Handbook of Laser Micro- and Nano-Engineering*, pp. 1325–1359, 2021, doi: 10.1007/978-3-030-63647-0_26.

[17] C. W. Visser, R. Pohl, C. Sun, G. W. Römer, B. Huis In 'T Veld, and D. Lohse, "Toward 3D Printing of Pure Metals by Laser-Induced Forward Transfer," *Advanced Materials*, vol. 27, no. 27, pp. 4087–4092, Jul. 2015, doi: 10.1002/ADMA.201501058.

[18] M. Feinaeugle, R. Pohl, T. Bor, T. Vaneker, and G. Römer, "Printing of complex free-standing microstructures via laser-induced forward transfer (LIFT) of pure metal thin films," *Addit Manuf*, vol. 24, pp. 391–399, Dec. 2018, doi: 10.1016/j.addma.2018.09.028.

[19] Q. Li, D. Grojo, A.-P. Alloncle, and P. Delaporte, "Dynamics of double-pulse laser printing of copper microstructures," *Appl Surf Sci*, vol. 471, pp. 627–632, Mar. 2019, doi: 10.1016/j.apsusc.2018.12.052.

[20] B. Liu, Z. Hu, Y. Che, A. Allenic, K. Sun, and X. Pan, "Growth of ZnO nanoparticles and nanorods with ultrafast pulsed laser deposition," *Appl Phys A Mater Sci Process*, vol. 93, no. 3, pp. 813–818, Nov. 2008, doi: 10.1007/S00339-008-4754-1.

[21] S. Richter, S. Nolte, and A. Tünnermann, "Ultrashort Pulse Laser Welding - A New Approach for High- Stability Bonding of Different Glasses," *Phys Procedia*, vol. 39, pp. 556–562, Jan. 2012, doi: 10.1016/j.phpro.2012.10.073.

[22] S. Richter *et al.*, "Ultrashort pulse laser welding of glasses without optical contacting," *https://doi.org/10.1117/12.2250389*, vol. 10094, pp. 118–125, Feb. 2017, doi: 10.1117/12.2250389.

[23] O. P. Ciuca, R. M. Carter, P. B. Prangnell, and D. P. Hand, "Characterisation of weld zone reactions in dissimilar glass-to-aluminium pulsed picosecond laser welds," *Mater Charact*, vol. 120, pp. 53–62, Oct. 2016, doi: 10.1016/j.matchar.2016.08.013.

[24] T. Baldacchini and R. Zadoyan, "In situ and real time monitoring of two-photon polymerization using broadband coherent anti-Stokes Raman scattering microscopy," *Optics Express, Vol. 18, Issue 18, pp. 19219-19231*, vol. 18, no. 18, pp. 19219–19231, Aug. 2010, doi: 10.1364/OE.18.019219.

[25] E. Yulianto, S. Chatterjee, V. Purlys, and V. Mizeikis, "Imaging of latent three-dimensional exposure patterns created by direct laser writing in photoresists," *Appl Surf Sci*, vol. 479, pp. 822–827, Jun. 2019, doi: 10.1016/j.apsusc.2019.02.033.

[26] L. Kallioniemi, S. Annurakshita, and G. Bautista, "Third-harmonic generation microscopy of undeveloped photopolymerized structures," *OSA Continuum, Vol. 3, Issue 11, pp. 2961-2967*, vol. 3, no. 11, pp. 2961–2967, Nov. 2020, doi: 10.1364/OSAC.405126.

[27] R. Pohl, C. W. Visser, G. W. Römer, D. Lohse, C. Sun, and B. Huis in 'T Veld, "Ejection regimes in picosecond laser-induced forward transfer of metals," *Phys Rev Appl*, vol. 3, no. 2, p. 024001, Feb. 2015, doi: 10.1103/PHYSREVAPPLIED.3.024001/FIGURES/7/MEDIUM.

[28] A.-P. Alloncle, D. Grojo, P. Delaporte, and Q. Li, "Jetting regimes of double-pulse laser-induced forward transfer," *Optical Materials Express, Vol. 9, Issue 8, pp. 3476-3486*, vol. 9, no. 8, pp. 3476–3486, Aug. 2019, doi: 10.1364/OME.9.003476.

[29] M. Sanz, M. Castillejo, S. Amoruso, G. Ausanio, R. Bruzzese, and X. Wang, "Ultra-fast laser ablation and deposition of TiO2," *Applied Physics A 2010 101:4*, vol. 101, no. 4, pp. 639–644, Jul. 2010, doi: 10.1007/S00339-010-5916-5.

[30] S. Amoruso *et al.*, "Structural characterization of nanoparticles-assembled titanium dioxide films produced by ultrafast laser ablation and deposition in background oxygen," *Appl Surf Sci*, vol. 270, pp. 307–311, Apr. 2013, doi: 10.1016/j.apsusc.2013.01.021.

[31] A. Nguyen, A. Koroleva, B. N. Chichkov, K. Obata, R. J. Narayan, and S. D. Gittard, "Fabrication of microscale medical devices by two-photon polymerization with multiple foci via a spatial light modulator," *Biomedical Optics Express, Vol. 2, Issue 11, pp. 3167-3178*, vol. 2, no. 11, pp. 3167–3178, Nov. 2011, doi: 10.1364/BOE.2.003167.

[32] S. K. Saha, D. Wang, V. H. Nguyen, Y. Chang, J. S. Oakdale, and S. C. Chen, "Scalable submicrometer additive manufacturing," *Science (1979)*, vol. 366, no. 6461, pp. 105–109, Oct. 2019, doi: 10.1126/SCIENCE.AAX8760/SUPPL_FILE/AAX8760S1.MP4.

[33] Q. Geng, D. Wang, P. Chen, and S. C. Chen, "Ultrafast multi-focus 3-D nano-fabrication based on two-photon polymerization," *Nature Communications 2019 10:1*, vol. 10, no. 1, pp. 1–7, May 2019, doi: 10.1038/s41467-019-10249-2.

[34] R. C. Y. Auyeung, H. Kim, N. A. Charipar, A. J. Birnbaum, S. A. Mathews, and A. Piqué, "Laser forward transfer based on a spatial light modulator," *Applied Physics A 2010 102:1*, vol. 102, no. 1, pp. 21–26, Oct. 2010, doi: 10.1007/S00339-010-6054-9.

[35] Y. Nakata *et al.*, "Nanodot array deposition via single shot laser interference pattern using laser-induced forward transfer," *International Journal of Extreme Manufacturing*, vol. 2, no. 2, p. 025101, May 2020, doi: 10.1088/2631-7990/AB88BF.

[36] D. Wu, S. Z. Wu, J. Xu, L. G. Niu, K. Midorikawa, and K. Sugioka, "Hybrid femtosecond laser microfabrication to achieve true 3D glass/polymer composite biochips with multiscale features and high performance: the concept of ship-in-a-bottle biochip," *Laser Photon Rev*, vol. 8, no. 3, pp. 458–467, May 2014, doi: 10.1002/LPOR.201400005.

[37] L. Jonušauskas *et al.*, "Hybrid subtractive-additive-welding microfabrication for lab-on-chip applications via single amplified femtosecond laser source," *Optical Engineering*, vol. 56, no. 09, p. 1, Sep. 2017, doi: 10.1117/1.OE.56.9.094108/.

[38] A. Ovsianikov *et al.*, "Laser printing of cells into 3D scaffolds," *Biofabrication*, vol. 2, no. 1, p. 014104, Mar. 2010, doi: 10.1088/1758-5082/2/1/014104.

[39] X. Wang, J. Zhang, X. Mei, B. Xu, and J. Miao, "Laser fabrication of fully printed graphene oxide microsensor," *Opt Lasers Eng*, vol. 140, p. 106520, May 2021, doi: 10.1016/j.optlaseng.2020.106520.

[40] M.-W. Pan, R. E. Benner, and L. M. Smith, "Continuous Lasers for Raman Spectrometry," in *Handbook of Vibrational Spectroscopy*, John Wiley & Sons, Ltd, 2006. doi: 10.1002/0470027320.S0403.

[41] F. Aljekhedab, "Enhancement of Cortical Bone Ablation Using Ultrafast Pulsed Lasers," McMaster University, Hamilton, 2019.

[42] S. K. Sundaram and E. Mazur, "Inducing and probing non-thermal transitions in semiconductors using femtosecond laser pulses," *Nature Materials 2002 1:4*, vol. 1, no. 4, pp. 217–224, 2002, doi: 10.1038/nmat767.

[43] B. Nie, H. Huang, S. Bai, and J. Liu, "Femtosecond laser melting and resolidifying of high-temperature powder materials," *Appl Phys A Mater Sci Process*, vol. 118, no. 1, pp. 37–41, Jan. 2015, doi: 10.1007/S00339-014-8897-Y/FIGURES/6.

[44] M. E. Fermann and I. Hartl, "Ultrafast fibre lasers," *Nature Photonics 2013 7:11*, vol. 7, no. 11, pp. 868–874, Oct. 2013, doi: 10.1038/nphoton.2013.280.

[45] S. Liu and Y. C. Shin, "Additive manufacturing of Ti6Al4V alloy: A review," *Mater Des*, vol. 164, p. 107552, Feb. 2019, doi: 10.1016/J.MATDES.2018.107552.

[46] W. S. Gora *et al.*, "Enhancing Surface Finish of Additively Manufactured Titanium and Cobalt Chrome Elements Using Laser Based Finishing," *Phys Procedia*, vol. 83, pp. 258–263, Jan. 2016, doi: 10.1016/J.PHPRO.2016.08.021.

[47] J. Bonse, S. v. Kirner, and J. Krüger, "Laser-Induced Periodic Surface Structures (LIPSS)," *Handbook of Laser Micro- and Nano-Engineering*, pp. 879–936, 2021, doi: 10.1007/978-3-030-63647-0_17.

[48] I. Mingareev *et al.*, "Femtosecond laser post-processing of metal parts produced by laser additive manufacturing," *J Laser Appl*, vol. 25, no. 5, p. 052009, Oct. 2013, doi: 10.2351/1.4824146.

[49] N. Worts, J. Jones, and J. Squier, "Surface structure modification of additively manufactured titanium components via femtosecond laser micromachining," *Opt Commun*, vol. 430, pp. 352–357, Jan. 2019, doi: 10.1016/J.OPTCOM.2018.08.055.

[50] S. H. Huang, P. Liu, A. Mokasdar, and L. Hou, "Additive manufacturing and its societal impact: a literature review," *The International Journal of Advanced Manufacturing Technology 2012 67:5*, vol. 67, no. 5, pp. 1191–1203, Oct. 2012, doi: 10.1007/S00170-012-4558-5.

[51] M. Javaid, A. Haleem, R. P. Singh, R. Suman, and S. Rab, "Role of additive manufacturing applications towards environmental sustainability," *Advanced Industrial and Engineering Polymer Research*, vol. 4, no. 4, pp. 312–322, Oct. 2021, doi: 10.1016/J.AIEPR.2021.07.005.

[52] D. Herzog, V. Seyda, E. Wycisk, and C. Emmelmann, "Additive manufacturing of metals," *Acta Mater*, vol. 117, pp. 371–392, Sep. 2016, doi: 10.1016/J.ACTAMAT.2016.07.019.

[53] T. H. Maiman, "Stimulated Optical Radiation in Ruby," *Nature 1960 187:4736*, vol. 187, no. 4736, pp. 493–494, 1960, doi: 10.1038/187493a0.

[54] "NobelPrize.org." https://www.nobelprize.org/prizes/physics/ (accessed Sep. 16, 2022).

[55] F. J. McClung and R. W. Hellwarth, "Giant Optical Pulsations from Ruby," *J Appl Phys*, vol. 33, no. 3, p. 828, Jun. 1962, doi: 10.1063/1.1777174.

[56] K. Kuhn, *Laser engineering*. 1997.

[57] D. J. Ottaway *et al.*, "Short-pulse actively Q-switched Er:YAG lasers," *Optics Express, Vol. 24, Issue 14, pp. 15341-15350*, vol. 24, no. 14, pp. 15341–15350, Jul. 2016, doi: 10.1364/OE.24.015341.

[58] C. Rullière, *Femtosecond laser pulses : principles and experiments*. 2013. Accessed: Mar. 08, 2022. [Online]. Available: https://books.google.com/books/about/Femtosecond_Laser_Pulses.html?id=3RbpCAAAQBAJ

[59] A. Penzkofer, "Passive Q-switching and mode-locking for the generation of nanosecond to femtosecond pulses," *Applied Physics B Photophysics and Laser Chemistry*, vol. 46, no. 1, pp. 43–60, May 1988, doi: 10.1007/BF00698653.

[60] D. H. Sutter *et al.*, "Self-starting 6.5-fs pulses from a Ti:sapphire laser using a semiconductor saturable absorber and double-chirped mirrors," *IEEE Journal on Selected Topics in Quantum Electronics*, vol. 4, no. 2, pp. 169–177, Mar. 1998, doi: 10.1109/2944.686720.

[61] L. E. Hargrove, R. L. Fork, and M. A. Pollack, "LOCKING OF He–Ne LASER MODES INDUCED BY SYNCHRONOUS INTRACAVITY MODULATION," *Appl Phys Lett*, vol. 5, no. 1, p. 4, Nov. 2004, doi: 10.1063/1.1754025.

[62] A. J. Demaria, D. A. Stetser, and H. Heynau, "SELF MODE-LOCKING OF LASERS WITH SATURABLE ABSORBERS," *Appl Phys Lett*, vol. 8, no. 7, p. 174, Nov. 2004, doi: 10.1063/1.1754541.

[63] P. M. W. French, "The generation of ultrashort laser pulses," *Reports on Progress in Physics*, vol. 58, no. 2, p. 169, Feb. 1995, doi: 10.1088/0034-4885/58/2/001.

[64] W. Sibbett, A. A. Lagatsky, C. T. A Brown, D. E. Spence, and P. N. Kean, "The development and application of femtosecond laser systems," *Optics Express, Vol. 20, Issue 7, pp. 6989-7001*, vol. 20, no. 7, pp. 6989–7001, Mar. 2012, doi: 10.1364/OE.20.006989.

[65] U. Keller, "Ultrafast solid-state laser oscillators: a success story for the last 20 years with no end in sight," *Applied Physics B*, vol. 100, no. 1, pp. 15–28, Jul. 2010, doi: 10.1007/s00340-010-4045-3.

[66] D. J. Kuizenga and A. E. Siegman, "FM and AM Mode Locking of the Homogeneous Laser—Part Ii: Experimental Results in a Nd: YAG Laser with Internal FM Modulation," *IEEE J Quantum Electron*, vol. 6, no. 11, pp. 709–715, 1970, doi: 10.1109/JQE.1970.1076344.

[67] C. v. Shank and E. P. Ippen, "Subpicosecond kilowatt pulses from a mode-locked cw dye laser," *Appl Phys Lett*, vol. 24, no. 8, p. 373, Oct. 2003, doi: 10.1063/1.1655222.

[68] P. F. Moulton, "Spectroscopic and laser characteristics of Ti:Al_2O_3," *JOSA B, Vol. 3, Issue 1, pp. 125-133*, vol. 3, no. 1, pp. 125–133, Jan. 1986, doi: 10.1364/JOSAB.3.000125.

[69] D. E. Spence, P. N. Kean, and W. Sibbett, "60-fsec pulse generation from a self-mode-locked Ti:sapphire laser," *Optics Letters, Vol. 16, Issue 1, pp. 42-44*, vol. 16, no. 1, pp. 42–44, Jan. 1991, doi: 10.1364/OL.16.000042.

[70] H. C. Kapteyn and M. M. Murnane, "FEMTOSECOND LASERS: THE NEXT GENERATION," *Optics and Photonics News, Vol. 5, Issue 3, pp. 20-*, vol. 5, no. 3, pp. 20-, Mar. 1994, doi: 10.1364/OPN.5.3.000020.

[71] M. Piché, "Beam reshaping and self-mode-locking in nonlinear laser resonators," *Opt Commun*, vol. 86, no. 2, pp. 156–160, Nov. 1991, doi: 10.1016/0030-4018(91)90552-O.

[72] C. C. Davis, "Lasers and electro-optics, second edition," *Lasers and Electro-Optics, Second Edition*, vol. 9780521860291, pp. 1–867, Jan. 2013, doi: 10.1017/CBO9781139016629.

[73] U. Keller *et al.*, "Semiconductor saturable absorber mirrors (SESAM's) for femtosecond to nanosecond pulse generation in solid-state lasers," *IEEE Journal of Selected Topics in Quantum Electronics*, vol. 2, no. 3, pp. 435–453, Sep. 1996, doi: 10.1109/2944.571743.

[74] M. D. Perry and G. Mourou, "Terawatt to Petawatt Subpicosecond Lasers," *Science (1979)*, vol. 264, no. 5161, pp. 917–924, May 1994, doi: 10.1126/SCIENCE.264.5161.917.

[75] D. Strickland and G. Mourou, "Compression of amplified chirped optical pulses," *Opt Commun*, vol. 56, no. 3, pp. 219–221, Dec. 1985, doi: 10.1016/0030-4018(85)90120-8.

[76] G. Sargsjan, U. Stamm, C. Unger, W. Zschocke, and M. Ledig, "Characteristics of a neodymium-doped fiber laser mode-locked with a linear external cavity," *Opt Commun*, vol. 86, no. 6, pp. 480–486, Dec. 1991, doi: 10.1016/0030-4018(91)90149-8.

[77] M. E. Fermann, M. Hofer, F. Haberl, and S. P. Craig-Ryan, "Femtosecond Fibre Laser," *Electron Lett*, vol. 26, no. 20, pp. 1737–1738, 1990, doi: 10.1049/EL:19901109.

[78] M. N. Zervas and C. A. Codemard, "High power fiber lasers: A review," *IEEE Journal on Selected Topics in Quantum Electronics*, vol. 20, no. 5, 2014, doi: 10.1109/JSTQE.2014.2321279.

[79] G. Chang and Z. Wei, "Ultrafast Fiber Lasers: An Expanding Versatile Toolbox," *iScience*, vol. 23, no. 5, p. 101101, May 2020, doi: 10.1016/J.ISCI.2020.101101.

[80] S.-S. Wellershoff, J. Hohlfeld, J. Güdde, and E. Matthias, "The role of electron–phonon coupling in femtosecond laser damage of metals," *Applied Physics A 1999 69:1*, vol. 69, no. 1, pp. S99–S107, Dec. 1999, doi: 10.1007/S003399900305.

[81] B. N. Chichkov, C. Momma, S. Nolte, F. von Alvensleben, and A. Tünnermann, "Femtosecond, picosecond and nanosecond laser ablation of solids," *Applied Physics A 1996 63:2*, vol. 63, no. 2, pp. 109–115, 1996, doi: 10.1007/BF01567637.

[82] C. Wu, M. S. Christensen, J. M. Savolainen, P. Balling, and L. v. Zhigilei, "Generation of subsurface voids and a nanocrystalline surface layer in femtosecond laser irradiation of a single-crystal Ag target," *Phys Rev B Condens Matter Mater Phys*, vol. 91, no. 3, p. 035413, Jan. 2015, doi: 10.1103/PHYSREVB.91.035413/FIGURES/9/MEDIUM.

[83] D. S. Ivanov and L. v. Zhigilei, "Effect of Pressure Relaxation on the Mechanisms of Short-Pulse Laser Melting," *Phys Rev Lett*, vol. 91, no. 10, p. 105701, Sep. 2003, doi: 10.1103/PHYSREVLETT.91.105701/FIGURES/3/MEDIUM.

[84] M. v. Shugaev *et al.*, "Fundamentals of ultrafast laser–material interaction," *MRS Bull*, vol. 41, no. 12, pp. 960–968, Dec. 2016, doi: 10.1557/MRS.2016.274.

[85] B. Rethfeld, K. Sokolowski-Tinten, D. von der Linde, and S. I. Anisimov, "Ultrafast thermal melting of laser-excited solids by homogeneous nucleation," *Phys Rev B*, vol. 65, no. 9, p. 092103, Feb. 2002, doi: 10.1103/PhysRevB.65.092103.

[86] J. Cheng *et al.*, "A review of ultrafast laser materials micromachining," *Opt Laser Technol*, vol. 46, no. 1, pp. 88–102, Mar. 2013, doi: 10.1016/j.optlastec.2012.06.037.

[87] I. H. Chowdhury and X. Xu, "HEAT TRANSFER IN FEMTOSECOND LASER PROCESSING OF METAL," *http://dx.doi.org/10.1080/716100504*, vol. 44, no. 3, pp. 219–232, 2011, doi: 10.1080/716100504.

[88] S. Anisimov, B. L. Kapeliovich, and T. Perelman, "Electron emission from metal surfaces exposed to ultrashort laser pulses," *Journal of Experimental and Theoretical Physics*, vol. 39, no. 2, pp. 375–377, 1974, Accessed: Mar. 10, 2022. [Online]. Available: https://www.semanticscholar.org/paper/Electron-emission-from-metal-surfaces-exposed-to-Anisimov-Kapeliovich/1676b0b4ded724bd383c863a365743df1eb32937

[89] R. F. , J. Haglund, "Photophysics and Photochemistry of Ultrafast Laser Materials Processing," in *3D Laser Microfabrication*, Wiley-VCH, 2006, pp. 139–179.

[90] L. J. Lewis and D. Perez, "Laser ablation with short and ultrashort laser pulses: Basic mechanisms from molecular-dynamics simulations," *Appl Surf Sci*, vol. 255, no. 10, pp. 5101–5106, Mar. 2009, doi: 10.1016/j.apsusc.2008.07.116.

[91] K. H. Leitz, B. Redlingshöer, Y. Reg, A. Otto, and M. Schmidt, "Metal Ablation with Short and Ultrashort Laser Pulses," *Phys Procedia*, vol. 12, no. PART 2, pp. 230–238, Jan. 2011, doi: 10.1016/J.PHPRO.2011.03.128.

[92] J. Bonse, S. Hohm, S. v. Kirner, A. Rosenfeld, and J. Kruger, "Laser-Induced Periodic Surface Structures-A Scientific Evergreen," *IEEE Journal of Selected Topics in Quantum Electronics*, vol. 23, no. 3, pp. 109–123, May 2017, doi: 10.1109/JSTQE.2016.2614183.

[93] Z. Lin and L. v. Zhigilei, "Time-resolved diffraction profiles and atomic dynamics in short-pulse laser-induced structural transformations: Molecular dynamics study," *Phys Rev B Condens Matter Mater Phys*, vol. 73, no. 18, p. 184113, May 2006, doi: 10.1103/PHYSREVB.73.184113/FIGURES/12/MEDIUM.

[94] B. Rethfeld, K. Sokolowski-Tinten, D. von der Linde, and S. I. Anisimov, "Ultrafast thermal melting of laser-excited solids by homogeneous nucleation," *Phys Rev B*, vol. 65, no. 9, p. 092103, Feb. 2002, doi: 10.1103/PhysRevB.65.092103.

[95] M. Z. Mo *et al.*, "Heterogeneous to homogeneous melting transition visualized with ultrafast electron diffraction," *Science (1979)*, vol. 360, no. 6396, pp. 1451–1455, Jun. 2018, doi: 10.1126/SCIENCE.AAR2058.

[96] B. Stuart, M. Feit, S. Herman, A. Rubenchik, B. Shore, and M. Perry, "Nanosecond-to-femtosecond laser-induced breakdown in dielectrics," *Phys Rev B*, vol. 53, no. 4, p. 1749, Jan. 1996, doi: 10.1103/PhysRevB.53.1749.

[97] A. Rousse *et al.*, "Non-thermal melting in semiconductors measured at femtosecond resolution," *Nature 2001 410:6824*, vol. 410, no. 6824, pp. 65–68, Mar. 2001, doi: 10.1038/35065045.

[98] J. Graves and R. Allen, "Response of GaAs to fast intense laser pulses," *Phys Rev B*, vol. 58, no. 20, p. 13627, Nov. 1998, doi: 10.1103/PhysRevB.58.13627.

[99] R. Stoian, D. Ashkenasi, A. Rosenfeld, and E. E. B. Campbell, "Coulomb explosion in ultrashort pulsed laser ablation of Al2O3," *Phys Rev B*, vol. 62, no. 19, p. 13167, Nov. 2000, doi: 10.1103/PhysRevB.62.13167.

[100] N. M. Bulgakova, R. Stoian, A. Rosenfeld, I. v. Hertel, and E. E. B. Campbell, "Electronic transport and consequences for material removal in ultrafast pulsed laser ablation of materials," *Phys Rev B*, vol. 69, no. 5, p. 054102, Feb. 2004, doi: 10.1103/PhysRevB.69.054102.

[101] S. S. Mao *et al.*, "Dynamics of femtosecond laser interactions with dielectrics," *Applied Physics A 2004 79:7*, vol. 79, no. 7, pp. 1695–1709, Nov. 2004, doi: 10.1007/S00339-004-2684-0.

[102] L. v Keldysh, "IONIZATION IN THE FIELD OF A STRONG ELECTROMAGNETIC WAVE," *J. Exptl. Theoret. Phys. (U.S.S.R.)*, vol. 20, no. 5, pp. 1945–1957, 1965.

[103] N. Bloembergen, "Laser Induced Electric Breakdown in Solids," *IEEE J Quantum Electron*, vol. 10, no. 3, pp. 375–386, 1974, doi: 10.1109/JQE.1974.1068132.

[104] S. Lei *et al.*, "Ultrafast Laser Applications in Manufacturing Processes: A State-of-the-Art Review," *Journal of Manufacturing Science and Engineering, Transactions of the ASME*, vol. 142, no. 3, Mar. 2020, doi: 10.1115/1.4045969.

[105] M. Lenzner, F. Krausz, J. Krüger, and W. Kautek, "Photoablation with sub-10 fs laser pulses," *Appl Surf Sci*, vol. 154–155, pp. 11–16, Feb. 2000, doi: 10.1016/S0169-4332(99)00432-8.

[106] J. Yang, Y. Zhao, N. Zhang, Y. Liang, and M. Wang, "Ablation of metallic targets by high-intensity ultrashort laser pulses," *Phys Rev B Condens Matter Mater Phys*, vol. 76, no. 16, p. 165430, Oct. 2007, doi: 10.1103/PHYSREVB.76.165430/FIGURES/11/MEDIUM.

[107] N. Bärsch, K. Körber, A. Ostendorf, and K. H. Tönshoff, "Ablation and cutting of planar silicon devices using femtosecond laser pulses," *Applied Physics A 2003 77:2*, vol. 77, no. 2, pp. 237–242, 2003, doi: 10.1007/S00339-003-2118-4.

[108] S. Nikumb *et al.*, "Precision glass machining, drilling and profile cutting by short pulse lasers," *Thin Solid Films*, vol. 477, no. 1–2, pp. 216–221, Apr. 2005, doi: 10.1016/J.TSF.2004.08.136.

[109] F. Aljekhedab, W. Zhang, H. K. Haugen, G. R. Wohl, M. M. El-Desouki, and Q. Fang, "Influence of environmental conditions in bovine bone ablation by ultrafast laser," *J Biophotonics*, vol. 12, no. 6, p. e201800293, Jun. 2019, doi: 10.1002/JBIO.201800293.

[110] L. Bayer, X. Ye, P. Lorenz, and K. Zimmer, "Studies on perovskite film ablation and scribing with ns-, ps- and fs-laser pulses," *Appl Phys A Mater Sci Process*, vol. 123, no. 10, pp. 1–8, Oct. 2017, doi: 10.1007/S00339-017-1234-5/FIGURES/10.

[111] C. Shan, F. Chen, Q. Yang, Z. Jiang, and X. Hou, "3D Multi-Microchannel Helical Mixer Fabricated by Femtosecond Laser inside Fused Silica," *Micromachines (Basel)*, vol. 9, no. 1, Jan. 2018, doi: 10.3390/MI9010029.

[112] B. Pecholt, M. Vendan, Y. Dong, and P. Molian, "Ultrafast laser micromachining of 3C-SiC thin films for MEMS device fabrication," *The International Journal of Advanced Manufacturing Technology 2007 39:3*, vol. 39, no. 3, pp. 239–250, Sep. 2007, doi: 10.1007/S00170-007-1223-5.

[113] T. A. Labutin, V. N. Lednev, A. A. Ilyin, and A. M. Popov, "Femtosecond laser-induced breakdown spectroscopy," *J Anal At Spectrom*, vol. 31, no. 1, pp. 90–118, Dec. 2015, doi: 10.1039/C5JA00301F.

[114] C. L. Li, C. J. Fisher, R. Burke, and S. Andersson-Engels, "Orthopedics-Related Applications of Ultrafast Laser and Its Recent Advances," *Applied Sciences 2022, Vol. 12, Page 3957*, vol. 12, no. 8, p. 3957, Apr. 2022, doi: 10.3390/APP12083957.

[115] J. P. Colombier, P. Combis, F. Bonneau, R. le Harzic, and E. Audouard, "Hydrodynamic simulations of metal ablation by femtosecond laser irradiation," *Phys Rev B Condens Matter Mater Phys*, vol. 71, no. 16, p. 165406, Apr. 2005, doi: 10.1103/PHYSREVB.71.165406/FIGURES/7/MEDIUM.

[116] C. Wu and L. v. Zhigilei, "Microscopic mechanisms of laser spallation and ablation of metal targets from large-scale molecular dynamics simulations," *Appl Phys A Mater Sci Process*, vol. 114, no. 1, pp. 11–32, Jan. 2014, doi: 10.1007/S00339-013-8086-4/FIGURES/9.

[117] L. Orazi, L. Romoli, M. Schmidt, and L. Li, "Ultrafast laser manufacturing: from physics to industrial applications," *CIRP Annals*, vol. 70, no. 2, pp. 543–566, Jan. 2021, doi: 10.1016/J.CIRP.2021.05.007.

[118] E. T. Karim, Z. Lin, and L. v. Zhigilei, "Molecular dynamics study of femtosecond laser interactions with Cr targets," *AIP Conf Proc*, vol. 1464, no. 1, p. 280, Jul. 2012, doi: 10.1063/1.4739881.

[119] B. J. Garrison, T. E. Itina, and L. v. Zhigilei, "Limit of overheating and the threshold behavior in laser ablation," *Phys Rev E*, vol. 68, no. 4, p. 041501, Oct. 2003, doi: 10.1103/PhysRevE.68.041501.

[120] B. Rethfeld, D. S. Ivanov, M. E. Garcia, and S. I. Anisimov, "Modelling ultrafast laser ablation," *J Phys D Appl Phys*, vol. 50, no. 19, p. 193001, Apr. 2017, doi: 10.1088/1361-6463/50/19/193001.

[121] T. D. Ngo, A. Kashani, G. Imbalzano, K. T. Q. Nguyen, and D. Hui, "Additive manufacturing (3D printing): A review of materials, methods, applications and challenges," *Compos B Eng*, vol. 143, pp. 172–196, Jun. 2018, doi: 10.1016/j.compositesb.2018.02.012.

[122] S. H. Huang, P. Liu, A. Mokasdar, and L. Hou, "Additive manufacturing and its societal impact: a literature review," *The International Journal of Advanced Manufacturing Technology 2012 67:5*, vol. 67, no. 5, pp. 1191–1203, Oct. 2012, doi: 10.1007/S00170-012-4558-5.

[123] H. Lee, C. H. J. Lim, M. J. Low, N. Tham, V. M. Murukeshan, and Y.-J. Kim, "Lasers in additive manufacturing: A review," *International Journal of Precision Engineering and Manufacturing-Green Technology*, vol. 4, no. 3, pp. 307–322, Jul. 2017, doi: 10.1007/s40684-017-0037-7.

[124] D. Herzog, V. Seyda, E. Wycisk, and C. Emmelmann, "Additive manufacturing of metals," *Acta Mater*, vol. 117, pp. 371–392, Sep. 2016, doi: 10.1016/j.actamat.2016.07.019.

[125] T. DebRoy *et al.*, "Additive manufacturing of metallic components – Process, structure and properties," *Prog Mater Sci*, vol. 92, pp. 112–224, Mar. 2018, doi: 10.1016/j.pmatsci.2017.10.001.

[126] O. Abdulhameed, A. Al-Ahmari, W. Ameen, and S. H. Mian, "Additive manufacturing: Challenges, trends, and applications:," *https://doi.org/10.1177/1687814018822880*, vol. 11, no. 2, pp. 1–27, Feb. 2019, doi: 10.1177/1687814018822880.

[127] I. A. Polozov, E. v. Borisov, V. S. Sufiiarov, and A. A. Popovich, "Selective laser melting of copper alloy," *Физика и механика материалов*, vol. 74, no. 1, pp. 65–71, 2020, doi: 10.18720/MPM.4312020_8.

[128] D. A. Ramirez *et al.*, "Open-cellular copper structures fabricated by additive manufacturing using electron beam melting," *Materials Science and Engineering: A*, vol. 528, no. 16–17, pp. 5379–5386, Jun. 2011, doi: 10.1016/J.MSEA.2011.03.053.

[129] R. Neugebauer, B. Mller, M. Gebauer, and T. Tppel, "Additive manufacturing boosts efficiency of heat transfer components," *Assembly Automation*, vol. 31, no. 4, pp. 344–347, 2011, doi: 10.1108/01445151111172925/FULL/XML.

[130] T. Q. Tran *et al.*, "3D Printing of Highly Pure Copper," *Metals 2019, Vol. 9, Page 756*, vol. 9, no. 7, p. 756, Jul. 2019, doi: 10.3390/MET9070756.

[131] S. D. Jadhav, P. P. Dhekne, S. Dadbakhsh, J. P. Kruth, J. van Humbeeck, and K. Vanmeensel, "Surface Modified Copper Alloy Powder for Reliable Laser-based Additive Manufacturing," *Addit Manuf*, vol. 35, p. 101418, Oct. 2020, doi: 10.1016/J.ADDMA.2020.101418.

[132] M. Roccetti Campagnoli, M. Galati, and A. Saboori, "On the processability of copper components via powder-based additive manufacturing processes: Potentials, challenges and feasible solutions," *J Manuf Process*, vol. 72, pp. 320–337, Dec. 2021, doi: 10.1016/J.JMAPRO.2021.10.038.

[133] T. I. El-Wardany, Y. She, V. N. Jagdale, J. K. Garofano, J. J. Liou, and W. R. Schmidt, "Challenges in Three-Dimensional Printing of High-Conductivity Copper," *Journal of Electronic Packaging, Transactions of the ASME*, vol. 140, no. 2, Jun. 2018, doi: 10.1115/1.4039974/368005.

[134] S. Wünscher, R. Abbel, J. Perelaer, and U. S. Schubert, "Progress of alternative sintering approaches of inkjet-printed metal inks and their application for manufacturing of flexible electronic devices," *J Mater Chem C Mater*, vol. 2, no. 48, pp. 10232–10261, Nov. 2014, doi: 10.1039/C4TC01820F.

[135] C. W. Cheng and J. K. Chen, "Femtosecond laser sintering of copper nanoparticles," *Appl Phys A Mater Sci Process*, vol. 122, no. 4, pp. 1–8, Apr. 2016, doi: 10.1007/S00339-016-9814-3/FIGURES/6.

[136] S. Arakane, M. Mizoshiri, and S. Hata, "Direct patterning of Cu microstructures using femtosecond laser-induced CuO nanoparticle reduction," *Jpn J Appl Phys*, vol. 54, no. 6, Jun. 2015, doi: 10.7567/JJAP.54.06FP07.

[137] M. M and H. S, "Direct Writing of Cu-based Micro-temperature Sensors onto Glass and Poly(dimethylsiloxane) Substrates Using Femtosecond Laser Reductive Patterning of CuO Nanoparticles," *Research & Reviews: Journal of Material Sciences*, vol. 4, no. 4, pp. 47–54, 2016, doi: 10.4172/2321-6212.1000155.

[138] M. Mizoshiri and K. Yoshidomi, "Cu Patterning Using Femtosecond Laser Reductive Sintering of CuO Nanoparticles under Inert Gas Injection," *Materials (Basel)*, vol. 14, no. 12, Jun. 2021, doi: 10.3390/MA14123285.

[139] N. K. Roy *et al.*, "A comprehensive study of the sintering of copper nanoparticles using femtosecond, nanosecond, and continuous wave lasers," *J Micro Nanomanuf*, vol. 6, no. 1, pp. 1–21, Mar. 2018, doi: 10.1115/1.4038455/368902.

[140] N. K. Roy, D. Behera, O. G. Dibua, C. S. Foong, and M. A. Cullinan, "A novel microscale selective laser sintering (μ-SLS) process for the fabrication of microelectronic parts," *Microsystems & Nanoengineering 2019 5:1*, vol. 5, no. 1, pp. 1–14, Dec. 2019, doi: 10.1038/s41378-019-0116-8.

[141] P. Tolias, "Analytical expressions for thermophysical properties of solid and liquid tungsten relevant for fusion applications," *Nuclear Materials and Energy*, vol. 13, pp. 42–57, Dec. 2017, doi: 10.1016/J.NME.2017.08.002.

[142] J. Xie, H. Lu, J. Lu, X. Song, S. Wu, and J. Lei, "Additive manufacturing of tungsten using directed energy deposition for potential nuclear fusion application," *Surf Coat Technol*, vol. 409, p. 126884, Mar. 2021, doi: 10.1016/J.SURFCOAT.2021.126884.

[143] A. v. Müller *et al.*, "Additive manufacturing of pure tungsten by means of selective laser beam melting with substrate preheating temperatures up to 1000 ∘C," *Nuclear Materials and Energy*, vol. 19, pp. 184–188, May 2019, doi: 10.1016/J.NME.2019.02.034.

[144] X. Zhou, X. Liu, D. Zhang, Z. Shen, and W. Liu, "Balling phenomena in selective laser melted tungsten," *J Mater Process Technol*, vol. 222, pp. 33–42, Aug. 2015, doi: 10.1016/J.JMATPROTEC.2015.02.032.

[145] D. Liu *et al.*, "Microstructural aspects of additive manufacturing of AlLi alloys with high Li content," *Mater Des*, vol. 198, p. 109323, Jan. 2021, doi: 10.1016/J.MATDES.2020.109323.

[146] T. Ullsperger *et al.*, "Laser powder bed fusion of ultra-high molecular weight polyethylene (UHMWPE) using near-infrared ultrashort laser pulses," *Mater Des*, vol. 210, p. 110048, Nov. 2021, doi: 10.1016/J.MATDES.2021.110048.

[147] S. Bai and J. Liu, "Additive manufacturing of bimetallic structures," *SN Appl Sci*, vol. 2, no. 7, pp. 1–9, Jul. 2020, doi: 10.1007/S42452-020-2918-6/FIGURES/9.

[148] J. v. Crivello and E. Reichmanis, "Photopolymer materials and processes for advanced technologies," *Chemistry of Materials*, vol. 26, no. 1, pp. 533–548, Jan. 2014, doi: 10.1021/CM402262G/ASSET/IMAGES/MEDIUM/CM-2013-02262G_0025.GIF.

[149] C. N. LaFratta, J. T. Fourkas, T. Baldacchini, and R. A. Farrer, "Multiphoton Fabrication," *Angewandte Chemie International Edition*, vol. 46, no. 33, pp. 6238–6258, Aug. 2007, doi: 10.1002/ANIE.200603995.

[150] M. Malinauskas, M. Farsari, A. Piskarskas, and S. Juodkazis, "Ultrafast laser nanostructuring of photopolymers: A decade of advances," *Phys Rep*, vol. 533, no. 1, pp. 1–31, Dec. 2013, doi: 10.1016/J.PHYSREP.2013.07.005.

[151] V. Harinarayana and Y. C. Shin, "Two-photon lithography for three-dimensional fabrication in micro/nanoscale regime: A comprehensive review," *Opt Laser Technol*, vol. 142, p. 107180, Oct. 2021, doi: 10.1016/J.OPTLASTEC.2021.107180.

[152] A. Selimis, V. Mironov, and M. Farsari, "Direct laser writing: Principles and materials for scaffold 3D printing," *Microelectron Eng*, vol. 132, pp. 83–89, Jan. 2015, doi: 10.1016/J.MEE.2014.10.001.

[153] V. F. Paz *et al.*, "Development of functional sub-100 nm structures with 3D two-photon polymerization technique and optical methods for characterization," *J Laser Appl*, vol. 24, no. 4, p. 042004, Jul. 2012, doi: 10.2351/1.4712151.

[154] M. He, Z. Zhang, C. Cao, G. Zhou, C. Kuang, and X. Liu, "3D Sub-Diffraction Printing by Multicolor Photoinhibition Lithography: From Optics to Chemistry," *Laser Photon Rev*, vol. 16, no. 2, p. 2100229, Feb. 2022, doi: 10.1002/LPOR.202100229.

[155] J. Wichmann and S. W. Hell, "Breaking the diffraction resolution limit by stimulated emission: stimulated-emission-depletion fluorescence microscopy," *Optics Letters, Vol. 19, Issue 11, pp. 780-782*, vol. 19, no. 11, pp. 780–782, Jun. 1994, doi: 10.1364/OL.19.000780.

[156] T. F. Scott, B. A. Kowalski, A. C. Sullivan, C. N. Bowman, and R. R. McLeod, "Two-color single-photon photoinitiation and photoinhibition for subdiffraction photolithography," *Science (1979)*, vol. 324, no. 5929, pp. 913–917, May 2009, doi: 10.1126/SCIENCE.1167610/SUPPL_FILE/SCOTT.SOM.PDF.

[157] N. Li, R. R. Gattass, E. Gershgoren, H. Hwang, and J. T. Fourkas, "Achieving 1/20 resolution by one-color initiation and deactivation of polymerization," *Science (1979)*, vol. 324, no. 5929, pp. 910–913, May 2009, doi: 10.1126/SCIENCE.1168996/SUPPL_FILE/LI_SOM.PDF.

[158] A. Ovsianikov, B. Chichkov, P. Mente, N. A. Monteiro-Riviere, A. Doraiswamy, and R. J. Narayan, "Two Photon Polymerization of Polymer–Ceramic Hybrid Materials for Transdermal Drug Delivery," *Int J Appl Ceram Technol*, vol. 4, no. 1, pp. 22–29, Jan. 2007, doi: 10.1111/J.1744-7402.2007.02115.X.

[159] H. Jeon, H. Hidai, D. J. Hwang, and C. P. Grigoropoulos, "Fabrication of arbitrary polymer patterns for cell study by two-photon polymerization process," *J Biomed Mater Res A*, vol. 93A, no. 1, pp. 56–66, Apr. 2010, doi: 10.1002/JBM.A.32517.

[160] S. Juodkazis, V. Mizeikis, K. K. Seet, M. Miwa, and H. Misawa, "Two-photon lithography of nanorods in SU-8 photoresist," *Nanotechnology*, vol. 16, no. 6, p. 846, Apr. 2005, doi: 10.1088/0957-4484/16/6/039.

[161] I. Sakellari *et al.*, "Two-photon polymerization of titanium-containing sol–gel composites for three-dimensional structure fabrication," *Applied Physics A 2010 100:2*, vol. 100, no. 2, pp. 359–364, Jul. 2010, doi: 10.1007/S00339-010-5864-0.

[162] X. M. Duan, H. B. Sun, K. Kaneko, and S. Kawata, "Two-photon polymerization of metal ions doped acrylate monomers and oligomers for three-dimensional structure fabrication," *Thin Solid Films*, vol. 453–454, pp. 518–521, Apr. 2004, doi: 10.1016/J.TSF.2003.11.126.

[163] T. Baldacchini *et al.*, "Acrylic-based resin with favorable properties for three-dimensional two-photon polymerization," *J Appl Phys*, vol. 95, no. 11, p. 6072, May 2004, doi: 10.1063/1.1728296.

[164] D. Paipulas *et al.*, "Combination of additive and subtractive laser 3D microprocessing in hybrid glass/polymer microsystems for chemical sensing applications," *Optics Express, Vol. 25, Issue 21, pp. 26280-26288*, vol. 25, no. 21, pp. 26280–26288, Oct. 2017, doi: 10.1364/OE.25.026280.

[165] G. Kumi, C. O. Yanez, K. D. Belfield, and J. T. Fourkas, "High-speed multiphoton absorption polymerization: fabrication of microfluidic channels with arbitrary cross-sections and high aspect ratios," *Lab Chip*, vol. 10, no. 8, pp. 1057–1060, Apr. 2010, doi: 10.1039/B923377F.

[166] L. Amato, Y. Gu, N. Bellini, S. M. Eaton, G. Cerullo, and R. Osellame, "Integrated three-dimensional filter separates nanoscale from microscale elements in a microfluidic chip," *Lab Chip*, vol. 12, no. 6, pp. 1135–1142, Feb. 2012, doi: 10.1039/C2LC21116E.

[167] A. Takaura, S. Maruo, and Y. Saito, "Optically driven micropump with a twin spiral microrotor," *Optics Express, Vol. 17, Issue 21, pp. 18525-18532*, vol. 17, no. 21, pp. 18525–18532, Oct. 2009, doi: 10.1364/OE.17.018525.

[168] A. Ovsianikov, B. Chichkov, P. Mente, N. A. Monteiro-Riviere, A. Doraiswamy, and R. J. Narayan, "Two Photon Polymerization of Polymer–Ceramic Hybrid Materials for Transdermal Drug Delivery," *Int J Appl Ceram Technol*, vol. 4, no. 1, pp. 22–29, Jan. 2007, doi: 10.1111/J.1744-7402.2007.02115.X.

[169] S. D. Gittard *et al.*, "Fabrication of Polymer Microneedles Using a Two-Photon Polymerization and Micromolding Process," *https://doi.org/10.1177/193229680900300211*, vol. 3, no. 2, pp. 304–311, Mar. 2009, doi: 10.1177/193229680900300211.

[170] M. M. Nava *et al.*, "Synthetic niche substrates engineered via two-photon laser polymerization for the expansion of human mesenchymal stromal cells," *J Tissue Eng Regen Med*, vol. 11, no. 10, pp. 2836–2845, Oct. 2017, doi: 10.1002/TERM.2187.

[171] J. Mačiulaitis *et al.*, "Preclinical study of SZ2080 material 3D microstructured scaffolds for cartilage tissue engineering made by femtosecond direct laser writing lithography," *Biofabrication*, vol. 7, no. 1, p. 015015, Mar. 2015, doi: 10.1088/1758-5090/7/1/015015.

[172] B. Dhandayuthapani, Y. Yoshida, T. Maekawa, and D. S. Kumar, "Polymeric scaffolds in tissue engineering application: A review," *Int J Polym Sci*, vol. 2011, 2011, doi: 10.1155/2011/290602.

[173] J. Torgersen, X. H. Qin, Z. Li, A. Ovsianikov, R. Liska, and J. Stampfl, "Hydrogels for Two-Photon Polymerization: A Toolbox for Mimicking the Extracellular Matrix," *Adv Funct Mater*, vol. 23, no. 36, pp. 4542–4554, Sep. 2013, doi: 10.1002/ADFM.201203880.

[174] J. Maciulaitis *et al.*, "Customization of direct laser lithography-based 3D scaffolds for optimized in vivo outcome," *Appl Surf Sci*, vol. 487, pp. 692–702, Sep. 2019, doi: 10.1016/J.APSUSC.2019.05.065.

[175] P. Timashev *et al.*, "Novel biodegradable star-shaped polylactide scaffolds for bone regeneration fabricated by two-photon polymerization," *Nanomedicine (Lond)*, vol. 11, no. 9, pp. 1041–1053, May 2016, doi: 10.2217/NNM-2015-0022.

[176] F. Klein *et al.*, "Two-Component Polymer Scaffolds for Controlled Three-Dimensional Cell Culture," *Advanced Materials*, vol. 23, no. 11, pp. 1341–1345, Mar. 2011, doi: 10.1002/ADMA.201004060.

[177] B. Richter *et al.*, "Guiding Cell Attachment in 3D Microscaffolds Selectively Functionalized with Two Distinct Adhesion Proteins," *Advanced Materials*, vol. 29, no. 5, p. 1604342, Feb. 2017, doi: 10.1002/ADMA.201604342.

[178] Q. Sun, S. Juodkazis, N. Murazawa, V. Mizeikis, and H. Misawa, "Freestanding and movable photonic microstructures fabricated by photopolymerization with femtosecond laser pulses," *Journal of Micromechanics and Microengineering*, vol. 20, no. 3, p. 035004, Feb. 2010, doi: 10.1088/0960-1317/20/3/035004.

[179] G. Cojoc *et al.*, "Optical micro-structures fabricated on top of optical fibers by means of two-photon photopolymerization," *Microelectron Eng*, vol. 87, no. 5–8, pp. 876–879, May 2010, doi: 10.1016/J.MEE.2009.12.046.

[180] M. Malinauskas, H. Gilbergs, A. Ukauskas, V. Purlys, D. Paipulas, and R. Gadonas, "A femtosecond laser-induced two-photon photopolymerization technique for structuring microlenses," *Journal of Optics*, vol. 12, no. 3, p. 035204, Feb. 2010, doi: 10.1088/2040-8978/12/3/035204.

[181] J. Li *et al.*, "Two-photon polymerisation 3D printed freeform micro-optics for optical coherence tomography fibre probes," *Scientific Reports 2018 8:1*, vol. 8, no. 1, pp. 1–9, Oct. 2018, doi: 10.1038/s41598-018-32407-0.

[182] P. I. Dietrich *et al.*, "In situ 3D nanoprinting of free-form coupling elements for hybrid photonic integration," *Nature Photonics 2018 12:4*, vol. 12, no. 4, pp. 241–247, Mar. 2018, doi: 10.1038/s41566-018-0133-4.

[183] T. Gissibl, S. Thiele, A. Herkommer, and H. Giessen, "Two-photon direct laser writing of ultracompact multi-lens objectives," *Nature Photonics 2016 10:8*, vol. 10, no. 8, pp. 554–560, Jun. 2016, doi: 10.1038/nphoton.2016.121.

[184] T. Gissibl, S. Thiele, A. Herkommer, and H. Giessen, "Sub-micrometre accurate free-form optics by three-dimensional printing on single-mode fibres," *Nature Communications 2016 7:1*, vol. 7, no. 1, pp. 1–9, Jun. 2016, doi: 10.1038/ncomms11763.

[185] C. R. Ocier *et al.*, "Direct laser writing of volumetric gradient index lenses and waveguides," *Light: Science & Applications 2020 9:1*, vol. 9, no. 1, pp. 1–14, Dec. 2020, doi: 10.1038/s41377-020-00431-3.

[186] M. Vaezi, H. Seitz, and S. Yang, "A review on 3D micro-additive manufacturing technologies," *The International Journal of Advanced Manufacturing Technology 2012 67:5*, vol. 67, no. 5, pp. 1721–1754, Nov. 2012, doi: 10.1007/S00170-012-4605-2.

[187] E. H. Waller, S. Dix, J. Gutsche, A. Widera, and G. von Freymann, "Functional Metallic Microcomponents via Liquid-Phase Multiphoton Direct Laser Writing: A Review," *Micromachines 2019, Vol. 10, Page 827*, vol. 10, no. 12, p. 827, Nov. 2019, doi: 10.3390/MI10120827.

[188] E. H. Waller and G. von Freymann, "From photoinduced electron transfer to 3D metal microstructures via direct laser writing," *Nanophotonics*, vol. 7, no. 7, pp. 1259–1277, Jun. 2018, doi: 10.1515/NANOPH-2017-0134/ASSET/GRAPHIC/J_NANOPH-2017-0134_FIG_008.JPG.

[189] Z. C. Ma, Y. L. Zhang, B. Han, Q. D. Chen, and H. B. Sun, "Femtosecond-Laser Direct Writing of Metallic Micro/Nanostructures: From Fabrication Strategies to Future Applications," *Small Methods*, vol. 2, no. 7, p. 1700413, Jul. 2018, doi: 10.1002/SMTD.201700413.

[190] N. Takeyasu, T. Tanaka, and S. Kawata, "Fabrication of 3D metal/polymer microstructures by site-selective metal coating," *Applied Physics A 2007 90:2*, vol. 90, no. 2, pp. 205–209, Oct. 2007, doi: 10.1007/S00339-007-4298-9.

[191] A. Radke, T. Gissibl, T. Klotzbücher, P. v. Braun, and H. Giessen, "Three-Dimensional Bichiral Plasmonic Crystals Fabricated by Direct Laser Writing and Electroless Silver Plating," *Advanced Materials*, vol. 23, no. 27, pp. 3018–3021, Jul. 2011, doi: 10.1002/ADMA.201100543.

[192] A. Ishikawa, F. Formanek, K. Chiyoda, N. Takeyasu, S. Kawata, and T. Tanaka, "Three-dimensional fabrication of metallic nanostructures over large areas by two-photon polymerization," *Optics Express, Vol. 14, Issue 2, pp. 800-809*, vol. 14, no. 2, pp. 800–809, Jan. 2006, doi: 10.1364/OPEX.14.000800.

[193] R. A. Farrer *et al.*, "Selective functionalization of 3-D polymer microstructures," *J Am Chem Soc*, vol. 128, no. 6, pp. 1796–1797, Feb. 2006, doi: 10.1021/JA0583620/ASSET/IMAGES/MEDIUM/JA0583620N00001.GIF.

[194] X. Wendy Gu and J. R. Greer, "Ultra-strong architected Cu meso-lattices," *Extreme Mech Lett*, vol. 2, no. 1, pp. 7–14, Mar. 2015, doi: 10.1016/J.EML.2015.01.006.

[195] J. K. Gansel *et al.*, "Gold helix photonic metamaterial as broadband circular polarizer," *Science (1979)*, vol. 325, no. 5947, pp. 1513–1515, Sep. 2009, doi: 10.1126/SCIENCE.1177031/SUPPL_FILE/GANSEL.SOM.PDF.

[196] A.-C. Pons *et al.*, "Multiphoton laser direct writing of two-dimensional silver structures," *Optics Express, Vol. 13, Issue 4, pp. 1275-1280*, vol. 13, no. 4, pp. 1275–1280, Feb. 2005, doi: 10.1364/OPEX.13.001275.

[197] T. Tanaka, A. Ishikawa, and S. Kawata, "Two-photon-induced reduction of metal ions for fabricating three-dimensional electrically conductive metallic microstructure," *Appl Phys Lett*, vol. 88, no. 8, p. 081107, Feb. 2006, doi: 10.1063/1.2177636.

[198] S. Maruo and T. Saeki, "Femtosecond laser direct writing of metallic microstructures by photoreduction of silver nitrate in a polymer matrix," *Optics Express, Vol. 16, Issue 2, pp. 1174-1179*, vol. 16, no. 2, pp. 1174–1179, Jan. 2008, doi: 10.1364/OE.16.001174.

[199] A. Takami *et al.*, "Femtosecond laser direct writing of metal microstructure in a stretchable poly(ethylene glycol) diacrylate (PEGDA) hydrogel," *Optics Letters, Vol. 41, Issue 7, pp. 1392-1395*, vol. 41, no. 7, pp. 1392–1395, Apr. 2016, doi: 10.1364/OL.41.001392.

[200] R. Ameloot *et al.*, "Metal–Organic Framework Single Crystals as Photoactive Matrices for the Generation of Metallic Microstructures," *Advanced Materials*, vol. 23, no. 15, pp. 1788–1791, Apr. 2011, doi: 10.1002/ADMA.201100063.

[201] E. Blasco *et al.*, "Fabrication of Conductive 3D Gold-Containing Microstructures via Direct Laser Writing," *Advanced Materials*, vol. 28, no. 18, pp. 3592–3595, May 2016, doi: 10.1002/ADMA.201506126.

[202] C. B. Arnold, P. Serra, and A. Piqué, "Laser Direct-Write Techniques for Printing of Complex Materials," *MRS Bull*, vol. 32, no. 1, pp. 23–31, 2007, doi: 10.1557/MRS2007.11.

[203] A. Piqué, R. C. Y. Auyeung, H. Kim, N. A. Charipar, and S. A. Mathews, "Laser 3D micro-manufacturing," *J Phys D Appl Phys*, vol. 49, no. 22, p. 223001, May 2016, doi: 10.1088/0022-3727/49/22/223001.

[204] A.-P. Alloncle, R. Bouffaron, J. Hermann, M. Sentis Anne-Patricia Alloncle, M. Sentis, and J. Hermann, "Laser-induced forward transfer of 40 nm Chromium film using ultrashort laser pulses," *https://doi.org/10.1117/12.677445*, vol. 6263, no. 31, pp. 205–210, May 2006, doi: 10.1117/12.677445.

[205] S. Bera *et al.*, "Optimization study of the femtosecond laser-induced forward-transfer process with thin aluminum films," *Applied Optics, Vol. 46, Issue 21, pp. 4650-4659*, vol. 46, no. 21, pp. 4650–4659, Jul. 2007, doi: 10.1364/AO.46.004650.

[206] J. Mikšys, G. Arutinov, and G. R. B. E. Römer, "Pico- to nanosecond pulsed laser-induced forward transfer (LIFT) of silver nanoparticle inks: a comparative study," *Appl Phys A Mater Sci Process*, vol. 125, no. 12, pp. 1–11, Dec. 2019, doi: 10.1007/S00339-019-3085-8/FIGURES/11.

[207] C. Grivas, D. P. Banks, I. Zergioti, and W. E. Robert, "Ballistic laser-assisted solid transfer (BLAST) from a thin film precursor," *Optics Express, Vol. 16, Issue 5, pp. 3249-3254*, vol. 16, no. 5, pp. 3249–3254, Mar. 2008, doi: 10.1364/OE.16.003249.

[208] C. M. Othon, A. Laracuente, H. D. Ladouceur, and B. R. Ringeisen, "Sub-micron parallel laser direct-write," *Appl Surf Sci*, vol. 255, no. 5, pp. 3407–3413, Dec. 2008, doi: 10.1016/J.APSUSC.2008.09.058.

[209] A. Klini, A. Manousaki, C. Fotakis, D. Gray, and P. A. Loukakos, "Laser Induced Forward Transfer of metals by temporally shaped femtosecond laser pulses," *Optics Express, Vol. 16, Issue 15, pp. 11300-11309*, vol. 16, no. 15, pp. 11300–11309, Jul. 2008, doi: 10.1364/OE.16.011300.

[210] I. Zergioti *et al.*, "Microdeposition of metal and oxide structures using ultrashort laser pulses," *Applied Physics A 1998 66:5*, vol. 66, no. 5, pp. 579–582, 1998, doi: 10.1007/S003390050717.

[211] J. Zhang *et al.*, "Sacrificial-layer free transfer of mammalian cells using near infrared femtosecond laser pulses," *PLoS One*, vol. 13, no. 5, p. e0195479, May 2018, doi: 10.1371/JOURNAL.PONE.0195479.

[212] I. Zergioti, A. Karaiskou, D. G. Papazoglou, C. Fotakis, M. Kapsetaki, and D. Kafetzopoulos, "Femtosecond laser microprinting of biomaterials," *Appl Phys Lett*, vol. 86, no. 16, p. 163902, Apr. 2005, doi: 10.1063/1.1906325.

[213] I. Zergioti, D. G. Papazoglou, A. Karaiskou, C. Fotakis, E. Gamaly, and A. Rode, "A comparative schlieren imaging study between ns and sub-ps laser forward transfer of Cr," *Appl Surf Sci*, vol. 208–209, no. 1, pp. 177–180, Mar. 2003, doi: 10.1016/S0169-4332(02)01363-6.

[214] M. v. Shugaev and N. M. Bulgakova, "Thermodynamic and stress analysis of laser-induced forward transfer of metals," *Applied Physics A 2010 101:1*, vol. 101, no. 1, pp. 103–109, May 2010, doi: 10.1007/S00339-010-5767-0.

[215] A. I. Kuznetsov, B. N. Chichkov, and R. Kiyan, "Laser fabrication of 2D and 3D metal nanoparticle structures and arrays," *Optics Express, Vol. 18, Issue 20, pp. 21198-21203*, vol. 18, no. 20, pp. 21198–21203, Sep. 2010, doi: 10.1364/OE.18.021198.

[216] D. Munoz-martin, Y. Chen, M. Morales, and C. Molpeceres, "Overlapping Limitations for ps-Pulsed LIFT Printing of High Viscosity Metallic Pastes," *Metals 2020, Vol. 10, Page 168*, vol. 10, no. 2, p. 168, Jan. 2020, doi: 10.3390/MET10020168.

[217] Q. Guo, M. Wang, Z. Zhang Qitong Guo, and Z. Zhang, "The dynamics and deposition results of femtosecond laser-induced liquid film forward transfer," *https://doi.org/10.1117/12.2602410*, vol. 11885, pp. 65–70, Jun. 2021, doi: 10.1117/12.2602410.

[218] P. R. Willmott and J. R. Huber, "Pulsed laser vaporization and deposition," *Rev Mod Phys*, vol. 72, no. 1, p. 315, Jan. 2000, doi: 10.1103/RevModPhys.72.315.

[219] S. Fähler, M. Störmer, and H. U. Krebs, "Origin and avoidance of droplets during laser ablation of metals," *Appl Surf Sci*, vol. 109–110, pp. 433–436, Feb. 1997, doi: 10.1016/S0169-4332(96)00782-9.

[220] G. Perna, V. Capozzi, S. Pagliara, M. Ambrico, and D. Lojacono, "Reflectance and photoluminescence characterization of CdS and CdSe heteroepitaxial films deposited by laser ablation technique," *Thin Solid Films*, vol. 387, no. 1–2, pp. 208–211, May 2001, doi: 10.1016/S0040-6090(01)00793-3.

[221] D. B. Chrisey *et al.*, "Laser deposition of polymer and biomaterial films," *Chem Rev*, vol. 103, no. 2, pp. 553–576, Feb. 2003, doi: 10.1021/CR010428W.

[222] A. v. Rode, B. Luther-Davies, and E. G. Gamaly, "Ultrafast ablation with high-pulse-rate lasers. Part II: Experiments on laser deposition of amorphous carbon films," *J Appl Phys*, vol. 85, no. 8, p. 4222, Apr. 1999, doi: 10.1063/1.370334.

[223] E. G. Gamaly, A. v. Rode, and B. Luther-Davies, "Ultrafast Laser Ablation and Film Deposition," in *Pulsed Laser Deposition of Thin Films: Applications-Led Growth of Functional Materials*, John Wiley & Sons, Ltd, 2006, p. 118. doi: 10.1002/9780470052129.CH5.

[224] R. McCann, S. S. Roy, P. Papakonstantinou, J. A. McLaughlin, and S. C. Ray, "Spectroscopic analysis of a-C and a-CNx films prepared by ultrafast high repetition rate pulsed laser deposition," *J Appl Phys*, vol. 97, no. 7, p. 073522, Mar. 2005, doi: 10.1063/1.1874300.

[225] A. Zakery, A. v. Rode, B. Luther-Davies, M. Samoc, and Y. Ruan, "Low-loss waveguides in ultrafast laser-deposited As_2S_3 chalcogenide films," *JOSA B, Vol. 20, Issue 9, pp. 1844-1852*, vol. 20, no. 9, pp. 1844–1852, Sep. 2003, doi: 10.1364/JOSAB.20.001844.

[226] P. S. Banks *et al.*, "Short-pulse laser deposition of diamond-like carbon thin films," *Appl Phys A Mater Sci Process*, vol. 69, no. 7, 1999, doi: 10.1007/S003390051415.

[227] M. Okoshi, K. Higashikawa, and M. Hanabusa, "Pulsed laser deposition of ZnO thin films using a femtosecond laser," *Appl Surf Sci*, vol. 154–155, pp. 424–427, Feb. 2000, doi: 10.1016/S0169-4332(99)00392-X.

[228] J. Perrière *et al.*, "Comparison between ZnO films grown by femtosecond and nanosecond laser ablation," *J Appl Phys*, vol. 91, no. 2, p. 690, Dec. 2001, doi: 10.1063/1.1426250.

[229] E. Millon *et al.*, "Growth of heteroepitaxial ZnO thin films by femtosecond pulsed-laser deposition," *J Appl Phys*, vol. 88, no. 11, p. 6937, Nov. 2000, doi: 10.1063/1.1324679.

[230] M. Pervolaraki, P. Komninou, J. Kioseoglou, A. Othonos, and J. Giapintzakis, "Ultrafast pulsed laser deposition of carbon nanostructures: Structural and optical characterization," *Appl Surf Sci*, vol. 278, pp. 101–105, Aug. 2013, doi: 10.1016/J.APSUSC.2013.03.015.

[231] X. Chen and S. S. Mao, "Titanium dioxide nanomaterials: Synthesis, properties, modifications and applications," *Chem Rev*, vol. 107, no. 7, pp. 2891–2959, Jul. 2007, doi: 10.1021/CR0500535/ASSET/CR0500535.FP.PNG_V03.

[232] M. Murakami, B. Liu, Z. Hu, Z. Liu, Y. Uehara, and Y. Che, "Burst-mode femtosecond pulsed laser deposition for control of thin film morphology and material ablation," *Applied Physics Express*, vol. 2, no. 4, pp. 0425011–0425013, Apr. 2009, doi: 10.1143/APEX.2.042501/XML.

[233] Y. Inoue *et al.*, "Size control and luminescence properties of Eu2+:LiCaAlF6 particles prepared by femtosecond pulsed laser ablation," *J Appl Phys*, vol. 122, no. 13, p. 133107, Oct. 2017, doi: 10.1063/1.4996626.

[234] C. Maddi *et al.*, "Structural, Spectroscopic, and Excitonic Dynamic Characterization in Atomically Thin Yb3+-Doped MoS2, Fabricated by Femtosecond Pulsed Laser Deposition," *Adv Opt Mater*, vol. 7, no. 21, p. 1900753, Nov. 2019, doi: 10.1002/ADOM.201900753.

[235] T. Tamaki, W. Watanabe, J. Nishii, and K. Itoh, "Welding of transparent materials using femtosecond laser pulses," *Japanese Journal of Applied Physics, Part 2: Letters*, vol. 44, no. 20–23, p. L687, May 2005, doi: 10.1143/JJAP.44.L687/XML.

[236] K. Sugioka and Y. Cheng, "Femtosecond laser three-dimensional micro- and nanofabrication," *Appl Phys Rev*, vol. 1, no. 4, p. 041303, Dec. 2014, doi: 10.1063/1.4904320.

[237] H. Huang, L. M. Yang, and J. Liu, "Ultrashort pulsed fiber laser welding and sealing of transparent materials," *Applied Optics, Vol. 51, Issue 15, pp. 2979-2986*, vol. 51, no. 15, pp. 2979–2986, May 2012, doi: 10.1364/AO.51.002979.

[238] D. Hélie, M. Bégin, F. Lacroix, and R. Vallée, "Reinforced direct bonding of optical materials by femtosecond laser welding," *Applied Optics, Vol. 51, Issue 12, pp. 2098-2106*, vol. 51, no. 12, pp. 2098–2106, Apr. 2012, doi: 10.1364/AO.51.002098.

[239] S. Richter, S. Döring, A. Tünnermann, and S. Nolte, "Bonding of glass with femtosecond laser pulses at high repetition rates," *Applied Physics A 2011 103:2*, vol. 103, no. 2, pp. 257–261, Mar. 2011, doi: 10.1007/S00339-011-6369-1.

[240] I. Miyamoto, A. Horn, and J. Gottmann, "Local Melting of Glass Material and Its Application to Direct Fusion Welding by Ps-laser Pulses," *JLMN-Journal of Laser Micro/Nanoengineering*, vol. 2, no. 1, 2007, doi: 10.2961/jlmn.2007.01.0002.

[241] I. Miyamoto, A. Horn, J. Gottmann, D. Wortmann, and F. Yoshino, "Fusion welding of glass using femtosecond laser pulses with high-repetition rates," *Journal of Laser Micro Nanoengineering*, vol. 2, no. 1, pp. 57–63, Mar. 2007, doi: 10.2961/JLMN.2007.01.0011.

[242] H. Takai, K. Micorikawa, K. Sugioka, and M. Iida, "Efficient microwelding of glass substrates by ultrafast laser irradiation using a double-pulse train," *Optics Letters, Vol. 36, Issue 14, pp. 2734-2736*, vol. 36, no. 14, pp. 2734–2736, Jul. 2011, doi: 10.1364/OL.36.002734.

[243] D. Wu *et al.*, "Absorption mechanism of the second pulse in double-pulse femtosecond laser glass microwelding," *Optics Express, Vol. 21, Issue 20, pp. 24049-24059*, vol. 21, no. 20, pp. 24049–24059, Oct. 2013, doi: 10.1364/OE.21.024049.

[244] S. Richter, F. Zimmermann, S. Döring, A. Tünnermann, and S. Nolte, "Ultrashort high repetition rate exposure of dielectric materials: Laser bonding of glasses analyzed by micro-Raman spectroscopy," *Appl Phys A Mater Sci Process*, vol. 110, no. 1, pp. 9–15, Jan. 2013, doi: 10.1007/S00339-012-7478-1/FIGURES/7.

[245] W. Watanabe, S. Onda, T. Tamaki, K. Itoh, and J. Nishii, "Space-selective laser joining of dissimilar transparent materials using femtosecond laser pulses," *Appl Phys Lett*, vol. 89, no. 2, p. 021106, Jul. 2006, doi: 10.1063/1.2221393.

[246] D. Hélie, R. Vallée, and S. Gouin, "Assembling an endcap to optical fibers by femtosecond laser welding and milling," *Optical Materials Express, Vol. 3, Issue 10, pp. 1742-1754*, vol. 3, no. 10, pp. 1742–1754, Oct. 2013, doi: 10.1364/OME.3.001742.

[247] H. M. Shanshool *et al.*, "Parameters Affecting the Welding of Transparent Materials Using Femtosecond Laser Pulses," *Lasers in Manufacturing and Materials Processing*, vol. 7, no. 1, pp. 59–73, Mar. 2020, doi: 10.1007/S40516-019-00108-9/FIGURES/6.

[248] D. P. Hand, J. Chen, R. M. Carter, and R. R. Thomson, "Avoiding the requirement for pre-existing optical contact during picosecond laser glass-to-glass welding," *Optics Express, Vol. 23, Issue 14, pp. 18645-18657*, vol. 23, no. 14, pp. 18645–18657, Jul. 2015, doi: 10.1364/OE.23.018645.

[249] I. Miyamoto, K. Cvecek, and M. Schmidt, "Crack-free conditions in welding of glass by ultrashort laser pulse," *Optics Express, Vol. 21, Issue 12, pp. 14291-14302*, vol. 21, no. 12, pp. 14291–14302, Jun. 2013, doi: 10.1364/OE.21.014291.

[250] G. Cheng, G. Zhang, R. Stoian, and W. Zhao, "Femtosecond laser Bessel beam welding of transparent to non-transparent materials with large focal-position tolerant zone," *Optics Express, Vol. 26, Issue 2, pp. 917-926*, vol. 26, no. 2, pp. 917–926, Jan. 2018, doi: 10.1364/OE.26.000917.

[251] H. Chen, J. Duan, L. Deng, and X. Zeng, "Picosecond laser welding of glasses with a large gap by a rapid oscillating scan," *Optics Letters, Vol. 44, Issue 10, pp. 2570-2573*, vol. 44, no. 10, pp. 2570–2573, May 2019, doi: 10.1364/OL.44.002570.

[252] I. Alexeev, K. Cvecek, C. Schmidt, I. Miyamoto, T. Frick, and M. Schmidt, "Characterization of Shear Strength and Bonding Energy of Laser Pro- duced Welding Seams in Glass," *undefined*, vol. 7, no. 3, pp. 279–283, Nov. 2012, doi: 10.2961/JLMN.2012.03.0009.

[253] J. A. Fernie, R. A. L. Drew, and K. M. Knowles, "Joining of engineering ceramics," *http://dx.doi.org/10.1179/174328009X461078*, vol. 54, no. 5, pp. 283–331, Sep. 2013, doi: 10.1179/174328009X461078.

[254] E. H. Penilla *et al.*, "Ultrafast laser welding of ceramics," *Science (1979)*, vol. 365, no. 6455, pp. 803–808, Aug. 2019, doi: 10.1126/SCIENCE.AAW6699/SUPPL_FILE/AAW6699_PENILLA_SM.PDF.

[255] R. Carter *et al.*, "Picosecond laser welding of optical to metal components," *https://doi-org.libaccess.lib.mcmaster.ca/10.1117/12.2213227*, vol. 9736, pp. 244–253, Mar. 2016, doi: 10.1117/12.2213227.

[256] Y. Ozeki *et al.*, "Direct welding between copper and glass substrates with femtosecond laser pulses," *Applied Physics Express*, vol. 1, no. 8, pp. 0826011–0826013, Aug. 2008, doi: 10.1143/APEX.1.082601/XML.

[257] G. Zhang and G. Cheng, "Direct welding of glass and metal by 1 kHz femtosecond laser pulses," *Applied Optics, Vol. 54, Issue 30, pp. 8957-8961*, vol. 54, no. 30, pp. 8957–8961, Oct. 2015, doi: 10.1364/AO.54.008957.

[258] Y. Wang, Y. Li, S. Ao, Z. Luo, and D. Zhang, "Welding of 304 stainless steel and glass using high-repetition-frequency femtosecond laser," *Mater Res Express*, vol. 8, no. 10, p. 106523, Oct. 2021, doi: 10.1088/2053-1591/AC30B1.

[259] Q. Y. Lu and C. H. Wong, "Additive manufacturing process monitoring and control by non-destructive testing techniques: challenges and in-process monitoring," *https://doi.org/10.1080/17452759.2017.1351201*, vol. 13, no. 2, pp. 39–48, Apr. 2017, doi: 10.1080/17452759.2017.1351201.

[260] Z. Y. Chua, I. H. Ahn, and S. K. Moon, "Process monitoring and inspection systems in metal additive manufacturing: Status and applications," *International Journal of Precision Engineering and Manufacturing-Green Technology 2017 4:2*, vol. 4, no. 2, pp. 235–245, Apr. 2017, doi: 10.1007/S40684-017-0029-7.

[261] H. Rezaeifar and M. A. Elbestawi, "On-line melt pool temperature control in L-PBF additive manufacturing," *International Journal of Advanced Manufacturing Technology*, vol. 112, no. 9–10, pp. 2789–2804, Feb. 2021, doi: 10.1007/S00170-020-06441-0/TABLES/6.

[262] W. E. Frazier, "Metal additive manufacturing: A review," *J Mater Eng Perform*, vol. 23, no. 6, pp. 1917–1928, Apr. 2014, doi: 10.1007/S11665-014-0958-Z/FIGURES/9.

[263] I. Yadroitsev, P. Krakhmalev, and I. Yadroitsava, "Selective laser melting of Ti6Al4V alloy for biomedical applications: Temperature monitoring and microstructural evolution," *J Alloys Compd*, vol. 583, pp. 404–409, Jan. 2014, doi: 10.1016/J.JALLCOM.2013.08.183.

[264] S. Clijsters, T. Craeghs, S. Buls, K. Kempen, and J. P. Kruth, "In situ quality control of the selective laser melting process using a high-speed, real-time melt pool monitoring system," *The International Journal of Advanced Manufacturing Technology 2014 75:5*, vol. 75, no. 5, pp. 1089–1101, Aug. 2014, doi: 10.1007/S00170-014-6214-8.

[265] M. Doubenskaia, M. Pavlov, and Y. Chivel, "Optical System for On-Line Monitoring and Temperature Control in Selective Laser Melting Technology," *Key Eng Mater*, vol. 437, pp. 458–461, 2010, doi: 10.4028/WWW.SCIENTIFIC.NET/KEM.437.458.

[266] Z. Chen, X. Zong, J. Shi, and X. Zhang, "Online Monitoring Based on Temperature Field Features and Prediction Model for Selective Laser Sintering Process," *Applied Sciences 2018, Vol. 8, Page 2383*, vol. 8, no. 12, p. 2383, Nov. 2018, doi: 10.3390/APP8122383.

[267] R. J. Hebert, "Viewpoint: metallurgical aspects of powder bed metal additive manufacturing," *J Mater Sci*, vol. 51, no. 3, pp. 1165–1175, Feb. 2016, doi: 10.1007/S10853-015-9479-X/FIGURES/4.

[268] B. Guo, J. Sun, Y. F. Lu, and L. Jiang, "Ultrafast dynamics observation during femtosecond laser-material interaction," *International Journal of Extreme Manufacturing*, vol. 1, no. 3, p. 032004, Sep. 2019, doi: 10.1088/2631-7990/AB3A24.

[269] L. Jonušauskas, S. Juodkazis, and M. Malinauskas, "Optical 3D printing: bridging the gaps in the mesoscale," *Journal of Optics*, vol. 20, no. 5, p. 053001, Apr. 2018, doi: 10.1088/2040-8986/AAB3FE.

[270] T. Baldacchini, M. Zimmerley, C. H. Kuo, E. O. Potma, and R. Zadoyan, "Characterization of microstructures fabricated by two-photon polymerization using coherent anti-stokes raman scattering microscopy," *Journal of Physical Chemistry B*, vol. 113, no. 38, pp. 12663–12668, Sep. 2009, doi: 10.1021/JP9058998/SUPPL_FILE/JP9058998_SI_001.PDF.

[271] K. Obata, A. El-Tamer, L. Koch, U. Hinze, and B. N. Chichkov, "High-aspect 3D two-photon polymerization structuring with widened objective working range (WOW-2PP)," *Light: Science & Applications 2013 2:12*, vol. 2, no. 12, pp. e116–e116, Dec. 2013, doi: 10.1038/lsa.2013.72.

[272] Y. Boiko *et al.*, "Cationic two-photon induced polymerization with high dynamic range," *Optics Express, Vol. 8, Issue 10, pp. 571-584*, vol. 8, no. 10, pp. 571–584, May 2001, doi: 10.1364/OE.8.000571.

[273] Y. Nakata and T. Okada, "Time-resolved microscopic imaging of the laser-induced forward transfer process," *Applied Physics A 1999 69:1*, vol. 69, no. 1, pp. S275–S278, 1999, doi: 10.1007/S003390051399.

[274] M. Feinaeugle, A. P. Alloncle, P. Delaporte, C. L. Sones, and R. W. Eason, "Time-resolved shadowgraph imaging of femtosecond laser-induced forward transfer of solid materials," *Appl Surf Sci*, vol. 258, no. 22, pp. 8475–8483, Sep. 2012, doi: 10.1016/J.APSUSC.2012.04.101.

[275] T. v. Kononenko, P. Alloncle, V. I. Konov, and M. Sentis, "Shadowgraphic imaging of laser transfer driven by metal film blistering," *Applied Physics A 2010 102:1*, vol. 102, no. 1, pp. 49–54, Oct. 2010, doi: 10.1007/S00339-010-6083-4.

[276] B. H. In'T Veld, L. Overmeyer, M. Schmidt, K. Wegener, A. Malshe, and P. Bartolo, "Micro additive manufacturing using ultra short laser pulses," *CIRP Annals*, vol. 64, no. 2, pp. 701–724, Jan. 2015, doi: 10.1016/J.CIRP.2015.05.007.

[277] J. v. Gordon *et al.*, "Defect structure process maps for laser powder bed fusion additive manufacturing," *Addit Manuf*, vol. 36, p. 101552, Dec. 2020, doi: 10.1016/J.ADDMA.2020.101552.

[278] M. Malinauskas *et al.*, "Ultrafast laser processing of materials: from science to industry," *Light Sci Appl*, vol. 5, no. 8, Aug. 2016, doi: 10.1038/LSA.2016.133.

[279] C. R. K. Marrian and D. M. Tennant, "Nanofabrication," *Journal of Vacuum Science & Technology A: Vacuum, Surfaces, and Films*, vol. 21, no. 5, p. S207, Sep. 2003, doi: 10.1116/1.1600446.

[280] L. Jonušauskas, D. Gailevičius, S. Rekštytė, S. Juodkazis, M. Malinauskas Linas Jonušauskas, and M. Malinauskas, "Synchronization of linear stages and galvo-scanners for efficient direct laser fabrication of polymeric 3D meso-scale structures," *https://doi.org/10.1117/12.2287669*, vol. 10523, pp. 132–139, Feb. 2018, doi: 10.1117/12.2287669.

[281] J. I. Kato, N. Takeyasu, Y. Adachi, Sun Hong-Bo, and S. Kawata, "Multiple-spot parallel processing for laser micronanofabrication," *Appl Phys Lett*, vol. 86, no. 4, p. 044102, Jan. 2005, doi: 10.1063/1.1855404.

[282] X. Z. Dong, Z. S. Zhao, and X. M. Duan, "Micronanofabrication of assembled three-dimensional microstructures by designable multiple beams multiphoton processing," *Appl Phys Lett*, vol. 91, no. 12, p. 124103, Sep. 2007, doi: 10.1063/1.2789661.

[283] L. Yang *et al.*, "Parallel direct laser writing of micro-optical and photonic structures using spatial light modulator," *Opt Lasers Eng*, vol. 70, pp. 26–32, Jul. 2015, doi: 10.1016/J.OPTLASENG.2015.02.006.

[284] G. Vizsnyiczai, L. Kelemen, and P. Ormos, "Holographic multi-focus 3D two-photon polymerization with real-time calculated holograms," *Optics Express, Vol. 22, Issue 20, pp. 24217-24223*, vol. 22, no. 20, pp. 24217–24223, Oct. 2014, doi: 10.1364/OE.22.024217.

[285] J. Wang, S. Sun, H. Zhang, S. Hasegawa, P. Wang, and Y. Hayasaki, "Holographic Femtosecond Laser Parallel Processing Method Based on the Fractional Fourier Transform," *Opt Lasers Eng*, vol. 146, p. 106704, Nov. 2021, doi: 10.1016/J.OPTLASENG.2021.106704.

[286] B. Mills *et al.*, "Single-pulse multiphoton polymerization of complex structures using a digital multimirror device," *Optics Express, Vol. 21, Issue 12, pp. 14853-14858*, vol. 21, no. 12, pp. 14853–14858, Jun. 2013, doi: 10.1364/OE.21.014853.

[287] C.-Y. Chang, C.-H. Lien, L.-C. Cheng, P. J. Campagnola, S.-J. Chen, and Y.-C. Li, "Fast multiphoton microfabrication of freeform polymer microstructures by spatiotemporal focusing and patterned excitation," *Optics Express, Vol. 20, Issue 17, pp. 19030-19038*, vol. 20, no. 17, pp. 19030–19038, Aug. 2012, doi: 10.1364/OE.20.019030.

[288] V. Hahn *et al.*, "Rapid Assembly of Small Materials Building Blocks (Voxels) into Large Functional 3D Metamaterials," *Adv Funct Mater*, vol. 30, no. 26, p. 1907795, Jun. 2020, doi: 10.1002/ADFM.201907795.

[289] F. Zacharatos, M. Makrygianni, and I. Zergioti, "Laser-Induced Forward Transfer (LIFT) Technique as an Alternative for Assembly and Packaging of Electronic Components," *IEEE Journal of Selected Topics in Quantum Electronics*, vol. 27, no. 6, Nov. 2021, doi: 10.1109/JSTQE.2021.3084443.

[290] E. Biver *et al.*, "High-speed multi-jets printing using laser forward transfer: time-resolved study of the ejection dynamics," *Optics Express, Vol. 22, Issue 14, pp. 17122-17134*, vol. 22, no. 14, pp. 17122–17134, Jul. 2014, doi: 10.1364/OE.22.017122.

[291] D. Puerto, E. Biver, A. P. Alloncle, and P. Delaporte, "Single step high-speed printing of continuous silver lines by laser-induced forward transfer," *Appl Surf Sci*, vol. 374, pp. 183–189, Jun. 2016, doi: 10.1016/J.APSUSC.2015.11.017.

[292] R. C. Y Auyeung *et al.*, "Laser forward transfer using structured light," *Optics Express, Vol. 23, Issue 1, pp. 422-430*, vol. 23, no. 1, pp. 422–430, Jan. 2015, doi: 10.1364/OE.23.000422.

[293] A. Piqué, H. Kim, R. C. Y. Auyeung, and S. Mathews, "Spatially modulated laser pulses for printing electronics," *Applied Optics, Vol. 54, Issue 31, pp. F70-F77*, vol. 54, no. 31, pp. F70–F77, Nov. 2015, doi: 10.1364/AO.54.000F70.

[294] D. J. Heath *et al.*, "Dynamic spatial pulse shaping via a digital micromirror device for patterned laser-induced forward transfer of solid polymer films," *Optical Materials Express, Vol. 5, Issue 5, pp. 1129-1136*, vol. 5, no. 5, pp. 1129–1136, May 2015, doi: 10.1364/OME.5.001129.

[295] A. Narazaki, T. Sato, R. Kurosaki, Y. Kawaguchi, and H. Niino, "Nano- and microdot array formation of FeSi2 by nanosecond excimer laser-induced forward transfer," *Applied Physics Express*, vol. 1, no. 5, pp. 0570011–0570013, May 2008, doi: 10.1143/APEX.1.057001/XML.

[296] J. Qi *et al.*, "Femtosecond laser induced selective etching in fused silica: optimization of the inscription conditions with a high-repetition-rate laser source," *Optics Express, Vol. 26, Issue 23, pp. 29669-29678*, vol. 26, no. 23, pp. 29669–29678, Nov. 2018, doi: 10.1364/OE.26.029669.

[297] K. Sugioka *et al.*, "Femtosecond laser 3D micromachining: a powerful tool for the fabrication of microfluidic, optofluidic, and electrofluidic devices based on glass," *Lab Chip*, vol. 14, no. 18, pp. 3447–3458, Aug. 2014, doi: 10.1039/C4LC00548A.

[298] S. Kiyama, S. Matsuo, S. Hashimoto, and Y. Morihira, "Examination of etching agent and etching mechanism on femotosecond laser microfabrication of channels inside vitreous silica substrates," *Journal of Physical Chemistry C*, vol. 113, no. 27, pp. 11560–11566, Jul. 2009, doi: 10.1021/JP900915R/SUPPL_FILE/JP900915R_SI_001.PDF.

[299] D. Andrijec *et al.*, "Hybrid additive-subtractive femtosecond 3D manufacturing of nanofilter-based microfluidic separator," *Appl Phys A Mater Sci Process*, vol. 127, no. 10, pp. 1–7, Oct. 2021, doi: 10.1007/S00339-021-04872-4/FIGURES/5.

[300] J. Bonse *et al.*, "Tribological performance of sub-100-nm femtosecond laser-induced periodic surface structures on titanium," *Appl Surf Sci*, vol. 374, pp. 190–196, Jun. 2016, doi: 10.1016/J.APSUSC.2015.11.019.

[301] A. H. A. Lutey *et al.*, "Towards Laser-Textured Antibacterial Surfaces," *Scientific Reports 2018 8:1*, vol. 8, no. 1, pp. 1–10, Jul. 2018, doi: 10.1038/s41598-018-28454-2.

[302] S. v. Kirner *et al.*, "Mimicking bug-like surface structures and their fluid transport produced by ultrashort laser pulse irradiation of steel," *Appl Phys A Mater Sci Process*, vol. 123, no. 12, pp. 1–13, Dec. 2017, doi: 10.1007/S00339-017-1317-3/FIGURES/14.

[303] B. E. J. Lee, H. Exir, A. Weck, and K. Grandfield, "Characterization and evaluation of femtosecond laser-induced sub-micron periodic structures generated on titanium to improve osseointegration of implants," *Appl Surf Sci*, vol. 441, pp. 1034–1042, May 2018, doi: 10.1016/J.APSUSC.2018.02.119.

[304] B. Mills, J. A. Grant-Jacob, M. Praeger, M. D. T. McDonnell, and R. W. Eason, "Identification of spatial intensity profiles from femtosecond laser machined depth profiles via neural networks," *Optics Express, Vol. 29, Issue 22, pp. 36469-36486*, vol. 29, no. 22, pp. 36469–36486, Oct. 2021, doi: 10.1364/OE.431441.

[305] Y. Xie *et al.*, "Deep learning for the monitoring and process control of femtosecond laser machining," *Journal of Physics: Photonics*, vol. 1, no. 3, p. 035002, Jun. 2019, doi: 10.1088/2515-7647/AB281A.

[306] S. Park, Y. Kim, J. You, and S. W. Kim, "Damage-free cutting of chemically strengthened glass by creation of sub-surface cracks using femtosecond laser pulses," *CIRP Annals*, vol. 66, no. 1, pp. 535–538, Jan. 2017, doi: 10.1016/J.CIRP.2017.04.071.

[307] C. H. Hung and F. Y. Chang, "Curve micromachining on the edges of nitinol biliary stent by ultrashort pulses laser," *Opt Laser Technol*, vol. 90, pp. 1–6, May 2017, doi: 10.1016/J.OPTLASTEC.2016.10.018.

[308] F. Zhang *et al.*, "Temperature effects on the geometry during the formation of micro-holes fabricated by femtosecond laser in PMMA," *Opt Laser Technol*, vol. 100, pp. 256–260, Mar. 2018, doi: 10.1016/J.OPTLASTEC.2017.10.014.

[309] W. Zhao, X. Shen, H. Liu, L. Wang, and H. Jiang, "Effect of high repetition rate on dimension and morphology of micro-hole drilled in metals by picosecond ultra-short pulse laser," *Opt Lasers Eng*, vol. 124, p. 105811, Jan. 2020, doi: 10.1016/J.OPTLASENG.2019.105811.

[310] L. Kaden *et al.*, "Selective laser melting of copper using ultrashort laser pulses," *Applied Physics A 2017 123:9*, vol. 123, no. 9, pp. 1–6, Aug. 2017, doi: 10.1007/S00339-017-1189-6.

[311] G. Matras *et al.*, "10 kHz water-cooled Ti :Sapphire femtosecond laser," *Optics Express, Vol. 15, Issue 12, pp. 7528-7536*, vol. 15, no. 12, pp. 7528–7536, Jun. 2007, doi: 10.1364/OE.15.007528.

[312] S. Cho, J. Jeong, S. Hwang, and T. J. Yu, "Thermal lens effect model of Ti: Sapphire for use in high-power laser amplifiers," *Applied Physics Express*, vol. 11, no. 9, p. 092701, Sep. 2018, doi: 10.7567/APEX.11.092701/XML.

[313] A. Y. Vorobyev, V. M. Kuzmichev, N. G. Kokody, P. Kohns, J. Dai, and C. Guo, "Residual thermal effects in Al following single ns- and fs-laser pulse ablation," *Applied Physics A 2005 82:2*, vol. 82, no. 2, pp. 357–362, Nov. 2005, doi: 10.1007/S00339-005-3412-0.

[314] A. Ancona, A. Tünnermann, F. Röser, J. Limpert, K. Rademaker, and S. Nolte, "High speed laser drilling of metals using a high repetition rate, high average power ultrafast fiber CPA system," *Optics Express, Vol. 16, Issue 12, pp. 8958-8968*, vol. 16, no. 12, pp. 8958–8968, Jun. 2008, doi: 10.1364/OE.16.008958.

[315] A. Ancona *et al.*, "Femtosecond and picosecond laser drilling of metals at high repetition rates and average powers," *Optics Letters, Vol. 34, Issue 21, pp. 3304-3306*, vol. 34, no. 21, pp. 3304–3306, Nov. 2009, doi: 10.1364/OL.34.003304.

[316] S. M. Eaton *et al.*, "Transition from thermal diffusion to heat accumulation in high repetition rate femtosecond laser writing of buried optical waveguides," *Optics Express, Vol. 16, Issue 13, pp. 9443-9458*, vol. 16, no. 13, pp. 9443–9458, Jun. 2008, doi: 10.1364/OE.16.009443.

[317] R. Weber *et al.*, "Heat accumulation during pulsed laser materials processing," *Optics Express, Vol. 22, Issue 9, pp. 11312-11324*, vol. 22, no. 9, pp. 11312–11324, May 2014, doi: 10.1364/OE.22.011312.

[318] J. Finger, M. Reininghaus, von Alvensleben, A. Tünnermann, and H. Welling, "Effect of pulse to pulse interactions on ultra-short pulse laser drilling of steel with repetition rates up to 10 MHz," *Optics Express, Vol. 22, Issue 15, pp. 18790-18799*, vol. 22, no. 15, pp. 18790–18799, Jul. 2014, doi: 10.1364/OE.22.018790.

[319] S. M. Eaton *et al.*, "Heat accumulation effects in femtosecond laser-written waveguides with variable repetition rate," *Optics Express, Vol. 13, Issue 12, pp. 4708-4716*, vol. 13, no. 12, pp. 4708–4716, Jun. 2005, doi: 10.1364/OPEX.13.004708.

[320] I. Mingareev and A. Horn, "Time-resolved investigations of plasma and melt ejections in metals by pump-probe shadowgrpahy," *Applied Physics A 2008 92:4*, vol. 92, no. 4, pp. 917–920, May 2008, doi: 10.1007/S00339-008-4562-7.

[321] J. König, S. Nolte, and A. Tünnermann, "Plasma evolution during metal ablation with ultrashort laser pulses," *Opt Express*, vol. 13, no. 26, p. 10597, 2005, doi: 10.1364/OPEX.13.010597.

[322] A. Ostendorf *et al.*, "Femtosecond versus picosecond laser ablation," *https://doi.org/10.1117/12.597975*, vol. 5713, no. 12, pp. 1–8, Apr. 2005, doi: 10.1117/12.597975.

[323] S. Amoruso *et al.*, "Ultrashort laser ablation of solid matter in vacuum: a comparison between the picosecond and femtosecond regimes," *Journal of Physics B: Atomic, Molecular and Optical Physics*, vol. 38, no. 20, p. L329, Sep. 2005, doi: 10.1088/0953-4075/38/20/L01.

[324] P. P. Pronko, S. K. Dutta, J. Squier, J. v. Rudd, D. Du, and G. Mourou, "Machining of sub-micron holes using a femtosecond laser at 800 nm," *Opt Commun*, vol. 114, no. 1–2, pp. 106–110, Jan. 1995, doi: 10.1016/0030-4018(94)00585-I.

[325] S. S. Harilal, J. R. Freeman, P. K. Diwakar, and A. Hassanein, "Femtosecond laser ablation: Fundamentals and applications," *Springer Series in Optical Sciences*, vol. 182, pp. 143–166, 2014, doi: 10.1007/978-3-642-45085-3_6/FIGURES/12.

[326] A. Borowiec, H. F. Tiedje, and H. K. Haugen, "Wavelength dependence of the single pulse femtosecond laser ablation threshold of indium phosphide in the 400–2050 nm range," *Appl Surf Sci*, vol. 243, no. 1–4, pp. 129–137, Apr. 2005, doi: 10.1016/J.APSUSC.2004.09.105.

[327] R. N. Oosterbeek, S. Ashforth, O. Bodley, and M. C. Simpson, "Ablation threshold dependence on incident wavelength during ultrashort pulsed laser ablation," *Int J Nanotechnol*, vol. 14, no. 1–6, pp. 313–322, 2017, doi: 10.1504/IJNT.2017.082452.

[328] J. Gunasekaran, P. Sevvel, and I. J. Solomon, "Metallic materials fabrication by selective laser melting: A review," *Mater Today Proc*, vol. 37, no. Part 2, pp. 252–256, Jan. 2021, doi: 10.1016/J.MATPR.2020.05.162.

[329] P. K. Gokuldoss, S. Kolla, and J. Eckert, "Additive Manufacturing Processes: Selective Laser Melting, Electron Beam Melting and Binder Jetting—Selection Guidelines," *Materials*, vol. 10, no. 6, 2017, doi: 10.3390/MA10060672.

[330] K. G. Prashanth, S. Scudino, and J. Eckert, "Defining the tensile properties of Al-12Si parts produced by selective laser melting," *Acta Mater*, vol. 126, pp. 25–35, Mar. 2017, doi: 10.1016/J.ACTAMAT.2016.12.044.

[331] C. Y. Yap *et al.*, "Review of selective laser melting: Materials and applications," *Appl Phys Rev*, vol. 2, no. 4, p. 041101, Dec. 2015, doi: 10.1063/1.4935926.

[332] D. A. Hollander *et al.*, "Structural, mechanical and in vitro characterization of individually structured Ti–6Al–4V produced by direct laser forming," *Biomaterials*, vol. 27, no. 7, pp. 955–963, Mar. 2006, doi: 10.1016/J.BIOMATERIALS.2005.07.041.

[333] W. Xu *et al.*, "Additive manufacturing of strong and ductile Ti–6Al–4V by selective laser melting via in situ martensite decomposition," *Acta Mater*, vol. 85, pp. 74–84, Feb. 2015, doi: 10.1016/J.ACTAMAT.2014.11.028.

[334] G. Lutjering and J. C. Williams, "Alpha + Beta Alloys," in *Titanium*, Springer, Berlin, Heidelberg, 2007, pp. 203–258. doi: 10.1007/978-3-540-73036-1_5.

[335] H. Hassanin *et al.*, "Tailoring selective laser melting process for titanium drug-delivering implants with releasing micro-channels," *Addit Manuf*, vol. 20, pp. 144–155, Mar. 2018, doi: 10.1016/J.ADDMA.2018.01.005.

[336] E. Uhlmann, R. Kersting, T. B. Klein, M. F. Cruz, and A. V. Borille, "Additive Manufacturing of Titanium Alloy for Aircraft Components," *Procedia CIRP*, vol. 35, pp. 55–60, Jan. 2015, doi: 10.1016/J.PROCIR.2015.08.061.

[337] "ASM Material Data Sheet." https://asm.matweb.com/search/SpecificMaterial.asp?bassnum=MTP641 (accessed Sep. 16, 2022).

[338] I. Gurrappa, "Characterization of titanium alloy Ti-6Al-4V for chemical, marine and industrial applications," *Mater Charact*, vol. 51, no. 2–3, pp. 131–139, Oct. 2003, doi: 10.1016/J.MATCHAR.2003.10.006.

[339] S. Bagehorn, J. Wehr, and H. J. Maier, "Application of mechanical surface finishing processes for roughness reduction and fatigue improvement of additively manufactured Ti-6Al-4V parts," *Int J Fatigue*, vol. 102, pp. 135–142, Sep. 2017, doi: 10.1016/J.IJFATIGUE.2017.05.008.

[340] D. Wang, W. Dou, and Y. Yang, "Research on Selective Laser Melting of Ti6Al4V: Surface Morphologies, Optimized Processing Zone, and Ductility Improvement Mechanism," *Metals 2018, Vol. 8, Page 471*, vol. 8, no. 7, p. 471, Jun. 2018, doi: 10.3390/MET8070471.

[341] G. Pyka, G. Kerckhofs, I. Papantoniou, M. Speirs, J. Schrooten, and M. Wevers, "Surface Roughness and Morphology Customization of Additive Manufactured Open Porous Ti6Al4V Structures," *Materials 2013, Vol. 6, Pages 4737-4757*, vol. 6, no. 10, pp. 4737–4757, Oct. 2013, doi: 10.3390/MA6104737.

[342] Z. Chen, S. Cao, X. Wu, and C. H. J. Davies, "Surface roughness and fatigue properties of selective laser melted Ti–6Al–4V alloy," *Additive Manufacturing for the Aerospace Industry*, pp. 283–299, Jan. 2019, doi: 10.1016/B978-0-12-814062-8.00015-7.

[343] C. Wang *et al.*, "Enhanced Osseointegration of Titanium Alloy Implants with Laser Microgrooved Surfaces and Graphene Oxide Coating," *ACS Appl Mater Interfaces*, vol. 11, no. 43, pp. 39470–39483, Oct. 2019, doi: 10.1021/ACSAMI.9B12733/SUPPL_FILE/AM9B12733_SI_001.PDF.

[344] G. Strano, L. Hao, R. M. Everson, and K. E. Evans, "Surface roughness analysis, modelling and prediction in selective laser melting," *J Mater Process Technol*, vol. 213, no. 4, pp. 589–597, Apr. 2013, doi: 10.1016/J.JMATPROTEC.2012.11.011.

[345] J. Saurí *et al.*, "Relationships between surface free energy, surface texture parameters and controlled drug release in hydrophilic matrices," *Int J Pharm*, vol. 478, no. 1, pp. 328–340, Jan. 2015, doi: 10.1016/J.IJPHARM.2014.11.054.

[346] A. Ilin *et al.*, "Computer Aided Optimisation of the Thermal Management During Laser Beam Melting Process," *Phys Procedia*, vol. 56, no. C, pp. 390–399, Jan. 2014, doi: 10.1016/J.PHPRO.2014.08.142.

[347] S. Moradi, S. Kamal, P. Englezos, and S. G. Hatzikiriakos, "Femtosecond laser irradiation of metallic surfaces: effects of laser parameters on superhydrophobicity," *Nanotechnology*, vol. 24, no. 41, p. 415302, Sep. 2013, doi: 10.1088/0957-4484/24/41/415302.

[348] G. Schnell, U. Duenow, and H. Seitz, "Effect of Laser Pulse Overlap and Scanning Line Overlap on Femtosecond Laser-Structured Ti6Al4V Surfaces," *Materials 2020, Vol. 13, Page 969*, vol. 13, no. 4, p. 969, Feb. 2020, doi: 10.3390/MA13040969.

[349] R. Paschotta and Society of Photo-optical Instrumentation Engineers., "Field guide to lasers," p. 139, 2008, Accessed: Sep. 17, 2022. [Online]. Available: https://books.google.com/books/about/Field_Guide_to_Lasers.html?id=02s6wyYULYAC

[350] V. Vercillo *et al.*, "Design Rules for Laser-Treated Icephobic Metallic Surfaces for Aeronautic Applications," *Adv Funct Mater*, vol. 30, no. 16, p. 1910268, Apr. 2020, doi: 10.1002/ADFM.201910268.

[351] A. Cunha *et al.*, "Femtosecond laser surface texturing of titanium as a method to reduce the adhesion of Staphylococcus aureus and biofilm formation," *Appl Surf Sci*, vol. 360, pp. 485–493, Jan. 2016, doi: 10.1016/J.APSUSC.2015.10.102.

[352] S. Rung *et al.*, "Possibilities of Dry and Lubricated Friction Modification Enabled by Different Ultrashort Laser-Based Surface Structuring Methods," *Lubricants 2019, Vol. 7, Page 43*, vol. 7, no. 5, p. 43, May 2019, doi: 10.3390/LUBRICANTS7050043.

[353] L. Orazi, I. Gnilitskyi, and A. P. Serro, "Laser nanopatterning for wettability applications," *J Micro Nanomanuf*, vol. 5, no. 2, Jun. 2017, doi: 10.1115/1.4035956/369675.

[354] L. Piccolo, K. Puleo, M. Sorgato, G. Lucchetta, and D. Masato, "Modeling the replication of submicron-structured surfaces by micro injection molding," *Mater Des*, vol. 198, p. 109272, Jan. 2021, doi: 10.1016/J.MATDES.2020.109272.

[355] E. J. Y. Ling, J. Saïd, N. Brodusch, R. Gauvin, P. Servio, and A. M. Kietzig, "Investigating and understanding the effects of multiple femtosecond laser scans on the surface topography of stainless steel 304 and titanium," *Appl Surf Sci*, vol. 353, pp. 512–521, Oct. 2015, doi: 10.1016/J.APSUSC.2015.06.137.

[356] K. M. Tanvir Ahmmed, C. Grambow, and A. M. Kietzig, "Fabrication of micro/nano structures on metals by femtosecond laser micromachining," *Micromachines (Basel)*, vol. 5, no. 4, pp. 1219–1253, 2014, doi: 10.3390/MI5041219.

[357] M. Nosonovsky and B. Bhushan, "Hierarchical roughness optimization for biomimetic superhydrophobic surfaces," *Ultramicroscopy*, vol. 107, no. 10–11, pp. 969–979, Oct. 2007, doi: 10.1016/J.ULTRAMIC.2007.04.011.

[358] A. Y. Vorobyev and C. Guo, "Enhanced absorptance of gold following multipulse femtosecond laser ablation," *Phys Rev B Condens Matter Mater Phys*, vol. 72, no. 19, p. 195422, Nov. 2005, doi: 10.1103/PHYSREVB.72.195422/FIGURES/7/MEDIUM.

[359] K. Kuršelis, R. Kiyan, and B. N. Chichkov, "Formation of corrugated and porous steel surfaces by femtosecond laser irradiation," *Appl Surf Sci*, vol. 258, no. 22, pp. 8845–8852, Sep. 2012, doi: 10.1016/J.APSUSC.2012.05.102.

[360] W. Perrie, M. Gill, G. Robinson, P. Fox, and W. O'Neill, "Femtosecond laser micro-structuring of aluminium under helium," *Appl Surf Sci*, vol. 230, no. 1–4, pp. 50–59, May 2004, doi: 10.1016/J.APSUSC.2003.12.035.

[361] M. v. Shugaev *et al.*, "Laser-Induced Thermal Processes: Heat Transfer, Generation of Stresses, Melting and Solidification, Vaporization, and Phase Explosion," *Handbook of Laser Micro- and Nano-Engineering*, pp. 1–81, 2020, doi: 10.1007/978-3-319-69537-2_11-1.

[362] A. Cunha, A. P. Serro, V. Oliveira, A. Almeida, R. Vilar, and M. C. Durrieu, "Wetting behaviour of femtosecond laser textured Ti-6Al-4V surfaces," *Appl Surf Sci*, vol. 265, pp. 688–696, Jan. 2013, doi: 10.1016/J.APSUSC.2012.11.085.